Composites of Biopolymers and Tungsten Disulphide Nanotubes

by

Eimear Mary Magee

A thesis submitted in partial fulfilment of the requirements for

the degree of

Doctor of Philosophy in Engineering

University of Warwick

Warwick Manufacturing Group

International Institute for Nanocomposites Manufacturing

February 2023

Contents

Contents ii
List of Figures iv
List of Tables x
List of Abbreviations xii
Acknowledgements xiv
Declaration of Authorship xv
Abstract 1
Chapter 1: Introduction 2
1.1 Background 2
1.2 Research problem 4
1.3 Research Strategy 5
1.4 Structure of thesis 7
1.5 Contribution to knowledge 9
1.6 Aims and Objectives 10
Chapter 2: Literature Review 13
2.1.0 Tungsten Disulfide Nanotubes 13
2.1.1 Synthesis and Structure of WS_2 NTs 14
2.1.2 Properties of WS_2 NTs 19
2.2.0 Biopolymers 23
2.2.1 Poly(lactic acid) 25
2.2.2 Synthesis and structure of PLA 27
2.2.3 Properties of PLA 29
2.2.4 Chitosan 31
2.2.5 Synthesis and Structure of Chitosan 32
2.2.6 Properties of Chitosan 33
2.3.0 Nanocomposites 35
2.3.1 Methods of Nanocomposite preparation 35
2.3.2 Composites of PLA and WS_2 NTs 38
2.3.3 WS_2 Biopolymer Composites 43
2.3.4 Composites of WS_2 NTs and other Polymers 46
2.3.5 Surface Modification of WS_2 NTs 50
2.3.6 Composites of Chitosan and Nanofillers 52

2.4.0 Concluding remarks 56
Chapter 3: Materials and Methods 58
3.1. Materials 58
3.2 Sample Preparation 59
3.3 Characterisation Techniques 62
Chapter 4: Results and Discussion I 72
4.1 Introduction 72
4.2 Characterisation of WS_2 NTs 73
4.3 Characterisation of WS_2 NTs PLA Composites 88
4.4 Conclusions 100
Chapter 5: Results and Discussion II 102
5.1 Introduction 102
5.2 Characterisation of APTES Functionalised WS_2 NTs 103
5.3 Characterisation of APTES Functionalised WS_2 NTs composites of PLA 118
5.4 Conclusions 128
Chapter 6: Results and Discussion III 129
6.1 Introduction 129
6.2 Characterisation of Chitosan WS_2 NTs and Glycerol Composites 129
6.3 Conclusion 160
Chapter 7: Conclusions and Recommendations for Future Work 162
7.1 Conclusions 162
7.2 Recommendations for Future Work 167
Journal Publications and Conference Presentations 169
Appendix 170
Results and Discussion I: WS_2 NTs and Composites of PLA 170
Results and Discussion II: APTES Functionalised WS_2 NTs and Composites of PLA 172
Results and Discussion III: Composites of Chitosan WS_2 NTs and Glycerol 178
References 182

List of Figures

Figure 1. 1. Schematic diagram showing the outline of the experimental work undertaken and characterisation methods used. 8

Figure 2.1 a) Schematic representation of the INT-WS_2 multistep growth mechanism b) TEM image of a hollow-core multiwall WS_2 nanotube. The white scale bar represents 10 nm. c) Schematic illustration of a multiwalled WS_2 NT 16

Figure 2.2 TEM images of WS_2 layers where in a) the layers are clearly identified and b) broken layers of the WS_2 nanostructure can be observed (inset shows the hexagonal atomic arrangement of the WS_2 layer/sheet. 18

Figure 2.3 Classification of biopolymers 24

Figure 2.4 Chemical structure of a): L lactic acid and D-lactic acid, b) reaction pathway for the production of PLA via ROP synthesis. 27

Figure 2.5 Chemical structure of chin and chitosan 32

Figure 2.6 Stress-strain representing curves of PLA and PLA/ WS2-NT pre- and post-printed filament, compared to solvent-casted.15. Inset: (A) – cast film, (B)- printed film, (C) – printed wire. Rule-bar to scale. 39

Figure 2.7 High-resolution SEM image for PLA/PVDF-WS_2 NTs 42

Figure 2.8 a) Compressive modulus, b) compressive yield strength, c) flexural modulus and d) flexural yield strength of PPF nanocomposites as a function of nanoparticle loading concentration. 45

Figure 2.9 Formation of INT WS_2–bithiophene composites. 51

Figure 2.10 Representative stress-strain curves of a) chitosan/ZnO, b) chitosan/glycerol/ZnO and c) chitosan/PVOH/ZnO films as a function of ZnO content, plain chitosan-based films 54

Figure 3. 1. Screw profile used for twin screw extrusion of PLA and WS_2 NTs.....59

Figure 4.1. Electron microscopy images of WS_2 NTs. (a,b) SEM images under different magnifications and (c,d) TEM images an individual WS_2 NT, the former showing a closed end. 74

Figure 4.2. (a) STEM−EDS chemical analysis of WS_2 NTs, (b) TEM identification of incomplete NT wall structures, and (c) electron diffraction pattern of the WS_2 NTs. 75

Figure 4.3 (a) TGA−MS profile for WS_2 NTs with corresponding color change through heating and the characteristic ion current curves for WS_2 NTs, (b) sulfur-containing major products, (c) oxygen-containing products, and (d) OH-containing products. 77

Figure 4.4 Thermal analysis of WS_2 NTs in an N_2 atmosphere, a) TGA and inset corresponding colour of WS_2 NTs and b) through d) TGA-MS analysis volatile elements detected. 79

Figure 4.5. Raman spectra of (a) WS_2 NTs prior to thermal treatment and (b) WS_2 NTs post-TGA−MS (WO3) analysis. 81

Figure 4.6 XRD pattern of (a) WS_2 NTs and (b) WS_2 NTs post TGA−MS. 83

Figure 4.7 XPS Survey spectra of (a) WS_2 NTs, (b) WS_2 NTs post TGA-MS (i.e. WO_3) 84

Figure 4.8 XPS analysis showing the deconvoluted spectra of WS_2 NTs (a−d) and WO_3 (e−h). 86

Figure 4.9 SEM images of WO3 particles obtained post-TGA− MS analysis of WS_2 NTs.....87

Figure 4.10 a) GPC curves from light scattering (LS) (solid lines) and the refractive index (RI) (dashed lines) detectors. Measured molecular weight (Mw) of PLA with corresponding uncertainties, b) first measurement, c) second measurement and d) averaged results. Solid blue and red horizontal lines represent the Mw of PLA pellets and dried PLA pellets (before extrusion) respectively, and corresponding dashed lines represent associated uncertainties. Square markers identify the measured Mw of unfilled PLA and composites of PLA and WS_2 NTs as a function of WS_2 NT filler loading after extrusion and uncertainties with associated error bars. 89

Figure 4.11 (a) SEM image of a PLA composite with 3 wt % WS_2 NTs, (b) STEM-BF image of PLA 3.0 wt % WS_2, and (c−e) STEM-BF images of composites of PLA and 0.1, 0.5, and 3.0 wt % WS_2 NTs, respectively. 91

Figure 4.12 Representative stress-strain curves for neat PLA and composites of PLA and WS_2 NTs.....92

Figure 4.13 DSC (a) heating and (b) cooling curves of composites of PLA and WS_2 NTs in the 25−250 °C temperature range 95

Figure 4.14 Complete crystal formation of (a) neat PLA at 9 min, (b) 0.1 wt % WS_2 NT filled PLA at 45 s, and (c) 3wt % WS_2 NT-filled PLA at 2.25 min at 145 °C 97

Figure 4.15 (a,b) WAXS 2D patterns and 1D integrated profiles and (c,d) corresponding SAXS 2D patterns and integrated 1D profiles for the as received PLA pellet, extruded PLA, and composites of WS_2 NT and PLA.....99

Figure 5.1 FTIR transmittance spectra of, a) WS_2 NTs and APTES, b) APTES functionalized WS_2 NTs in ratios of 1:1, 1:2 and 1:4, c) spectra enlarged in the range 1700-1200cm^{-1} and d) in the range 1150-600cm^{-1}.....104

Figure 5.2 a) TGA weight loss curves and b) DTA curves for WS_2 NTs, APTES and APTES modified WS2 NTs at different ratios.....106

Figure 5.3 Raman spectra of WS_2 NTs and APTES modified WS_2 NTs.....109

Figure 5.4 Survey XPS spectra a) WS_2 NTs b) WS_2:APTES 1:1 c) WS_2:APTES 1:2, d) WS_2:APTES 1:4.....112

Figure 5.5 Deconvoluted XPS spectra, a) C 1s, b) O 1s, c) W 4f , d) S 2s, e) Si 2p f) N 1s regions from the XPS spectra of WS2-APTES at a ratio of 1:4.....113

Figure 5.6 SEM and STEM imaging of APTES functionalised WS_2 NTs. a-c) SEM images of WS_2NTs: APTES at 1:1,1:2 and 1:4, respectively. d) STEM of WS_2 NTs: APTES at 1:4, and e) STEM and EDS mapping of the WS_2NTs-APTES 1:4 sample. 116

Figure 5.7 ζ potential for WS_2 NTs, and change in ζ for APTES-WS_2 NTs with increasing APTES content. 117

Figure 5.8 FTIR spectra of for PLA, a blend of PLA and APTES composites of PLA with APTES modified WS_2 NTs.....118

Figure 5.9 Schematic representation of WS_2 NTs interaction with APTES and composites of APTES modified WS_2 NT and PLA mechanism. 119

Figure 5.10 a) Representative optical photographs of film samples of PLA alone and corresponding composites and SEM micrographs of b) composite of PLA and APTES modified WS_2 NTs (1:4), c) unmodified WS_2 NTs, d) composite of PLA and WS_2 NTs:APTES 1:4 at higher magnification and e) composite of PLA WS_2 NTs:APTES 1:4 with corresponding EDS of highlighted area.....120

Figure 5.11 Representative stress-strain curves for neat PLA relative to those for a) blends of PLA and APTES and b) composites of PLA and APTES modified WS_2 NTs. 123

Figure 5.12 DSC thermograms for PLA and its blends with APTES and composites with APTES modified WS_2 NTs showing a) first cooling cycle and b) second heating cycle. 125

Figure 6.1 FTIR transmittance spectra for a) WS_2 NTs, unprocessed chitosan powder, b) glycerol and the interaction of glycerol WS_2 NTs, c) chitosan and composites of chitosan and WS_2 NTs. 130

Figure 6.2 FTIR transmittance spectra for chitosan, chitosan:glycerol (CG) blend (80:20) and composites of this blend with up to 2wt% WS_2 NTs in the wavenumber ranges, a) 3800-2600cm^{-1} b) 1800-1200cm^{-1} and c) 1200-800cm^{-1}.....133

Figure 6.3 ATR-FTIR mapping for a) chitosan, b) CG blend (80:20) and composites of the CG blend with c) 0.1wt%, d) 0.5wt% e) 1.0wt% and f) 2.0wt% WS_2 NTs, where i) are optical microscope images of the film surfaces, ii) is the integrated intensity of the amide II peak and iii) are the corresponding individual pixel spectra extracted from different regions (red, blue, and green). 135

Figure 6.4 Representative stress-strain curves for neat chitosan films and a) composites of chitosan and WS_2 NTs and b) composites of CG and WS_2 NTs. 138

Figure 6.5 a) TGA and b) DTGA curves for chitosan and composites of chitosan and WS_2 NTs and, c) TGA and d) DTGA curves for CG (80:20) blend and composites of CG and WS_2 NTs in an oxygen atmosphere. 142

Figure 6.6 a) TGA and b) DTGA curves for chitosan and composites of chitosan and WS_2 NTs and, c) TGA and d) DTGA curves for CG (80:20) blend and composites of CG and WS_2 NTs in an N_2 atmosphere.....144

Figure 6.7 XRD patterns of a) WS_2 NTs and unprocessed chitosan powder b) composites of chitosan and WS_2 NTs and c) CG blend and WS_2 NTs.....146

Figure 6.8 Raman spectra of WS_2 NTs and composites of a) chitosan and WS_2 NTs and b) CG and WS_2 NTs showing the $E2g1$ and $A1g$ modes. 148

Figure 6.9 a) photographs showing the increased flexibility of chitosan films containing glycerol and WS_2 NTs a) chitosan, b) composites of chitosan and WS_2 NTs, c) CG and d) composite of CG and 2wt% WS_2 NTs. 150

Figure 6.10 SEM micrographs of Chitosan WS_2 composites in comparison to Chitosan WS_2 Glycerol composites of corresponding wt% WS_2 NTs. 151

Figure 6.11 ζ potenial values for chitosan alone in comparison to composites of chitosan and WS2 NTs with (CG) and without glycerol. 153

Figure 6.12 Antibacterial effect of bacterial a) Chitosan and WS_2 NTs composites and b) Chitosan Glycerol WS_2 composites viability against **i))** *S. aureus* (, **(i))** *E. coli*, **iii))** *P. fluorescens* viability over a period of 8 hours. Decrease in fluorescence intensity indicating unviable bacteria for each NTs were calculated every 2 hours in comparison with positive control – (*=p<0.05, **=p<0.01, ***=p<0.001). 158

List of Tables

Table 2.1 Physical properties of PLA, PLLA and PDLA, including density, ρ , tensile strength, σ, elastic modulus, E, ultimate tensile strain, ε, glass transition temperature, T_g and melting temperature, T_m 29

Table 4.1 Elemental Ratio of WS_2 NTs and WS_2 NTs Post TGA-MS (i.e., WO_3)...85

Table 4. 2 Tensile mechanical properties of composites of PLA and WS_2 NTs.....93

Table 4.3 Thermal Parameters Determined from DSC Measurements of Extruded PLA and Composites of PLA and WS_2 NTs.....94

Table 5.1 Grafting density APTES on the surface of WS_2 NTs.....108

Table 5. 2 Element atomic % extrapolated from deconvoluted XPS data for WS_2 NTs and APTES functionalized WS_2 NTs.....111

Table 5.3 Tensile mechanical Properties of PLA and blends of PLA and APTES.121

Table 5.4 Tensile mechanical properties of PLA and composites of PLA APTES modified WS_2 NTs 122

Table 5.5 DSC parameters for neat PLA, blends of PLA and APTES, and composites of PLA and APTES modified WS_2 NTs. 126

Table 6.1 O-H and N-H peak positions for chitosan, CG blend (80:20) and composites of CG and WS_2 NTs.....132

Table 6.2 Tensile mechanical properties of chitosan and composites of chitosan and WS_2 NTs 139

Table 6.3 Tensile mechanical properties of CG (80:20) blend and composites of CG and WS_2 NTs.....140

Table 6.4 Peak maxima from DTGA curves for chitosan, (CG) blend (80:20) and composites of chitosan and WS_2 NTs and, CG and WS_2 NTs.....143

Table 6.5 Peak positions for the E^1_{2g} and A_{1g} modes and the ratio of E^1_{2g} to A_{1g} peak intensities for WS_2 NTs and composites of WS_2 NTs with chitosan and with CG. 149

Table 6.6 Permebility coefficient for oxygen (P'O2), carbon dioxide (P'CO2) and water vapour (P'WV) for chitosan, CG and composites of chitosan and WS_2 NTs with and without glycerol.....155

Table 6.7 Percentage decrease in bacterial viability from relative fluorescence intensity measured after 8 hours for Chitosan and Chitosan WS_2 NTs films. 159

Table 6.8 Percentage decrease in bacteria viability from relative fluorescence intensity measured after 8 hours for Chitosan Glycerol and Chitosan Glycerol WS_2 NTs films. 159

List of Abbreviations

OD: Zero Dimension

1D: One Dimension

2D: Two Dimension

APTES: Aminopropyltriethoxysilane

AR: Aspect Ratio

BRS: Bioresorbable Scaffolds

CNT: Carbon Nanotube

DD: Degree of Deacetylation

DSC: Differential Scanning Calorimetry

FBR: Fluidised Bed Rector

FTIR: Fourier transform Infrared

GPC: Gel Permeation Chromatography

IF: Inorganic Fullerene

INT: Inorganic Nanotube

MoS_2: Molybdenum Disulphide

NT: Nanotube

PLA: Poly (lactic acid)

POM: Polarised Optical Microscopy

SAXS: Small Angle X-ray Scattering

SEM: Scanning Electron Microscopy

TEM: Transmission Electron Microscopy

TGA: Thermo-gravimetric analysis

TGA-MS: Thermo-gravimetric analysis-mass spectroscopy

TMD: Transition-Metal Dichalcogenides

VSG: Vapor-Solid-Gas

WAXS: Wide Angle X-ray Scattering

XPS: X-Ray Photoemission Spectroscopy

XRD:X-Ray Diffraction

WS_2: Tungsten Disulphide

wt%: Weight Percentage

Acknowledgements

First and foremost, I would like to thank Prof. Tony McNally, for giving me this opportunity, and the unwavering guidance and support throughout this research project. I could not have asked for more from a mentor and supervisor during this time.

I would like to thank to Prof. Julia Kornfield and her group for welcoming me during my time in Caltech. With a special thanks to Dr Tiziana Di Luccio for being a great support and mentor for my studies, as well as welcoming me into her home and ensuring I made the most of the great opportunities given to me.

I would like to acknowledge my PhD colleagues, Dr Azzurra Miraglia, Dr Lorena Amoroso, Dr Valentina Guerra, Dr Syeda Abbas, Dr Chris Ellingford and David Reinoso, for supporting me throughout the years and making some great memories.

I would like to thank Roger Casements Coventry LGFA team and management. This team have been my home from home, having the best time with the best group of people. They all have been an unbelievable support system and will never forget my time at this club.

To my family and friends, who have always supported and encouraged me throughout my education. Those who always understood my absence at times and always welcoming me back with open arms.

To my parents, Michael and Annette, I am so grateful for your unconditional encouragement and support in my education. I wouldn't be in the position I am today without you and all of your hard work over the years. Thank you.

Finally, a special thanks to Paddy, for always being there for me, the continued support and reassurance whenever needed. Thank you for your patience and everything you have done for me over the years and for giving me something to look forward to at the end of my studies.

Declaration of Authorship

This thesis is submitted to the University of Warwick in support of my application for the degree of Doctor of Philosophy in Engineering. It has been composed by myself and has not been submitted in any previous application for any degree to any another university or higher education institution or as any part of any other submission to the University of Warwick, unless otherwise acknowledged. It describes the work carried out from October 2018 to February 2023.

The work presented included data generated and data analysis was carried out by the author except in the cases outlined below:

X-Ray Photoelectron Spectroscopy measurements and data processed by Marc Walker, Department of Physics, University of Warwick.

Wide and Small Angle X-Ray Scattering (WAXS, SAXS) were measured at APS beamline 5-ID-D at the Argonne National Laboratories by Dr Tiziana Di Luccio, Division of Chemistry and Chemical Engineering, California Institute of Technology.

Thermo-gravimetric analysis-Mass Spectroscopy (TGA-MS) analysis was done by Dr Esra Ozdemir, International institute of Nanocomposites, University of Warwick.

Gas permeability experimentation was performed by Prof. Stefano Farris, Department of Food, Environmental and Nutritional Sciences, University of Milan.

Antibacterial examination of Chitosan WS_2 Glycerol composites were performed by Andrea Dsouza, under the supervision of Dr Chrystala Constantinidou, Interdisciplinary Biomedical Research Building, Warwick Medial School, University of Warwick.

Transmission Electron Microscopy and Electron Diffraction Images were taken by Dr Fengwei Tang.

Parts of this thesis has been published by the author prior to submission:

Magee, E., et al., WS2 Nanotubes as a 1D Functional Filler for Melt Mixing with Poly(lactic acid):Implications for Composites Manufacture. ACS Applied Nano Materials, 2022. 5(5): p. 6385-6397.

Magee E, Tang F, Walker M, Zak A, Tenne R, McNally T. Silane functionalization of WS_2 nanotubes for interaction with poly (lactic acid). Nanoscale. 2023;15(16):7577-90.

Abstract

Tungsten disulphide nanotubes (WS_2NTs) continue to attract interest as functional fillers for biopolymers. However, the combined technical challenges of effective dispersion of WS_2NTs in polymer matrices and the promotion of strong interfacial interactions still need to be addressed. This work describes extensive characterisation of WS_2NTs and WS_2NTs nanocomposites in two model biopolymers, poly(lactic acid) (PLA) and chitosan.

WS_2NTs were found to be thermally stable in air up to 400 °C and have aspect ratios up to 1000. When composites of PLA and WS_2NTs, the shear stresses during extrusion resulted in breakage of NTs and a decrease in AR by >95%. Consequently, mechanical properties of nanocomposites, prepared by melt mix extrusion, were unchanged but also due to the poor interfacial interaction between NTs and PLA. Addition of WS_2NTs induced heterogeneous nucleation of PLA and resulted in an increase in the rate of crystallisation and crystalline content by 15%.

To promote interfacial interaction between WS_2NTs and PLA matrix, functionalization of WS_2NTs using 3-aminopropyltriethoxysilane (APTES) was found to bind to the surface of NTs through the formation of siloxane networks. To avoid reduction of aspect ratio, composites of the APTES modified WS_2NTs and PLA were prepared by solvent casting. The elongation at break and tensile toughness of the composite films produced using APTES functionalised WS_2 were 600% that of the unfilled PLA.

The mechanical properties of chitosan were also enhanced on inclusion of WS_2NTs, while glycerol helped promote the formation of a polyelectrolyte complex between the negatively charged NT surface and the positively charged amine groups of chitosan. The resultant films were much stronger (+40%) and tougher (+74%) that glycerol plasticised chitosan without sacrificing stiffness and ductility. The addition of WS_2 NTs to glycerol plasticised chitosan improved the gas barrier properties of the chitosan, with a 50% and 80% reduction in O_2 and CO_2 permeability respectively. Additionally, these composites displayed antimicrobial efficacy against both Gram-positive and Gram-negative bacteria.

Chapter 1: Introduction

1.1 Background

Nanotechnology and nanoengineering has become a focal point for research combining various sciences to understand material properties at the nanoscale level [1]. Nanomaterials are an interesting class of materials defined by having one or more dimensions in the range of 1 to 100 nm and typically consist of carbon, metal, metal oxides or organic matter[2].

Nanoparticles exhibit unique physical parameters, chemical and biological properties at the nanoscale in comparison to the bulk counterpart material with higher length scales [3]. These phenomena are due to a relatively larger surface area to the volume ratio, increased reactivity or stability in a chemical process, as well as enhanced mechanical and thermal properties[4].

Inorganic Nanotubes (NTs) have generated significant interest in several areas of material physics, chemistry and engineering over the past three decades since the discovery by R. Tenne et al. in 1993 [5, 6] of WS_2, from the prior exploration of analogous structures of carbon nanotubes. Various 1D nanostructures have since been developed from a range of materials, including metal dichalcogenides, halides, oxides as well as nitrides and are amongst the most studied nanomaterials [7]. Tungsten disulphide nanotubes (WS_2 NTs) continue to attract interest as they have been shown to display a wide range of interesting properties, demonstrating superior mechanical [8, 9] , thermal [10-12] , optical and electrical [13-15] properties. The development of these properties has led to advancements and the potential for nanomaterials to be applied in industry in many fields, including , energy storage [16], environmental [17, 18], as well as in medical device industries [19-25].

Additionally, WS_2 NTs have gained intense attention for application as functional fillers for inclusion in composites to generate what is termed, polymer nanocomposites [26-33]. This new class of polymer composite can exhibit exceptional properties through the translation of the properties from the nanomaterial of interest to the polymer matrix, although, this can only be achieved if several technical challenges are overcome. These include, but are not limited to, the effective dispersion of the nanomaterial in the polymer matrix and the promotion of strong interfacial interactions between components.

Currently biopolymers are also of great interest since the global issue of plastics pollution has come to the forefront of environmental concern. Biopolymers are used, and in development for use, in food applications and expansion in to the pharmaceutical and medical industries due to their unique properties, as well as meeting the growing demands for sustainability and environmental safety. Poly(lactic acid) (PLA) has been one of the most studied biopolymers for its biodegradable properties, while chitosan possesses natural biocompatibility and biodegradability as well as efficient antibacterial activity[34]. These biopolymers, one synthetic (PLA), the other natural starch (chitosan) derived from natural sources are promising materials for food packaging, healthcare applications such as tissue engineering or regenerative medicine and cardiovascular implant dressings for wounds amongst others [35-38]. Composites of biopolymers and nanomaterials may provide a route to generate sustainable advanced materials which offer a high degree of biocompatibility and biodegradability combined with desirable functionality[39-43].

1.2 Research problem

There is an increased demand for new high performance lightweight materials which can offer an alternative to petroleum based plastic materials[44]. Biopolymers have been introduced in various applications where sustainable and biodegradable solutions are needed, as well as being innovative materials for medical applications.

However, biopolymers have some major limitations, such as low mechanical strength, high brittleness, low resistance to prolonged processing temperatures, and poor heat distortion temperature[45]. The incorporation of nanoparticles in biopolymer matrices can overcome these limitations, and exhibit improved thermal, mechanical, processing capability as well as antimicrobial efficacy and decreased gas permeability which are desirable properties for use in the food and medical device industries[46].

WS_2 NTs have been used as a functional nanofiller for biopolymers due to their attractive mechanical and thermal properties, combined with their nontoxic action, this opens up WS_2 NTs for a plethora of potential other applications, such as for use in reinforcing polymers, adhesives, textiles, packaging particularly medical devices such as prosthesis, tissue engineering amongst others [47, 48]. Although, it should be noted that translating these useful filler properties to a polymer matrix has significant challenges. Any enhancement in the properties of polymer composites depend on the type of nanoparticle, their size and shape, concentration and interactions with the polymer matrix. The single most critical problem with polymer nanocomposites is the prevention of particle agglomeration, due to their high surface energy [49]. Consequently, insufficient dispersion of NTs within the polymer matrix as well as poor interfacial interaction result in composites with limited application potential.

To improve the dispersion of nanoparticles, including WS_2 NTs, within a polymer matrix, it is essential to obtain effective mixing during processing as well as understand filler surface chemistry and filler-filler, polymer-filler and polymer-polymer interfacial interaction [50]. Therefore, different processing strategies and to a much lesser extent NT surface modification have been employed to optimise NT dispersion and promote strong interfacial interactions with the biopolymer matrix.

1.3 Research Strategy

In this research project, WS_2 NTs are studied as a functional filler for two model biopolymers, one synthetic, PLA and the other naturally derived, chitosan. This work examines the impact of the inclusion of WS_2 NTs on the properties of these biopolymers with a view to possible application in the medical device and/or packaging industries.

For this purpose, the WS_2 NTs obtained are characterised in detail including thermal and chemical properties, as well as structure and morphology, with a particular focus on the surface chemistry and thermal stability of the NTs. This information is fundamental to understanding interfacial interaction and NT dispersion within biopolymers and any subsequent impact on composite properties. Additionally, this knowledge would further help optimise NT surface modification.

The dispersion and interfacial interactions of WS_2 NTs with PLA and chitosan is specifically examined based on chemical and physical structure of each component. Furthermore, different processing strategies to produce each composite are employed in an attempt to optimise the transfer of the desirable properties of WS_2 NTs to the biopolymer to form a useful composite.

For PLA, previously the inclusion of WS_2 NTs was readily achieved as they are easily dispersed in PLA due to the NTs being organophilic [51]. However, there are few previous reports where these composites are prepared via melt-blending, by way of example, in a twin screw extruder, a less environmentally contentious, more sustainable, and readily scalable method [52]. However, there may be limitations with this method, in that the high shear forces applied to the NTs during mixing may induce damage and chopping of NTs and consequently reduce NT AR. Consequently, the impact of extrusion on NTs will be analysed and the resulting properties of composites of PLA and WS_2 NTs examined.

To promote interfacial interactions between the NTs and polymers, as a mechanism for stress transfer, a strategy for the functionalisation of the surface of WS_2 NTs using a silane is investigated. Aminopropyltriethoxysilane (APTES) is an organosilane molecule which has been vastly explored for surface modification of other carbon based nanoparticles through the incorporation of covalent and noncovalent binding [53]. Therefore, APTES was identified as a sustainable and cheap route to promoting interfacial interactions between the two composite components. It is anticipated that grafting of the APTES through the formation of siloxane networks on the WS_2 NT surface would promote interaction via the pendant amine and hydroxyl groups of APTES with PLA.

Given the significant improvements achieved in mechanical properties of PLA on addition of WS_2 NTs, it was anticipated that a similar approach might yield equally encouraging results with a biopolymer derived from nature i.e. chitosan from chitin. Chitosan is a promising material for antimicrobial applications in the food industry as it is also biodegradable, nontoxic and biocompatible, as well as relatively cheap and there is abundant availability in nature[54]. Chitosan has been extensively explored

and the use of glycerol as a plasticiser, is widely used in conjunction with some nano-fillers to improve mechanical properties of chitosan films [55]. However, WS_2 NTs have not previously been explored as a functional nano-filler in a chitosan matrix. It is anticipated that the WS_2 NTs will readily disperse in the chitosan network and glycerol will increase interfacial interaction between components through hydrogen and amine bonding to form a network via polyelectrolyte complexation. The physicochemical, functional and antimicrobial properties of composites of chitosan and WS_2 NTs with and without glycerol are studied and their applicability as a food packaging material assessed.

1.4 Structure of thesis

The structure of this thesis is outlined in Figure 1.1, Chapter 1 provides an introduction to the research project and lists the project aims and objectives highlighting the novelty of the work completed. Chapter 2 provides an in-depth review of the relevant previously published literature describing the current state-of-the-art in the field. Chapter 3 describes in detail the extensive experimental work completed, including processing procedures and characterisation methods utilised. The results from the extensive characterisation of the WS_2 NTs are described in Chapter 4. The NTs were characterised using various techniques including the assessment of their thermal stability and thus suitability for melt mixing at elevated temperatures with PLA. In the second part of this chapter composites of PLA and WS_2 NTs were prepared and characterised to examine the efficiency of the melt mixing process at dispersing NTs in the PLA matrix, with experimental highlighted in Figure 1.1. The role the inclusion the NTs played, if any, on the crystallisation behaviour of PLA was also investigated.

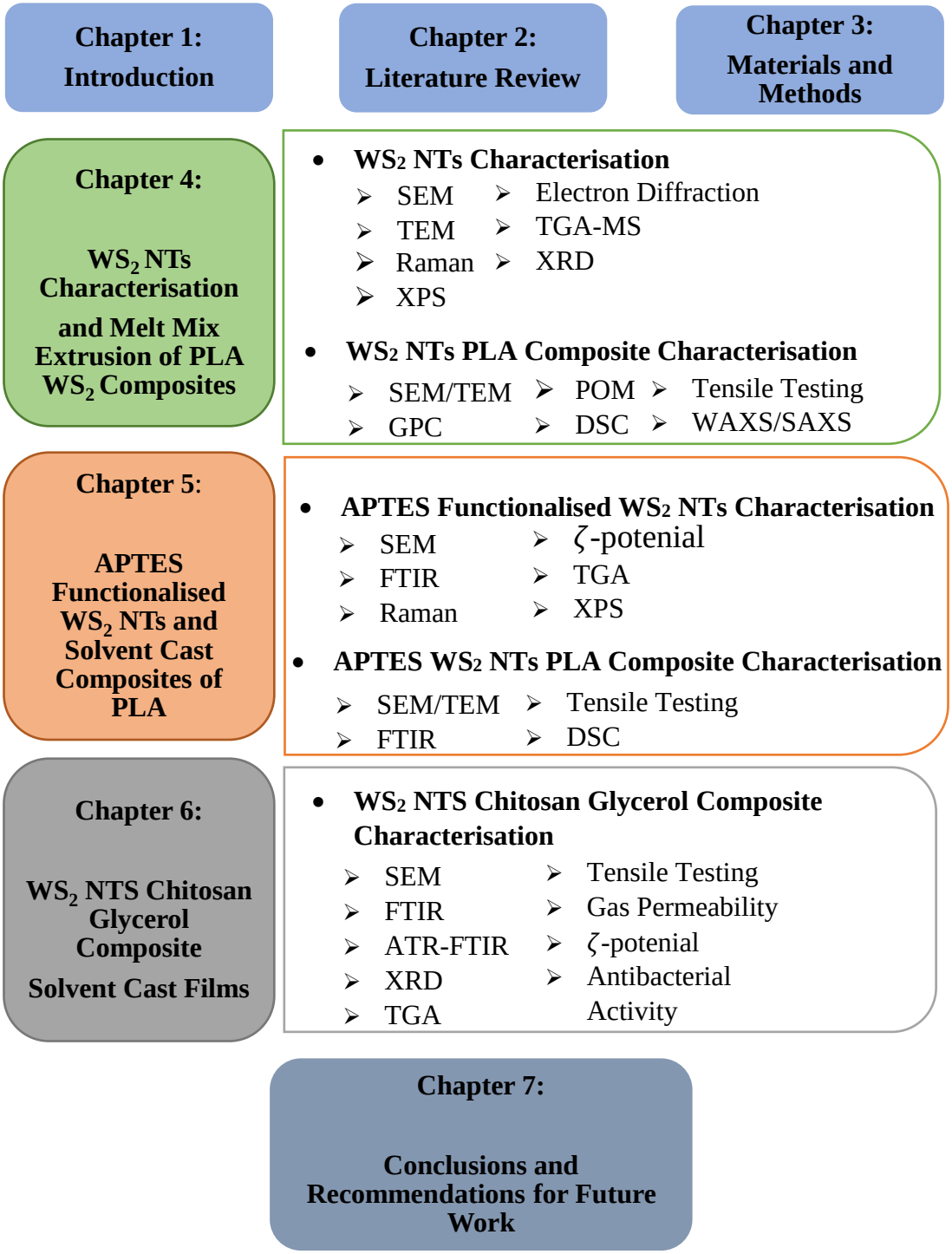

Figure 1. 1. Schematic diagram showing the outline of the experimental work undertaken and characterisation methods used.

Chapter 5 describes the study of the silane functionalisation of WS_2 NTs with APTES which is extended to include characterisation of the degree of silane grafting on the surface of the NTs by several methods, Figure 1.1. APTES functionalised WS_2 NTs were added to PLA to form composites via solvent casting. The influence of APTES on NT dispersion as well as mechanical and thermal properties of the resultant composites were studied to assess the part functionalisation plays in enhancing the mechanical properties of PLA.

Chapter 6 describes the dispersion and interfacial interaction of WS_2 NTs in a chitosan matrix using the experimental procedures listed in Figure 1.1. Additionally, the effect of inclusion of a glycerol plasticiser at a fixed concentration of 20wt% chitosan and WS_2 NTs on chitosan properties are also discussed in this chapter. The application of these composites in food packaging in particular is further discussed.

Finally, in Chapter 7, the most important conclusions from the project are discussed as well as suggestions and recommendation for future work.

1.5 Contribution to knowledge

This PhD research project provides a significant contribution to the development and understanding of WS_2 NTs and their application in the field of biopolymer composites. The work conducted provides an understanding of the fundamental structure and properties of WS_2 NTs, with a view to optimising dispersion and promoting interfacial interactions between 1D inorganic WS_2 NTs and biopolymers such that novel composites can be produced with enhanced physical properties that can be applied in industry.

The work conducted provides an in-depth characterisation of WS_2 NTs, through adding to the existing knowledge of WS_2 NTs, including their thermal profile and stability as well as a detailed understanding of NT surface chemistry, which was previously widely unreported. Understanding the thermal stability of WS_2 NTs is important for the viability of NT application in melt mixing methods to produce PLA nanocomposites.

Additionally, the surface chemistry of WS_2 NTs is vital for the development and promotion of interfacial interactions between the NT surface and PLA. The novelty in this work lies in the facile silane surface functionalisation of WS_2 NTs which promotes interfacial interaction between the NTs and the PLA matrix resulting in significant improvements in mechanical properties.

The inclusion of WS_2 NTs in another model biopolymer was demonstrated by inclusion in a chitosan with and without the addition of a plasticiser, glycerol. In this aspect of the work, the formation of a polyelectrolyte complex between the negatively charged NT surface and the glycerol plasticised chitosan was explored.

1.6 Aims and Objectives

The aims of this project are:

1. To investigate the structural, thermal stability and chemical properties of WS_2 NTs.
2. To prepare composites of WS_2 NTs and PLA via industrially viable and sustainable methods i.e., melt-mixing/extrusion.

3. To investigate the impact of composite preparation on the AR of the WS_2 NTs the role inclusion of the WS_2 NTs have on the morphology, thermal and crystalline properties of two model biopolymers, PLA and chitosan.

4. To functionalise WS_2 NTs using a cheap and scalable approach that promotes interfacial interactions between WS_2 NTs and APTES.

5. To prepare composites of silane functionalised WS_2 NTs and PLA, though solution casting method, and determine the effectiveness of silane functionalisation on NT dispersion and interaction with the PLA matrix.

6. To prepare composites of chitosan and WS_2 NTs in film form by solvent casting, and determine the role of glycerol as plasticising agent on the chitosan properties.

7. To examine the interaction between WS_2 NTs, chitosan and glycerol and identify the potential of WS_2 NT filled chitosan to form polyelectrolyte complexes.

The objectives of this project are:

1. To characterise the morphology, thermal and chemical structure of WS_2 NTs, with particular focus on the surface chemistry and thermal stability of the NTs, using Scanning Electron Microscopy (SEM)/Transmission Electron Microscopy (TEM), Thermo-gravimetric analysis-mass spectroscopy (TGA-MS), and X-Ray Photoemission Spectroscopy (XPS), X-Ray Diffraction (XRD), and Raman spectroscopy.

2. To study the effect of melt mixing WS_2 NTs and PLA in an extruder on the aspect ratio of the NTs and consequently on the mechanical properties and the

crystallization behaviour of composites of PLA and WS_2 NTs using SEM/TEM, Wide Angle X-ray Scattering (WAXS)/ Small Angle X-ray Scattering (SAXS), Polarised Optical Microscopy (POM), Differential Scanning Calorimetry (DSC) and tensile testing.

3. To characterise and determine the mechanism by which interfacial interactions are promoted between APTES modified WS_2 NTs using various techniques, including Fourier Transform Infrared (FTIR), X-Ray Photoemission Spectroscopy (XPS), TGA and Raman.

4. To study the extent of dispersion of and interfacial interaction between silane functionalised WS_2 NTs and a PLA matrix, prepared by solvent casting methods, by examining the effect of NT addition on the morphology, mechanical and thermal properties of chitosan using SEM, tensile testing and DSC.

5. To characterise the dispersion and interfacial interaction of WS_2 NTs in chitosan and determining the impact of glycerol plasticiser on solvent cast composite properties, investigated using a combination of FTIR, tensile testing, Raman spectroscopy, XRD and TGA. Additionally, to examine the gas permeability and antibacterial properties of these composites for possible application in food packaging.

Chapter 2: Literature Review

In the following literature review, the synthesis and structure of WS_2 NTs is firstly reviewed. The understanding of the current literature to date is vital for the development of WS_2 NTs filled biopolymers as well as being able to identify the progression in WS_2 NTs synthesis to date. This is followed by a section outlining the unique and attractive properties of WS_2 NTs which can be utilised for application with biopolymers. This is then followed by a review of the current literature on biopolymers, specifically PLA and chitosan, describing the synthesis, structure as well as the biopolymer properties. The limited published literature on composites of WS_2 NTs and PLA is extensively reviewed, including surface modification of WS_2 NTs and chitosan-based composites.

2.1.0 Tungsten Disulfide Nanotubes

Tungsten disulphide nanotubes (WS_2 NTs) were discovered and first reported in 1992 [5]. WS_2 are classified as layered transition-metal dichalcogenides (TMD), of the type MX_2, with M a transition-metal atom (Mo, W, etc.) and X a chalcogen atom (S, Se, or Te). One layer of M atoms is sandwiched between two layers of X atoms. W is the heaviest transition metal and the larger size of the W atom can be utilized in the tuning TMD properties [56]. Due to the unique opportunity for discovery and optimisation, WS_2 NTs have generated significant interest in areas of material physics, chemistry and engineering over the past three decades and the potential of this 1D material is now being realised for several applications.

2.1.1 Synthesis and Structure of WS_2 NTs

Numerous strategies have been employed for the synthesis of inorganic nanotubes which have been refined over the years by various workers to produce different classes of inorganic nanotubes (INTs). This has been achieved through the modification and precise control of several parameters to determine diffusion and nucleation rates [57]. Methods of synthesis include laser ablation and electrical arching [58-60], templating [61, 62], hydrothermal reactions [63, 64] and chemical vapour deposition [65-67]. These methods have been reviewed and detailed accounts for production of various INTs presented [68]. Understanding the mechanism for the synthesis of WS_2 NTs is of great importance in determining the physical properties of WS_2 and their applications.

Inorganic WS_2 nanoparticles were first synthesised by Tenne et al [5], where it was first shown WS_2 could form closed cage fullerene-like (IF) nanoparticles and NTs. Since then, the synthesis of WS_2 NTs has become a focus point of optimisation in the development of inorganic NTs in order to achieve highly crystalline nanostructures. Various groups have demonstrated synthesis of WS_2 NTs including ball milling [69] which yielded large quantities of open-ended WS_2 nanotubes with an average length of 5 μm, an outer diameter of 25−50 nm. Various groups synthesised WS_2 NTs via a two-step hydrothermal route [70-72] where by NTs are synthesised from WO_{3-x} nanorods were reduced with H_2S to obtain a very high yield of multiwalled WS_2 nanotubes. Most recently, Rahman et. al. [73] highlighted the importance of chalcogenization (the process of replacing oxygen atoms by chalcogen atoms) timing during as well as the reaction to produce NTs with a diameter of approximately 20nm, and micrometre lengths consistently.

Additionally, Fluidised Bed Rector (FBR) methods were reported [74-76] for the synthesis of WS_2 NTs, amongst other inorganic nanoparticles, in order to optimise the growth mechanism. However, the development of scalable processes for the synthesis of WS_2 NTs has been a significant area of optimisation. Zak's group, which supplied the WS_2 NTs for this research project, has led this field of INT research over the last 30 years including the large-scale production of highly crystalline and increasingly pure WS_2 NTs [77-80]. Whereby, WS_2 NTs synthesis was developed using catalyst-free vapor-gas-solid (VSG) in a vertical FBR which has resulted in large-scale production of WS_2 NTs for scaled-up production method providing a few hundred grams of pure WS_2 NTs per batch. Most recently, Zak's group has further developed this method, by using a horizontal FBR and optimising control of gas flow conditions [81, 82]. This process is shown schematically in Figure 2.1a [82] showing the multistep process.

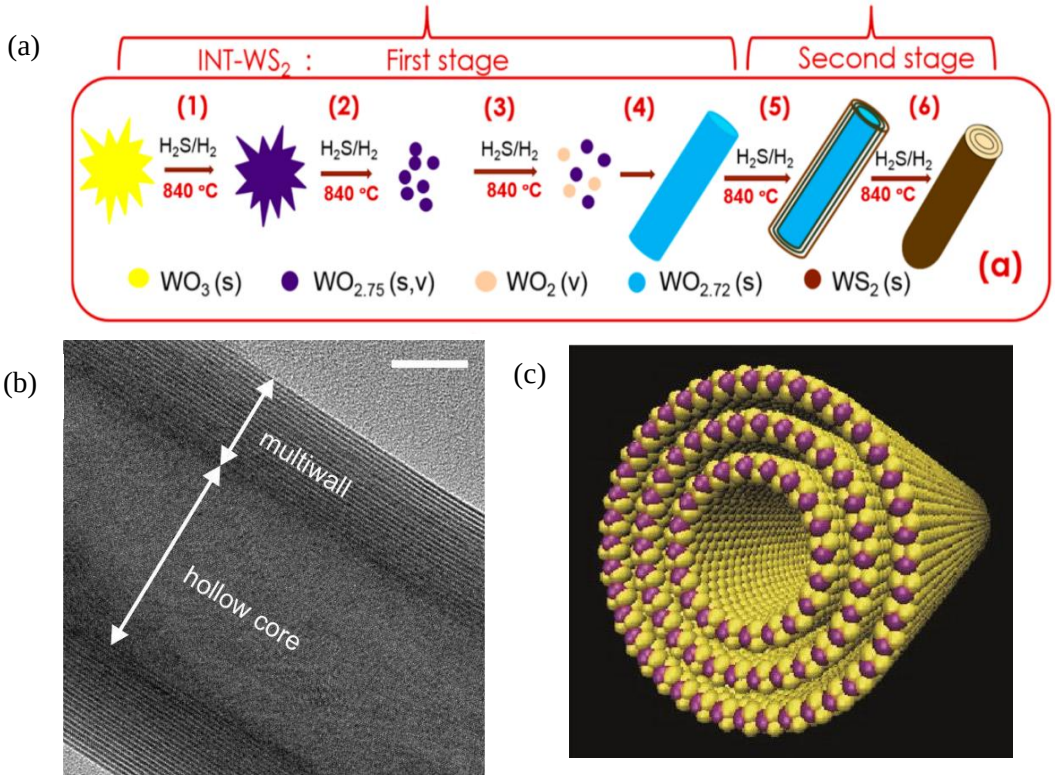

Figure 2.1 a) Schematic representation of the INT-WS_2 multistep growth mechanism b) TEM image of a hollow-core multiwall WS_2 nanotube. The white scale bar represents 10 nm. c) Schematic illustration of a multiwalled WS_2 NT

WS_2 NTs are synthesised in two main stages, firstly the growth of tungsten suboxide nanowhiskers occurs in 4 steps as outlined in Figure 2.1 a) (1)-(4) in a sequence of sub reactions via a vapor-solid-gas (VSG) method: (1) reduction of the WO_3 solid precursor by H_2 into a volatile tungsten suboxide ($WO_{2.75}$) phase, (2) its evaporation, (3) additional partial reduction of the vapor into a non-volatile WO_2 oxide phase, and (4) one-dimensional $WO_{2.72}$ nanowhisker formation.

The chemical condensation of the hot oxide vapor results in 1D $WO_{2.72}$ nanowhiskers growth of tens of micrometres in length, which is vital for INTs preparation. The synthesis of the nanowhiskers is interrupted by the formation of a stable $W_{18}O_{49}$ ($WO_{2.72}$) suboxide phase. This begins the second stage of the synthesis

process, whereby sulfurization of the oxide nanowhiskers by H_2S/H_2 gases via the "solid−gas" reaction proceeds, as shown in steps (5) and (6), Figure 2.1a.

Zak has proven for WS_2 NTs that the majority of nanotubes range from 10 to 20 microns in length and 20-120 nm in diameter, giving them AR of up to 1000. The multiwalled nanotube structure has identified a hollow core, as shown in Figure 2.1 b [83], in the range 8-16nm [84], that occupies up to 70% of their total volume while the number of walls possible varies between 3 and 25 in each nanotube [85].

The crystal structure of WS_2 NTs involves the stacking of sheets consisting of W atoms sandwiched by two planes of S atoms (space group P63/mmc) packed into an individual layer of WS as structurally depicted in Figure 2.1 c) [86]). This three atomic plane structure is held together by strong covalent bonds and these triple layers are stacked together, similar to graphite, by van der Waals interactions separated by 6.18Å for WS_2 [87], generating multi-walled nanotubes composed of concentric cylinders. The atomic arrangement of nanostructures is vital for the understanding of growth mechanisms to be fully optimised as well as providing an insight to the physical properties for future application [88]. Golub et al.[89]and Damnjanović et al.[90] explained in detail the crystal structure of WS_2 NTs, showing the interaction of the tungsten atom between sulphur sheets and the various phases of their coordination and stacking, leading to differences in their electronic and mechanical properties. The electron configuration between the metal and chalcogen atoms determines the "interlayer mutual arrangement" of the sulphur sheets to be either octahedral (tightly packed) or trigonal prismatic (not so tightly packed) nearest neighbour to the surrounding sulphur atoms. Of which, the trigonal prismatic arrangement is favoured

for WS_2 electron configuration as it is the most stable, however in reality both octahedral and trigonal prismatic structures are present [91].

However, WS_2 NT structural defects were be studied by TEM investigation by

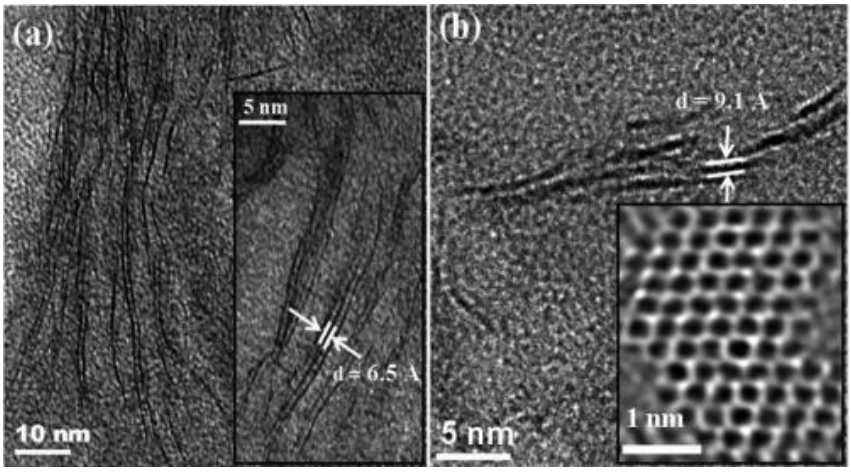

Figure 2.2 TEM images of WS_2 layers where in a) the layers are clearly identified and b) broken layers of the WS_2 nanostructure can be observed (inset shows the hexagonal atomic arrangement of the WS_2 layer/sheet.

Rao et al. [92], see Figure 2.2 TEM images of WS2 layers where in a) the layers are clearly identified and b) broken layers of the WS2 nanostructure can be observed (inset shows the hexagonal atomic arrangement of the WS2 layer/sheet. and these workers found that the number of layers in any one NT is not always consistent throughout the length of the nanotube as seen in Figure 2.2 b). These broken layers therefore interfere with the layer spacing, increasing the distance between walls to as much as 0.9nm. This identifies the need for further understanding of the nature of the layer structure and development through synthesis as this may impact on the properties and applications of the NTs [88].

With evidence for such structural defects, chemical composition analysis of WS_2 NTs was studied by Višic et al [93]. A significant level of contaminants was

found to be present in the chemical configuration, with 15% carbon and 20% oxygen species detected. Späth et al [94] interpreted the presence of oxygen to be a consequence of the synthesis process, from the oxide core. Tenne et al [95] has demonstrated that nanostructures with defects are more prone to absorb water molecules. It should also be noted, the surface of the nanotubes has been shown to undergo oxidation of the tungsten atoms from exposure to ambient conditions over a period of time, and also incomplete sulphurisation of the nanotubes results, as WO_x peaks are detected in XPS spectra. This oxidation of the nanotubes therefore could alter the intrinsic properties of the nanotubes, as described by Houben et al [96], including induced defects in the NT wall structure. Such identified defects in the nanotube structure can act as providing more acceptor sites for new chemical elements to the nanotube surface. It has been found carbon on the surface of the WS_2 NTs, as it known to react and bind to the surface of tungsten atoms. This explains why carbon is typically found loosely attached to the surface and therefore it can be removed by catalytic reactions [48, 94].

2.1.2 Properties of WS_2 NTs

WS_2 NTs have shown to possess a unique structural configuration, atomic arrangement as well as chemical bonding and composition, which has generated unique distinguishable properties including mechanical, electronic, optical, and thermal [97]. It is evident that physical characterisation of WS_2 NTs is vital in the understanding of development of these materials, as it is recognised the behaviour at the nanoscale differs to that of their bulk counterparts [2]. In many circumstances the properties on 1D, particularly which of TMD's, including WS_2 NTs have shown to possess properties superior to that of their equivalents on larger dimensions [98]. This

phenomenon is due to a relatively larger surface area to the volume, increased reactivity or stability in a chemical process, enhanced mechanical strength amongst others [99]. Additionally, comparative studies of WS_2 and carbon nanotubes have shown the functional properties of WS_2 NTs to exceed that of carbon nanotubes in all areas of investigation including mechanical, thermal and tribological properties [100, 101] .

WS_2 NTs exhibit superior mechanical properties as they have a Young's modulus up to 150 GPa and tensile strength above 16 GPa [102]. Furthermore, the interlayer shear modulus was found to be 2 GPa and WS_2 is able to withstand shock waves of up to 21 GPa [8]. Višic [48] outlined due to the three-layer S–W–S structure, they cannot be easily bent, are not flexible, and are always straight, preventing their entanglement. This attractive mechanical behaviour and other properties such as tribological of WS_2 NTs make them excellent candidates for various applications including for reinforcement of polymer matrices. Furthermore, in the absence of aromaticity, WS_2 NTs do not impart strong π–π interactions on each other and less likely to form strong agglomerations.

WS_2 NTs have the ability to impart elasticity and allows particles to roll instead of slide when acting as a solid-state lubricant, due to its chemical inertness and the hollow cage structure [103]. Apart from being developed as lubricants, WS_2 has also been used in the development of rechargeable batteries as it contributes to fast-ion conductivity [104] and has been shown to improve the performance of lithium (Li) ion battery anodes [105]. WS_2 can be fabricated in to well-ordered mesoporous materials with high surface area and narrow pore size distribution to deliver excellent high rate

capability to Li ion batteries[106]. Individual WS_2 NTs have also shown to have superconducting properties, which was established through ionic gating [86, 107]. Additionally, Zhang et al [108] identified Bulk Photovoltaic Effect, novel in nanomaterials, demonstrating the potential for application in harvesting solar energy. This effective semi-conducting behaviour under ambient conditions, was explained by Wang et al. [109] to be due to strong interlayer coupling in WS_2 and because it undergoes a significant transition from an indirect band gap to a direct one with a decreasing numbers of layers.

However, the most intriguing property that has generated interest especially in the biomedical field is the promising biocompatibility properties of WS_2 NTs. Appel et. al [110] tested WS_2 NTs against human kidney cells (HEK293f) and a Salmonella typhimurium (TA10 strain) and found WS_2 NTs did not cause cell death and mutation. Further research using salivary gland cells has shown that WS_2 NTs did not affect cell growth, proliferation kinetics as well as cell viability. Interestingly, findings also identified uptake of WS_2 NTs by the cells accumulated in the cytoplasmic vesicles but the cell morphology remained unchanged [111]. Additionally, the cytotoxicity of WS_2 NTs in human bronchial epithelial cells were studied [112]. NTs were proven to remain non-toxic as well as having significant capacity to induce protective antioxidant/detoxification defence mechanisms. Furthermore, Teo et al [113] examined the cytotoxicity of WS_2, as well as other TMD nanoparticles, and found toxicity levels to be lower than that of analogues of carbon nanoparticles. These properties are vital for application of WS_2 NTs in the medical industry, and to date their use has been demonstrated in biosensors, drug delivery, bone tissue engineering,

as well as in dental applications such as orthodontic wires and in dental creams [114-117].

The unique and, at times, superior properties exhibited by WS_2 NTs has also led to their inclusion as a functional additive for polymer matrices. The addition of nanoparticles to polymers has been widely investigated over the past few decades as it has proven that the addition of nanoparticles at low weight percentages (< 5.0wt%) can have significant impact on properties of some polymers [118]. The translation of these properties from the NTs to the polymer matrices of interest can be used to enhance specific properties such as mechanical, thermal or electrical, yielding functional composite materials primarily due to the large surface area of nanoparticles in polymer matrix [119]. Most significantly, due to the prominent biocompatibility of WS_2 NTs, and possible biomedical applications as discussed above, the incorporation of WS_2 NTs as a functional nanofiller in biopolymers has generated increasing research interest.

In the following section the studies describing the development of composites of biopolymers. In particular, there is a focus on both Poly(lactic acid)(PLA) and chitosan as they are the model polymers used in this work. The current methods of composite preparation are described and further examine the current literature of WS_2 NTs biopolymer composites.

2.2.0 Biopolymers

Biopolymers have become a focal point of research due to their favourable characteristics such as biodegradability, nontoxicity and biocompatibility [120]. Such distinctive properties are highly desirable in a range of industries including food packaging [121-123], pharmaceutical and medical [124-128], as well as in environmental [129-131] applications due to their potential to remove certain negative impacts that petro-derived polymers can have on the environment. Specifically, biopolymers have had an extensive impact on the medical device industry with applications in drug delivery, tissue engineering, antibacterial/antiviral, biosensors and wound healing [124, 126, 127, 132-136].

Biopolymers were defined by Rebelo et al.[137] as polymers produced by living organisms which can be derived from microbial systems, extracted from plants, or chemically synthesized from basic biological systems. Biopolymers have undergone significant review [129-131, 138-141], therefore can be classified based on various factors. For instance, dependent on biodegradability, monomeric units, application, polymer backbone as well as origin [142]. From this perspective, biopolymers have been classified as natural or synthetic biopolymers as outlined in Figure 2.3.

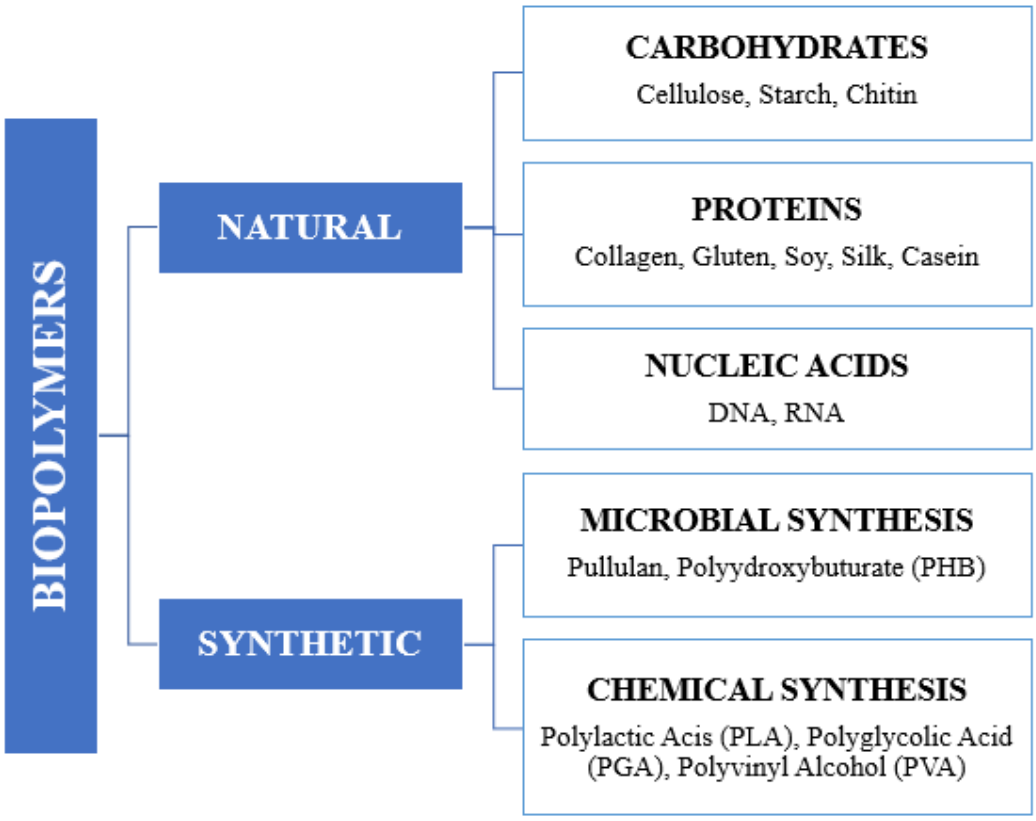

Figure 2.3 Classification of biopolymers

Natural biopolymers have some significant advantages in comparison to synthetic biopolymers, including lower toxicity, bioactivity and effective biological function. However, there are significant drawbacks such as limited material properties and too difficult or processable at scale and using continuous processes [143]. Starch-based biopolymers, also known as polysaccharides, are widely used due to their abundance and they can be processed, albeit challenging, with existing methods (e.g., synthesis through film extraction and injection moulding) [144]. Biopolymers from starch, soy protein, gelatin and casein are suitable for food coating, food packaging and biomedical applications amongst others due to their biocompatibility properties [145, 146]. Polysaccharides (starch) perform different physiological functions and

may have various applications in tissue engineering and regenerative medicine as well as food packaging [147-149]. Proteins are extensively used in drug delivery and as tissue engineering scaffolds [150-152]. While, nucleic acid based biopolymers may have application as functional materials in the medical industry, as they store, transmit, and express genetic information, and have a role in drug delivery, biosensors, and a scaffold for many biodegradable materials [142, 153].

Conversely, synthetic biopolymers have many advantages for application in industry, including improved control over chemical composition, mechanical properties and processability. Due to the option to vary synthesis methods, a range of synthetic biopolymers with a broad of bulk properties are now available [154]. Synthetic biopolymers can be synthesized by microbes or produced through fermentation, including Pullulan which is produced by the fungus Aureobasidium pullulans. Other biopolymers are chemically synthesised, such as PGA which can be produced chemically by polycondensation of the γ-glutamic acid dimer[142]. Synthetic biopolymer have also been largely identified for application in the medical industry for tissue engineering, scaffolding, drug delivery, food packaging amongst other applications [36].

2.2.1 Poly(lactic acid)

PLA is one of the most widely researched and promising synthetic biopolymers that can be used to substitute conventional petroleum-based polymers. PLA has useful mechanical properties and the relatively low amount of energy used for its production, potential biodegradability and biocompatibility as well high industrial production capacity which are all attractive properties to industry [155]. Carothers et al.[156] developed a method to polymerize lactic acid and create PLA,

which was patented by (DuPont) in 1954 [157]. However, due to the high production cost as well as the ability to only produce low molecular weight polymer, PLA was rarely used. In the early 1990s, Cargill Inc. succeeded in polymerizing high-molecular-weight PLA on an industrial scale and commercialized the PLLA polymer and introduced the trade name, Nature Works [158]. Consequently, PLA, and its derivatives have been extensively studied over the last 30years, gaining a leading role in the biomedical field, as well as in food packaging and agricultural film as a replacement for petro-derived films [157]. As of 2019, PLA has an annual worldwide production of 395,500 ton and produced by various companies, inclusive of NatureWorks, Corbion and Futerro [159].

2.2.2 Synthesis and structure of PLA

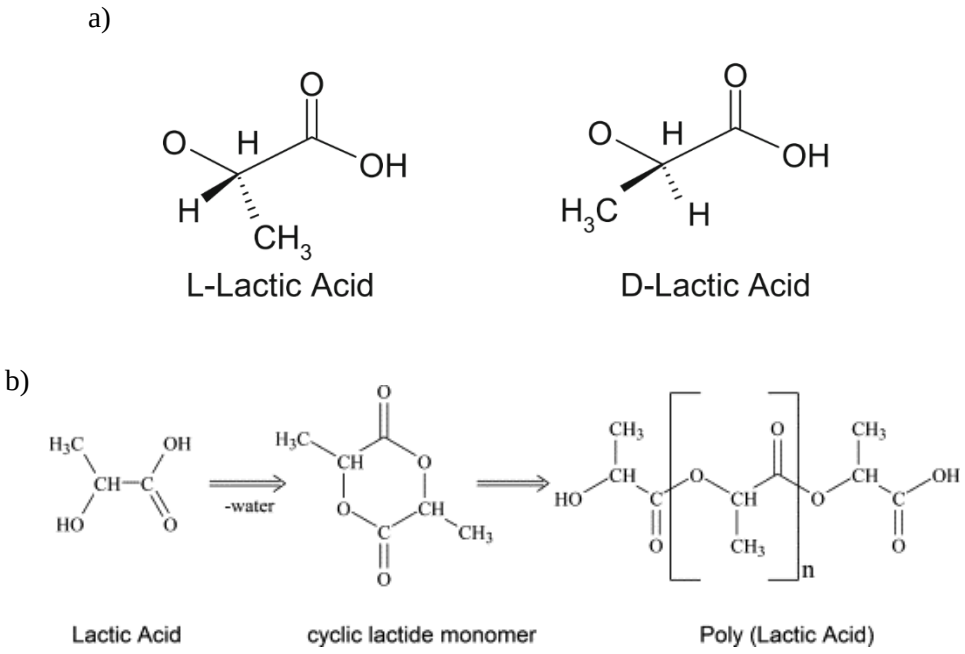

Figure 2.4 Chemical structure of a): L lactic acid and D-lactic acid, b) reaction pathway for the production of PLA via ROP synthesis.

PLA is a synthetic aliphatic polyester derived from natural sources such as corn and sugar beets. The single monomer of PLA, lactic acid (2-hydroxyl proponoic acid), is obtained by chemical synthesis or microbial fermentation of the natural resource. Lactic acid has two optically active stereoisomers, L(+) and D(−) isomers (Figure 2.4 [160]). The production of lactic acid is mainly from fermentation techniques rather than chemical synthesis due to limitations of the synthetic route, including high manufacturing costs, limited capacity, and its inability to make only the L(+) enantiomer [161]. Natural fermentation will generally yield a mixture of the two enantiomers in the approximate proportions 99.5% (L) form and 0.5% (D) form with an asymmetric carbon and it exists in two optically active configurations. The two isomers have identical physical properties, with the exception that the L-isomer

rotates plane polarized light clockwise while the D-isomer rotates it anti-clockwise[162].

There are three routes in which PLA is produced from the lactic acid monomer which have been extensively reviewed [163-168]. Firstly, the conventional process is by the polycondensation of lactic acid, which is carried out under high vacuum and temperature and, solvent is used to extract the by-products. This method leads to low molecular weight, brittle polymer due to difficulties of removing water and impurities. Secondly, azeotropic dehydrative condensation of the lactic acid method can produce PLA of high molecular weight. However, drawbacks include that of degradation of PLA polymer, hydrolysis as well as toxicity from the catalysts used. Lastly, the most successful method to produce PLA polymer is via the production of lactide prepared by decompression of lactic acid, and further processed by ring-opening polymerization (ROP) [169]. This results in a high molecular weight polymer, produced in mild conditions, and is now used commercially. Production of PLA via the lactide route allows for superior control of the polymer properties by controlling the optical sequence of the polymer backbone through polymerizing a controlled mixture of L and D isomers to yield variation of the isomers (L / D ratio). Depending on the proportion of D- and L-isomer, PLA with different properties can be tailored with different molecular weight, crystallinity, and melting point of the product (PLA). Highly crystalline polymer can be achieved through less than 2% D-lactide content, resulting in PLLA. While fully amorphous materials can be produced by the inclusion of greater than 15% D-lactide content, PDLA [170]. Consequently, development of the sterocomplex is a novel way to dictate many properties of the final polymer.

2.2.3 Properties of PLA

The mechanical properties of PLA based polymers can be varied to a large extent depending not only on the stereochemical structure but, additionally by controlling polymer crystallinity, molecular weight and crystalline orientation. Table 2.1 [171] lists the values of some physical and mechanical properties of PLA, PLLA and PDLA which are expressed in ranges as the values are dependent on specific material characteristics as well as the testing method used.

Table 2.1 Physical properties of PLA, PLLA and PDLA, including density, ρ , tensile strength, σ, elastic modulus, E, ultimate tensile strain, ε, glass transition temperature, T_g and melting temperature, T_m

Property	**PLA**	**PLLA**	**PDLA**
ρ (gcm^{-3})	1.21 - 1.25	1.24 – 1.30	1.25 -1.27
σ (MPa)	21 - 60	15.5 - 150	27.6 - 50
E (GPa)	0.35 - 0.5	2.7 – 4.14	1 – 3.45
ε (%)	2.5 – 6.0	3.0 – 10.0	2.0 – 10.0
T_g (°C)	45 - 60	55 - 65	50 - 60
T_m (°C)	150 - 162	170 - 200	N/A

It is evident that PLLA has an elastic modulus up to ten times greater than that of PLA, due to its crystalline nature, while PLLA has up to three times greater tensile strength in comparison to PLA. There is a strong connection between crystallisation and, mechanical and thermal properties of these polymers which has been widely

reported [172]. As the molecular weight of PLA increases, the tensile strength and modulus increase [173]. Although the tensile strength and elastic modulus has shown to be comparable to poly(ethylene terephthalate) (PET) [174], PLA is a very brittle material with less than 10% elongation at break. This in turn limits its use in the applications where plastic deformation at higher stress levels is critical.

The thermal properties of PLA are listed in Table 2.1 with characteristic T_g and T_m values given. It can be noted the highly amorphous PDLA does not exhibit a melting point due to significantly slow rate of crystallisation. These properties enable PLA to be classified as a "thermoplastic" polymer [175]. A major useful attribute is that it can be heated to its melting point, cooled, and reheated again. Therefore, polymer processing with conventional methods, such as extrusion and injection moulding, can be used but with caution due to the possibility of thermally induced degradation of the polymer. Chemical processing of PLA is also an option due to its solubility in dioxane, acetonitrile, chloroform, methylene chloride, 1,1,2-trichloroethane and dichloroacetic acid. It is only partially soluble in ethyl benzene, toluene, acetone and tetrahydrofuran and, only when heated to boiling temperature. This can be useful for processes such as electrospinning and film forming [171, 176].

One of the most favourable characteristics of PLA is that it is considered both biocompatible as well as biodegradable. The degradation of PLA is achieved by abiotic processes, via hydrolysis of the ester bond and enzymes degrade the residual oligomers to final mineralization. Moreover, PLA degradation products are non-toxic making it a natural choice for biomedical and short term packaging applications[177]. Additionally, as an eco-friendly polymer, PLA requires 55% less energy to be

produced in comparison to that of petroleum-based polymers [171, 178]. Consequently, lower greenhouse gas emissions and fossil energy use apply, and there is a cost-effective method for production at a commercial level.

Clearly, PLA possesses unique properties as a biopolymer, some already utilised by industry as it is an attractive replacement for polymers such as PE, PP, PS and PET[177, 179] , but in certain applications only. However, due to the polymer being inherently brittle and having low impact strength, due to its limited ability to crystallize and low crystalline content there are several limitations to further use of PLA.

2.2.4 Chitosan

Chitosan is a low-cost and multipurpose natural polysaccharide which has been found limited use for various applications in the agriculture, pharmacy, and biomedical industries[180, 181] . Chitosan has generated great interest since it was first discovered in 1811 by C. Roget from the synthesis of D-glucosamine (an amino sugar) of chitin, which was later named chitosan by Hoppe-Seyler (1894). Further work on the development of chitosan was reported by Prudded in 1970 [182] [183]. Since then, chitosan and its derivatives has been used as a biopolymer with a few vital commercial areas.

2.2.5 Synthesis and Structure of Chitosan

Chitosan is a naturally derived polysaccharide, derived from chitin which is typically sourced from marine waste like crustaceans, the waste exoskeletons of crabs, shrimp, arthropods, and microorganisms such as fungi. Chitin is placed as the second most abundant natural biopolymer after cellulose[184]. Its chemical structure consists of solely N-acetyl-D-glucosamine, whereas the structure of chitosan is obtained from the deacetylation of chitin which can be composed of both N-acetyl-D-glucosamine and glucosamine[185].

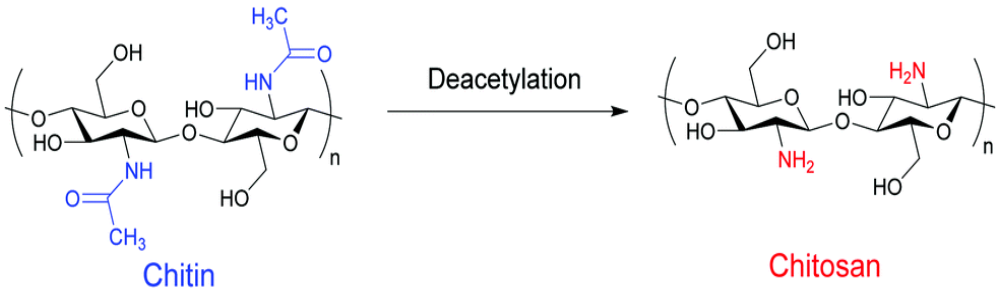

Figure 2.5 Chemical structure of chin and chitosan

Chitosan is obtained by deacetylation (alkaline hydrolysis) of chitin. Chitin is first extracted form crab and/or shrimp shell waste whereby it is washed and crushed into smaller sizes. Harsh processing is carried out by a demineralizing and deproteinizing treatment using HCl, and NaOH respectively, to remove minerals (mainly $CaCO_3$) and proteins. Finally, the chitin obtained is further deacetylated into chitosan by concentrated alkali treatment [186]. Following the process of deacetylation, chitosan can be obtained in different forms like powder, fibre, and sponges from the solution.

The Degree of Deacetylation (DD) of chitin to produce chitosan is a vital factor in the determining the polysaccharide properties. The 'ideal' chitosan structure as depicted in Figure 2.5 [187] is that to have 100% DD, however this is particularly difficult to obtain, as it is dependent on the source of the chitin as well as the efficiency of the manufacturing processes [188]. Variation of the DD content of chitosan determines the molecular weight, crystallinity, ionic concentration, pH, and the distribution of acetyl groups along with influencing the solubility of chitosan. This is because a higher DD yields a higher concentration of amino groups in the molecule, and protonation of the $-NH_2$ functional groups [189]. It is generally found a N-deacetylation degree between 55% and 70% is called a low degree of deacetylation; 70%–85% is medium; 85%–95% is high and between 95%–100% is ultra-high [190].

2.2.6 Properties of Chitosan

The solubility of chitosan is enhanced due to the presence of amino groups and hydroxyl functionalities [191]. Chitosan is readily soluble in acidic solutions, and from literature in acetic, nitric and formic acids at 1-3% solutions. Essentially an acidic environment with pH below 6, is widely used for possessing and application of chitosan [192]. Higher molecular weight chitosan has been reported to have good film-forming properties as a result of intra- and intermolecular hydrogen bonding [193].

Chitosan is considered to exhibit superior properties including biodegradability, non-toxicity, and biocompatibility, attracting applications in the medical industry. The chemical structure of chitosan, with the presence of amino groups results in chitosan having intrinsic efficacy towards killing many bacteria, both

Gram positive and Gram-negative, fungi and viruses [194]. It is understood that the positively charged amino groups of chitosan may interact with anionic groups on the cell membranes of microorganisms, change the permeability of the membranes, leading to the death of microbial cells [195]. Additionally, degradation of chitosan releases harmless amino sugars which can be completely absorbed by the human body [196], making it very attractive as a functional biomaterials. Consequently, chitosan has been widely studied for its use in generating medical scaffolds for tissue engineering and tissue regeneration [42, 186, 196, 197].

There is also considerable interest in chitosan in the food science and technology sector due to the attractive antibacterial and 'encapsulation technology' properties [198]. This research has established chitosan matrices to be used in food packaging where it is used to protect the encapsulated materials, i.e., bioactive compounds, additives, or flavours, control their release to the environment and reduce their toxicity. Additionally, chitosan has environmental application, such as in the treatment of wastewater for the removal of pollutants, dyes, and metal ions [199, 200]. Furthermore, chitosan has also found application in the agricultural sector, such as a micronutrient, fertilizer, pesticide, and for herbicide delivery in [201-203]

However, chitosan does have limitations such as hydrophilicity, relatively poor mechanical properties as well as low gas permeability [204]. Furthermore, processing chitosan is much more difficult than other biopolymers and it has low transparency and poor thermal stability. These all significantly impact the application of chitosan in industry.

2.3.0 Nanocomposites

The physical and chemical properties of polymers (i.e., mechanical, thermal stiffness, resilience, conductivity of heat and electricity, resistance to corrosion, transparency, colour, etc.) are determined by the types of monomer, degree of polymerization, and bonding pattern/order [129]. However, as discussed, limited mechanical properties such as durability, tensile strength and ductility as well as limited processing capability, and long-term stability are significant drawbacks for applying PLA and chitosan in industry[205].

Therefore, in order to overcome these limitations in the properties of biopolymers, the dispersion of inorganic nanoparticles, such as WS_2 NTs, in biopolymer matrices has become an expanding area of significant research in material science [206].

2.3.1 Methods of Nanocomposite preparation

To optimise the properties of composites of polymers and nanoparticles, it is vital that the nanoparticles are dispersed effectively in the polymer matrix with favourable interfacial interaction between components while ensuring the nanoparticle retains a high aspect ratio. Good dispersion of NTs is necessary to take advantage of the effective high surface area of the NTs to provide interfacial interaction between the NT and the polymer matrix.[207]. However, to achieve uniform dispersion of NTs within the polymer matrix poses a significant technical challenge as the NTs have a strong tendency to agglomerate due to their nano-size and high surface energy [208-210]. Various processing methods have been employed to prepare composites of

polymers and nanoparticles [119, 211-214], however in this research melt mixing techniques and solution mixing are only studied.

Melt mixing is one of the main methods for the manufacturing of polymer compounds and products for industry due to the viability of being able to produce in high volumes at low cost, while also seen as environmentally sustainable due to the absence of solvents [215]. This method comprises heating the raw polymer until molten, and the nanoparticles are added and the molten composite is subject to heat helical screw (single or twin screw) which rotates to compress the raw plastic and nanoparticle together to homogeneous melt. The mixing with screws imparts a high shear stress environment in order to blend components during mixing, which in turn is suggested to de-aggregate nanoparticles. A more uniform dispersion may also be achieved through increasing duration time, which may result in better dispersion and electrical and thermal conductivities [216].

However, the melt mixing method also has several drawbacks. Relatively weak interfacial interaction can exist between the polymer and nanoparticles [212]. Also, dependent on the strength of the processing conditions, a decrease in AR of NTs could be affected [217], in turn impacting the ability of NTs mechanical reinforcement of polymer matrix.. Additionally, the morphology of the fabricated blends strongly influences the final properties of the system, and because of the heating and cooling process, this will significantly impact the crystallisation and further properties of the composite [218].

Solution casting is a common method for the production of thin film composites. This method comprises polymers are dissolved in common solvent, and under continuous stirring nanofillers are dispersed in the solution until a homogeneous solution is formed. Subsequently, the solution is cast into a mould and the solvent is evaporated [219]. Although. this method is only applicable to the polymers which are soluble in any solvents. Additionally, solvent removal from the composite is a problem for the wide use of this method, as it may change the physiochemical properties of the resultant composite, with the possibility of a plasticising impact on the mechanical properties [220, 221].

However, beyond the processing conditions of nanocomposites, the surface modification of nanoparticles has the opportunity to increase the chemical interaction between the two phases of composite and aid in the dispersion of INTs which can be utilised in the polymer matrix [222]. The surface modification of INTs and other nanoparticles has been examined through various strategies such as thiols, amines, ligands, carboxylic acids and as well as biomolecules [223-228]. The surface modification of nanoparticles however remains an important chemical challenge which has undergone significant developments.

It is evident from these reviews that different processing technologies do not yield equivalent results due to the physical and chemical differences between polymers, processing efficiency and nano particle filler. Consequently, the choice of composite fabrication method plays a critical role in mechanical and physical properties of polymer bio-nanocomposites and characterization of surface chemistry

and structure of nanofiller and biopolymer is essential in understanding the structural complexity of bio-nanocomposites.

2.3.2 Composites of PLA and WS_2 NTs

WS_2 NTs as a reinforcing agent in PLA has undergone research for the development and optimisation of composite properties through various methods of processing techniques for application in the biomedical field. Naffakh et al [229-231] was the first to investigate this advanced biopolymer-based nanocomposite via conventional melt mix extrusion. Naffakh has extensively studied the crystallisation behaviour of PLA WS_2 NTs composite, in both isothermal and non-isothermal conditions, identifying the nucleating effect of WS_2 NTs in polymer matrix, which in turn altered the melt and cold crystallisation behaviour of PLA and led to an increase in mechanical properties. The degree of crystallinity is a key parameter in polymers because it has strong influence on both the chemical and mechanical properties. The crystalline phase improves the stiffness and tensile strength whilst the amorphous phase helps to absorb the impact energy.

Shalom et al [232] further examined processed melt extruded composite pellets by generating filament using a printing technique, Fused Filament Fabrication (FFF). The findings suggested that FFF processing improved the dispersion of NTs in PLA matrix, in comparison to melt extruded pellets, and consequently enhanced the mechanical properties of FFF PLA WS_2 composite increased the elastic modulus by 20%, yield strength by 23% and the strain-at-failure by 35%. These results were further compared to solvent cast PLA WS_2 NTs films where a higher degree of crystallinity was found, and negligible effects on the crystallinity of the FFF composite

samples were observed. The higher crystallinity of PLA WS_2 composites prepared via solvent casting resulted in superior mechanical performance of composites as shown in Figure 2.6 [232].

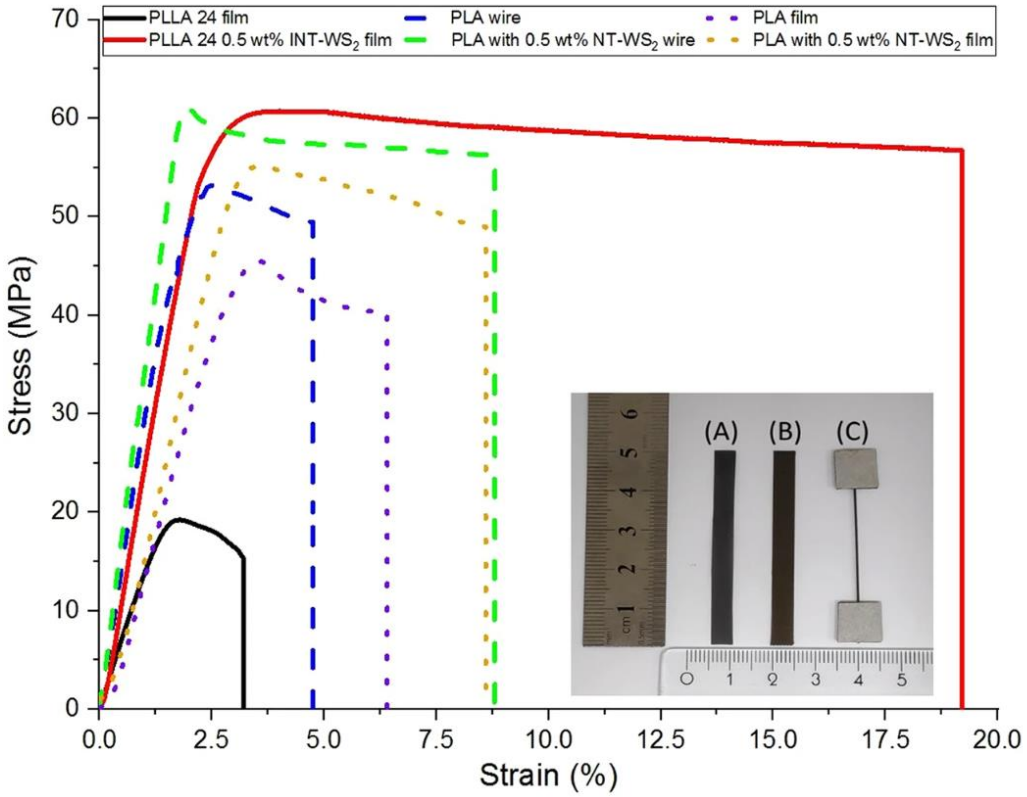

Figure 2.6 Stress-strain representing curves of PLA and PLA/ WS2-NT pre- and post-printed filament, compared to solvent-casted.15. Inset: (A) – cast film, (B)- printed film, (C) – printed wire. Rule-bar to scale.

Over all, in this study, it was determined that WS_2 NTs increase mechanical properties of PLA regardless of sample preparation method. However, it also highlights the significance of dispersion of NTs in the polymer as well as the degree of crystallinity of the polymer matrix and how these factors are influenced by methods of composite preparation.

Other studies have incorporated WS_2 NTs into PLA using solvent casting method [233, 234], and studied the effect of WS_2 NTs concentration on the strain-

induced crystallization of PLA as a consequence of uniaxial stretching at 90 °C and constant strain rate. These studies again identify the induced crystallinity due to the presence of NTs, however the effect of additional annealing shows evidence of a high degree of orientation of the polymeric chains in all stretched films which increases with annealing time at lower wt% of NTs. Additionally, it should be noted the influence of crystallinity did not significantly impact mechanical properties of PLA WS_2 NTs when investigated in these circumstances. The results discussed in this work emphases the impact the choice of processing conditions of a novel PLA WS_2 NTs nanocomposites as well as the impact of the polymer chemistry.

Most recently, PLA WS_2 composites went under significant review for application as bioresorbable scaffolds (BRS) [235]. Composites were prepared using melt extrusion method, and shaped using a tube expansion apparatus. This method of preparation resulted in NTs characteristic nucleating effect, effective dispersion in PLA and aligning of NTs along the axis of the PLA tube during extrusion. Due to this favourable result, this experimental procedure underwent further analysis as practical application as BRS. It was found WS_2 NTs as filler for PLA demonstrates mechanical properties increase the strength of BRS to enable thinner devices and as well as a significant increase radio-opacity to improve intraoperative visualization. Additionally, the biocompatibility of WS_2 NTs and PLA WS_2 composites were examined and presented in vitro biocompatibility.

The understanding of inorganic nanoparticles and polymer composite materials, the strength of interaction between the surface of NTs and polymer matrix, as previously discussed this can be done by functionalisation of NTs surface. Shalom

et al[236] explored the modification of WS_2 NTs through functionalization of WS_2 NTs using N-Methyl-2-pyrrolidone (NMP), polyethylenimine (PEI), polyethylene glycol (PEG). Functionalised NTs were then dispersed in PLA via solvent casting method. PEI-treated NTs identified improvements in the mechanical properties of PLA composite films, however this was only identified in the higher wt% of NTs. PEG did not show any impact on the mechanical properties of PLA WS_2 composite, and adhesion of the NMP-treated NTs to the polymer matrix was quite poor, which resulted in reduced ductility of the nanocomposites. This research did not explicitly identify chemical modification of the NTs surface or interaction mechanisms identified in composite matrix. Therefore, this signifies the importance of understanding and utilising the surface chemistry effectively in order to promote interfacial interaction between NTs and polymer, as it drastically impacts the performance of the composite.

WS_2 NTs were incorporated into PLA with hydroxyapatite (HA) composite using melt blending for potential application for bone tissue engineering scaffolds [237]. WS_2 NTs was shown to act as a nucleating agent and it also improved the dispersion of hydroxyapatite micro-particles in the PLA matrix reducing the mean particle size that led to a larger interfacial area between the particles and polymer matrix. In comparison to unfilled PLA HA composites, addition of WS_2 NTs increased the thermal stability of PLA as well enhancing mechanical properties. Very recently, this novel composite was further researched by Golan et al[238], prepared using a solvent cast method, and additionally using oleic acid (OA) as a dispersant by functionalising the NTs. This method was shown to have limited success as chemical analysis found there was no specific chemical bonding between any of the four

components (PLLA, HA, OA, and WS_2 NTs), which in turn led to a reduction of mechanical properties. Conversely, PLA/HA/WS_2 NTs films produced had higher hardness values as well as in increase in thermal stability of the films. These nanocomposites exhibited good biocompatibility and non-cytotoxicity and therefore have great potential as scaffolding in tissue engineering. Additionally, this research identified the potential for further research into specific functionalisation of WS_2 NTs to improve their interfacial interaction with the matrix and influence the mechanical behaviour of the nanocomposite.

Hybrid ternary blends, comprising two polymers and one inorganic nanofiller are being increasingly studied as a method of chemical copolymerization. Naffakh [239] has been a leading author in researching the incorporation of WS_2 NTs to modify multiple polymers' interfacial properties and phase morphologies. WS_2 NTs was incorporated into PLA and polypropylene (PP) blends where it was observed WS_2 NTs had a more prominent nucleating effect for the PLA-rich composites and the overall composites exhibited an increase in storage modulus of the respective PLA/PP blends.

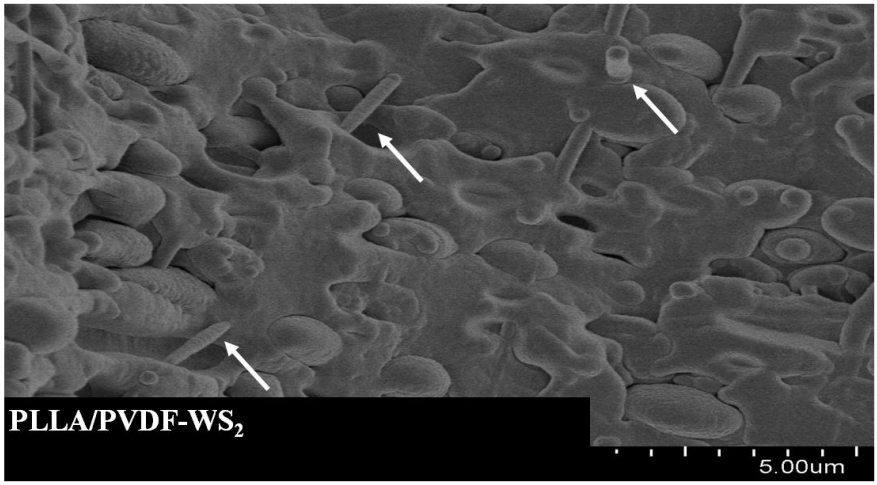

Figure 2.7 High-resolution SEM image for PLA/PVDF-WS_2 NTs

Additionally, similar results were established when WS_2 NTs were incorporated into PLA and poly(vinylidene fluoride) (PVDF) polymer blends [240]. Characteristic properties of WS_2 NTs acting as an effective nucleating agent and reinforcing filler in PLA/PVDF blends were again identified, and consequently greatly improving their thermal and dynamic-mechanical properties. It can be seen in Figure 2.7 [240] the dispersion of the WS_2 NTs from SEM was observed to be dispersed well and helped modify the blend interface morphology. The most recent study by Naffakh investigated the crystallization and thermal properties of PLA and Nylon 11 blends with WS_2 NTs [241]. It was found WS_2 NTs have a prominent impact on the crystallisation behaviour of PLA/Nylon 11 blends, also increasing thermal stability which was indicated by an increase of crystallisation temperate by $10°C$. The increased crystallinity, and thermal properties of all blends discussed are owed to the effective dispersion of WS_2 NTs and improved the compatibility of the two phases, representing another very promising route for the compatibilization of PLA WS_2 based blends.

2.3.3 WS_2 Biopolymer Composites

WS_2 NTs incorporated into other biopolymers have been investigated by various authors using a range of processing techniques which has undergone review for morphology, crystallization kinetics, mechanical and thermal properties with WS_2 NTs nanofiller.

Polyhydroxyalkanoate (PHA), and relative copolymers Poly(hydroxybutyrate-co-hydroxyvalerate) (PHBV) are synthesised as a natural polyester as a functional biopolymer thermoplastic, however are known for inferior thermal and mechanical properties and poor thermal stability due to slow rate of crystallisation [242]. WS_2 NTs

have shown to be successfully integrated into PHBV by Nafakh et al[243], Slivermman et al [244, 245] using solution mixing techniques prepared at various WS_2 NTs loadings ranging from 0.1 to 1.0 wt%, without the use of surface modifiers. The impact on polymer morphology and the understanding of the crystallisation kinetics was extensively researched using various techniques such as SAXS and WAXS, DSC and POM. It was found that WS_2 NTs again generates prominent nucleation activity, enhancing the nucleation capacity and crystallinity of PHBV matrix without altering its crystal structure. This was determined to be due to strong heterogeneous nucleating effect of WS_2 NTs in the matrix, as well as an improvement in the thermal stability in comparison to those of PHBV with increasing wt% of WS_2 NTs was found. Chen et al [246] studied the same PHBV WS_2 composite, however prepared by melt-blended in a twin-screw extruder, and Xiang et al.[247] prepared composites of PHBV and WS_2 composites via prepared via melt reactive processing. Results again identified an increase in crystallization rate and higher crystallinity, however most interestingly, two different crystalline forms, α-crystal and β-crystal, were found in the prepared which in turn induced mechanical toughness to increase by 300% in comparison to neat PHBV.

The influence of WS_2 NTs on the crystallization and thermal behaviour of poly (ethylene succinate) (PES), a semi-crystalline aliphatic polyester, prepared by solvent casting was studied by Asadi et al.[248, 249]. Similar results were obtained as previous reports as WS_2 NTs were shown to accelerate the crystallization process, while not altering the crystal structure, and an improvement of the thermal stability of PES was identified. However, study of the morphology identified that in both cases, there was an inhomogeneous dispersion of NTs at high weight volume, but seems that the

solution casting method is still successful in dispersing of low amounts (0.2–0.5%) of WS_2 NTs within PES matrix.

Lalwani et al.[250] investigated the efficacy of WS_2 NTs in Poly(propylene fumarate) (PPF), towards the fabrication of biodegradable polymeric implants for bone tissue engineering applications, in comparison to single walled and multiwalled carbon nanotubes (SWCNTs and MWCNTs). Nanocomposites were prepared via radical initiated thermal crosslinking, at low loadings of (0.01-0.2wt%). It was found that PPF compressive and flexural mechanical properties (Compressive modulus, compressive yield strength, flexural modulus and flexural modulus) for all

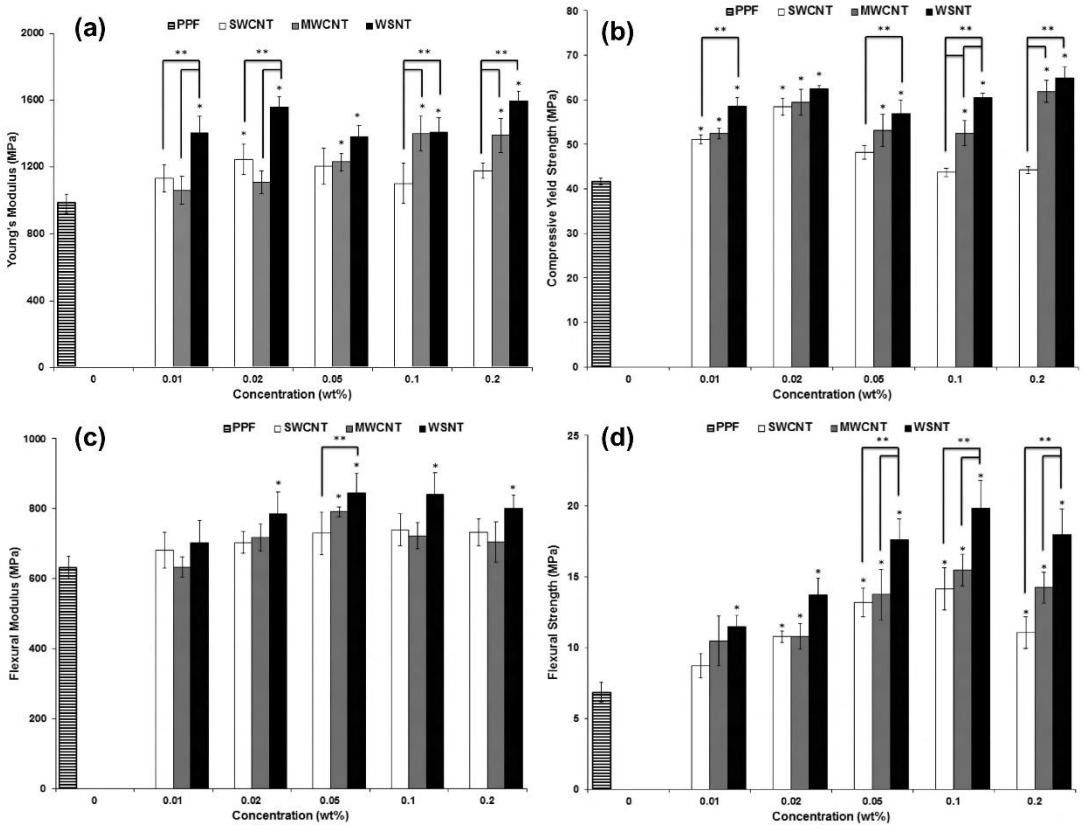

Figure 2.8 a) Compressive modulus, b) compressive yield strength, c) flexural modulus and d) flexural yield strength of PPF nanocomposites as a function of nanoparticle loading concentration.

concentrations of WS_2 NT identified most significantly better mechanical properties when compared to SWCNT and MWCNT nanocomposites as shown in Figure 2.8 [250].

These results were determined to be due to higher crosslinking density and uniform dispersion of WS_2 NT in the polymer matrix. The results of this study highlighted the influence of effective dispersion, while also acknowledging the importance of other factors such as interfacial interaction and AR of NTs which significantly impact the properties of polymer nanocomposites. Lalwani et al [251] further hypothesised, presence of structural defects and functional groups on the WS_2 NTs can lead to increased polymer-nanomaterial interaction, thereby increasing the mechanical properties.

2.3.4 Composites of WS_2 NTs and other Polymers

Taking advantage of evident INT properties, composites of WS_2 NTs with conventional polymer types have been studied.

Epoxy resins have application in adhesives, automobile, aerospace, wind energy and civil applications due to epoxy resin's outstanding characteristics like good adhesion to fibre reinforcements [252, 253]. Epoxy resin systems have also been used as matrices for nanoparticle systems to enhance epoxy's mechanical properties, damage resistance, extreme environmental resistance, and high-temperature performance, where by nanoparticles have undergone investigation as a functional filler [254]. WS_2 NTs as a functional filler was examined in epoxy by various authors and the mechanical, tribological and dielectric properties examined. Shnieder et al

[255] compared 0D/1D WS_2 and found both readily disperse and reinforce epoxy matrix identifying a reduction of coefficient of friction and wear of epoxy composites with WS_2. This was deemed due to effective lubricating properties of WS_2, however 1D WS_2 NTs, which, being of high AR, have larger reinforcing effect compared to the 0D nanoparticles.

The mechanical properties of the WS_2 NTs epoxy matrix found the adhesion, fracture toughness and strain energy all were most enhanced at 0.5wt% WS_2 NTs, while also identifying he adhesion, fracture toughness and strain energy release rate were studied. The INT-WS_2 were found to significantly improve all these properties. Additionally, improvement of the thermal properties, with T_g of neat epoxy is increased by 10%, identifying an increase in thermal stability of epoxy composite. These material enhancements show promise in the field of nanocomposite adhesives and coating, as well as for structural applications. [256-258]

Furthermore, dielectric and electrical properties of WS_2 NTs in epoxy matrix were examined by Bertasius et al.[259]. It was found that with increasing concentration of WS_2 NTs dielectric conductivity increases while electrical transport occurs between WS_2 NTs and epoxy matrix at higher temperatures (above 410 K). Therefore, it was suggested the WS_2 NTs can be used to improve novel electromagnetic shielding performance of composite. Sedova et al [15] further examined electrical characteristics of semiconductive WS_2 nanotubes/epoxy composites to be used as sensors for health monitoring of structural components. It was found for samples with 25wt% NTs content were able to serve sufficient electrical conductivity for application.

The effectiveness of WS_2 NTs polyurethane (PU) has been examined, as PU is used in numerous commercial applications such as coatings, flexible to rigid foams, sealants, and adhesives, as well as in many biomedical applications [260]. Dodiuk et al [261] studied the inclusion of WS_2 NTs in PU for advancement of mechanical properties. As previously discussed in other WS_2 NTs polymer composites, 0.5w% WS_2 NTs inclusion found the most effective enhancement of storage modulus (<100%), an increase of 20°C T_g, and 44% improvement on peel strength. Interestingly, there was no significant change in FTIR or XRD (i.e. chemical structure or crystallinity of the composite,) therefore this enhancements of nanocomposites can be deemed due to the AR and effective distribution of WS_2 NTs in PU composite. Additionally, Otorgust et al [101], provided an extremely insightful study of WS_2 NTs in PU polymer matrix, while also providing a comparative study of Carbon Nanotubes (CNT). In this study, the mechanical properties of PU again were found to be optimised at 0.6wt% WS_2 NTs, however changes in FTIR spectra identified shifting of peaks in shifting and splitting of the peaks in the ether group C-O-C which interacts with N-H group, which are indicative of structural changes in the nanocomposites using WS_2 nanofiller. Overall, this study identified WS_2 NTs exceeding their carbon counterparts in all of the measured aspects of thermosetting PU system, making them very suitable as nano reinforcements for this type of adhesives.

A similar comparative study with CNTs was conducted however in a poly(trimethylene terephthalate) (PTT) matrix, and the electrical properties are examined [100]. Similarly, WS_2 NTs (and CNTs) at 0.5wt% were found to readily disperse in PTT matrix, however enhancement of mechanical properties was not observed. PTT has unique mechanical properties due to the fast rate of crystallisation

[262], therefore it could be suggested NTs did not impact crystallinity and/or little to no reinforcement from interfacial interaction.

Poly(methyl methacrylate) (PMMA) is a thermoplastic, however limited mechanical properties have led to the use of WS_2 NTs as nonreinforcement [263, 264]. WS_2 NTs were found to readily disperse in PMMA through electrospinning processes, which resulted in forming aligned nanofiber meshes with mechanical properties which were up to 22 times increase in the elastic modulus and an associated increase of 35% and 30% in the tensile strength and toughness, respectively at 2wt%WS_2 PMMA composite. In comparison to melt extrusion method used for WS_2 NTs PMMA composite, mechanical properties produced increase of 39% for the flexural strength, 83% enhancement in strain at break, as well as increase of 13% for the tensile strength and of 25% in elongation at break were achieved for composites in comparison to neat PMMA. The reinforcing mechanism of WS_2 NTs was attributed to homogeneous distribution and alignment of INTs in the moulded samples. Furthermore, the impact of processing conditions is displayed and should be a major factor when considering the desired outcome of composites.

WS_2 NTs were incorporated into poly(ether-ether-ketone) (PEEK) by Naffakh et al [265]. Again, the effect of WS_2 NTs on the morphology, thermal stability, crystallization behaviour, thermal conductivity, mechanical and tribological properties was investigated. It was established with an increasing wt% of WS_2 NTs, up to 1.0wt%, an improvement of thermomechanical properties. Additionally, crystallisation kinetics were proven again to modify the crystallization behaviour of PEEK, whilst they do not alter its crystalline structure. Overall, the induced improved properties are shown to be obtained through good dispersion of NTs as well as strong interfacial interaction of NTs surface and polymer matrix.

2.3.5 Surface Modification of WS_2 NTs

It is evident from literature, homogeneous dispersion and interfacial interaction of INTs are significant factors in determining factors of composite properties. WS_2 NTs have already displayed great promise in a vast range of biopolymers, however the applications of NTs are intimately related to their surface chemistry and the interaction with the surrounding matrix. Therefore, there have been several publications on surface modification and functionalisation of WS_2 NTs[266].

Raichman et al. [267] used a Vilsmeier-Haack reagent that covalently bonds to the sulphur atoms to obtain a polycarboxylate coating resulting in NTs which are dispersible in polar liquids, including water. This was identified through the observation of characteristic peaks that indicate the presence of carboxyl, amine, and thiol groups on the surface of NTs. This method was further examined utilizing polythiophene derivatives again using Vilsmeier–Haack chemical reaction using 2,2′-bisthiophene-4-carboxaldehyde and $POCl_3$ as chemically reactive reagents as identified in Figure 2.9 [268]. This produces an acidic, covalently bound shell of polyCOOH functional groups.

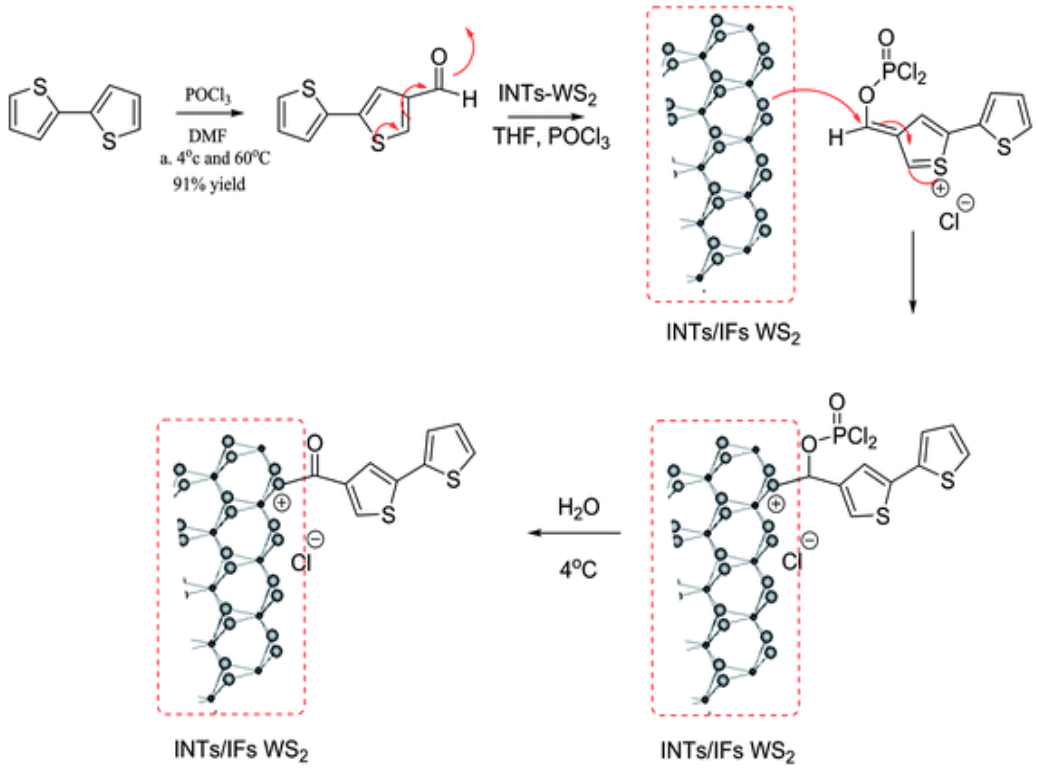

Figure 2.9 Formation of INT WS_2–bithiophene composites.

These functionalization strategies produce water-soluble WS_2, promoting development of WS_2 NTs into further into medical applications, like drug delivery and targeted therapy. Tahir et al. [269] also showed that a polymer coating with nitrilotriacetic acid side chains enables chemical attachment onto nanotubes and also serves as a chemical anchor for the binding of histidine-tagged proteins for further biomedical applications such as drug delivery.

Silane surface functionalisation of WS_2 NTs has not been widely investigated, with a few exceptions, and limited to where the matrix is an epoxy (see however [253]) or for other applications. Shahar *et al.* were the first to functionalize the surface of WS_2 fullerene-like nanoparticles with organo-silane molecules and reported better

dispersion in oil-based suspensions [270]. While Sade et al. studied the functionalisation of WS_2 NTs with both conformal humin-like coatings and APTES [271], the authors confirmed successful attachment of APTES to the surface of the NTs, though the hydroxyl groups exposed on the surface of NTs. Critically, the functional amine group of APTES is then available for further interaction with polymers.

2.3.6 Composites of Chitosan and Nanofillers

Due to the unique chemical structure and highly applicable properties of chitosan, the modification of chitosan though the functional groups enable it to react easily with other active compounds is a significant area of research. The studies discussed in this section identify TMD nanoparticles readily disperse and interact effectively chitosan matrix though solution casting methods of film preparation and have displayed opportunity for further biomedical applications. However, the attractive mechanical, biocompatible and non-toxic properties of WS_2 NTs in chitosan matrix has not yet been reported.

Although, Fakhri et al [272], examined 2D WS_2 nanoparticles and immobilized on chitosan and polycaprolactone as biodegradable polymers. It was found WS_2 increase the crystal size of chitosan composites, WS_2 identified increased antibacterial activity against both Escherichia coli and Staphylococcus aureus bacteria in comparison to the control. Furthermore, Liu et al[273] reported the use of 2D WS_2 nanosheets with chitosan nanoparticles, to be further developed into a complex composite with polydimethylsiloxane (PDMS) film, prepared through solution casting, to obtain triboelectric acetone sensor. The findings outlined the interaction

between WS_2 and chitosan through chemical analysis and identified hydrogen bonding between the two components, as well as W-O bonding, revealing the existence of hydroxyl functional groups at the edge of WS_2 sheets. This is suggestive of WS_2 NTs has significant potential for effective interfacial interaction in chitosan matrix for enhanced properties.

The successful incorporation of nanoparticles in the chitosan polymer matrix has been reviewed [180, 274, 275] identifying the vast range of nanoparticles utilized as effective reinforcement for chitosan film while also examining the effectiveness of antimicrobial/ antibacterial properties for biomedical industry application.

Analogous TMD with WS_2, Molybdenum Disulphide (MoS_2) has been examined as a functional nanofiller in chitosan [276] [277]. This in-depth study identified the interaction mechanism of chitosan-MoS_2 through amine reaction by surface chemical analysis. The antibacterial activity of composites found to achieve an enhanced effect, this was deemed due to the positive (amine) charge if composite which induces reactive oxygen species (ROS) resulting in close interaction will cell membrane and highly efficient antibacterial activity.

In recent years the development of other nanoparticles such as ZnO in chitosan for food packaging as well as biomedical applications. Various studies have identified the significant binding between the ZnO nanoparticles and chitosan's amino and hydroxyl groups, while additionally portraying enhanced antibacterial activity[278-282].

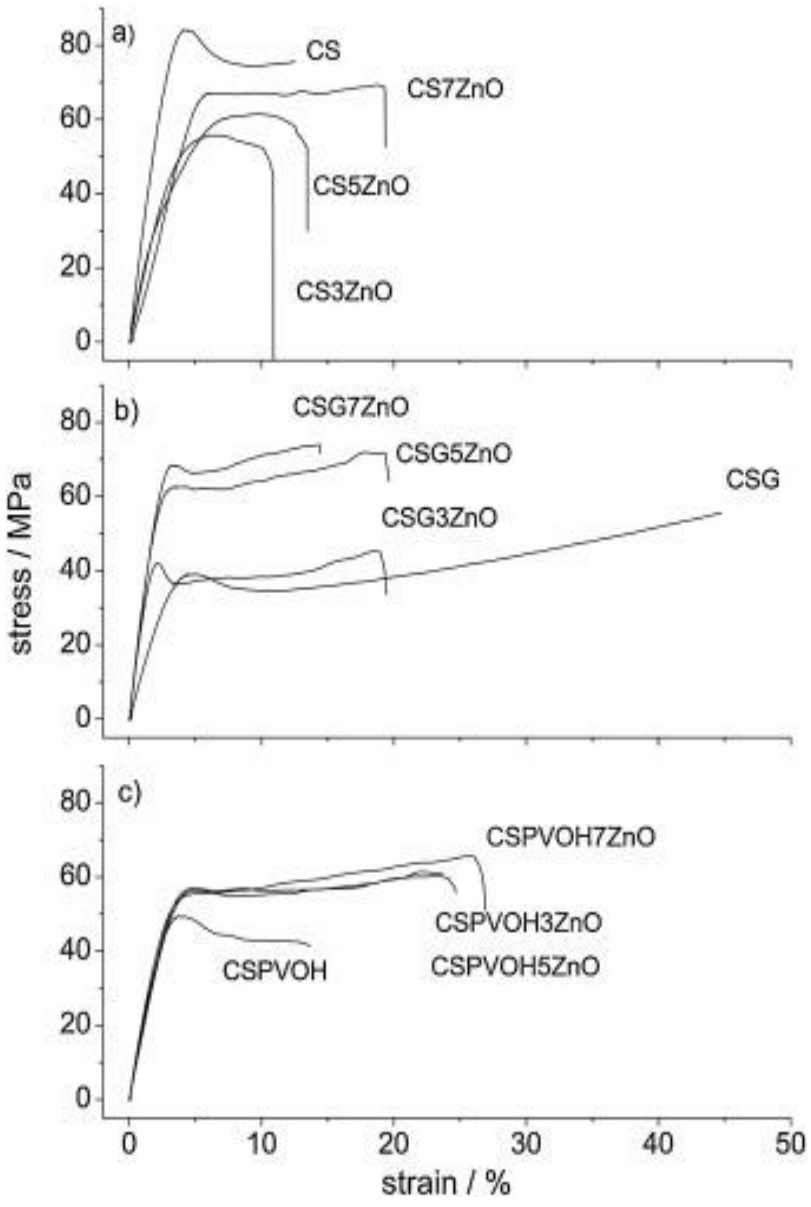

Figure 2.10 Representative stress-strain curves of a) chitosan/ZnO, b) chitosan/glycerol/ZnO and c) chitosan/PVOH/ZnO films as a function of ZnO content, plain chitosan-based films

Boura-Theodoridou et al [283] however examined ZnO chitosan composite with the use of glycerol and NaOH treatment for the optimisation of interfacial interaction through intermolecular hydrogen bonding. Based on the results obtained, it identified the effective interactions between O-H and N-H of chitosan, glycerol/NaOH and ZnO nanoparticle surface. The effective interactions was evidently translated to the enhancement of mechanical properties shown in Figure 2.10 [283].

Addition of ZnO in chitosan/glycerol films leads in considerable enhancement of the stiffness by 140 % increase, and strength increase of 50%, and up to 75 % reduction of the strain at break. This finding further reaffirms the mechanical properties are dependent on the chemical interactions between the different function groups of the obtained films. Chitosan ZnO composite films contain a significant amount of protonated amino groups that contribute towards the antimicrobial behaviour against both Gram-positive and Gram-negative bacteria. However, the use of NaOH/glycerol results in the deprotonation of chitosan, and consequently does not lead to an enhancement of antimicrobial impact against bacteria.

Similar studies were performed with the use of a number of inorganic nanoparticles, including TiO_2 [284, 285], Ag [286], silica [287] and Graphite Oxide(GO) [288, 289] which identify the use of glycerol (15-30wt% to chitosan biopolymer) used as a plasticiser and aid in the intermolecular interaction with chitosan nanocomposites. Plasticizers reduce intermolecular forces along the polymer chains, thus increasing free volume and chain movements[290]. In turn, this modifies the mechanical properties of polymeric materials when they are added

to the polymer matrix due to increasing elasticity, however, it is found that thermal resistance of the plasticized film is lower than that of unplasticized films due to the weak intermolecular forces among chitosan structures. Glycerol is used as a functionality to promote interfacial interaction through intermolecular hydrogen bonding while also providing effective dispersion through solution casting of composite. Consequently, the use and concentration of glycerol if used needs to be taken into consideration which identifying the desired nanocomposite properties for further application.

Evidently, from the published literature that a range of nanoparticles and chitosan complexes have been studied. However, there is a significant gap in literature studies describing the incorporation of WS_2 NTs in chitosan biopolymer and the significant potential application potential biotechnology, medical device and food packaging properties.

2.4.0 Concluding remarks

It is clear from the published literature that the inclusion of WS_2 NTs in biopolymers provide an alternative route to further enhance and optimise biopolymer properties. WS_2 NTs have clearly shown to readily disperse in PLA as well as enhance thermal and mechanical properties in PLA matrices, but to a limited extent. The presence of the WS_2 NTs as also alters the crystallisation kinetics of PLA, addressing some of the disadvantages of PLA. However, it is also clear from the literature that there are still considerable areas that require major study, including;

- Understanding of the structure and morphology, thermal properties and surface chemistry of WS_2 NTs

- Understanding of the relationship between dispersion, aspect ratio as well as interfacial interaction of NTs in PLA.

- Appreciation of the effect of the shear forces applied during melt mixing has on the aspect ratio of the NTs.

- Successful functionalisation (e.g. silane) of the WS_2 NTs has not yet been achieved, as a route to promote interfacial interaction with PLA and the effects such functionalisation had on mechanical properties.

- WS_2 NTs has not yet been studied as a functional filler for the chitosan matrix. Therefore, the study of the inclusion of WS_2 NTs in chitosan matrix, polyelectrolyte complex formation and composites properties are required.

Chapter 3: Materials and Methods

This chapter describes the details of materials used as well as methods of sample preparation and characterisation of the WS_2 NTs and composites studied. The characterization of NTs was performed using a wide range of techniques for purposes of understanding the surface chemistry of NTs, the thermal profile of NTs and the impact of such on the structural and chemical properties of NTs.

3.1. Materials

The WS_2 NTs were kindly provided by Professor Rashef Tenne, Weizmann Institute, Israel and Professor Alla Zak from the Holon Institute of Technology, Israel.

Two grades of poly(lactic acid) (PLA) were used in these studies. Firstly, PLA (~98% L-isomer, <2% D-isomer, Ingeo 4032D), NatureWorks, a semi-crystalline biopolymer, transparent polymer, was supplied by Kornfield Group, Caltech, USA. The second was a PLA (~96% L-isomer, Luminy LX175) from Corbion, an amorphous, transparent PLA resin which was made from European sugar beet and Thai sugarcane.

The chitosan (poly(β-(1,4)-d-glucosamine) used, with a viscosity of about 200 mPa·s (i.e. 1% solution in 1% acetic acid at 20 °C) and a degree of deacetylation of ≥85 %, was supplied by Jinan Haidebei Marine Bioengineering Co., Ltd (China). The molecular mass of this chitosan is about 250 kDa.

(3-Aminopropyl)triethoxysilane (APTES) (98%) was purchased from Sigma Aldrich and used as received. Dichloromethane (DCM, 99.8%) were purchased by Sigma Aldrich, Acetic Acid Glacial (>95% Analytical Grade) Fisher Scientific UK Ltd Glycerol (≥99 % Analytical Grade) Fisher Scientific UK Ltd, all were used as received. Deionised water was used throughout the study.

3.2 Sample Preparation

3.2.1 Composites of PLA and WS_2 NTs by melt extrusion and injection moulding

Composites of PLA (NatureWorks 4032D) and WS_2 NTs were prepared by melt mixing in a twin-screw extruder with increasing WS_2 NT loading up to 3% by weight. In the first instance, PLA, in a pellet form, was cryo-milled to a powder (under liquid nitrogen) and dried in a dehumidifying dryer at 80 °C for 4 h. Compositions of PLA and WS_2 NTs in a powder form with 0.1, 0.3, 0.5, 1.0, and 3.0wt% of NTs were weighed and mixed by hand. The compositions were then melt compounded in a Prism Eurolab 16 mm twin-screw extruder (Thermo Fisher Scientific, USA) with 9 heating zones set from 140ºC at the feed end to 200ºC at the die. The screw profile of the extruder used is depicted in Figure 3.1, each zone with corresponding temperature profile and with one sheering zone, Zone 7 was implemented with 12 30° kneading

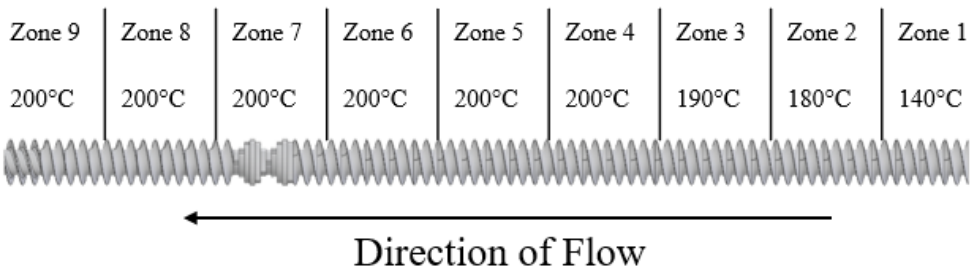

Figure 3. 1. Screw profile used for twin screw extrusion of PLA and WS_2 NTs

discs and a screw speed of 70rpm was employed throughout, to produce pellets of each composite formulation. This screw profile was used to optimise the dispersion of the NTs in PLA while also trying to preserve the aspect ratio of the fragile NTs, therefore the shear forces were minimised and elongation mixing promoted.

3.2.2 Preparation of Functionalized WS_2 -APTES

APTES was utilised to functionalize the surface of the WS_2 NTs via solution mixing. 0.25g of WS_2 NTs were dispersed in 30ml of DCM assisted by ultrasonic bath treatment (3min). The APTES was added to this solution in ratios of 1:1 (0.25g WS2 :1.057ml APTES), 1:2(0.25g WS_2 :0.5285ml APTES), 1:4 (0.25g WS2 :0.2643ml APTES), density of APTES 0.946g/ml. The WS_2 APTES DCM solutions were mechanically stirred at 500rpm overnight at room temperature. The DCM APTES WS_2 NTs solution was then filtered using a Buchner funnel and washed with deionised water. The silane modified WS_2 NTs were dried at room temperature for 8 h followed by drying at 40 °C under vacuum for 12 hours.

3.2.3 Preparation of composites of PLA and APTES modified WS_2 NTs in film form

Composites were prepared via solution mixing and solvent casting. PLA (Corbion ~96% L-isomer, Luminy LX175) (10g) was dissolved in 50 mL of dichloromethane under magnetic stirring in a 250 mL round-bottom flask at room temperature. 0.5wt% of WS_2 NTs (0.05g) were fully dispersed in 30ml of DCM assisted by ultrasonic bath treatment (3min) and finally the two solutions were mixed together and mechanically stirred. 0.5, 1.0 and 2.0 wt % APTES (0.05g/0.0526ml, 0.1g/0.1057ml, 0.2g/0.211ml) was then added, followed by stirring overnight to allow

the completion of the reaction. The resulting solutions were cast in petri dishes and dried at room temperature for 8 h followed by drying at 40 °C under vacuum for 12 h to produce the composite materials. These were then pressed in a Colin Press at 190 °C in a mould for 5 min and cooled to room temperature at a rate of 10 °C/min to obtain the final film with a thickness of ~0.5 mm.

3.2.4 Preparation of composites of chitosan and WS_2 NTs in film form

A chitosan solution was prepared by dissolving 2g of chitosan in beakers containing 100 mL of 1% acetic acid solution. The solution was stirred at ambient temperature for 4 h until complete dissolution of the chitosan. WS_2 NTs were added to 20 mL of the prepared 1% acetic acid and water solution at four levels of 0.1, 0.5, 1.0 and 2% (wt% chitosan) addition and ultrasound treatment was performed for 3 minutes on each solution at ambient temperature. The NTs dispersions were then added to the chitosan solutions. For glycerol plasticised films, 0.4g (20wt% chitosan) of glycerol was added to the chitosan WS_2 NT solution and stirred overnight. The solutions were then poured to petri dishes with 10cm diameter, and petri dishes were then transferred to fume hood under ambient conditions for 5 days. Dried films were peeled from the surface of the dishes and stored in vacuum sealed bags in a dark environment prior to analysis.

3.3 Characterisation Techniques

3.3.1 Fourier Transform Infra-Red Spectroscopy (FTIR)

FTIR measurements were carried out using a Bruker Tensor 27 spectrometer equipped with an attenuated total reflectance (ATR) crystal and evaluated using OPUS analysis software. Measurements were recorded in the wavenumber range of 500-4000 cm^{-1}. The resolution was set to 2 cm^{-1} and averaged over 12 scans to acquire each spectrum with background spectra removed.

3.3.2 Raman Spectroscopy

The Raman spectra of the WS_2 NTs were obtained using a 633nm Renishaw spectrometer. The equipment was calibrated with monocrystalline silicone samples with a characteristic peak at 520cm^{-1}. The experiment was performed under ambient conditions using 5% of maximum power to optimise results and avoid thermal or photochemical degrading of the sample. For the composites of chitosan and WS_2 NTs the Raman spectra were collected using a Horiba LabRam HR (660nm and 500nm laser) under ambient conditions using 50X magnification objective and 25% of laser power spot focused on the sample with an exposure time of 10 seconds and a minimum of 10 accumulations.

3.3.3 X-ray diffraction (XRD)

XRD measurements were performed at room temperature on a 3rd generation Malvern Panalytical Empyrean instrument equipped with multicore (iCore/dCore) optics and a Pixcel3D detector operating in 1D scanning mode. A Cu tube was used

giving Cu $K_{a1/2}$ radiation (1.5419Å). Scans were made in the range 5 – 70° 2θ with a step size of 0.131 °.

3.3.4 X-ray photoelectron spectroscopy (XPS)

XPS measurements were carried out using a Kratos Axis Ultra DLD spectrometer (Kratos Analytical, Manchester, UK). Samples were mounted on electrically conductive carbon tape upon the sample bar and loaded in to the spectrometer. Once an acceptable vacuum level had been reached, the samples were transferred to the main analysis chamber. The samples were illuminated by a monochromated Al Ka x-ray source (h*n* = 1486.7 eV) and also flooded with low energy electrons from a charge neutraliser in order to prevent the surface from becoming positively charged during the experiment. Data were collected in a hemispherical analyser using a pass energy of 160 eV for survey spectra and 20 eV for high resolution core level spectra (resolution approx. 0.4 eV). Data were analysed using the CasaXPS software package, using mixed Gaussian-Lorentzian (Voigt) lineshapes and Shirley backgrounds. The spectrometer was calibrated using the Ag $3d_{5/2}$ peak and Fermi edge of clean polycrystalline Ag prior to the start of the experiments, with the transmission function determined using various clean metallic foils. The binding energies of the data were adjusted during the analysis, using the C-C/C-H component in the C 1*s* region at 285.0 eV as the reference point.

3.3.5 Scanning Electron Microscopy (SEM)

SEM micrographs were obtained using a Zeiss-Sigma field emission instrument equipped with a Gemini column. An InLens detector was employed to

explore the morphology of the samples along with an acceleration voltage of 3 kV, an aperture size of 30 µm, and a working distance of 2- 4 mm. Before imaging, all the blends were cryo-fractured after immersion in liquid nitrogen for 30 min and samples were then broken. The fractured surface of all the samples was then mounted on an Al SEM stub using double-stick carbon tape and sputter-coated (~10 nm) using an Au/Pt or Carbon metal target (Cressington 108 auto) under a weak argon atmosphere to prevent charging and surface heating.

3.3.6 Transmission Electron Microscopy (TEM)

Prior to imaging the WS_2 NTs were dispersed in ethanol and sonicated for 3 minutes then transferred on to holy copper grids via drop casting.

Specimens for TEM imaging of the polymers of interest and their composites with WS_2 NTs were prepared by sectioning ultrathin samples (thickness typically ranging from 50 to 100 nm) using a Lycia RM2245 ultra-cryo-microtome equipped with Diatome 35° dry diamond knife. TEM analysis was carried out using a FEI (Thermo Fisher Scientific) Talos F200X. It had an X-FEG (Field Emission Gun) high-brightness electron source and was fitted with a Super-X EDS (Energy Dispersive X-ray Spectrometer) system. The EDS system had the integrated four silicon drift detectors with a solid angle of 0.9 srad for rapid chemical composition mapping. The microscope was operated at 200 kV throughout the analysis, and the data were acquired using either FEI TIATM or VeloxTM software where appropriate. In the STEM mode, High-Angle Annular Dark-Field (HAADF) and Bright-Field (BF) images were taken simultaneously.

3.3.7 Gel Permeation Chromatography (GPC)

The molecular weight distribution of extruded pellets of the unfilled and WS_2 NT filled PLA was determined by GPC Analysis. Extruded pellets were dissolved in tetrahydrofuran (THF) in the ratio 5mg of pellets: 1ml THF, assisted by ultra-sonication at 40°C for 1hr. 1.5ml of each solution was pipetted into an Eppendorf tube and centrifuged for 15min at 10,000rpm. 1ml of solution was extracted via a syringe and injected into the GPC instrument through a 0.25µm filter for analysis. The weight average molecular weight (M_w) before and after melt extrusion of unfilled PLA (pellets) and composites of PLA and WS_2 NTs (up to 3wt% loading) were determined. Any change in M_w of the PLA and the composites can be a measure of polymer degradation due to the melt extrusion process, or if addition of the WS_2 NTs or other impurities to the PLA induced degradation of the polymer and thus a reduction in M_w. The GPC curves were recorded using Refractive Index (RI) and Light Scattering (LS) detectors, show the molecular weight curves as a function of eluting time for the various materials. The RI and LS measurements for the PLA polymer samples were obtained within similar elution times, with only a small shift to higher elution time for the processed sample.

3.3.8 Thermogravimetric Analysis (TGA)

TGA was carried out using a Mettler Toledo thermal analyser, in alumina pans, over the temperature range of 25°C to 1000°C at a heating and cooling rate of $10°C$ min^{-1} under nitrogen and air atmosphere.

3.3.9 Thermogravimetric Analysis/Mass Spectrometry (TGA-MS)

TGA-MS of WS_2 NTs was performed using a Mettler Toledo TGA DSC1 and a Hiden HPR20 with HAL IV interface, the WS_2 NTs sample data was obtained for a temperature range of 20-1000°C at a heating rate of 10°C min^{-1}.

3.3.10 Differential Scanning Calorimetry (DSC)

The thermal properties of the polymers and composites were studied using a Mettler Toledo instrument (DSC1, model 700, 400W) equipped with a FRS5 thermocouple sensor, robotic sample changer and evaluated using a STARe Version 15.01 software package. Calibration was performed using Indium and Zinc standards. Non-isothermal scans were completed under nitrogen (flow rate of 50ml min^{-1}) using the following procedure: samples of 8±1 mg were placed into aluminium pans with pierced lids and heated from -20°C to 200°C at a heating rate of 10 °C min^{-1} (first heating) and held at this temperature for 2 min. to remove any thermal history. Samples were then cooled from 200°C to 20°C at 10 °C min^{-1} (first cooling) and held at 20°C for 2 min. Subsequently, the samples were re-heated (second heating) and cooled again using the same procedure as described above. The thermograms were used to estimate the glass transition temperature (T_g), crystallization temperature (T_c), melting temperature (T_m), change in enthalpy of melting (ΔH_m), and change in enthalpy of crystallization (ΔH_c). The percentage of crystallinity (X_c) of samples were calculated using equation1:

$$\left(\frac{\Delta H_m - \Delta H_{cc}}{\omega \Delta H_m^0}\right) x100 \quad (1)$$

where, ΔH_m, ΔH_{cc} are the changes in enthalpy of melting and cold crystallisation, respectively. ω is the weight fraction of PLA in each composite, and ΔH_m^0 is the melting enthalpy of a theoretically 100% crystalline PLA which has been reported to be 93.7 J/g [291].

3.3.11 Hot –Stage Polarised Optical Microscopy (POM)

Samples of PLA and composites of PLA andWS_2 NTs for examination by POM were cut in 50μm thick sections with a Tissue-Tek® Cryo3 cryostat microtome after being embedded and frozen in OCT (Optimal Cutting Temperature embedding material). Samples were placed between microscope slides and placed on a THMS600 Linkam scientific. Samples were heated from 20°C to 200°, at 10°C min^{-1}, held at 200°C for 5min, and cooled from 200°C to 20°C at a cooling rate of 10°C min^{-1}. Polarized light micrographs (4x magnification) of the PLA and all composites were obtained through crossed linear polarizers on a Zeiss Universal microscope equipped with a Canon EOS DS30 camera for image acquisition. Images were taken at equal intervals during sample heating and cooling cycles.

3.3.12 Wide and Small Angle X-Ray Scattering (WAXS, SAXS)

Simultaneous SAXS and WAXS measurements were acquired at the APS beamline 5-ID-D at the Argonne National Laboratories, USA. The extruded pellets of both unfilled PLA and WS_2 NT filled PLA at loadings of 0.1, 0.3, 0.5, 1.0 and 3.0 wt% WS2 NT were positioned with their long axis (extrusion direction) perpendicular to the incident X-Ray beam for acquisition in transmission mode. Diffraction patterns were acquired every 1s at an exposure of 0.1s for SAXS and 10s for WAXS, using X-

rays with wavelength of 0.7293Å, in three different axial positions and averaged afterwards. WAXS and SAXS images were acquired on Rayonix CCD detectors with a sample to detector distance of 200.51mm and 8.503m, respectively. The wavevector, q had been calibrated using a spinning silicon diffraction grid. Air scattering signal was subtracted from each scan to isolate scattering of the samples with respect to the background.

3.3.13 Zeta Potential

Measurements were conducted using an Anton Paar Litesizer 500 and samples were run in triplicate for 100 runs at 25°C, using a maximal voltage of 200V. WS_2 NTs and APTES functionalised WS_2 NTs samples were diluted with 0.5 ml methanol, and vigorously shaken to ensure good dispersion, then loaded into an Omega zeta potential cuvette. Chitosan, Glycerol, Chitosan WS_2 NTs, and Chitosan Glycerol and WS_2 NTs film composites are suspended in water solution, then loaded into an Omega zeta potential cuvette and measurements taken.

3.3.14 Tensile Mechanical Testing

Mechanical Testing were performed using an Instron 5800R instrument, with Bluehill 2 software. 5-7 dog bone shaped specimens were prepared by stamping out from films and tested, using a tensile crosshead speed of 1mm/min.

3.3.15 Attenuated Total Reflectance - Fourier Transform Infrared (ATR- FTIR) Mapping

FTIR-ATR spectra of film samples were collected using a Thermo Scientific - Nicolet iN 10MX instrument fitted with attenuated total reflectance (ATR) having Ge crystal at 45° using standard pressure (15Pa). Measurements were performed in the wavelength range of 4000-600cm^{-1} with a collection time of 5seconds for 16scans, an aperature size of 50µm and step size of 30µm x 30µm.

3.3.16 Gas Permeability Measurements

The barrier properties of films against oxygen, carbon dioxide and water vapour were assessed on a 50 cm^2 surface sample of each chitosan and corresponding composites of glycerol and WS_2 NTs with film thickness of 250 ± 50µm using a TotalPerm permeability analyzer (PermTech Srl, Pieve Fosciana, Italy) equipped with both an electrochemical and infrared sensor. Oxygen transmission rate (*O_2TR*), carbon dioxide transmission rate (*CO_2TR*) and water vapour transmission rate (*WVTR*) were determined according to the standard methods, ASTM F1927, F2476, and F1249, respectively, where a carrier flow rate (N_2) of 10 mL min^{-1} at 23°C and 65% relative humidity (RH) at one atmosphere pressure difference on the two sides of the specimen was used. *TR* values were then converted in permeability coefficients (*$P'O_2$*, *$P'CO_2$* and *P'WV*) according to the following equation (2):

$$P' = P \times t = \frac{TR}{\Delta p} \times t \qquad (2)$$

where, P' is the permeability coefficient [in mL μm m^{-2} ($24h^{-1}$) atm^{-1} for O_2 and CO_2, in g μm m^{-2} ($24h^{-1}$) atm^{-1} for WV], P is the permeance (defined as the ratio of the *TR* to the difference between the partial pressure of the gas on the two sides of the film, Δp), and t is the total thickness of the specimen. Three replicates were run for each sample.

3.3.17 Bacterial Viability

The antibacterial performance of chitosan WS_2 NTs with and without glycerol films were evaluated against the Gram-negative bacteria uropathogenic *E. coli* CFT073 and *P. fluorescens* and *S. aureus USA 300 JE2* – Gram positive bacteria. Bacteria were revived from glycerol stocks and streaked on Luria-Bertani (LB) agar (for *E. coli* and *P. fluorescens*) and Tryptic Soya (TSB) agar (for *S. aureus*). A single colony was picked from each plate and an overnight primary culture was set-up by inoculating the colony in LB broth (for *E. coli* and *P. fluorescens*) and TS broth (for *S. aureus*).

A stock solution of resazurin solution was prepared by dissolving 0.05g of resazurin powder in 10ml of 1XPBS. All experiments were carried out in sterile 24-well plates. 2ml of cation-adjusted Mueller Hinton Broth – II (MHB-II) was introduced in each well followed by the addition of 10ul stock resazurin solution to yield a final concentration of 25μg/ml. Wells containing MHB-II and resazurin were used as negative controls. Prior to the antibacterial assay, chitosan WS_2 NTs with and without glycerol films were sterilized by exposing them to ultraviolet radiation (BIO-LINK BLX-254, 80W) for 10 minutes. The UV-sterilized NTs were introduced in negative controls to observe any bacterial growth/contamination. Absence of bacterial

growth/contamination indicated successful UV-sterilization of NTs. Wells containing MHB-II and resazurin with bacteria were used a positive control. Test samples were introduced in the wells containing MHB-2 and resazurin. In positive controls and test wells, the overnight bacterial cultures were introduced such that the starting optical density (OD) of bacteria at 600 nm was 0.01. The plate was incubated at 37ºC, 110 RPM for 8 hours and fluorescence measurements at 585nm were measured every 2 hours over a period of 8 hours using the BMG Labtech FLUOstar Omega plate reader.

Chapter 4: Results and Discussion I

WS_2 NTs Characterisation and

Composites of Melt Extruded PLA WS_2 NTs

4.1 Introduction

The synthesis of WS_2 NTs has been refined and largely improved since they were first reported by Tenne *et al* [5, 6], recently via a new horizontal reactor (previously described in Chapter 2[82]). Therefore, the beginning of the experimental research will consist of an extensive characterisation of WS_2 NTs in order to competently understand the current chemical, thermal and morphological properties of WS_2 NTs. In particular, this chapter provides a comprehensive analysis of thermal behaviour of WS_2 NTs using thermogravimetry-mass spectrometry (TGA-MS) which has been reported once previously [292] but to date the thermal stability of WS_2 NTs has not been studied in detail. Additionally, previous studies paid little attention to the surface chemistry of the WS_2 NTs and to the effect of NT impurities. These properties are fundamental in the advancement of understanding WS_2 NTs on the manufacturing of thermoplastics-based composites with WS_2 NTs prepared by melt mix extrusion which is presently the most industry relevant technologies for large-scale production of thermoplastic composites.

Furthermore, this chapter examines WS_2 PLA composites prepared by melt mix extrusion method (explained in Chapter 3). PLA (Nature works Ingeo 4032D) semi-crystalline polymer was chosen for this experimental process due to being an extrusion grade biopolymer as well as crystallinity properties have proven interesting

as previously discussed in the literature review (Chapter 2). This chapter further studies the impact of the sheer forces applied during melt mixing on the aspect ratio (AR) of the NTs, which has rarely been studied [263], while it is a relevant factor in reinforcement of the polymer on addition of the 1D filler, and the consequential effect on the mechanical properties and, crystallization behaviour of PLA.

4.2 Characterisation of WS_2 NTs

NTs morphology, prior to processing was studied using SEM techniques as shown in Figure4.1. Figure4.1 a) identifies a bundle of WS_2 NTs where the NTs typically have a diameter of about 50nm and lengths in the low tens of microns, resulting in aspects ratio's (AR) up to 1000. Figure 4.1 b, clearly identifies NTs have predominantly a closed ended structure, a consequence of the synthesis method employed the closed ends of the WS_2 NTs used in this study can be further clearly seen in the TEM image in Figure 4.1c).

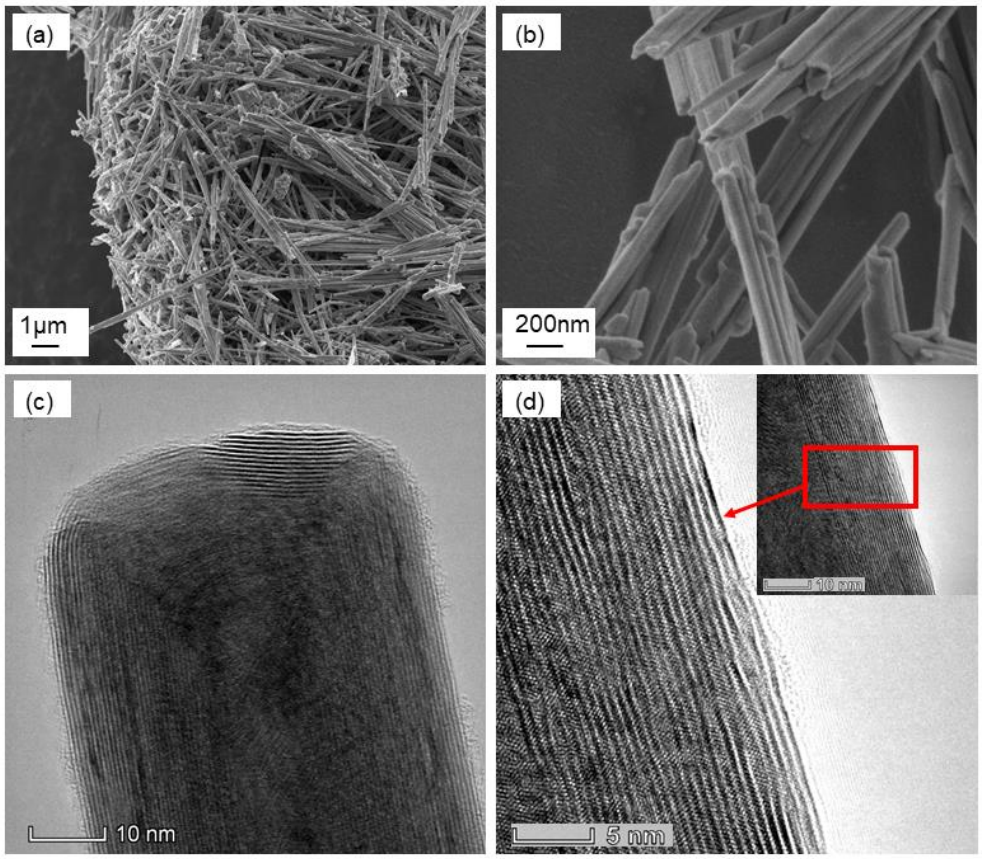

Figure 4.1. Electron microscopy images of WS_2 NTs. (a,b) SEM images under different magnifications and (c,d) TEM images an individual WS_2 NT, the former showing a closed end.

TEM imaging of the WS_2 NTs also revealed the multi-walled structure of these NTs. The TEM images were analysed using ImageJ software to determine the width and length of NTs, as well as the number of walls in the multiwall structures and hence the spacing between the walls. Figure 4.2 c) and d) displays the closed end structure of NTs as well as along the length of the NT structure respectively. A large range of dimensions were found, as the widths of NTs varied from 52nm to110nm, and the lengths from 2.45µm - 65.6µm. This large distribution in tube dimensions results in a broad range of NT AR, as reported previously [78]. Additionally, the number of walls varied from 13 to 28 along the length of the NTs imaged, Figure 4.1 d), but at the closed ends Figure 4.1 c) the number of walls ranged from 8 to 23.

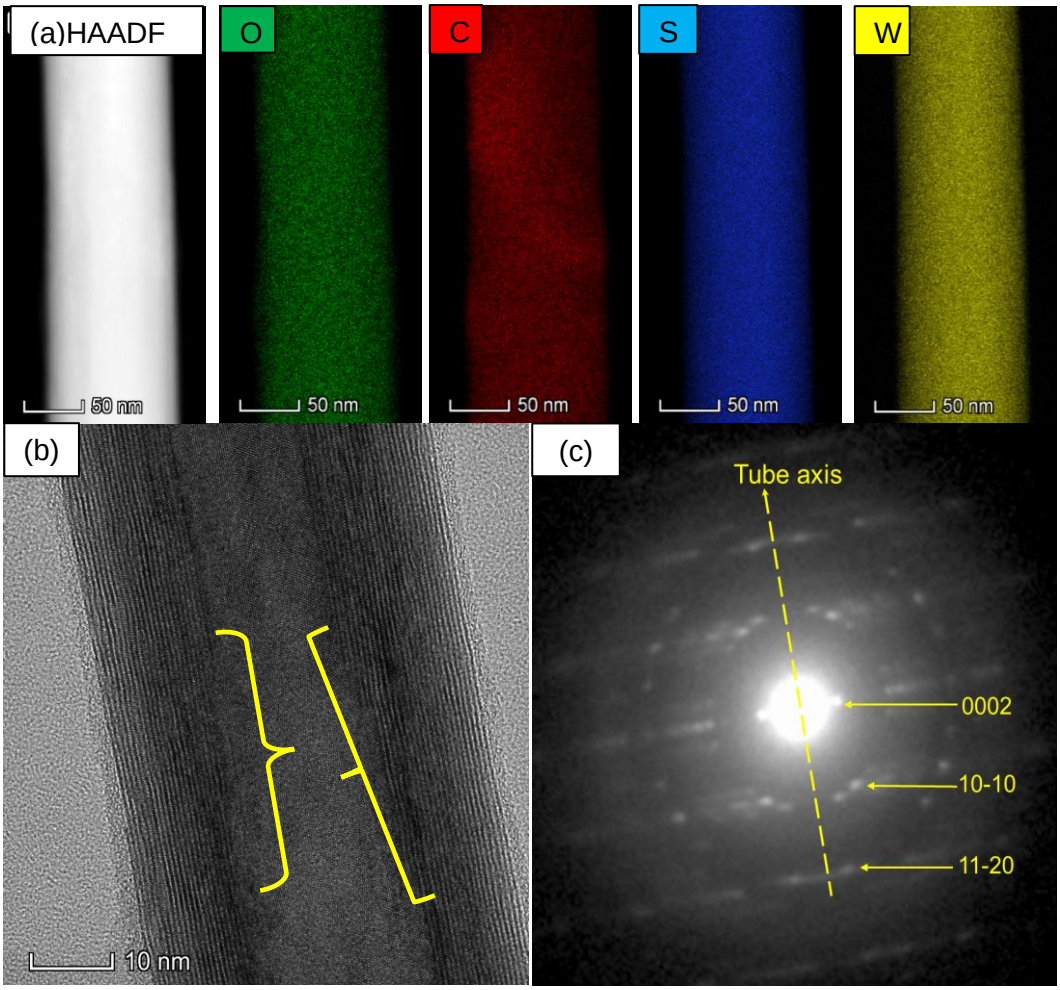

Figure 4.2. (a) STEM−EDS chemical analysis of WS_2 NTs, (b) TEM identification of incomplete NT wall structures, and (c) electron diffraction pattern of the WS_2 NTs.

The variation of the number of walls along the length of NTs is highlighted by the yellow lines in Figure 4.2 c). This reduction of the number of concentric walls along the NT is suggested to be due incompletion of wall growth during the synthesis process. However, it should be noted, that while there is some variation in the dimensions of the NTs, the wall spacing between neighbouring layers of individual NTs is consistent at approximately 0.65nm, in agreement with that expected from calculations reported previously [293]. Figure 4.2 exhibits STEM-EDS analysis used to identify the chemical composition of the NTs, where both W and S were detected

within the WS_2 NT structure, however oxygen and carbon from airborne contaminants are also found, in agreement with previous reports [93]. The electron diffraction pattern (Figure 4.2 c)) reveals a multi-helical structure and, the 0002 basal plane and 10-10 and 11-20 prismatic planes are assigned from Miller-Bravais indices. The chirality within a single NT is due to the thickness of the walls altering the magnitude of the strain on the wall curvature and consequently the geometry of the NTs. Consequently, incompletion of walls within the multi-layered S-W-S structure leads to a change in NT chirality, a phenomenon determined by the growth process controlling both NT thickness and the number of NT walls [294]. The observation of inconsistencies in the wall structure is important as it is at these positions along the NTs that rupture may occur due to the stresses applied during melt mixing in extruders.

When melt mixing any 0D/1D/2D material in conjunction with a polymer, it is critical the nanofiller used is thermally stable at the temperature required for the melt mixing process. In this instance, PLA processing temperature is 200°C, while for polymers commonly used in industry the melt mixing temperature is much higher. Thermal analysis of the WS_2 NTs was performed by TGA in an air atmosphere, Figure 4.3a), where a total mass loss of ~8% was detected when the sample was heated to 550°C, with no further mass loss at higher temperatures, up to 1000°C. A small mass loss of 1.7% was detected below 400°C which can be attributed to evaporation of physisorbed water from the surface, inner core or in between the layers of the NTs [295].

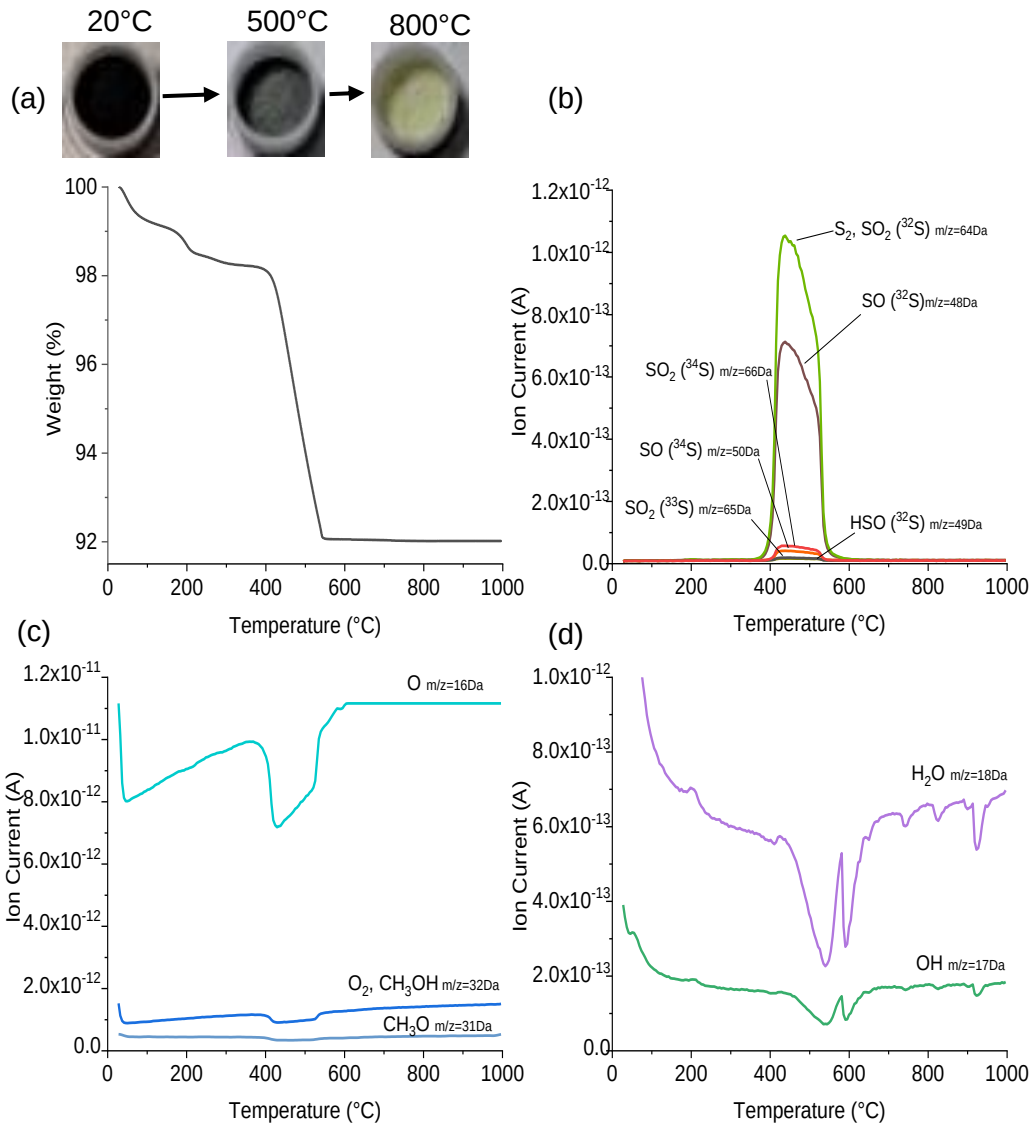

Figure 4.3 (a) TGA−MS profile for WS_2 NTs with corresponding color change through heating and the characteristic ion current curves for WS_2 NTs, (b) sulfur-containing major products, (c) oxygen-containing products, and (d) OH-containing products.

A further mass loss of 6.1% was measured between 400°C and 550°C. This weight loss progression as the temperature increased corresponded to a colour change of the WS_2 NTs powder from an original black (20°C) to dark grey (500°C) and then to a yellow/pale green (800°C) (see Figure 4.3 a)-top). This significant mass loss and colour change was not observed in an N_2 atmosphere (Figure 4.4), as WS_2 NTs are

known to be stable up to more than 1000°C in inert atmosphere [296]. TGA-MS analysis of the products evolved during the thermally induced degradation (oxidation) of the WS_2 NTs in the temperature region 400°C to 550°C shows an endothermic peak which can be assigned to the elimination of sulphur and absorption of oxygen ions and conversion of WS_2 to WO_3. The difference in molecular weights of two compounds (248 and 232, accordingly) is in a good agreement with the obtained mass loss (i.e. 248-232)/248 = 6.45 % vs. 6.1% from TGA). Moreover, the appearance of the yellow colour characteristic to WO_3 confirms this transformation. It can be seen also from the ion evolution profiles, Figure 4.3 b-d), the degradation products containing the same ions, sulphur, oxygen, and hydroxyl respectively, follow the same trend which indicates that the formation or elimination of the products takes place in the same degradation step. The major thermolysis products in Figure 4.3 b) were identified as sulphur containing fragments (m/z= 64, 48, 66, 50Da), where the base peak at 64Da is due to the elimination of both S_2 and SO_2 fragments as they contribute to the intensity of the same peak. Indeed, the possible reaction-oxidation of WS_2 NTs can be described as: $2WS_2 + 7O_2 = 2WO_3 + 4SO_2$.

Also, the most dominant peaks include ^{32}S isotope, as expected, considering the isotopic abundances of sulphur (^{32}S with the highest abundance of 95%) and the fragments with ^{34}S isotope (abundance of 4%) are less dominant, yet still exist. As the TGA-MS experiments were performed in atmospheric atmosphere, the primary degradation products could further react with oxygen to form additional bonds. The elimination of sulphur from WS_2 NTs in the 400°C to 550°C temperature range, resulted in the formation of additional sulphur species containing oxygen, which can be clearly seen from SO fragment apparent at 48Da. Therefore, in this temperature range the WS_2 NTs become completely oxidised and change chemical composition

from an induced sulphide via an oxide reaction to produce a yellow WO_3 (WO_x are usually blue or violet) powder.

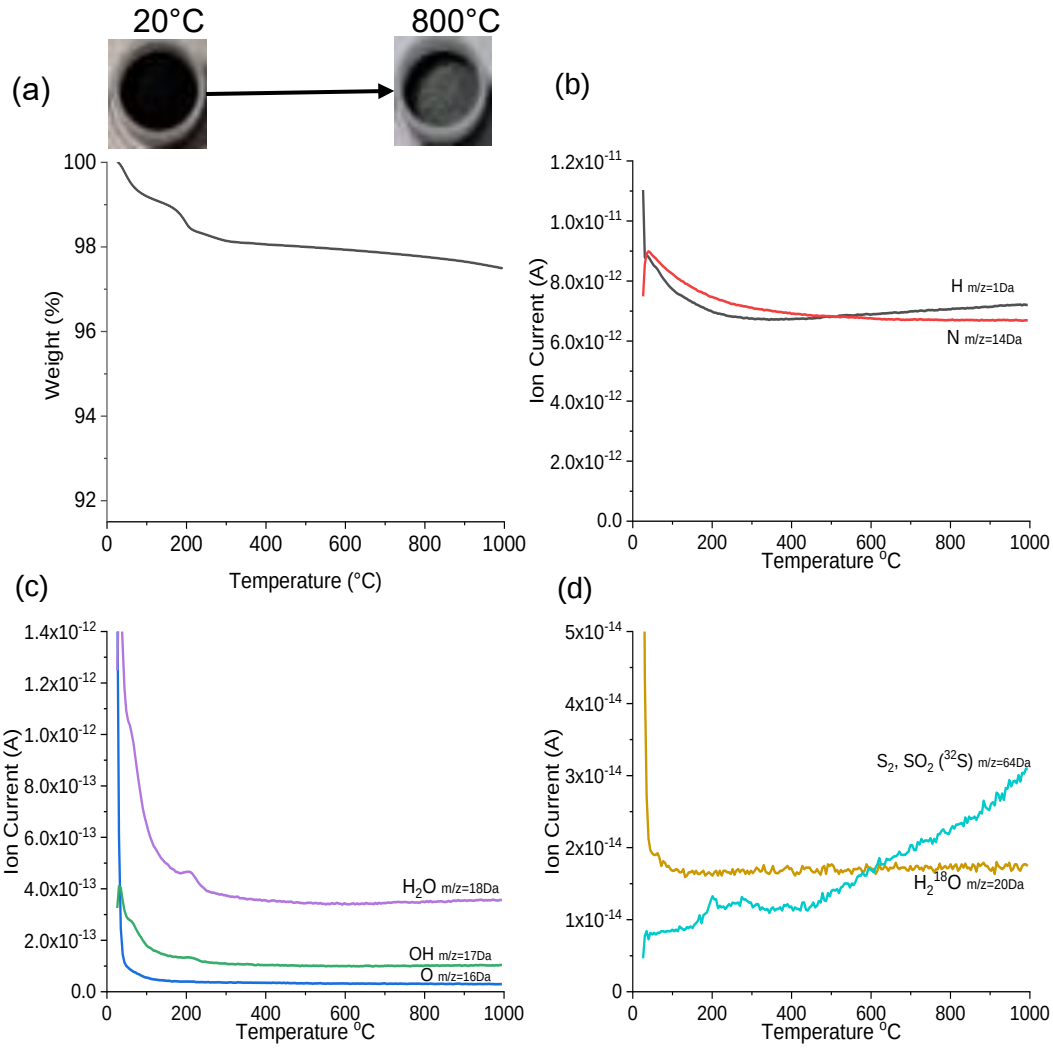

Figure 4.4 Thermal analysis of WS_2 NTs in an N_2 atmosphere, a) TGA and inset corresponding colour of WS_2 NTs and b) through d) TGA-MS analysis volatile elements detected.

Thermal analysis of WS_2 NTs in an N_2 atmosphere resulted in significantly different behaviour to that recorded in an air atmosphere in that there was no NT colour change observed after heating to 1000°C, see Figure 4.4 a), confirming there was no chemical reaction of the WS_2 NTs within the inert atmosphere. Additionally, TGA analysis

(Figure 4.4 a)) shows the same small weight loss of 1.9% by 300°C, corresponding to possibly the loss of bound water vapour within the NT sample. However, only a further weight loss of 0.6% between 400-1000°C (2.5% total) was obtained. TGA-MS correlates the mass loss to water vapour in the temperature region 0 -300°C, and from Figure 4.4 d) a very small amount ($3.1x10^{-10}$ SEM) of sulphur was detected, that eliminated from WS_2 when heated to 1000°C. WS_2 NTs have therefore shown to be stable within an inert atmosphere when heated up to temperatures of 1000°C showing no chemical reaction or significant change the chemical composition of the WS_2 NTs. This confirms there is insufficient oxygen contaminants within the NT structure to induce oxidation of WS_2 within an inert environment.

Raman spectroscopy was used to study the structural/composition changes generated by heating the WS_2 NTs to 550°C, see Figure 4.5. The most significant peaks observed in the spectra for the as received WS_2 NTs , are identified in Figure 4.5 a), E_{2g}^1 and A_{1g} active breathing and vibrational modes. The area of the spectrum expanded and shown in the inset of Figure 4.5 a) reveals the acoustic modes $E_{2g}^1(M) - LA(M); LA(M)$ (175cm^{-1}) $A_{1g}(M) - LA(M)$ (230cm^{-1}) $2LA(M) - 3E_{2g}^2(M)$ (265cm^{-1}) and $2LA(M) - 2E_{2g}^2(M)$ (296cm^{-1}) shown to be active in WS_2 crystal structures [297].

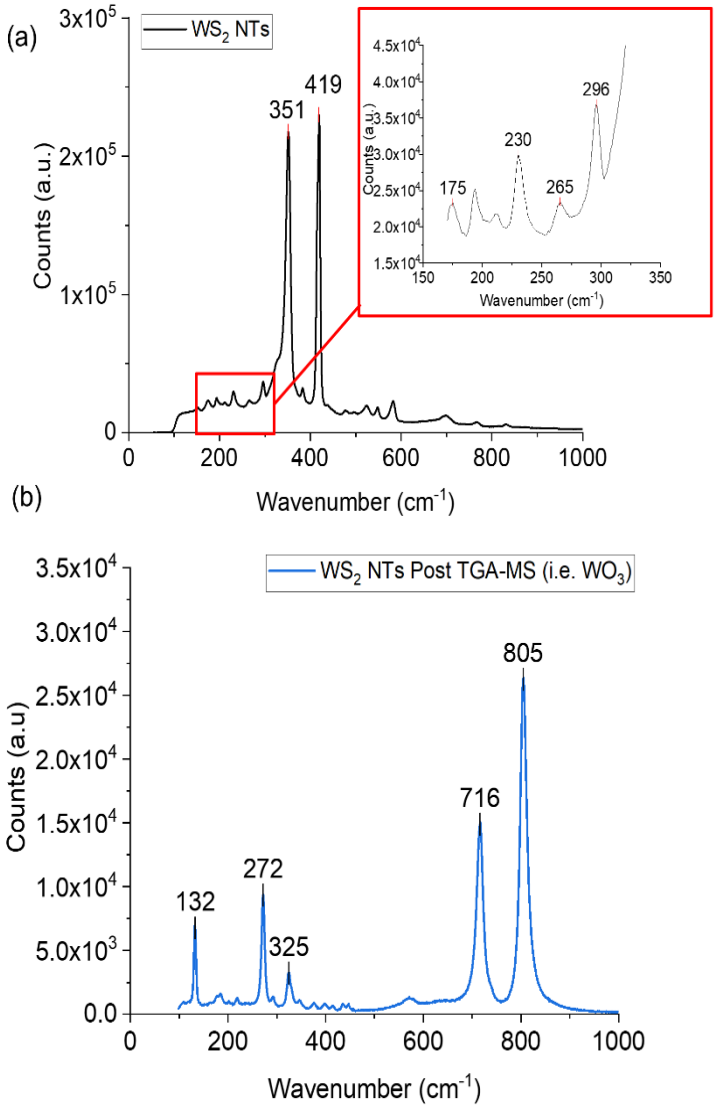

Figure 4.5. Raman spectra of (a) WS_2 NTs prior to thermal treatment and (b) WS_2 NTs post-TGA−MS (WO3) analysis.

However, due to the backscattering configuration along the surface perpendicular to the c-axis, E_{1g} is forbidden. Also, E_{2g}^2 is typically blocked by the notch filter owing to its low frequency ($30cm^{-1}$) [298]. Consequently, E_{2g}^1 and A_{1g} are the most prominent Raman modes found in the Raman spectra of WS_2 NTs. All the measurements are in excellent agreement with previous literature [13, 84, 298, 299]. Berkdemir *et al*. [300] suggested the overlap of the longitudinal acoustic phonon mode (2LA) is within $5cm^{-1}$ of E_{2g}^1, leading to a broadened peak as well as an increase in

intensity of the band at 172cm^{-1} which is due to the impact of the number of layers within the NT walls of non-zone-centre LA phonons.

Additionally, it should be noted there is a slight increase in the base of the A_{1g} (419cm^{-1}) peak, which has been described by Staiger *et al.* [298] to correlate with the emergence of a peak at 416cm^{-1} associated with the B_{1u} active mode. The B_{1u} mode has been found to be silent in other WS_2 structures and incidentally is a unique feature of WS_2 NT structures due to the geometrical curvature of the WS_2 layers in NTs.

Figure 4.5 b) shows the Raman spectrum for the yellow powder obtained after heating the sample to 800°C, where a significantly different Raman spectrum compared to the neat NTs was obtained, clearly identifying notable changes in chemical composition and structure. Peaks known to correlate with monoclinic WO_3 nanostructures were observed [301, 302] with peaks at 132cm^{-1}, 272cm^{-1} and 325cm^{-1} assigned to O-W-O deformation vibrations, and at 716cm^{-1} and 805cm^{-1} attributed to the stretching vibration of O-W-O molecules. This is consistent with the data from the TGA-MS measurements as the WS_2 NTs became completely oxidised from the heating process to produce crystalline WO_3.

From XRD analysis of the WS_2 NTs (Figure 4.6 a) the most intense peak observed was at $2\theta = 14.2$ corresponding to the (002) crystallographic plane, which is typically a sharp peak associated with the S-W-S layered structure of the NTs. In the insert the expanded region of the (002) peak of WS_2 is shown. This peak is shifted to lower angle compared to the diffraction peak of 2H-WS_2 flakes (red dashed line). This shift shows that the interlayer spacing in the nanotubes is larger than that of WS_2 flakes, which was attributed in the past to relaxation of the bending strain in the

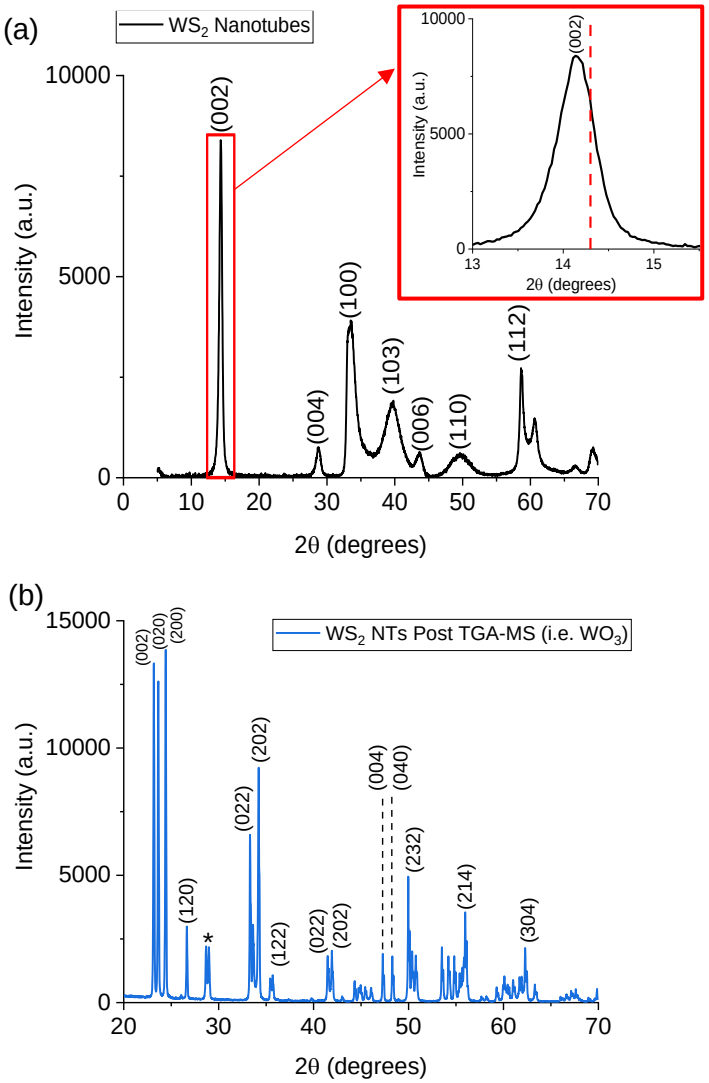

Figure 4.6 XRD pattern of (a) WS_2 NTs and (b) WS_2 NTs post TGA−MS.

nanotubes [78]. Peaks occurring at higher angles, such as those corresponding to (006) and (112) planes, are related to the elongated periodic layered structure of the WS_2 NT, therefore generating broader and less intense peaks in the spectra [94, 303].

The basal planes identified, (101) and (103), have higher intensities and broadened peaks, which identify with the 3D atomic structure of cylindrical NTs, analogous with their carbon nanotube counterparts, due to the similarity in nanostructure [304]. Figure 4.6 b) shows the XRD profile of the WS_2 NTs post TGA-MS analysis, clearly identifying a significant change in crystallographic plane

alignment. Structural planes were determined using computational analysis, some of which are identified in Figure 4.6 b), corresponding to monoclinic WO_3 nanostructures, with d-spacings of 3.8Å. It is noteworthy to highlight that in the WO_3 spectra, the peak marked with (*) in Figure 4.6 b) overlap with the (004) and (101) planes (2θ= 28.8° and 33.6°, respectively) of the WS_2 NTs [85, 305]. Broadening of these XRD peaks in the WS_2 NTs spectrum, is attributed to the submicron sizes of the NTs.

Evident from previous literature, the surface chemistry analysis of WS_2 NT is of critical importance for understanding and promoting interfacial interaction between NTs and PLA, among other polymers. XPS measurements were also performed to identify the chemical composition of WS_2 NTs pre and post TGA-MS, with survey spectra identified in Figure 4.7 and composition outlined in Table 4.1 with corresponding deconvoluted spectra analysis of WS_2 NTs (Figure 4.8 a-d) as well as on the WO_3 yellow product (Figure 4.8 e-h) (Tabulated data see Appendix Tables A1 and A2).

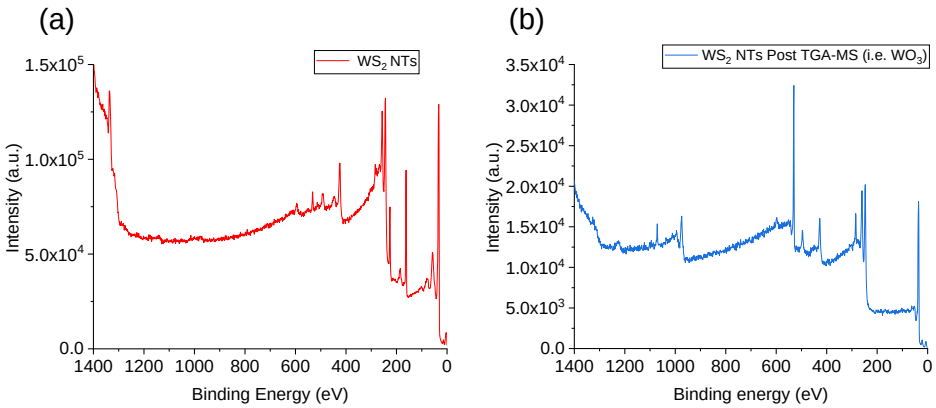

Figure 4.7 XPS Survey spectra of (a) WS_2 NTs, (b) WS_2 NTs post TGA-MS (i.e. WO_3)

The XPS for WS_2 NTs shows phases identified for tungsten, sulphur, and of airborne impurities such as carbon and oxygen, consistent with the results of the STEM-EDS analysis (Figure 4.2) Analysis of the chemical composition of the WS_2 NTs from XPS determined 23.5at% tungsten and 49.3at% sulphur, providing a concentration ratio of 1: 2.1 for W:S, in good agreement with the existing literature [93, 293]. XPS analysis of the NTs post TGA-MS confirms the chemical composition to be WO_3 with 15.0% tungsten and 51.3% oxygen detected, correlating to a 1:3.3 ratio of W:O. Additionally, no sulphur was detected, indeed no peaks are identified in the sulphur 2*p* region (Figure 4.8 f), consistent with the TGA-MS data in that there was complete elimination of sulphur ions and oxidation of tungsten by heating the WS_2 NTs above 400°C.

Table 4.1 Elemental Ratio of WS_2 NTs and WS_2 NTs Post TGA-MS (i.e., WO_3)

Sample	**Na**	**O**	**C**	**S**	**W**
WS_2	0	7.25	19.97	49.26	23.51
WO_3	4.53	51.27	29.25	0	14.95

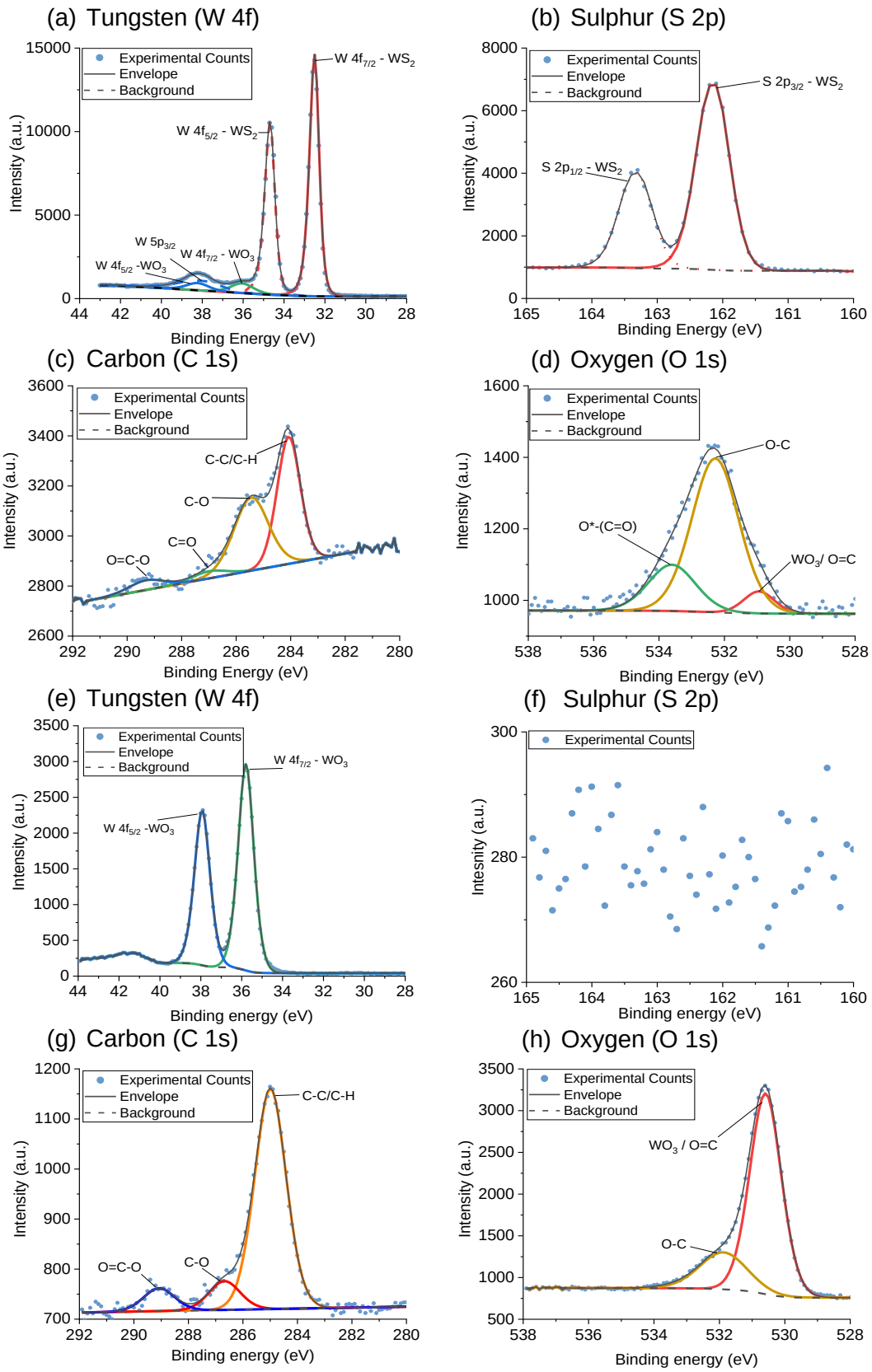

Figure 4.8 XPS analysis showing the deconvoluted spectra of WS_2 NTs (a–d) and WO_3 (e–h).

Specifically, Figure 4.8 a) and b) show the deconvoluted XPS spectra for W $4f_{7/2}$ and W $4f_{5/2}$ peaks at 32.5eV and 34.7eV and S $2p_{3/2}$ and S $2p_{1/2}$ peaks at 162.1eV and 163.3eV from WS_2, in agreement with the data reported in the literature [306]. From Figure 4.8 a), small peaks from W $4f_{7/2}$ and W $4f_{5/2}$ WO_3 are also identified, attributed to the relatively high concentration of oxygen (7.3%) detected within the NT sample. The associated peaks, clearly seen in Figure 4.8 e) are derived from WO_3 obtained by heating the WS_2 NTs, which undergo complete oxidation to WO_3 nanostructures. The level of oxygen detected for the WS_2 NTs (19.9at%) is much less than that reported previously [93]. Additionally, significant amounts of carbon is detected for both the WS_2 NTs (20.0at%) and WO_3 (29.3at%) samples, Figure 4.8c) and g), possibly associated with defects in the nanostructure surface or most likely from physisorption of hydrocarbons from atmospheric contamination, as carbon is known to react and bind to the surface of tungsten atoms and is typically found loosely attached to the surface [93, 293, 307, 308].

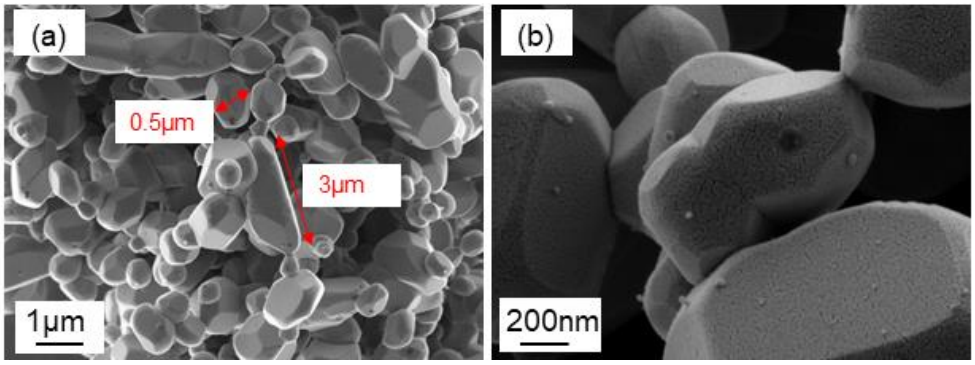

Figure 4.9 SEM images of WO3 particles obtained post-TGA− MS analysis of WS_2 NTs

SEM imaging of the pale yellow/ green powder exhibited in Figure 4.9, identifies collapse of 1D morphology of the WS_2 NTs and recrystallization into micron-sized 3D crystals of WO_3 due to the heating process. The NT structure (as seen in Figure

4.1) is no longer observed. These WO_3 structures were obtained by oxidation of the curved and cylindrical WS_2 NTs, collapse and sintering of a few WO_3 crystals, resulting in diameters ranging from 0.5µm to 3µm. The image in Figure 4.9 b) shows the surface of the WO_3 particles to be cracked, a consequence of the WO_3 particles being annealed at the elevated temperatures used. Under these conditions, the WS_2 NTs are completely oxidised to WO_3 below 550°C and no further reaction occurs above this temperature.

In summary, WS_2 NTs are thermally stable up to at least 400 °C in air, a temperature well above that used to melt process most polymers and 0D/1D/2D nanoparticles. XPS, XRD, TGA-MS and Raman data confirmed the highly crystalline structure of the NTs and detection of oxygen and carbon contaminants most likely from the environment.

4.3 Characterisation of WS_2 NTs PLA Composites

Given the potential medical and other applications where maintaining the molecular weight of the polymer is critical, for WS_2 NT filled PLA, it is pertinent to assess if the oxygen and carbon moieties play any part in the thermal degradation of the polymer during melt mixing. Therefore, in order to determine the impact of these contaminants Gel Permeation Chromatography (GPC) was used to study the molecular weight of PLA and composites of PLA and WS_2 NTs, prior to and post melt mixing in an extruder, see Figure 4.10. A reduction in the molecular weight (M_w) of the PLA and the composites are a measure of polymer degradation, which can be used as an indicator of impact of the inclusion of WS_2 NTs, oxygen/carbon contaminants and/or the melt extrusion process. The GPC curves shown in Figure 4.10 a) are recorded using Refractive Index (RI) and Light Scattering (LS) detectors and display the M_w curves

as a function of eluting time for the various materials. The RI and LS measurements for the PLA polymer samples were obtained within similar elution times, with only a small shift to higher elution time for the processed sample. This small shift in M_w values may indicate a low level of thermal-induced degradation due to processing.

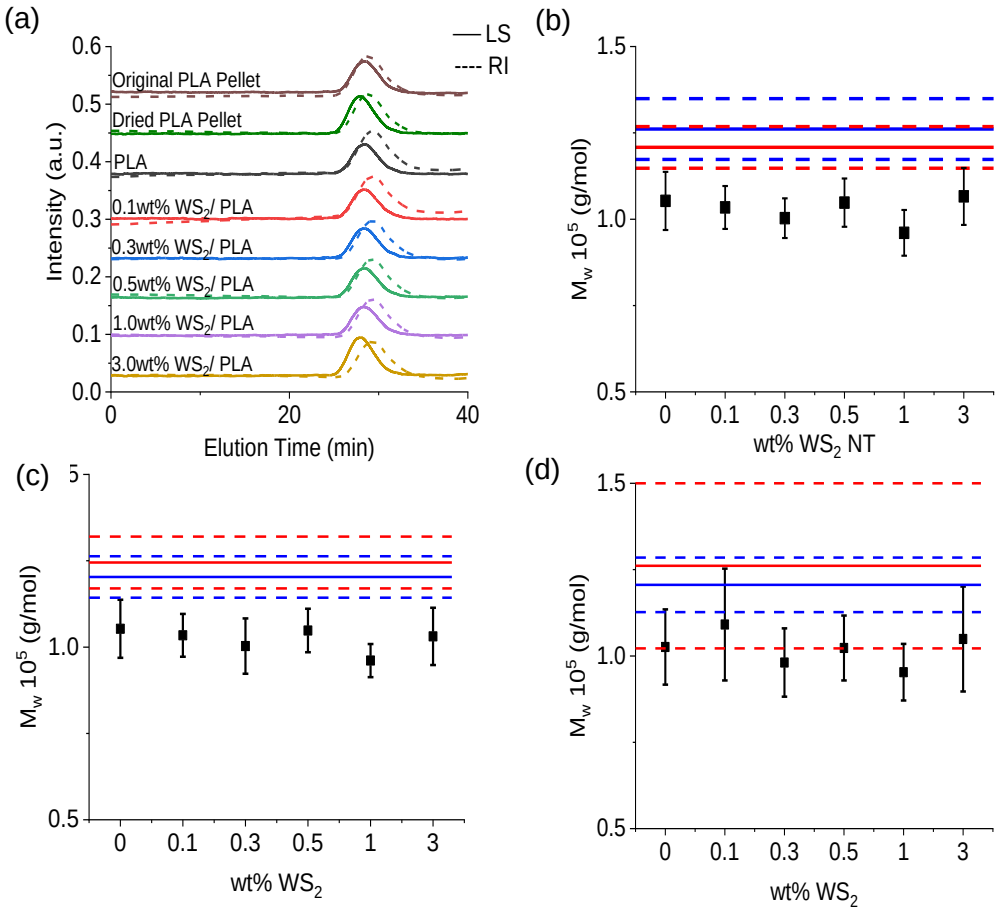

Figure 4.10 a) GPC curves from light scattering (LS) (solid lines) and the refractive index (RI) (dashed lines) detectors. Measured molecular weight (Mw) of PLA with corresponding uncertainties, b) first measurement, c) second measurement and d) averaged results. Solid blue and red horizontal lines represent the Mw of PLA pellets and dried PLA pellets (before extrusion) respectively, and corresponding dashed lines represent associated uncertainties. Square markers identify the measured Mw of unfilled PLA and composites of PLA and WS_2 NTs as a function of WS_2 NT filler loading after extrusion and uncertainties with associated error bars.

Figure 4.10 b) through d) show the molecular weight of samples determined using GPC computational software from the RI trace. The horizontal lines identify the M_w of PLA pellets and dried PLA pellets before extrusion were $1.26\pm0.08x10^5$ g/mol and $1.20\pm0.06x10^5$ g/mol respectively, highlighting the importance of drying the PLA before extrusion. The M_w of the unfilled PLA and composites of PLA and WS_2 NTs after melt extrusion was $1.1\pm0.05x10^5$ g/mol. This small decrease of $\sim0.2x10^5$ g/mol after extrusion correlates with the shift seen in the RI and LS peaks identified in Figure 4.10 a), again indicating the processing procedure resulted in a small degree of PLA degradation. However, it also clearly shows that incorporation of WS_2 NTs does not impact the M_w of the PLA at any loading.

The dispersion of the NTs within the polymer post melt extrusion was examined by SEM and STEM-BF imaging. SEM imaging of cross-sections of the fractured surfaces of the composite samples (Figure 4.11 a) show that individual NTs of 1µm-2µm length are embedded and dispersed effectively within the PLA matrix. However, the length and therefore the AR of the NTs was significantly reduced post melt processing (Figure 4.11 b)). Additionally, the NTs are both well dispersed and distributed in the polymer. The STEM-BF images in Figure 4.11 c) through e) show that the NT lengths are in the range 200nm to 800nm post processing. This clearly identifies the chopping of NTs due to sheer forces during extrusion which results in the shortening of the length of NTs. However, the width of the NTs is much less affected by the extrusion process and are in a similar range, 30nm to100nm to that prior the processing.

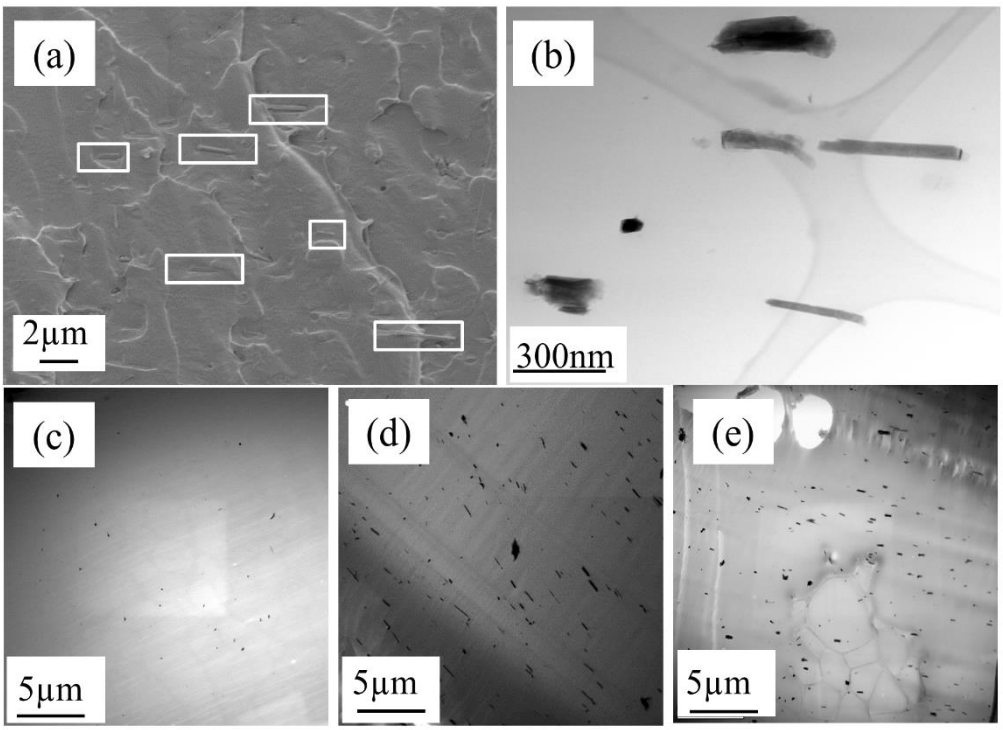

Figure 4.11 (a) SEM image of a PLA composite with 3 wt % WS_2 NTs, (b) STEM-BF image of PLA 3.0 wt % WS_2, and (c–e) STEM-BF images of composites of PLA and 0.1, 0.5, and 3.0 wt % WS_2 NTs, respectively.

This significant reduction in the length (and thus aspect ratio, AR<10) of the NTs is a consequence of the forces applied during mixing in a twin-screw extruder resulting in substantial breakage of the NTs to lengths down to the sub-micron level. The shear stresses (forces) applied during melt mixing in the twin-screw extruder are sufficient to result in an approximate 95% plus reduction in AR to <10 and this will significantly affect the quasi-static mechanical properties of these composites. The NT walls seem to be unravelled after the processing and there is a catastrophic breakage of the NTs, see Figure 4.11 e), resulting in a significant decrease of the AR of the NTs to ~10. Therefore, it can be determined, shear stresses and extensional forces applied during melt mixing of PLA and the NTs induces a strain on the walls of NTs causing the outer layers of the NTs to break. The shear modulus of the WS_2 NTs has been

recently measured experimentally to be ~70-80GPa [309]. The STEM-BF images in Figure 4.11 c) through e) show that the NT lengths are in the range 100nm to 300nm post processing. This clearly identifies the chopping of NTs due to shear forces applied during extrusion which results in the shortening of the length of NTs. However, the width of the NTs is much less affected by the extrusion process and are in a similar range, 70nm to110nm to that prior the processing.

Tensile mechanical testing as used to examine the impact of NTs, albeit at much smaller AR, to identify mechanical reinforcement of WS_2 NTs in PLA matrix, shown in Figure 4.12 and Table 4.2. This is clearly seen from the tensile mechanical properties of the composites relative to the unfilled polymer as the Young's modulus (E), tensile strength (σ) and elongation at break (ε_b) of the PLA are slightly decreased

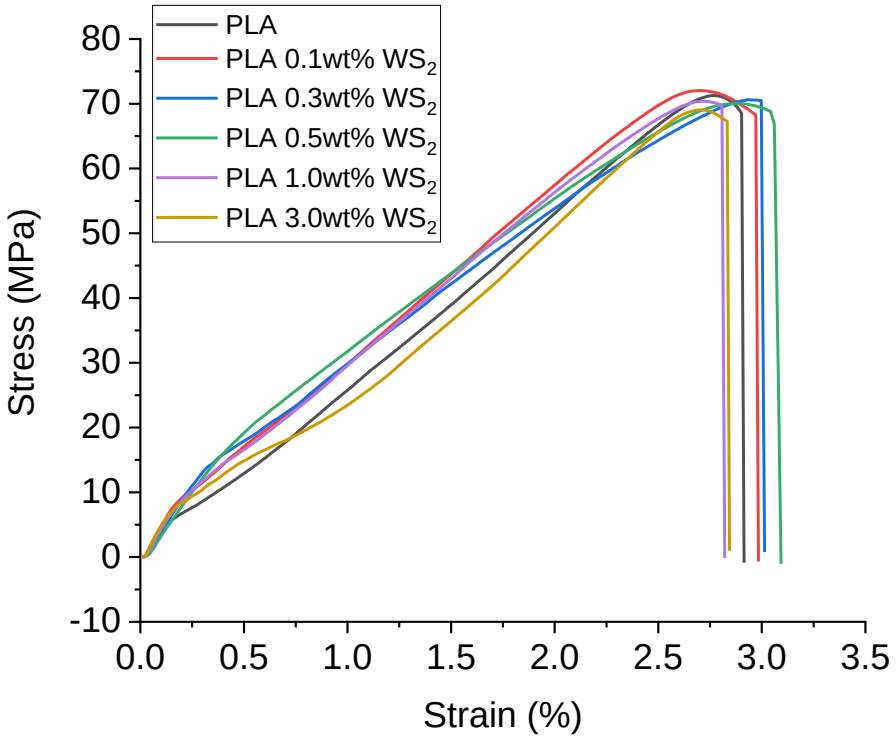

Figure 4.12 Representative stress-strain curves for neat PLA and composites of PLA and WS_2 NTs

or unchanged, within experimental error, but a ~30% decrease in tensile toughness was obtained. Consequently, although the NTs are highly dispersed in the PLA, their AR post mixing is so small that they cannot contribute to the reinforcement of the polymer matrix. Similar behaviour has just been reported for composites of poly(caprolactone) with another 1D filler, sepiolite needles, the AR of the needles was low and reduced further as a consequence of melt mixing in a micro-compounder [310].

Table 4. 2 Tensile mechanical properties of composites of PLA and WS_2 NTs.

Sample	**Young's Modulus MPa**	**Maximum tensile stress MPa**	**Elongation at break %**	**Tensile toughness Jm^{-3}**
PLA	3284 ± 913	72.12 ± 0.84	2.9 ± 0.32	146.55 ± 5.44
PLA 0.1wt% WS_2 NT	2773 ± 187	72.11 ± 0.83	2.98 ± 0.34	167.82 ± 6.15
PLA 0.3wt% WS_2 NT	2896 ± 276	71.86 ± 1.98	3.02 ± 0.46	131.87 ± 10.63
PLA 0.5wt% WS_2 NT	2441 ± 274	70.22 ± 1.20	3.08 ± 0.40	143.85 ± 12.55
PLA 1.0wt% WS_2 NT	2837 ± 122	70.06 ± 2.52	2.78 ± 0.40	107.28 ± 11.78
PLA 3.0wt% WS_2 NT	3123 ± 201	68.46 ± 1.19	2.82 ± 0.30	104.90 ± 14.48

Given WS_2 NTs are known to have a strong nucleating effect on semi-crystalline polymers, including that discussed in Chapter 2, the crystallisation behaviour of PLA on addition of the NTs was studied using DSC, hot stage polarised optical microscopy (POM) and WAXS/SAXS. From DSC measurements (Figure 4.13), the glass transition temperature (T_g), melting temperature (T_m), enthalpy of melting (ΔH_m), crystallisation temperature (T_c), enthalpy of crystallisation (ΔH_c) and the percentage crystalline content (X_c) were determined, see Table 4.3. The addition

of WS_2 NTs had no effect on the T_g and T_m of PLA, they remained essentially the same (~59°C and 168°C, respectively) independent of NT concentration.

Figure 4.13 a) shows the thermograms obtained after the second heating cycle, the melt processed PLA sample exhibits a cold crystallisation peak (T_{cc}) at 108°C, in contrast to the composites, which do not show a T_{cc} peak at all. The identification of a T_{cc} indicates the PLA sample was in a more amorphous state at room tempertaure with respect to the composites and crystallization occurred during heating. Notably, the disappearance of the T_{cc} of PLA with the addition of WS_2 NTs suggests a strong nucleating effect on PLA inducing a higher degree of PLA crystallization.

Table 4.3 Thermal Parameters Determined from DSC Measurements of Extruded PLA and Composites of PLA and WS_2 NTs

Sample	**T_g (°C)**	**T_m (°C)**	**ΔH_m (J/g)**	**T_c (°C)**	**ΔH_c (J/g)**	**X_c (%)**
PLA	59	170	37	-	-	-
PLA 0.1wt% WS_2 NTs	60	166	39	119	41	44
PLA 0.3wt% WS_2 NTs	60	167	39	121	40	43
PLA 0.5wt% WS_2 NTs	59	167	39	121	42	45
PLA 1.0wt% WS_2 NTs	59	167	37	122	42	44
PLA 3.0wt% WS_2 NTs	59	168	43	122	45	47

Additionally, Figure 4.13 b) shows the cooling curves and the crystallization peak (T_c) of the composites clearly for all WS_2 NT loadings. However, PLA itself does not have an obvious T_c peak upon cooling, behaviour associated with the slow rate of crystallisation of PLA. T_c of the PLA increased by ~3°C with increasing WS_2 NT loading, but with a modest increase in crystallinity by 3.5%. However, these results demonstrate the inclusion of the NTs alters the nucleation and crystallisation behaviour of the PLA.

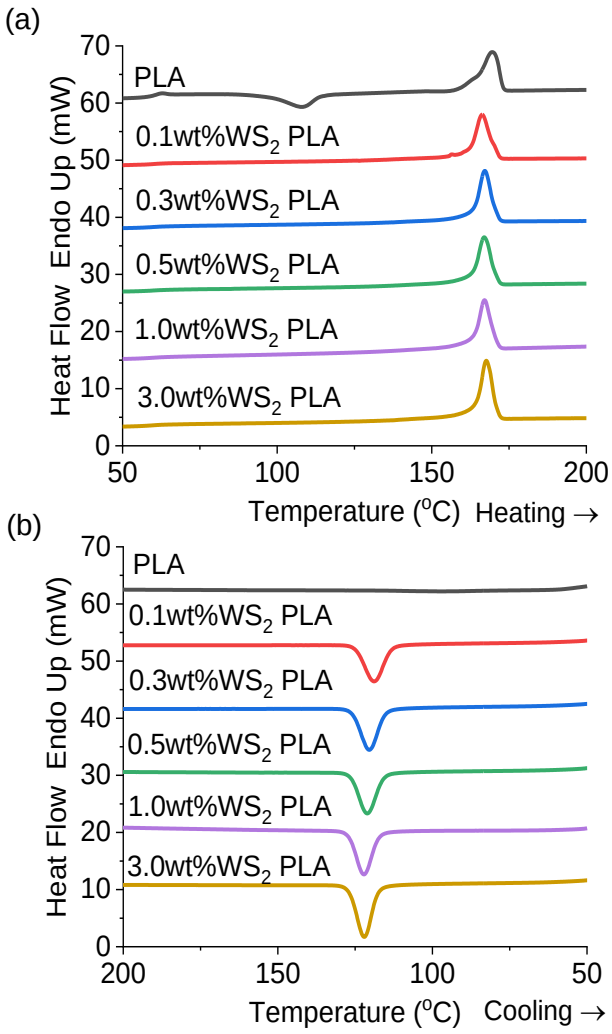

Figure 4.13 DSC (a) heating and (b) cooling curves of composites of PLA and WS_2 NTs in the 25−250 °C temperature range

The effective role of WS_2 NTs in promoting nucleation of PLA crystals was further studied by examining the composites under polarised light with an optical microscope equipped with a hot stage to investigate the rate of crystallisation and crystal morphology as a function of WS_2 NT loading during heating and cooling cycles. The conditions chosen for the polarised light thermal cycles replicated the heating protocol used for the DSC measurements. Observation of the crystallisation of unfilled PLA and composites of PLA and WS_2 NTs when cooling at a rate of $10K.min^{-1}$ confirmed the slow rate of crystallization of PLA (Figure 4.14a)). However, inclusion of WS_2 NTs to PLA results in the crystallization of PLA at a much higher rate (Figure 4.14 (b)-c)). Therefore, the sample was held at the temperature at which crystallisation began, and the time taken for complete micrographs show that spherulite formation begins at 145℃. Figure 4.14 shows the variation in spherulite morphology for unfilled PLA compared with the composites with up to 3wt% WS_2 NT loading. For unfilled PLA (Figure 4.14 a)) significantly larger spherulites are formed, due to the slower rate of crystallization and the longer time taken to complete spherulite growth, measured at 9 minutes. The spherulite size for the composites (Figure 4.14 b)-c)) are much smaller and more densely populated. The WS_2 NTs act as nucleating points for crystallisation of the PLA, which is in agreement with previous outcomes of WS_2 nanofiller in PLA.

The time taken for complete crystallization of the PLA with WS_2 NT loadings of up to 0.1wt% Figure 4.14 b) was approximately 45 seconds and loadings of 3wt% WS_2 NT (Figure 4.14 c) the time taken for complete crystallisation increased to 2.25 minutes. It can be observed the densely populated nucleation sites with increasing wt% of WS_2 NT in, making identification of the exact time for complete crystallisation difficult to accurately determine. Overall, it is clear the inclusion of WS_2 NTs to this

PLA has a significant impact on the crystallisation kinetics and structure of the polymer.

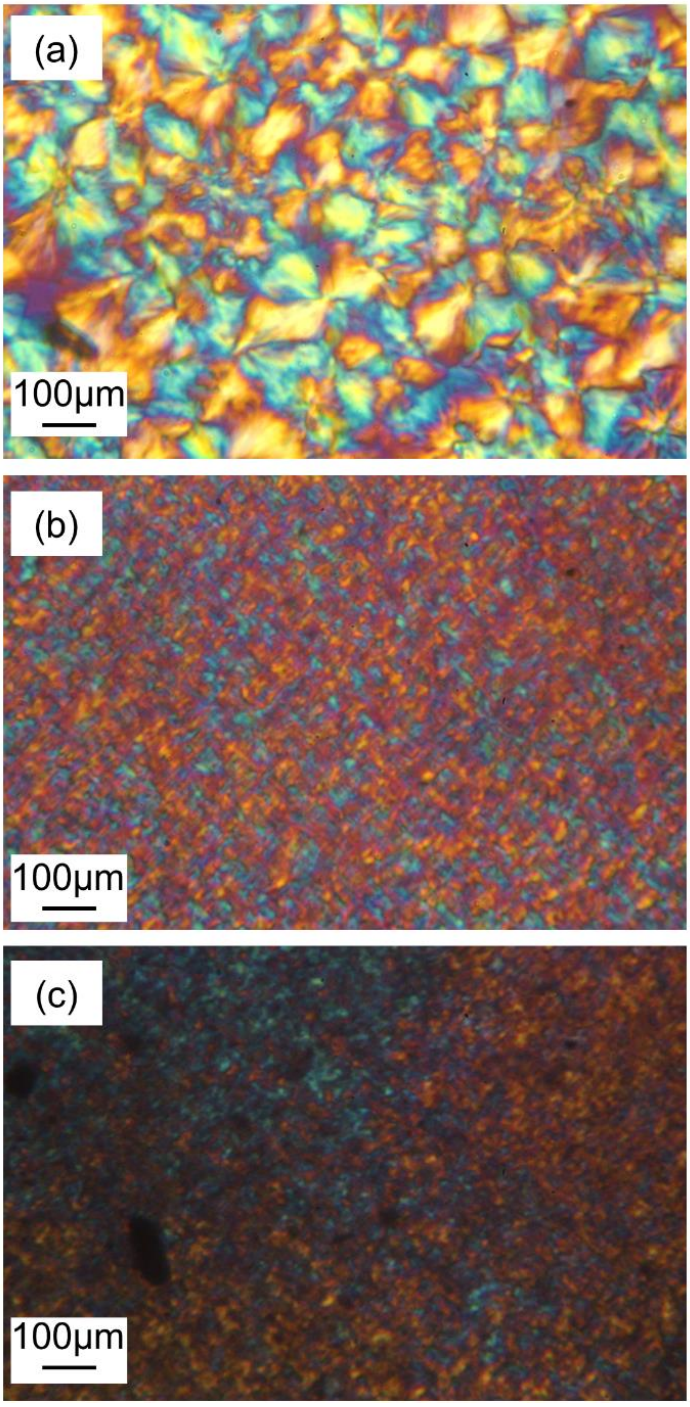

Figure 4.14 Complete crystal formation of (a) neat PLA at 9 min, (b) 0.1 wt % WS_2 NT filled PLA at 45 s, and (c) 3wt % WS_2 NT-filled PLA at 2.25 min at 145 °C

WAXS and SAXS measurements were performed to further investigate the crystalline structure of extruded unfilled and WS_2 NT filled PLA composites in comparison to the as received PLA pellets before any thermo-mechanical processing. The WAXS and SAXS 2D patterns and integrated 1D profiles were measured simultaneously and are shown in Figure 4.15.

All background intensity of the 2D profiles was subtracted and the 1D WAXS (Figure 4.15 a)) intensities normalised to the background to provide a better comparison of the relative intensities of the extruded samples. From the WAXS pattern (Figure 4.15 a), the extruded PLA sample exhibits an amorphous halo also visible in the integrated 1D curve (Figure 4.15 b) with no observable crystalline peaks. This result highlights the role that the extrusion process plays in generating a completely amorphous phase in the polymer that was initially very crystalline, see 2D pattern and integrated curve of the pellet, Figure 4.15 a) and b). The SAXS pattern of the extruded PLA shows no significant feature, while the PLA pellet pattern exhibits a clear intensity ring (Figure 4.15 c) that gives rise to a broad peak in the 1D integrated profile (Figure 4.15 d). In the WAXS patterns of the WS_2 NTs composites, the WS_2 NTs crystalline peaks are clearly identifiable the main peak is attributed to the (002) reflection positioned at $q=1.01Å^{-1}$ in excellent agreement with the XRD analysis of the WS_2 NTs (Figure 4.5a). The other peaks are attributed to the (004), (100) and (103) reflections of WS_2. The 1D WAXS profiles show a systematic increase in the intensity of the WS_2 peaks with increasing WS_2 NT loading.

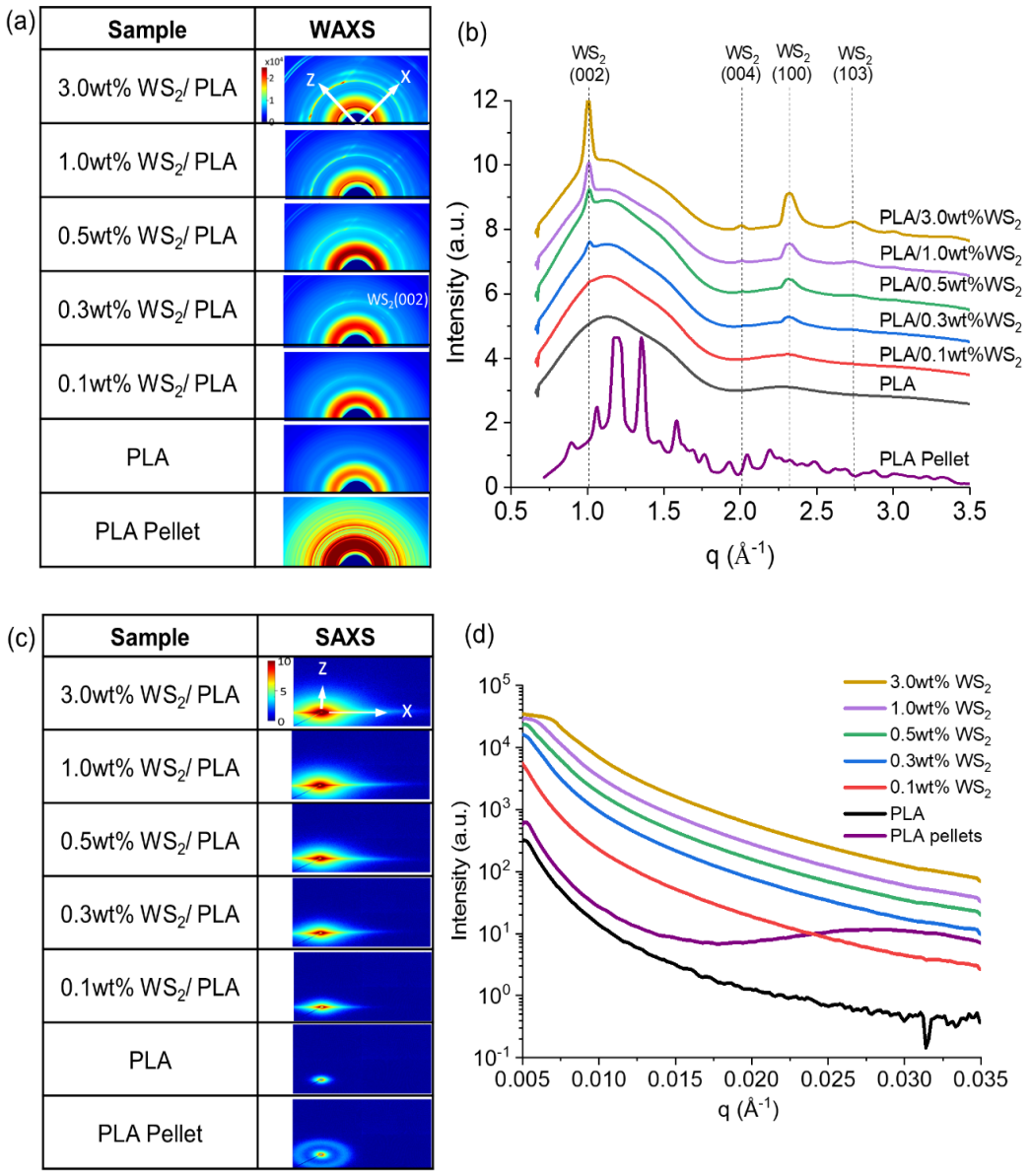

Figure 4.15 (a,b) WAXS 2D patterns and 1D integrated profiles and (c,d) corresponding SAXS 2D patterns and integrated 1D profiles for the as received PLA pellet, extruded PLA, and composites of WS_2 NT and PLA

Moreover, a progressive reduction of the intensity of the amorphous halo until 15% for the composites with 3.0wt% WS_2 NTs loading in comparison to the extruded unfilled PLA indicates an increase in the overall PLA crystalline content supporting the DSC results. Nevertheless, the crystalline domains formed in the nanocomposites

are too small to give rise to a diffraction peak of PLA, due to strong nucleating effect of the WS_2 NTs, in agreement with the POM images in Figure 4.14b-c.

The 1D SAXS profile for the composites with 1.0 and 3.0wt% WS_2 NTs (Figure 4.15 d) shows a saturation of the signal for q-values below $0.0075A^{-1}$ due to the elevated scattering from the NTs at the higher concentrations. However, in the detector linear regime (above $q=0.0075A^{-1}$), the signal is reliable and the increase in the scattering intensity with increasing WS_2 NTs loading is noticeable. It can be attributed to the high electron density of WS_2.

Moreover, consistent 1D profiles for all WS_2 NT loadings suggests an even dispersion and distribution of the NTs within the polymer matrix. This is further clarified form the 2D SAXS as the horizontally stretched pattern is suggestive of a homogenous alignment and distribution of WS_2 NTs with the PLA from extrusion [235]. This finding agrees with the NT alignment seen in the TEM images of the composites, while additionally generating ordering of the polymer chains. The inclusion of NTs provides surfaces from which the polymer can crystallise, confirming the role of WS_2 NTs as a nucleation agent for PLA.

4.4 Conclusions

WS_2 NTs were proven to be highly crystalline multi-wall nanoparticles, with 8 - 28 walls with a consistent wall spacing of 0.65nm and having widths in the range 52nm - 110nm and lengths in the range 2.45μm-65.6μm. The WS_2 NTs were thermally stable in air atmosphere up to 400°C, while further heating in the region between 400-550°C induced oxidation of tungsten via formation of SO_2/SO gas, resulting in the formation of yellow WO_3 micron-sized particles. That the WS_2 NTs are thermally

stable to at least 400°C confirms the NTs can be melt mixed with polymers without thermally induced degradation.

Surface chemistry analysis of WS_2 NTs by XPS and STEM-EDS detected levels of oxygen and carbon, known in this instance to be airborne contaminations absorbed on a large surface area and inside the layers of tubular nanostructures.

Composites of WS_2 NTs in PLA were examined after melt-mix extrusion. While WS_2 NTs were shown to readily disperse and distributed in the PLA matrix, the consequential impact of shear stresses applied during twin-screw extrusion resulted in a significant chopping and therefore a reduction of AR of the NTs of >95% to approximately 10, down to lengths between 200nm and 800nm. This led to the mechanical properties of the PLA remaining unchanged upon inclusion of the WS_2 NTs as the much shorter chopped NTs provided no reinforcement. However, the much-shortened NTs did act as nucleating sites for PLA crystallization resulting in an increased T_c for PLA with increasing WS_2 NT loading and a slightly higher degree of crystalline content.

Chapter 5: Results and Discussion II

APTES Functionalised WS_2 NTs and Solution Cast Composites of PLA

5.1 Introduction

In this chapter, the functionalisation of WS_2 NTs using APTES and their application as a functional filler for PLA is examined. The effectiveness of the silane grafting to the surface of NTs is investigated as an approach to enhance NT dispersion in the polymer matrix and promote strong interfacial interaction between the WS_2 NTs and PLA as a route for improving the mechanical properties of PLA.

The surface chemistry of WS_2 NTs, determined in Chapter 4, can be utilised to modify the surface of NTs with silane (3-aminopropyl)triethoxysilane (APTES) which has previously successfully grafted via a hydrolysis mechanism on the surface of nanoparticles [311-316]. The functionalisation mechanism between APTES and WS_2 NTs at various ratios (1:1, 1:2 and 1:4) is studied.

APTES modified WS_2 NTs (at a constant 0.5wt% WS_2 NTs) are further dispersed in amorphous grade PLA (Corbion ~96% L-isomer, Luminy LX175) via solution casting method. Amorphous grade PLA was chosen to determine if any changes in mechanical properties were derived from the nanotubes alone and not any effect inclusion of the nanotubes had on changing the crystalline morphology of the polymer, as previously seen in Chapter 4. Furthermore, in an attempt to preserve the AR of NTs, the method of nanocomposite preparation was changed to solution casting

of films, as melt mix extrusion method previously proved to be too severe on WS_2 NTs structure and morphology (Chapter 4). The role of APTES and WS_2 NTs in PLA composites on the mechanical, crystalline, and thermal properties are determined.

5.2 Characterisation of APTES Functionalised WS_2 NTs

To determine if APTES functionalisation of the NTs was successful, the FTIR spectra of WS_2 NTs:APTES in the ratios 1:1,1:2 and 1:4 (Figure 5.1 b)) in comparison with the spectra for WS_2 NTs and APTES alone (Figure 5.1a)) were recorded. The FTIR spectrum of WS_2 NTs does not display any peaks in the infrared due to the WS_2 having no dipole moment as a result of its symmetry which causes a change in polarizability [317]. APTES displays characteristic peaks at 3383cm^{-1} and 2974cm^{-1} which are related to amine NH_2 stretching. Peaks at 1604cm^{-1} and 1483cm^{-1} and related peaks are assigned to NH_2 deformation bending modes of amine groups, which are strongly bonded in the hydrogen to the silanol groups to form cyclic structures [318]. Peaks at 1442cm^{-1} and 1390cm^{-1} correlate to O-H bending, while those at 1294cm^{-1} and 1165cm^{-1} are associated with C-O stretching of the aromatic ester. Asymmetric and symmetric Si-O-Si vibrations were recorded at 1073cm^{-1} and 765cm^{-1}, as well as a Si-O-C asymmetric peak at 1100cm^{-1} [319]. Si-OH stretching and bending vibrations are observed at 954cm^{-1} and 853cm^{-1}, respectively [320]. The peak at 677cm^{-1} is associated with N-H bending.

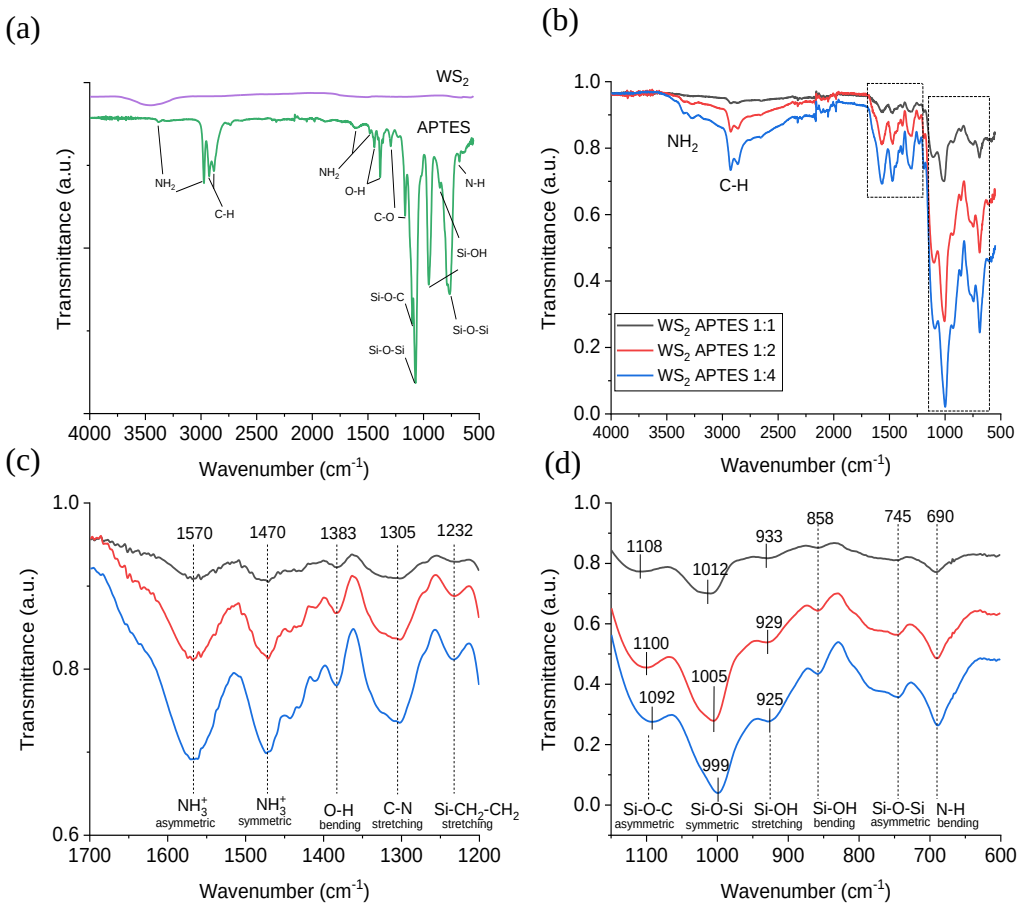

Figure 5.1 FTIR transmittance spectra of, a) WS_2 NTs and APTES, b) APTES functionalized WS_2 NTs in ratios of 1:1, 1:2 and 1:4, c) spectra enlarged in the range 1700-1200cm^{-1} and d) in the range 1150-600cm^{-1}.

For the APTES functionalized WS_2 NTs at all ratios (Figure 5.1b)), similar FTIR transmittance spectra were obtained, and with increasing silane content the intensity of all peaks increases monotonically, suggesting successful grafting of the silane moiety to the NT surface (See Appendix Table A.3 for full list of assigned peak positions). The spectra for APTES modified WS_2 NTs shows a shift of the N-H stretching vibrations with respect to neat APTES from 3383cm^{-1} and 2974cm^{-1} to 3348cm^{-1} and 3270cm^{-1}, which are superimposed on a broad peak in the 3500-2500cm^{-}

^{1} region associated with O-H stretching mode as a result of water absorption in the sample. However, the evolution of new bands is identified and depicted in Figure 5.1c)), the one at 1570cm^{-1} is assigned to the asymmetric -NH_3^+ deformation mode, with the corresponding symmetric -NH_3^+ mode at 1470cm^{-1} [312]. The band at 1305cm^{-1} is characteristic of C-N stretching in amines, while Si-CH_2-R vibrational modes are typically observed in the range 1250-1200cm^{-1} [321], therefore the band at 1232cm^{-1} is associated with Si-CH_2-CH_2. An O-H band is observed again for the functionalized NTs but is shifted to 1383cm^{-1}.

For APTES modified WS_2 NTs, there is a shift of all peaks in the region 1150-600cm^{-1} (Figure 5.1d)) relative to pure APTES. The symmetric Si-O-Si vibrations are red-shifted by 61cm^{-1} from 1073cm^{-1} (APTES) to 1012cm^{-1} when grafted on to WS_2 NTs in the ratio of 1:1. A further shift of 7cm^{-1} to 1005cm^{-1} is observed for the WS_2 NTs:APTES 1:2 sample, and again a shift of a further 7cm^{-1} to 998cm^{-1} for WS_2 NTs:APTES 1:4. The asymmetric Si-O-Si vibration band is observed at the lower (relative to the symmetric Si-O-Si vibration) wavenumber of 745cm^{-1} irrespective of the ratio of WS_2 NTs to APTES. There was also a variation in the peak shift of band position for the asymmetric Si-O-C from 1100cm^{-1} for APTES to 1108cm^{-1}, 1100cm^{-1} and 1092cm^{-1} for 1:1, 1:2, 1:4 WS_2 NTs:APTES, respectively. Si-OH stretching and bending vibrations are observed at 929cm^{-1}, 858cm^{-1}and 780cm^{-1}, respectively [320]. Furthermore, the N-H bending peak blueshifts by 13cm^{-1} to 690cm^{-1} after the surface modification of the WS_2 NTs. These new bands, observed for APTES modified WS_2 NTs in comparison to APTES alone and shifting of the peaks with increased ratio of APTES, provides evidence for the formation of a siloxane network on the surface of the WS_2 NTs, confirming strong interaction of APTES with the surface of the NTs.

The effectiveness of surface functionalization of the WS_2 NTs with APTES was also investigated by studying the thermal stability of the surface modified NTs using thermogravimetric analysis under N_2 atmosphere, Figure 5.2. The onset of thermal degradation of APTES alone (even under a non-oxidative atmosphere) was just above ambient temperature with a 90% mass loss by 200 °C. In contrast, the WS_2 NTs are shown to be thermally stable across the whole temperature range (25°C-1000°C) examined with a total weight loss of just 2.5%, in agreement with Chapter 4 Figure 4.4). When bound to the WS_2 NTs the thermal decomposition profile of APTES

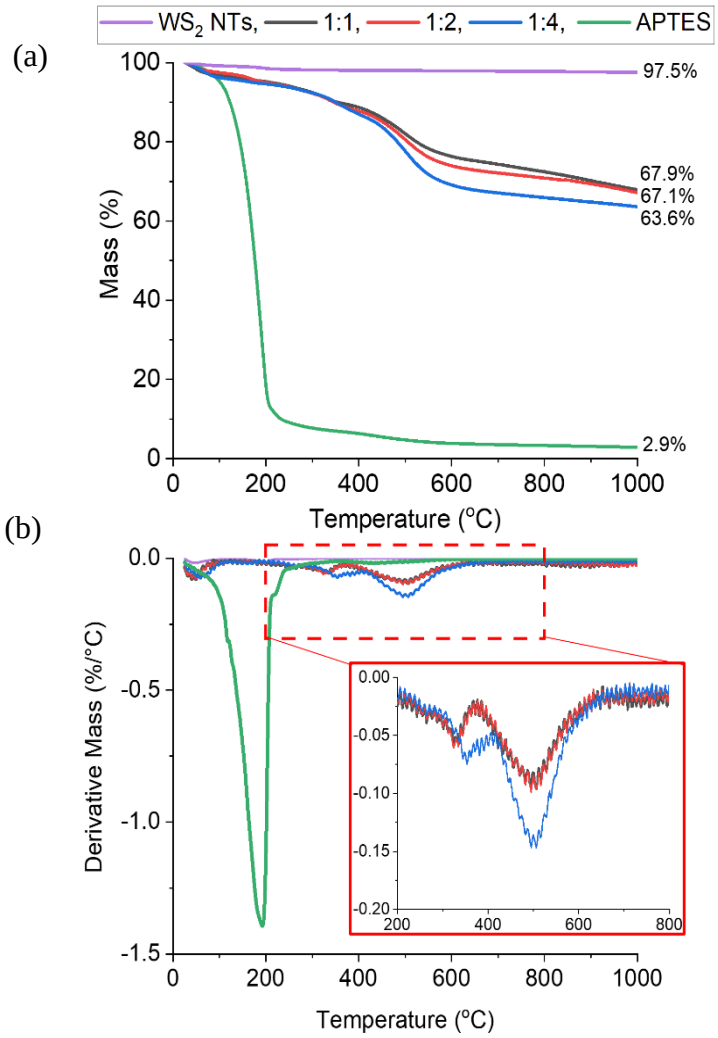

Figure 5.2 a) TGA weight loss curves and b) DTA curves for WS_2 NTs, APTES and APTES modified WS2 NTs at different ratios.

is shifted to higher temperatures with weight losses of 32.1%, 32.9% and 36.4%, for WS_2 NT: APTES in the ratios 1:1, 1:2 and 1:4, respectively. This increase in mass loss with increasing APTES concentration further supports the idea that the APTES is bound to the WS_2 NTs. Additionally, the DTG curves for the APTES modified WS_2 NTs (Figure 5.2 b)) show that, irrespective of the APTES concentration the weight loss occurs in three main stages. Below 100 °C, mass loss is attributed to the removal of water from the surface of the NTs. A second small peak with maxima at ~329°C for the 1:1 and 1:2 sample, increasing to 354 °C for the 1:4 sample, is associated possibly with the removal of residual surfactant. Above 400 °C a third peak with maxima at 500°C is observed perhaps derived from the decomposition of the functional groups chemically anchored to the surface of NTs given the increased grafting of APTES at a ratio of 1:4 (WS_2 NT: APTES) and the formation of a siloxane network. The extent of the grafting was estimated from further analysis of the TGA data [322]. After mass normalization, the number of grafted chains were calculated using Equation 5.1:

$$\mathrm{Chain_{graft}} = \frac{\mathrm{W_{loss}\%}}{(100 - \mathrm{W_{loss}\%}) \times \mathrm{Mw_{molecule}}} \times \mathrm{N_a} \qquad (5.1)$$

where, W_{loss}% represents the percentage weight loss (from TGA) in the temperature range 200 °C and 800 °C, $M_{w(molecule)}$ is the molecular weight of the grafted molecule of APTES (221.37 g mol^{-1}), and N_a is Avogadro's number ($6.02214076 \times 10^{23}$).

This temperature range was chosen assuming residual APTES was removed below 200°C. Knowing the specific surface area (SSA_{BET}) of the WS_2 NTs [323], from BET measurements = 19.19 m^2g^{-1} the coverage density (θ) can be readily calculated using equation 5.2 and the values are listed in Table 5.1:

$$\theta = \frac{\text{Chain}_{\text{graft}}}{\text{SSA}_{\text{BET}}} \tag{5.2}$$

The grafting density (σ), shown in Table 5.1, identifying an increase with increasing APTES concentration rendering the NTs more organophilic, suggestive of increased grafting of APTES on NTs surface.

Table 5.1 Grafting density APTES on the surface of WS_2 NTs

	W_{loss}% **(200-800°C)**	**Chain graft** **(mol g^{-1})**	**Θ (mol nm^{-2})**
WS_2 APTES 1:1	22.55	$7.92x10^{20}$	41.3
WS_2 APTES 1:2	28.41	$1.08x10^{21}$	56.3
WS_2 APTES 1:4	35.14	$1.47x10^{21}$	76.8

The Raman spectrum, Figure 5.3 of WS_2 NTs displays peaks characteristic to WS_2 at 351.1cm^{-1} and 419.0cm^{-1}, these are the most prominent Raman modes found in the spectra and are associated with the in-plane vibrations (E_{2g}) of chalcogen atoms and out-of-plane vibrations (A_{1g}) of chalcogen and transition metal atoms, respectively [300]. After functionalization with APTES, a slight blueshift of both peaks, the E^1_{2g} to 352.2cm^{-1} and the A_{1g} to 420.7cm^{-1} is observed for all APTES concentrations. This shift in peak position is representative of molecular absorption on the surface of the nanotubes [324]. The A_{1g} peak can be seen to split and the FWHM (full width at half maximum) increases with increasing APTES concentration (ΔFWHM$\approx$1.4cm^{-1} from neat WS_2 NTs to WS_2:APTES 1:4). Note that the splitting of the A_{1g} is attributed to the lower symmetry of the nanotube compared to the bulk, which induces a new peak B_{1u} at 416 cm^{-1}[298]. The changes in the shape of the A_{1g} peak is evidence for covalent functionalization due to the presence of functional

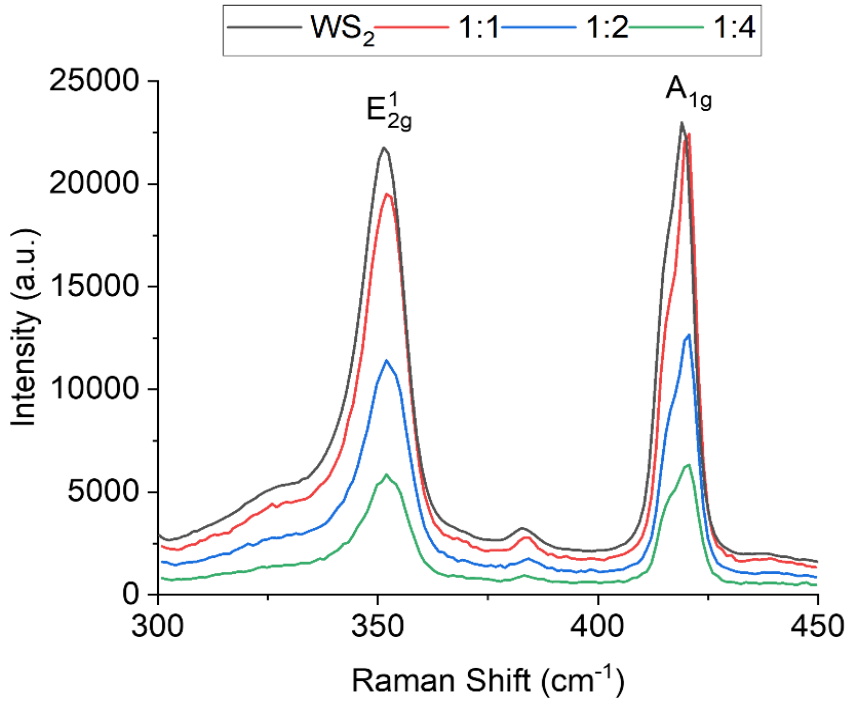

Figure 5.3 Raman spectra of WS_2 NTs and APTES modified WS_2 NTs.

groups attached to the chalcogen atoms on the surface of the sulphur atom of the WS_2 NTs [325]. The covalent bonding of the APTES to the outermost sulphur leads to loss of symmetry enhancing the B_{1u} Raman peak, which is a silent mode in bulk WS_2. Additionally, with increasing APTES concentration, the intensity of the peaks decreases, perhaps as a consequence of the APTES coating (siloxane network) on the surface of the NTs. These changes in the Raman spectra strongly support molecular physisorption of APTES on the surface of the WS_2 NTs.

To further determine if APTES functionalization of the WS_2 NT surface was successful, XPS spectra were recorded for all samples, see survey spectra Figure 5.5, and the relevant atomic percentages are listed in Table 5.2. For neat WS_2 NTs the atomic percentages and deconvoluted curves have been discussed in Chapter 4, consequently changes and identification of new elements confirm successful grafting of silane through carbon and oxygen. Both, carbon and oxygen have shown to be loosely attached to the surface of the NTs due to atmospheric conditions, while Si and N are also detected for the WS_2 NTs: APTES samples. Increased atomic % for C and O (Table 5.2) in comparison to WS_2 NTs is ascribed to the successful attachment of APTES to the WS_2 NTs. Additionally, I can be determined, the vast reduction of sulphur detected by XPS measurements is simply due to XPS being a surface level measurement, therefore APTES is successfully copiously on the surface of NTs.

Table 5. 2 Element atomic % extrapolated from deconvoluted XPS data for WS_2 NTs and APTES functionalized WS_2 NTs.

Sample	C	O	S	W	N	Si
WS_2 NTs	19.97	7.25	49.26	23.51	-	-
WS_2 APTES 1:1	48.72	23.93	1.34	0.7	11.17	14.13
WS_2 APTES 1:2	60.98	22.83	1.21	0.64	5.61	8.73
WS_2 APTES 1:4	55.6	23.18	0.89	0.38	8.03	11.92

Figure 5.5 shows representative deconvoluted spectra for the APTES functionalised WS_2 NT 1:4 (The remainder of the XPS data are presented in the Appendix Figures A1-A2 and Table A4-A6 where similar results were obtained). Deconvoluted peaks in the C 1*s* region (Figure 5.5. a)), display a similar chemical composition consisting of five components: C-C/C-H, C-N, C-O, C=O, O=C-O. The addition of APTES on the surface of WS_2 NTs is identified with the evolution of a new peak at 285.7eV from C-N bonding, characteristic of silane functionalisation of other NTs [25]. From the O 1s region (Figure 5.5 b)) peaks derived from WO_3/O=C, O-C/O-Si and O*(C=O) were recorded.

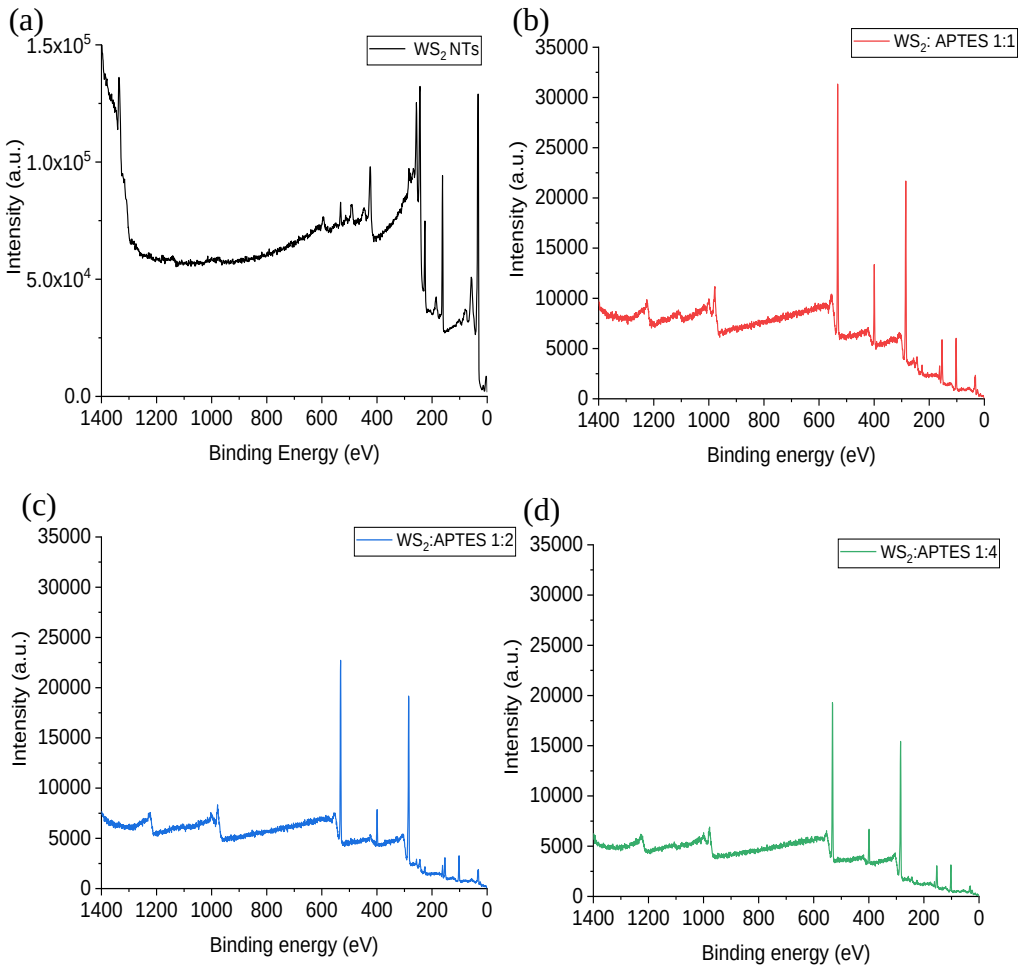

Figure 5.4 Survey XPS spectra a) WS_2 NTs b) WS_2:APTES 1:1 c) WS_2:APTES 1:2, d) WS_2:APTES 1:4

After functionalization with APTES, the evolution of another new peak at 532.35eV was observed, corresponding to O-Si/O-C bonding. The O-C peak due to atmospheric contamination was present prior to the addition of the APTES. The increase in peak intensity relative to the other components suggests O-Si bonding, which overlaps with O-C in binding energy. An increase of approximately 12% in the area under the oxygen peak confirms binding of the APTES to oxygen, which is attached to the surface of the WS_2 NTs.

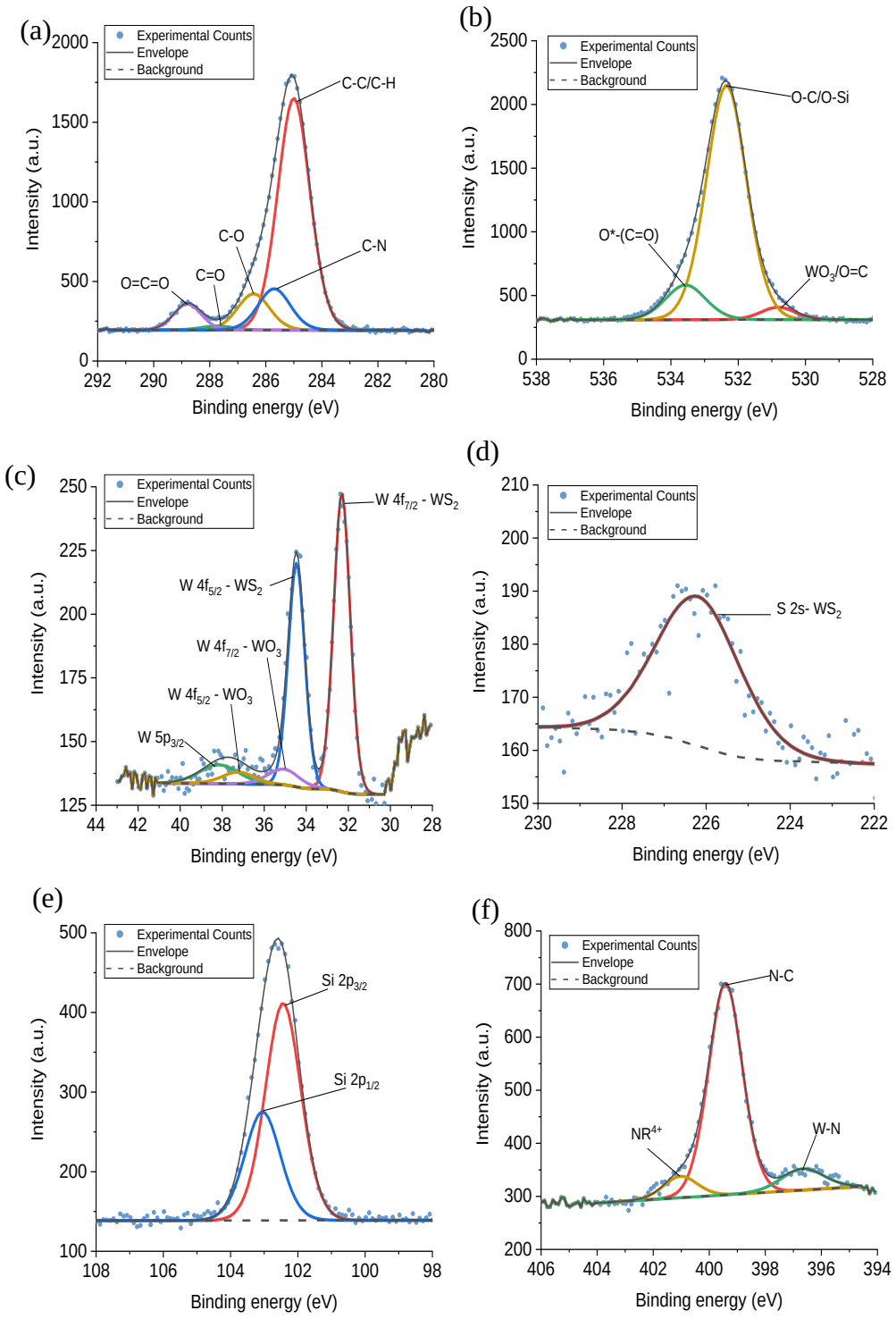

Figure 5.5 Deconvoluted XPS spectra, a) C 1s, b) O 1s, c) W 4f , d) S 2s, e) Si 2p f) N 1s regions from the XPS spectra of WS2-APTES at a ratio of 1:4.

The presence of different Si environments (Figure 5.5. e)) is confirmed from deconvoluted Si $2p_{3/2}$ and Si $2p_{1/2}$ data which correlates with Si-O-C or Si-O-Si in the two energy states, again further affirming grafting of APTES to surface molecules on the WS_2 NTs. For the N1s region (Figure 5.5. f)) deconvoluted peaks corresponding to N-C, NR^{4+} and evidence of W-N bonding for the WS_2 NTs:APTES 1:4 sample were obtained. The N-C bonding in characteristic of APTES, showing it is successfully attached to the surface of the NTs [326]. NR^{4+} bonding is suggestive of an amine reaction between APTES with molecules on the surface of the WS_2 NTs, however this cannot be confirmed with these XPS spectra. Additionally, the observed W-N bonding confirms successful functionalization of APTES to the WS_2 NTs, while it also suggests that by increasing the ratio of APTES to WS_2 NTs the grafting density of silane on the NT surface can be increased. For APTES functionalised WS_2 NTs, it should be noted that it is likely that the plasmon loss features from Si 2s photoemission overlap with the S 2p photoemission, possibly leading to incorrect identification of chemical environments and/or elemental composition. Therefore, for these samples, the S 2s region (Figure 5.5d)) was examined, however there is no indication of APTES interaction with sulphur atoms in this region.

SEM and STEM imaging were carried out to examine the NTs morphology after functionalisation with APTES, see Figure 5.6. The WS_2 NTs were well dispersed in the APTES silane network, forming a cohesive continuous morphology at all ratios, between the silane and the surface of the NTs. The aspect ratio of the NTs were also examined with NT lengths up to 6µm measured, and a small portion of significantly shortened NTs (see STEM image in Figure 5.6 d)), with lengths as small as 0.64µm observed, most likely due to the sonication process during sample preparation. Ultrasonication is widely used to disperse WS_2 NTs in solution however, it has been shown to induce breakage of NTs [256] [327]which also results in much shorter NT lengths and, in turn reduces the AR of the NTs.

This identifies a significant reduction in aspect ratio of similar to that of previous discussion in Chapter 4. From high resolution STEM images, (Figure 5.6 d) and e)), the APTES is seen to clearly coat the surface of the WS_2 NTs, an observation confirmed from EDS mapping. Tungsten (W) and sulphur (S) can be clearly identified for the NTs structure, while silicon (Si) from APTES is strongly attached to the surface of the NTs and is also surrounding the NTs. EDS analysis indicates also that carbon (C) and oxygen (O) (from the APTES) are found on the NT surface.

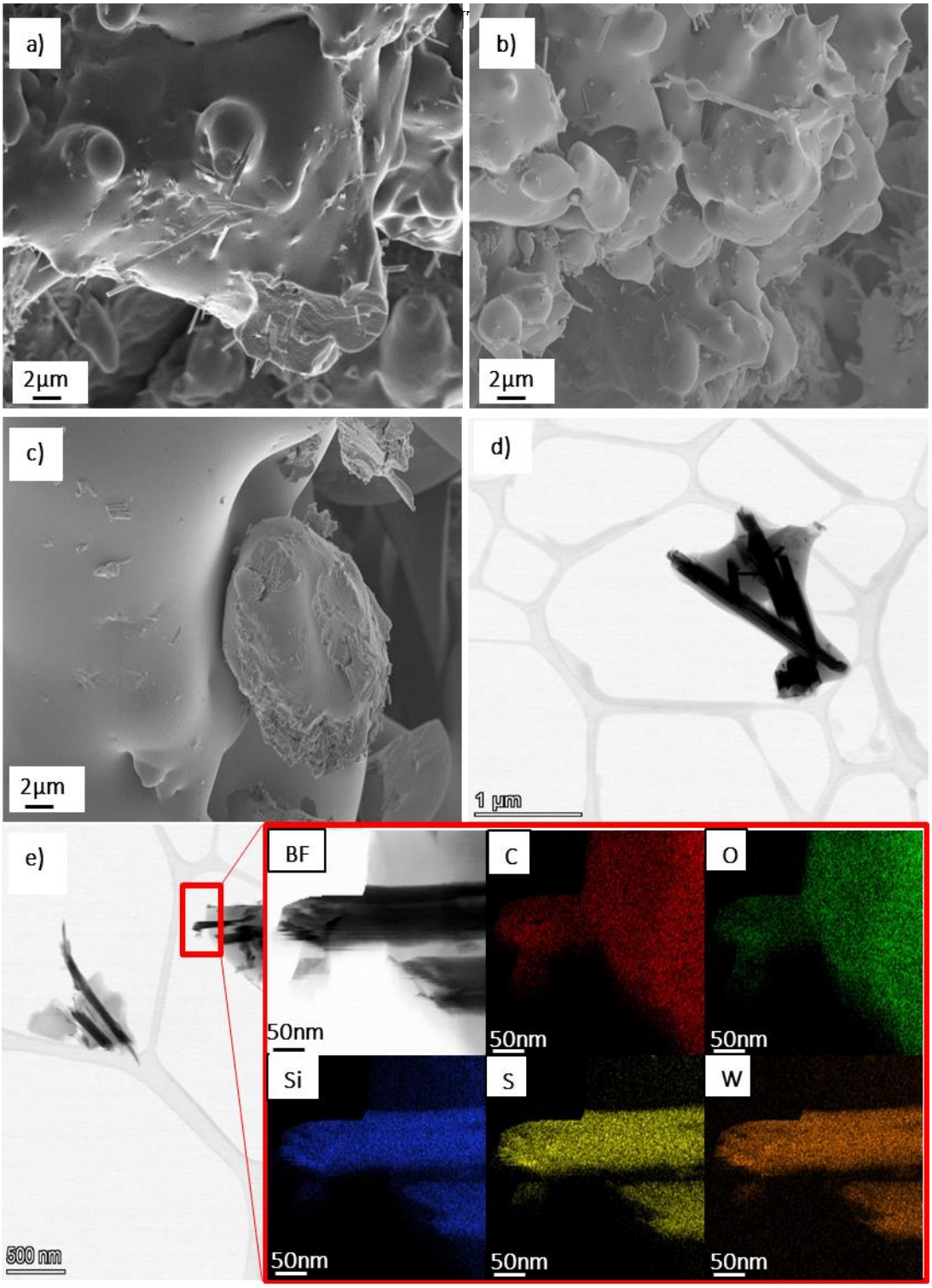

Figure 5.6 SEM and STEM imaging of APTES functionalised WS_2 NTs. a-c) SEM images of WS_2NTs: APTES at 1:1,1:2 and 1:4, respectively. d) STEM of WS_2 NTs: APTES at 1:4, and e) STEM and EDS mapping of the WS_2NTs-APTES 1:4 sample.

To confirm further the attachment of APTES to the surface of the WS_2 NTs, the zeta (**ς**) potential of the WS_2 NTs and APTES modified NTs with increasing APTES concentration were measured. WS_2 NTs alone (1:0) have a charge of -26.7±0.71mV, due to the sulphur atoms exposed on the surface of the NTs, which is in agreement with previous literature [328]. After reaction with APTES, the ζ potential values gradually become increasingly positive with increasing APTES concentration, Figure 5.7. The concentration of APTES is critical to the extent of functionalization and APTES grafted to the surface of the WS_2 NTs. The change in ζ potential is derived from the presence of amine groups (from APTES) on the NT surface, as amine groups are protonated to positively charged ammonium producing a higher ζ potential value [326, 329].

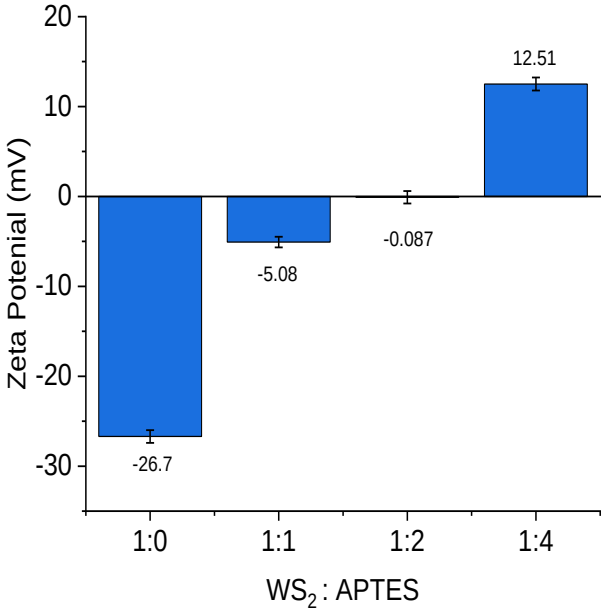

Figure 5.7 *ζ* potential for WS_2 NTs, and change in ***ζ*** for APTES-WS_2 NTs with increasing APTES content.

5.3 Characterisation of APTES Functionalised WS_2 NTs composites of PLA

The rationale for functionalising WS_2 NTs with APTES is to provide a route to aid effective dispersion of the NTs in polymers and to promote strong interfacial interactions between both, such that some bulk properties of the polymer can be improved. To examine this hypothesis, APTES modified WS_2 NTs were dispersed in PLA and solvent cast to produce films and the interaction mechanism and physical properties of composites studied.

PLA has previously shown to interact with APTES following a condensation and grafting mechanism that results in the formation of a N-H bond [330]. Consequently, FTIR analysis, shown in Figure 5.8, identifies the evolution of a band associated with N-H stretching at 2921cm^{-1} in the FTIR spectra that becomes more intense and shifts by 4cm^{-1} to 2925cm^{-1} with increasing APTES content.

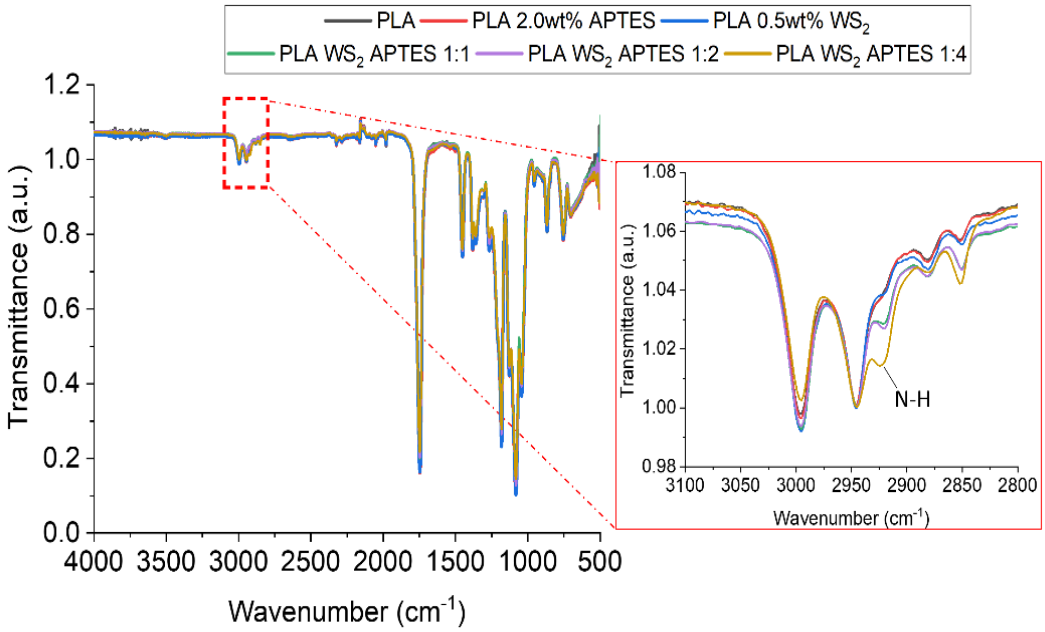

Figure 5.8 FTIR spectra of for PLA, a blend of PLA and APTES composites of PLA with APTES modified WS_2 NTs.

This interaction is further presented in Figure 5.9 as a schematic representation of interaction mechanism between all components of composite determined by chemical interaction findings of APTES WS_2 NTs and further representative of WS_2 APTES PLA via the formation of amine and hydroxyl bonding on NTs surface.

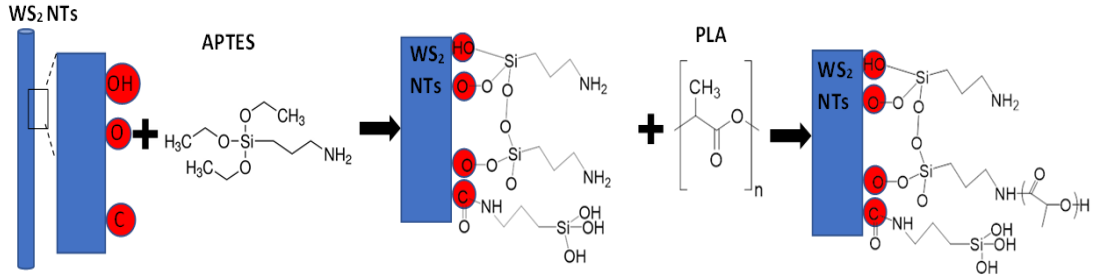

Figure 5.9 Schematic representation of WS_2 NTs interaction with APTES and composites of APTES modified WS_2 NT and PLA mechanism.

The optical photographs shown in Figure 5.10. a), compare film samples for neat PLA, composites of PLA and WS_2 NTs, and composites of PLA and APTES modified WS_2 NTs. In agreement with previous studies, the WS_2 NTs disperse very well within the PLA matrix, [231, 232, 331, 332]. Nevertheless, APTES functionalised WS_2 NTs are visibly much more uniformly dispersed, as seen from Figure 5.10a) images suggesting increased surface interaction and compatibility between APTES modified WS_2 NTs and the PLA matrix. Extensive SEM imaging of the composites of PLA and APTES modified WS_2 NTs (Figure 5.10 b) and d)) across the length scales did not show significant NT agglomerations and individual NTs were observed (Figure 5.10 b)), supporting uniform dispersion of the NTs in the PLA matrix. Unmodified WS_2 NTs (Figure 5.10c)) can be compared to NTs surface in APTES functionalised NTs PLA composite in Figure 5.10d, which clearly visually identifies surface modification of NTs in composites.

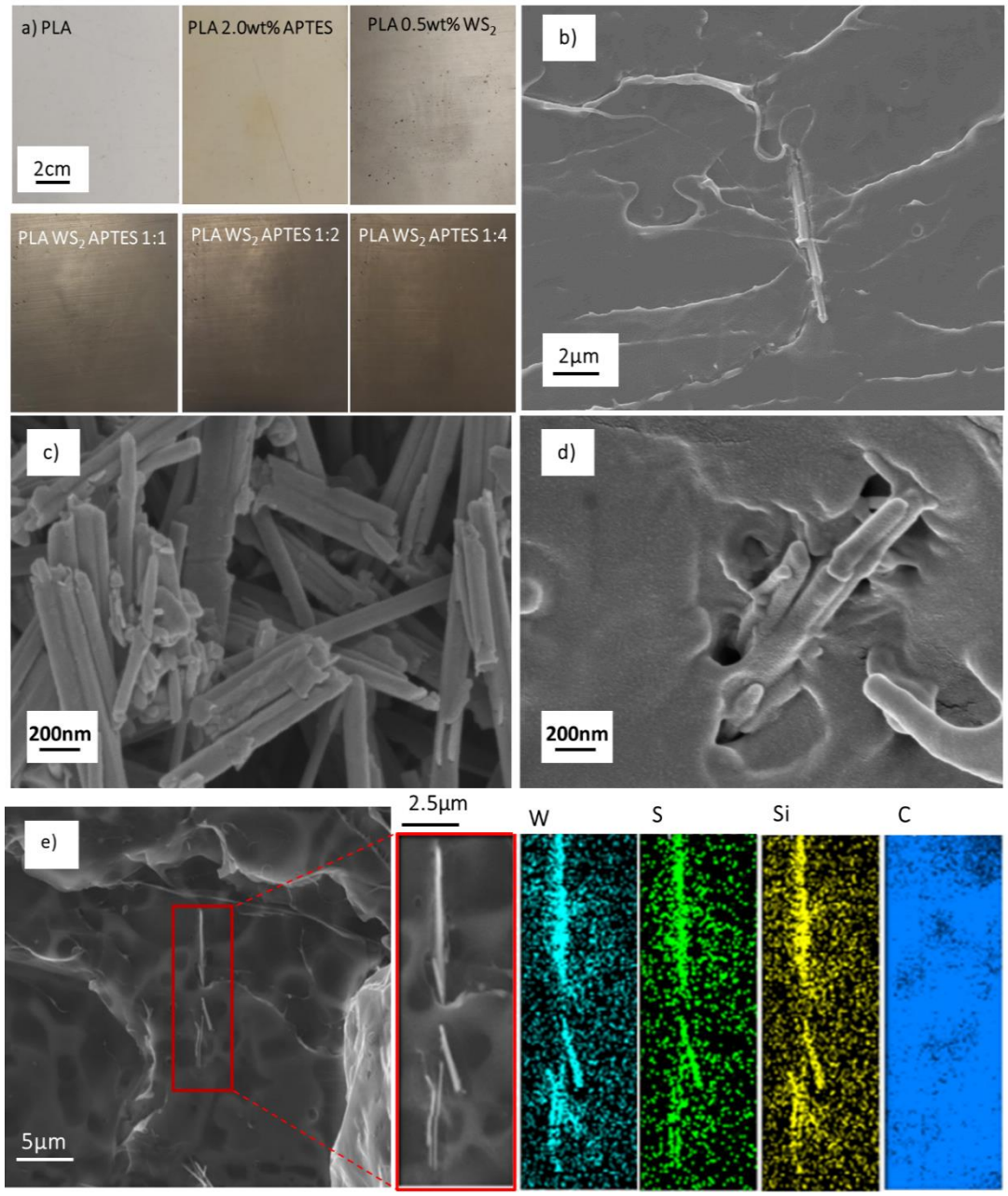

Figure 5.10 a) Representative optical photographs of film samples of PLA alone and corresponding composites and SEM micrographs of b) composite of PLA and APTES modified WS_2 NTs (1:4), c) unmodified WS_2 NTs, d) composite of PLA and WS_2 NTs:APTES 1:4 at higher magnification and e) composite of PLA WS_2 NTs:APTES 1:4 with corresponding EDS of highlighted area.

Additionally, SEM-EDS was used for surface elemental analysis of these composites, Figure 5.10. e). This analysis clearly identifies tungsten and sulphur from the NTs, while also confirming the presence of silicon from APTES only on the surface of NTs, in agreement with the EDS analysis reported in Figure 5. (The detected carbon on the entire analysed area stems from the carbon coating of the sample). This observation is further verification of silane functionalisation of the WS_2 NTs.

To assess the effectiveness of silane modification of the WS_2 NTs on the mechanical properties of PLA, tensile tests of neat PLA, blends of PLA and APTES as control samples and, composites of PLA and APTES modified WS_2 NTs were measured. Representative stress-strain curves for all the specimens are shown in Figure 5.11.

Table 5.3 Tensile mechanical Properties of PLA and blends of PLA and APTES

Sample	**Modulus** **MPa**	**Maximum tensile stress** **MPa**	**Elongation at Break** **%**	**Tensile toughness** **Jm^{-3}**
PLA	3414 ± 178	57 ± 4	33 ± 4	984 ± 103
PLA 0.5wt% APTES	3085± 114	50 ± 4	17 ± 3	406 ± 50
PLA 1.0wt% APTES	2883 ± 73	49 ± 2.5	3.3 ± 0.3	105 ± 12
PLA 2.0wt% APTES	3439 ± 72	54 ± 3	31 ± 2.5	101 ± 30

The Young's modulus (MPa), maximum tensile stress (MPa), elongation at break (%) and the tensile toughness (kJm^{-3}) as a function of the ratio of WS_2 NTs:APTES were determined and the values are listed in Tables 5.3 and 5.4. For the blends of PLA and APTES only, i.e. with no WS_2 NTs added, neat PLA had an elongation at break of ~33% with stress oscillation observed beyond necking [333]. Upon addition of 2wt% APTES to PLA, an initial decrease in tensile properties is observed before an increase to values approaching that of the PLA alone (Table 5.3). The mechanical properties with 1.0wt% APTES loading exhibit reduced performance compared to neat PLA, which may be associated with aminolysis causing scission of the polymer chains and the material becomes brittle [330, 334].

Table 5.4 Tensile mechanical properties of PLA and composites of PLA APTES modified WS_2 NTs

Sample	**Modulus** **MPa**	**Maximum tensile stress** **MPa**	**Elongation at break** **%**	**Tensile toughness** **Jm^{-3}**
PLA	3414 ± 178	57 ± 4	33 ± 4	984 ± 103
PLA 0.5wt% WS_2	2922 ± 148	54 ± 4	23 ± 2	582 ± 0.08
PLA WS_2 APTES 1:1	3222 ± 179	52 ± 3	51 ± 6	1482 ± 251
PLA WS_2 APTES 1:2	3493 ± 102	53 ± 1	84 ± 14	2610 ± 402
PLA WS_2 APTES 1:4	3323 ± 151	55 ± 2	208 ± 18	6886 ± 408

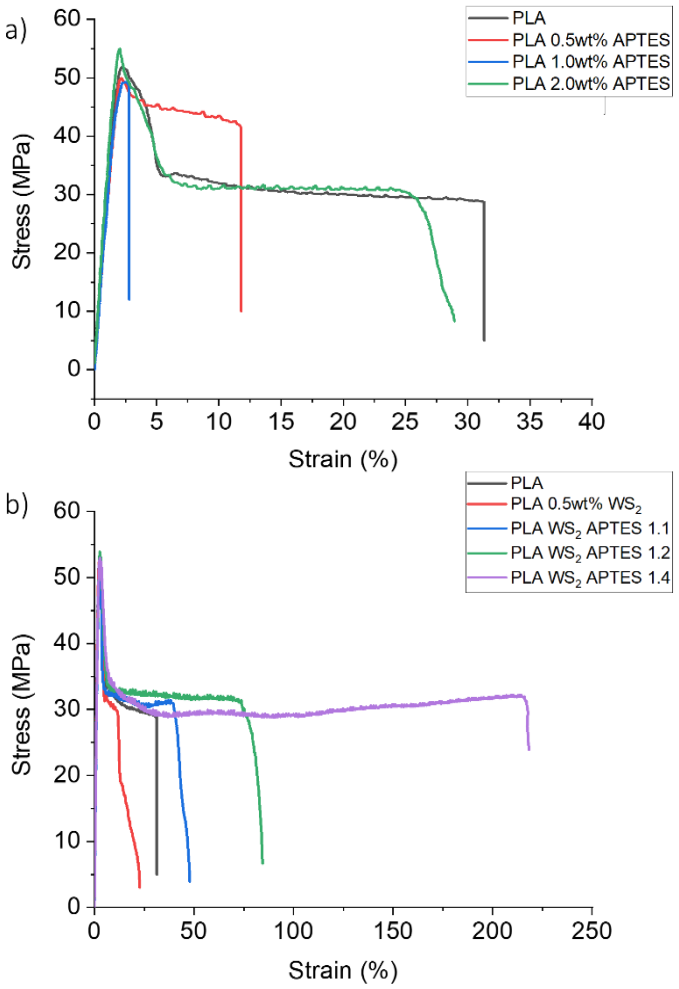

Figure 5.11 Representative stress-strain curves for neat PLA relative to those for a) blends of PLA and APTES and b) composites of PLA and APTES modified WS_2 NTs.

However, at 2wt% APTES the mechanical properties are similar to that of neat PLA. This suggests that at 2.0wt% APTES there is strong interfacial interactions with the polymer chains and the microstructure of PLA is not degraded when mixed with APTES. The inclusion of 0.5wt% unfunctionalised WS_2 NTs resulted in a degradation of mechanical properties, ~15% reduction in Young's modulus relative to neat PLA, indicative of poor interfacial interaction between the WS_2 NTs and the PLA matrix

[335], and consequently a reduction in PLA ductility and toughness. In contrast, inclusion of APTES functionalized WS_2 NTs to the same PLA resulted in a systematic increase in the tensile mechanical properties with increasing WS_2 NTs: APTES ratio, Figure 5.11. b). When the ratio of WS_2 NTs:APTES was 1:4 there was an enhancement in mechanical properties, including an almost 600% increase in elongation at break and tensile toughness from $0.99 kJm^{-3}$ to $6.88 kJm^{-3}$. Critically, there was little change in the maximum tensile strength and Young's modulus of PLA, irrespective of the WS_2 NT:APTES ratio. The significant increase in elongation at break and toughness on addition of APTES modified WS_2 NTs is a consequence of the improved and very strong interfacial interactions between the NTs and polymer and the role APTES is playing in aiding the dispersion of WS_2 NTs in the PLA matrix. The interaction via the amine and hydroxyl groups of APTES bound to the NTs and PLA provides a route for effective stress transfer at the interface from the polymer to the filler.

Given that WS_2 NTs have shown to nucleate PLA, as well as alter the crystallization behaviour of the matrix, the thermal properties of the composites were studied by DSC. DSC curves (cooling and melting curves) for unfilled PLA, blends of PLA and APTES, composites of PLA and unmodified WS_2 NTs and composites of PLA and APTES modified WS_2 NTs were recorded, see Figure 5.12, from which DSC parameters were determined and tabulated in Table 5.5.

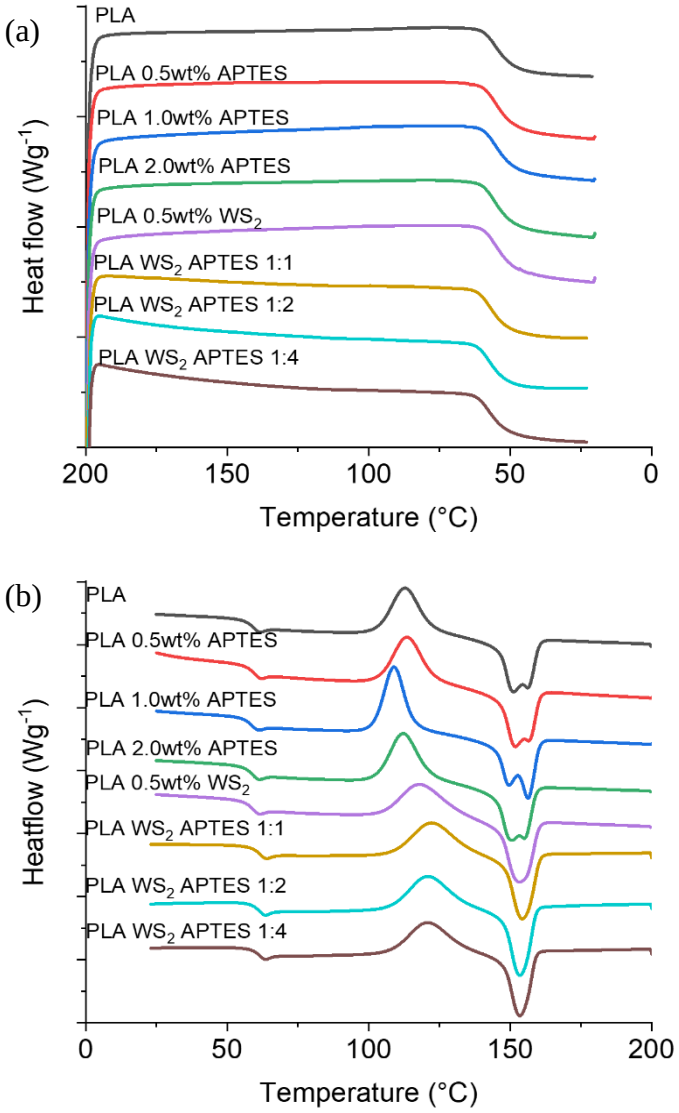

Figure 5.12 DSC thermograms for PLA and its blends with APTES and composites with APTES modified WS_2 NTs showing a) first cooling cycle and b) second heating cycle.

The T_g of neat PLA was determined to be $54°C$ and it remained constant on the addition of APTES or WS_2 NTs, as shown in Table 5.5. However, on addition of APTES modified WS_2 NTs, the T_g of PLA increased by $2°C$, although this is likley to be within instrument error. Given the fact that the change in T_g was minor, as was the

case with the Young's modulus and tensile strength of PLA on inclusion of silane functionalised WS_2 NTs, the change in the mechanical properties are not due to a plasticizing effect or major change in the PLA crystalline content [336].

Table 5.5 DSC parameters for neat PLA, blends of PLA and APTES, and composites of PLA and APTES modified WS_2 NTs.

Sample	T_g (°C)	T_{cc} (°C)	ΔH_{cc}	T_{m1} (°C)	T_{m2} (°C)	ΔH_m	X_c (%)
PLA	54	113	25	151	156	27	1.7
PLA 0.5wt% APTES	54	113	25	151	156	27	2.7
PLA 1.0wt% APTES	53	109	28	150	156	29	0.9
PLA 2.0wt% APTES	54	112	27	153	155	29	2.1
PLA 0.5wt% WS_2	54	118	24	153	-	28	4.2
PLA WS_2 APTES 1:1	56	122	24	154	-	28	3 .6
PLA WS_2 APTES 1:2	56	121	25	153	-	27	2.5
PLA WS_2 APTES 1:4	56	121	23	153	-	25	2.5

Moreover, the PLA used in this study was highly amorphous (at least 96% L-isomer) and the minor crystalline component very slow to crystallise, such that no crystalline peak is observed in the cooling curve (Figure 5.12. a)). However, a significant broad cold crystallisation peak is observed in the heating cycle (Figure

5.12. b)) for all the samples. The neat PLA has a broad T_{cc} peak centred at $113°C$, while the incorporation of WS_2 NTs shifted the T_{cc} by $5°C$ to $118°C$. The NTs have a strong nucleating effect on the PLA, but a limited effect on the overall crystalline content (X_c = 4.2%) due to the high L-isomer content. There is a further shift of $3°C$ in T_{cc} to $121°C$ upon inclusion of the APTES modified WS_2 NTs. This further shift, some $8°C$ higher than that for unfilled PLA is a consequnce of the better WS_2 NT dispersion and increased NT surface area available as nucleating sites for the polymer, but again the high L-isomer content hinders crystallite growth.

A doublet of melting peaks are observed (Figure 5.12 b) for the neat PLA and blends of PLA and APTES with T_{m1} at $151\pm1°C$ and T_{m2} at 155-156$°C$. Both peaks are characteristic of PLA and can be attributed to the melting–recrystallization–melting processes of PLA lamellae. The first peak is ascribed to the melting of new lamellae formed during the heating cycle (i.e. T_{cc}), the second peak is the melting-recrystallisation of primary thin lamellae at relatively higher temperature [337]. Interestingly, the DSC curves for the composites of APTES modified WS_2 NTs and PLA exhibit a single melting peak at $152°C$, which is attributed to the highly dispersed modified NTs promoting nucleation and PLA crystal growth. However, due to slow crystallisation kinetics of the PLA used in this study, the composites remain almost fully amorphous with a crystalline content remaining below 5%. Therefore, the significant enhancement in the ductility and toughness of the PLA on inclusion of APTES modified WS_2 NTs must be derived from the high level of dispersion and strong interfacial interactions between the APTES coated NTs and the polymer matrix and not because of changes in the PLA microstructure.

5.4 Conclusions

In summary, APTES was successfully grafted to the surface of WS_2 NTs, through the formation of siloxane networks on the NT surface. It was found with increasing concentration of APTES used lead to an increase of binding to the NT surface. Extensive characterisation of the APTES functionalised WS_2 NTs confirmed APTES formed siloxane networks bound to the surface of the NTs owing to the presence of functional oxygen and carbon groups attached to the surface sulphur atoms of the WS_2 NTs.

APTES modification of the WS_2 NT surface significantly improved the extent of WS_2 NT dispersion in the PLA matrix and promoted strong interfacial interactions between the NTs and PLA. This resulted in a significant increase in mechanical properties of composites including an increase of elongation at break, tensile toughness of PLA by 600% on inclusion of WS_2 NTs: APTES 1:4. This highlights the effectiveness of silane functionalization of 1D WS_2 NTs as a route to forming strong interfacial interactions between inorganic nanoparticles and polymers to produce composites with significantly enhanced ductility and toughness without sacrificing stiffness and strength, properties useful for further industry applications.

Chapter 6: Results and Discussion III

Composites of Chitosan WS_2 NTs and Glycerol

6.1 Introduction

This chapter examines the inclusion of WS_2 NTs in a chitosan (C) matrix, both with and without the use of glycerol (G). WS_2 NTs have shown to readily disperse in PLA, amongst other biopolymers, however WS_2 NTs in chitosan has, so far, been unexamined. We aim to exploit the polyelectrolyte complexation of positively charged chitosan with negatively charged surface of WS_2 NTs as a route to enhancing the properties of chitosan. To this end, the inclusion of WS_2 NTs at loadings up to 2 wt% in blends of chitosan and glycerol (20 wt%) is investigated and an attempt made to understand the role polyelectrolyte complexation plays in altering the thermal, mechanical, gas barrier and antimicrobial properties of chitosan.

6.2 Characterisation of Chitosan WS_2 NTs and Glycerol Composites

The chemical structure of composite components as well as the chemical interaction of chitosan WS_2 film blends are studied using FTIR as shown in Figure 6.1. The FTIR spectrum of WS_2 NTs (Figure 6.1a) does not display any peaks as discussed in Chapter 5 [317]. Unprocessed chitosan powder (Figure 6.1a C Powder) FTIR spectra displays characteristic CH symmetric and asymmetric peaks appear at 2926 and 2874cm^{-1}, and amine peaks at 3357 and 3289cm^{-1} superimposed on the OH band ranging from 2600cm^{-1} to 3670cm^{-1}.

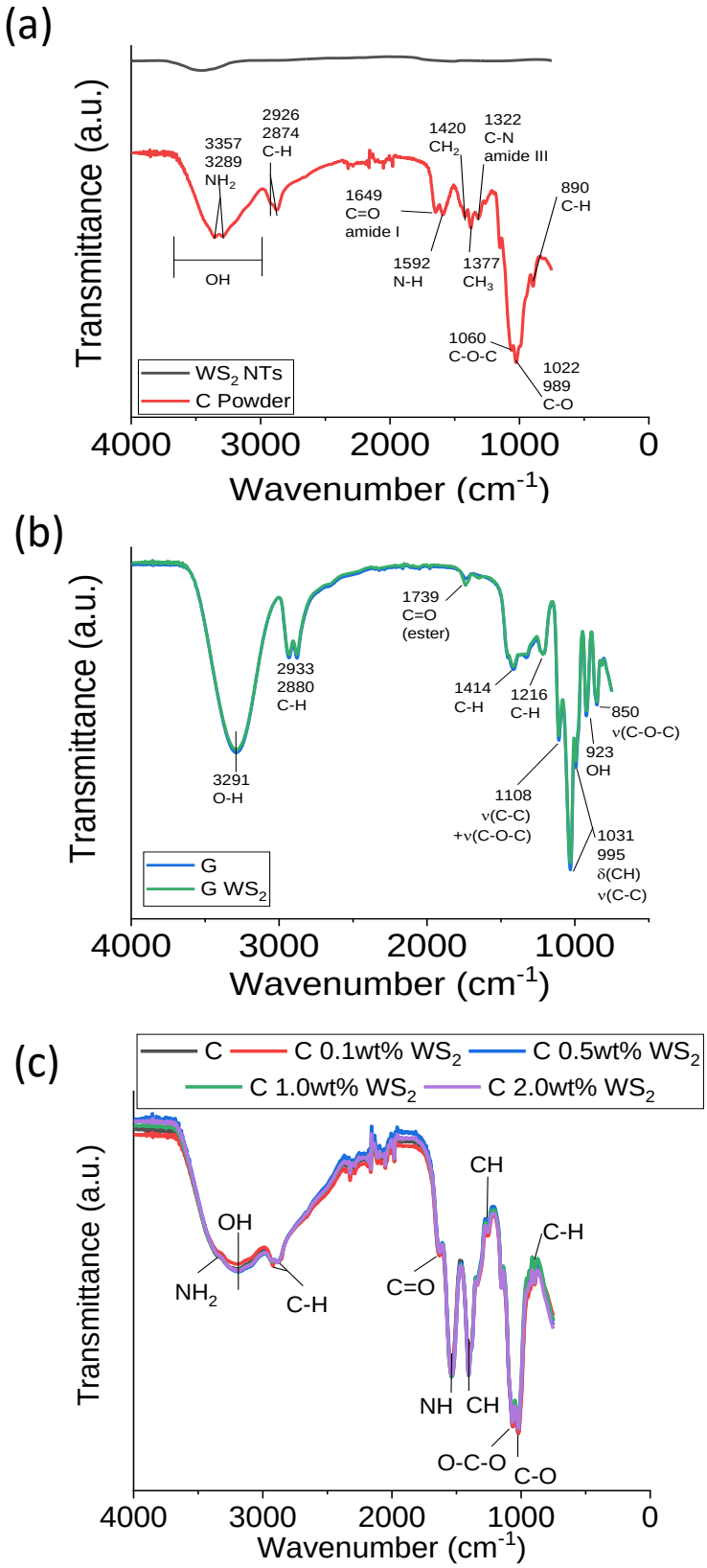

Figure 6.1 FTIR transmittance spectra for a) WS_2 NTs, unprocessed chitosan powder, b) glycerol and the interaction of glycerol WS_2 NTs, c) chitosan and composites of chitosan and WS_2 NTs.

C=O (Amide I) is identified at 1649cm^{-1}, 1592cm^{-1} NH_2 (amide II), CH_2 deformation and CH_3 symmetric deformation correlates to peaks 1420cm^{-1} and 1377cm^{-1}. The peak associated with C-N (1322cm^{-1},amine III) symmetry vibration at 1267cm^{-1} peak [338]. Peaks in the range of 1260-800cm^{-1} belong to the glycosidic ring, in particular, the band at 1153cm^{-1} corresponds to the glycosidic linkage, characteristic of the saccharide structure representing the C-O-C stretch. 1060cm^{-1} identifies the asymmetric stretching of C-O-C, while 1022cm^{-1} represents the C-O stretching vibration and 890cm^{-1} is attributed to C-H stretching [339-342].

FTIR analysis of pure glycerol (G) displayed in Figure 6.1b, identifies O-H stretching at 3291cm^{-1}, C-H symmetric and asymmetric stretching at 2932 and 2880cm^{-1} respectively. Peak at 1415cm^{-1} correlating to C-O-H bending. C-O stretching from 1450 cm^{-1} (primary alcohol) to 1100 cm^{-1} (secondary alcohol). 923 cm^{-1} identifies O-H bending[343, 344]. WS_2 NTs do not identify any significant chemical interaction as no peak shifts are identified in Figure 6.1b (G WS_2).

The FTIR spectra of all chitosan and chitosan WS_2 films obtained were similar except for that for unprocessed chitosan. The chitosan films were prepared using acetic acid solution, resulting in significant molecular interaction due to the protonation of the amine groups of chitosan and dissolution which allows film formation [341, 345, 346] (see Figure 6.1c). This behaviour can be seen from the significant reduction in the intensity of the NH_2 peaks to form a shoulder at 3354cm^{-1}, while there is a blueshift (13cm^{-1}) for Amine I to 1635cm^{-1} and for Amine III a blueshift (63cm^{-1}) to 1539cm^{-1}. Additionally, there are the emergence of new prominent peaks at 1540cm^{-1} (C=O) and 1406 cm^{-1} derived from N-H bending and stretching associated with Amine II [346, 347]. The characteristic glycosidic linkage of chitosan, observed in the range 800-

1200cm^{-1}, shows no change post processing. Therefore, the processing of the chitosan films mainly involved amine groups and hydrogen bonding.

The FTIR spectra for glycerol plasticised chitosan films are shown in Figure 6.2, where a shift of the OH peak by 58cm^{-1} to 3254cm^{-1}, Figure 6.2 a), in comparison to the neat chitosan film is observed. Additionally, there is a shift of 10cm^{-1} of the N-H bending (Amine II) peak from 1540cm^{-1} to 1550cm^{-1} with the addition of glycerol, Figure 6.2 b). The most significant changes in FTIR spectrum of CG films were seen in Figure 6.2 c). The chitosan C-O-C (1063cm^{-1}) and C-O (1021cm^{-1}) peaks merge to a single peak centred at 1027cm^{-1}, with the addition of glycerol, suggesting interactions between hydroxyl groups of chitosan and glycerol by hydrogen bonding. Additionally, there is an identifiable emergence of O-H and C-O-H peaks at 928cm^{-1} (blue shift of 5cm^{-1} in comparison to pure glycerol) and 850cm^{-1} respectively, which are attributed to glycerol peaks.

Table 6.1 O-H and N-H peak positions for chitosan, CG blend (80:20) and composites of CG and WS_2 NTs.

Sample	**O-H Peak position (cm^{-1})**	**N-H Peak position(cm^{-1})**
C	3196	1538
CG	3254	1550
CG 0.1wt%WS_2	3238	1546
CG 0.5wt%WS_2	3236	1544
CG 1.0wt%WS_2	3235	1542
CG 2.0wt%WS_2	3244	1547

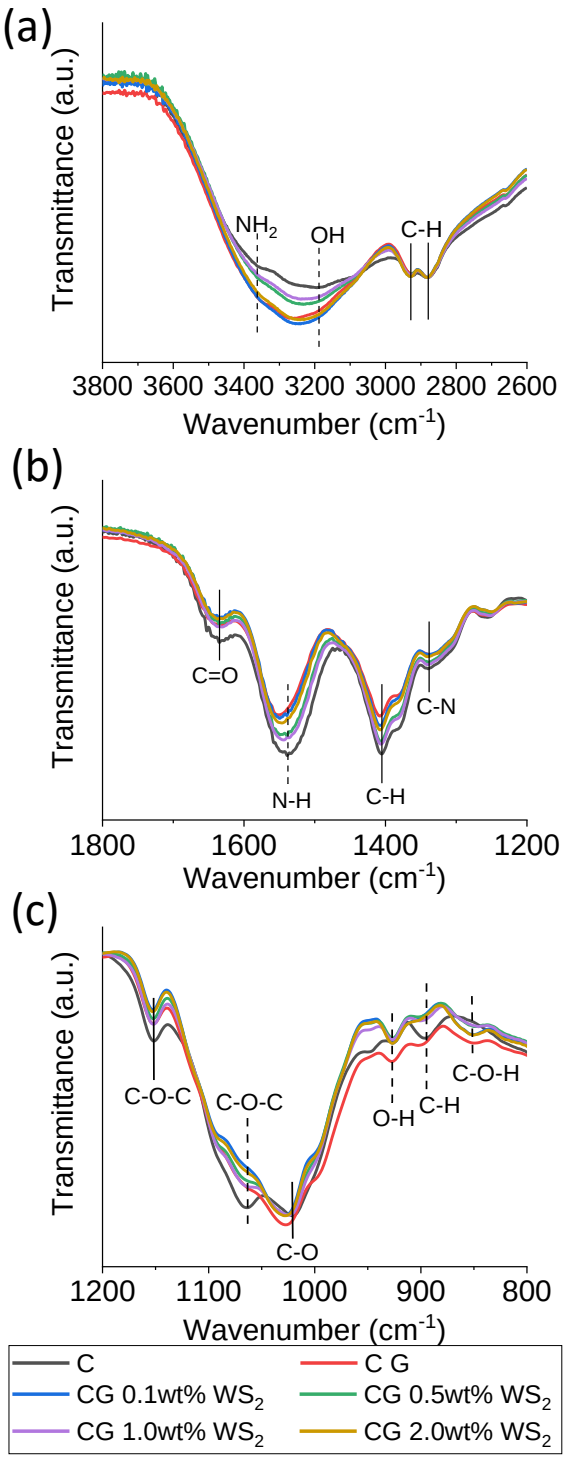

Figure 6.2 FTIR transmittance spectra for chitosan, chitosan:glycerol (CG) blend (80:20) and composites of this blend with up to 2wt% WS_2 NTs in the wavenumber ranges, a) 3800-2600cm^{-1} b) 1800-1200cm^{-1} and c) 1200-800cm^{-1}.

The introduction of WS_2 NTs to the CG matrix induces red shifting of the OH and N-H (bending) peaks, Figure 6.2 a) and b) and is dependent on the loading of WS_2 NTs, see Table 6.1. The shifting obtained for CG is associated with strong intermolecular hydrogen bonding between both but, also from a contribution associated with polyelectrolyte complexation between the positively charged amide groups of chitosan and the negatively charged oxygen species physiosorbed on the surface of the WS_2 NTs. Due to the variation of amine and hydroxyl interaction between WS_2 NTs in chitosan glycerol matrix, it could be suggested this is an indicator of the distribution of glycerol as well as NTs in the chitosan matrix.

To further explore polyelectrolyte complexation between chitosan and WS_2 NTs and, the distribution of the NTs and glycerol in the chitosan matrix, ATR-FTIR mapping was performed on the composites of CG and WS_2 NTs, Figure 6.3 (see full spectra obtained in Appendix Figures A3-A5). ATR-FTIR maps were produced by integrating the area under the band in the region 1535-1555cm^{-1}, attributed to the N-H amine II, (Figure 6.2 c)) where a significant shift in peak positions was observed on blending of glycerol with, or the inclusion of WS_2 NTs in chitosan. The area enclosed in the optical images (Figure 6.3 part i)) was mapped and the different regions are shown as different colours (Figure 6.3 part ii)) correlate with the variation in intensity of area under the curve. Moreover, it should be noted that any change in intensity measured does not always reflect changes in chemical composition or variation in the dispersion of glycerol and/or the WS_2 NTs in the chitosan matrix.

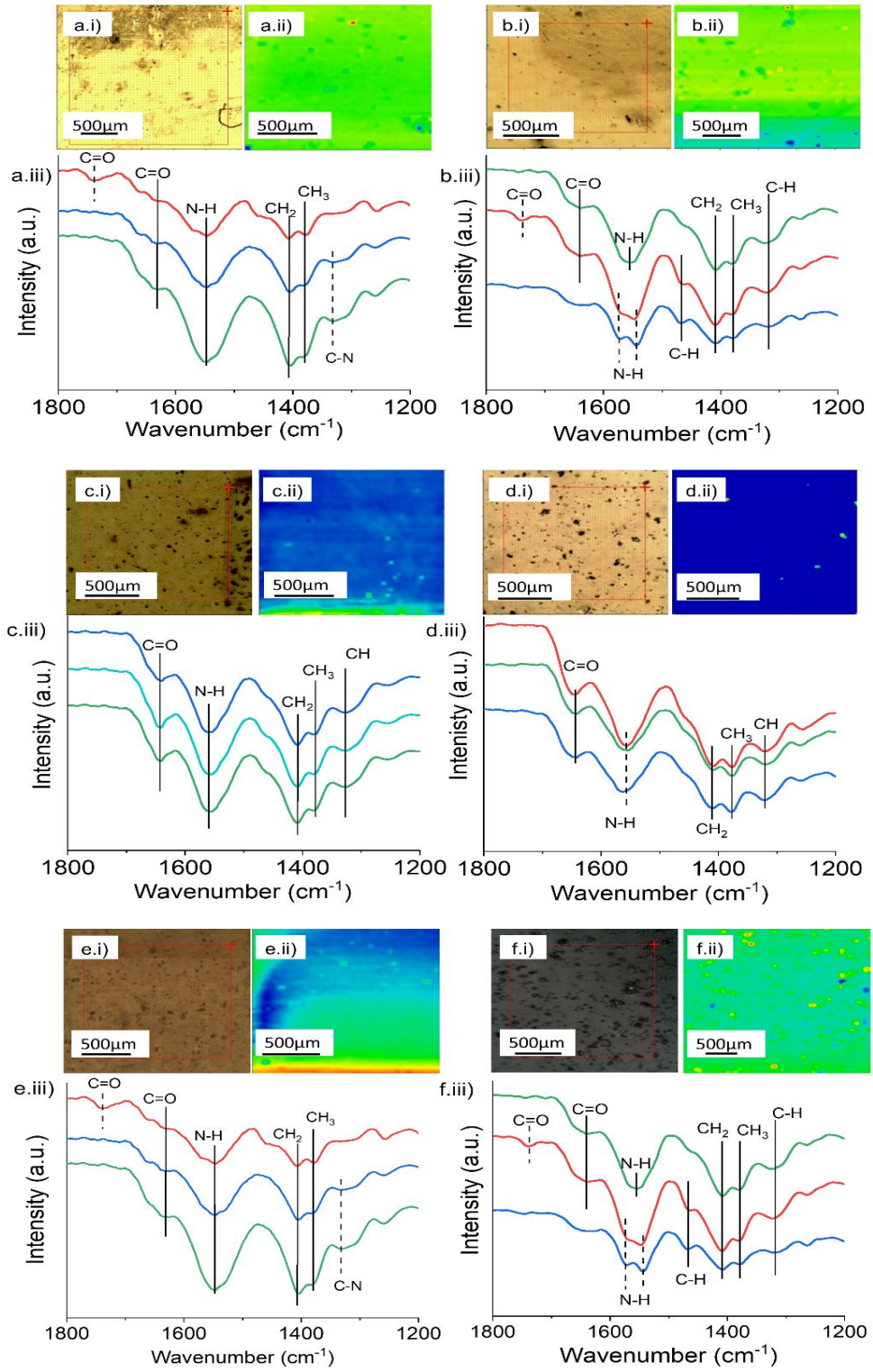

Figure 6.3 ATR-FTIR mapping for a) chitosan, b) CG blend (80:20) and composites of the CG blend with c) 0.1wt%, d) 0.5wt% e) 1.0wt% and f) 2.0wt% WS_2 NTs, where i) are optical microscope images of the film surfaces, ii) is the integrated intensity of the amide II peak and iii) are the corresponding individual pixel spectra extracted from different regions (red, blue, and green).

However, both can be determined from analysis of the FTIR spectra at different points on the colour contrast images. For chitosan itself, FTIR mapping (Figure 6.3 aiii)) shows spectra that are in the main typical of that expected for chitosan, however, there were individual points, red and blue intensity on the map, associated with changes in intensity of the N-H amide II peak at 1547cm^{-1}. Additionally, the spectra collected from the red areas display additional peaks at 1739cm^{-1} correlating to C=O stretching of esters, possibly from residual acetic acid in the chitosan films.

From the map recorded for the CG blend (Figure 6.3b)) significant changes in the FTIR spectrum of chitosan are observed, suggesting significant variation in chemical structure on blending with glycerol. However, the changes in colour are primarily associated with the changes in the measured intensity of the NH amine II peak. The red and blue colours are derived from a splitting of the NH amine II peak, with the characteristic peak at 1546cm^{-1} and an additional peak at 1571cm^{-1}. The latter may be attributed to either a glycerol impurity, COO- carboxylate ions, or this peak splitting could be an indication of the plasticisation of chitosan. Previous studies [348] reported the deconvolution of amine II, of which N-H bending is sensitive to hydrogen bonding. Consequently, the evolution of a peak at 1571cm^{-1} is attributed to hydrogen bonding of glycerol to the N-H bending (amine II) of chitosan, causing the shift to higher wavenumbers. There is an additional peak at 1466cm^{-1}, from C-H stretching of CH_2 [349] in glycerol.

On the inclusion of WS_2 NTs to the CG the intensity of the maps and spectra obtained during mapping were consistent, particularly for NT loadings up to1.0wt%, confirming uniform dispersion of the NTs in CG. (Figure 6.3 c)- e)). As was observed from the FTIR spectra (Figure 6.2), shifting of the N-H amine II peak is identified in the spectrum of each composite. As the WS_2 NT loading in CG increases to 0.5wt%

(Figure 6.3 d)) small regions seen as red and green lines reveal a shift of N-H peak to 1556cm^{-1}, i.e., N-H peak from CG (Figure 6.3 b)).

However, as the WS_2 NT loading in CG was increased to 2.0wt% (Figure 6.3 f)), there were much greater variations in the intensities and spectra obtained when mapping across the sample. The majority of the spectra collected correlate with the green/blue intensities obtained and originate from similar molecular interactions between C and G but, variations in intensities are due to the distribution of the NTs in CG as WS_2 is not IR active. Most evident change in the spectra was identified in the dark blue regions which yield spectra similar to that of CG (Figure 6.3 b)) showing deconvolution of the amine II peak at 1571cm^{-1} and 1547cm^{-1}, spectroscopic evidence for the mechanism by which glycerol plasticises chitosan.

ATR-FTIR mapping confirmed the intermolecular interaction between CG and WS_2 NTs is due to the hydrogen bonding and amine ionic interactions, achieved largely by uniform dispersion and distribution of WS_2 NTs, and glycerol in the chitosan matrix. However, when the WS_2 NT loading was increased to 2wt% the less uniform distribution of the NTs and glycerol in chitosan can be seen from regions (blue/yellow) of varied molecular interaction with chitosan. Consequently, it might be expected that certain properties of composites of WS_2 NTs and chitosan, or other positively charged biopolymers, could be optimised at relatively low WS_2 NT concentrations by exploiting the favourable molecular interactions between WS_2 NTs and glycerol with chitosan.

This hypothesis was tested by measuring the tensile mechanical properties of chitosan (C), CG and composites of C and CG with WS_2 NTs. The mechanical properties of chitosan and WS_2 composite films all display similar stress versus strain behaviour (Figure 6.4 a)) as chitosan films exhibit typical brittle behaviour and weak mechanical stability [289, 350, 351]. The addition of WS_2 NTs to the neat chitosan (Table 6.2), has a minimal effect on the stiffness and strength of the chitosan film but,

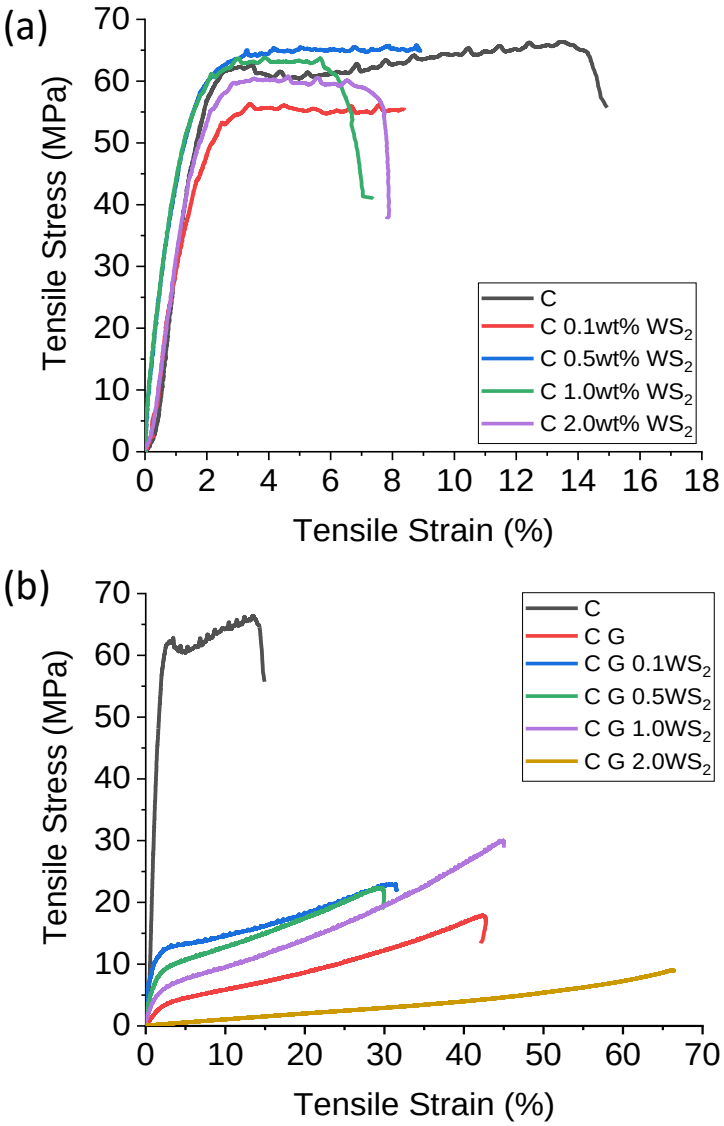

Figure 6.4 Representative stress-strain curves for neat chitosan films and a) composites of chitosan and WS_2 NTs and b) composites of CG and WS_2 NTs.

the elongation at break (a measure of ductility) and tensile toughness of chitosan are reduced by ~50%. This can be attributed to the limited interfacial interaction between the surface of the NTs and chitosan alone, as seen from our ATR-FTIR mapping experiments.

Table 6.2 Tensile mechanical properties of chitosan and composites of chitosan and WS_2 NTs

Sample	Young's Modulus MPa	Maximum tensile stress MPa	Elongation at break %	Tensile toughness Jm^{-3}
C	4273 ± 293	61 ± 3.6	15.2 ± 2.8	761 ± 67
C 0.1WS_2	3586 ± 356	56 ± 2.5	8.8 ± 1.8	454 ± 69.5
C 0.5WS_2	4269 ± 176	65 ± 3.5	8.5 ± 1.5	508 ± 49.4
C 1.0WS_2	4416 ± 274	66 ± 3.9	6.9 ± 2.5	289 ± 64.3
C 2.0WS_2	3714 ± 125	62 ± 4.5	7.6 ± 1.8	365 ± 72.2

The effect of inclusion of glycerol on the mechanical behaviour of chitosan and composites of chitosan WS_2 NTs are represented in stress-strain curves shown in Figure 6.4 b). As expected, the addition of glycerol to chitosan has a plasticising effect on chitosan. Consequently, the Young's modulus and maximum tensile stress are decreased, however a 300% increase of elongation is obtained. This is expected as addition of glycerol in the chitosan matrix increases polymer chain mobility by decreasing the chitosan intra-polymer chain intermolecular forces [289].

Table 6.3 Tensile mechanical properties of CG (80:20) blend and composites of CG and WS_2 NTs

Sample	Modulus MPa	Max. Tensile Stress MPa	Elongation at break %	Tensile Toughness Jm^{-3}
C	4273 ± 293	61 ± 3.6	15.2 ± 2.8	761 ± 67
C G	28.7 ± 0.2	17.9 ± 1.8	44.8 ± 1.3	396 ± 11
C G 0.1WS_2	45.6 ± 1.2	22.2 ± 2.9	32.4 ± 3.7	479 ± 42
C G 0.5WS_2	43.3 ± 1.1	22.5 ± 2.3	32.2 ± 2.9	473 ± 40
C G 1.0WS_2	36.4 ± 2.1	25.0 ± 7.6	46.6 ± 2.1	689 ± 67
C G 2.0WS_2	14.2 ± 0.4	9.5 ± 1.7	66.8 ± 3.5	242 ± 25

The addition of WS_2 NTs to the CG matrix results in a significant change in the mechanical properties of CG, Table 6.3. Even at low NT loadings up to 0.5wt%, the Young's modulus increases by 60%, the maximum tensile stress by 25% and tensile toughness by 20%, in comparison to CG films. The addition of WS_2 NTs to CG at loadings <1wt% a stronger (+40%), tougher (+74%) yet stiffer material, without sacrificing ductility. This behaviour is attributed to a combination of strong interfacial interaction between the NTs and glycerol and, chitosan. as well as the NTs being homogeneously dispersed in the CG matrix.

However, for a NT loading of 2wt% WS_2 NTs the plasticisation effect of glycerol is highlighted by a significant decrease in Young's modulus, maximum tensile stress as well as tensile toughness, while elongation at break of this composites increases by 50%. This result is in agreement with our observations from FTIR and ATR-FTIR mapping experiments, the increased NT loading is more difficult to disperse and the NT agglomerations play a lesser role in competition for

intermolecular interaction with CG. This result in more free glycerol so they plasticisation effect of glycerol on chitosan dominate. Further evidence for the extent of interaction between the composite components can be determined from thermal analysis, via TGA, of the composites in both air and nitrogen atmospheres.

TGA conducted in an oxygen atmosphere provides additional information on the thermal oxidation of chitosan and composites of chitosan and WS_2 NTs with and without glycerol (Figure 6.5 a)-b) and Figure 6.5 c)-d), respectively. Chitosan and composites of chitosan and WS_2 NTs display a similar degradation profile up to 400°C, clearly seen from the derivative curve shown in Figure 6.5 b). The first lower temperature process is from evaporation of water and has a peak maximum at 95°C, contributing to approximately 8% mass loss from chitosan. The second stage of thermal decomposition, with a peak maximum at 260°C, corresponds to the chemical degradation and deacetylation of chitosan, contributing to a 26% weight loss, while the addition of WS_2 NTs had a negligible impact on both these processes. The most significant difference in thermal degradation was observed above 400°C where the decomposition temperature (T_d) of chitosan is 573°C, and a 50% weight loss is recorded. This is associated with the oxidization of chitosan, and of the carbonaceous residue formed during the second step [352, 353]. The addition of WS_2 NTs resulted in a slight variation of derivative degradation peaks (±4°C) (Figure 6.5 b)). The thermal profile of WS_2 NTs previously discussed in Chapter 4 were shown to oxidise beyond 400°C.

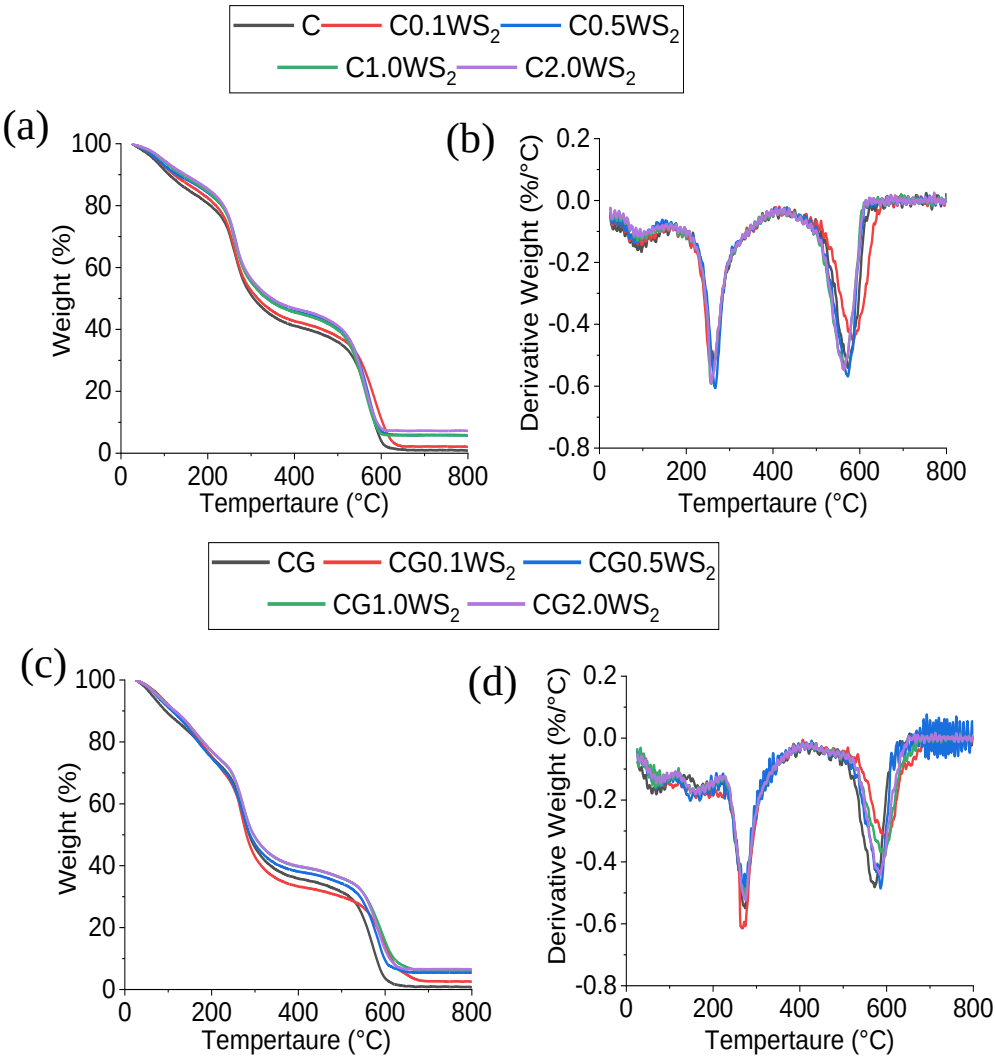

Figure 6.5 a) TGA and b) DTGA curves for chitosan and composites of chitosan and WS_2 NTs and, c) TGA and d) DTGA curves for CG (80:20) blend and composites of CG and WS_2 NTs in an oxygen atmosphere.

.

Table 6.4 Peak maxima from DTGA curves for chitosan, (CG) blend (80:20) and composites of chitosan and WS_2 NTs and, CG and WS_2 NTs

Sample	Stage1 ($°C$)	Stage2($°C$)	Stage3($°C$)	Stage 4($°C$)
C	95	259	573	-
C0.1WS_2	95	263	585	-
C0.5WS_2	95	266	572	-
C1.0WS_2	95	257	562	-
C2.0WS_2	95	258	563	-
CG	69	170	273	573
CG0.1WS_2	70	160	270	596
CG0.5WS_2	70	163	271	587
CG1.0WS_2	70	160	275	595
CG2.0WS_2	70	160	273	585

The peak maximum for the process associated with chemical degradation and deacetylation of chitosan increases from 260°C to 272°C with the addition of glycerol to chitosan and composites of chitosan and WS_2 NTs, induced by the significant increase in hydrogen bonding in the chitosan composite network. Interestingly, the inclusion of glycerol shifts the oxidation of the composites to higher temperatures, by as much as 33 °C with respect to the composites without glycerol (see Table 6.4). It may be that the polyelectrolyte complex formed displays intumescent behaviour and a barrier to the diffusion of oxygen results in increased thermal stability[353] particularly for up to a WS_2 NT loading of 1vwt%.

TGA of chitosan and composites in nitrogen atmosphere are plotted with corresponding derivative curves in Figure 6.6. Chitosan film as well as chitosan WS_2 films exhibit thermal degradation to occur in two stages. Firstly, between $60°C$-$170°C$, with peak temperature at temperature with maximum weight loss (T_d) of $114°C$, referring to water molecules release bound mainly in amino and hydroxyl groups of

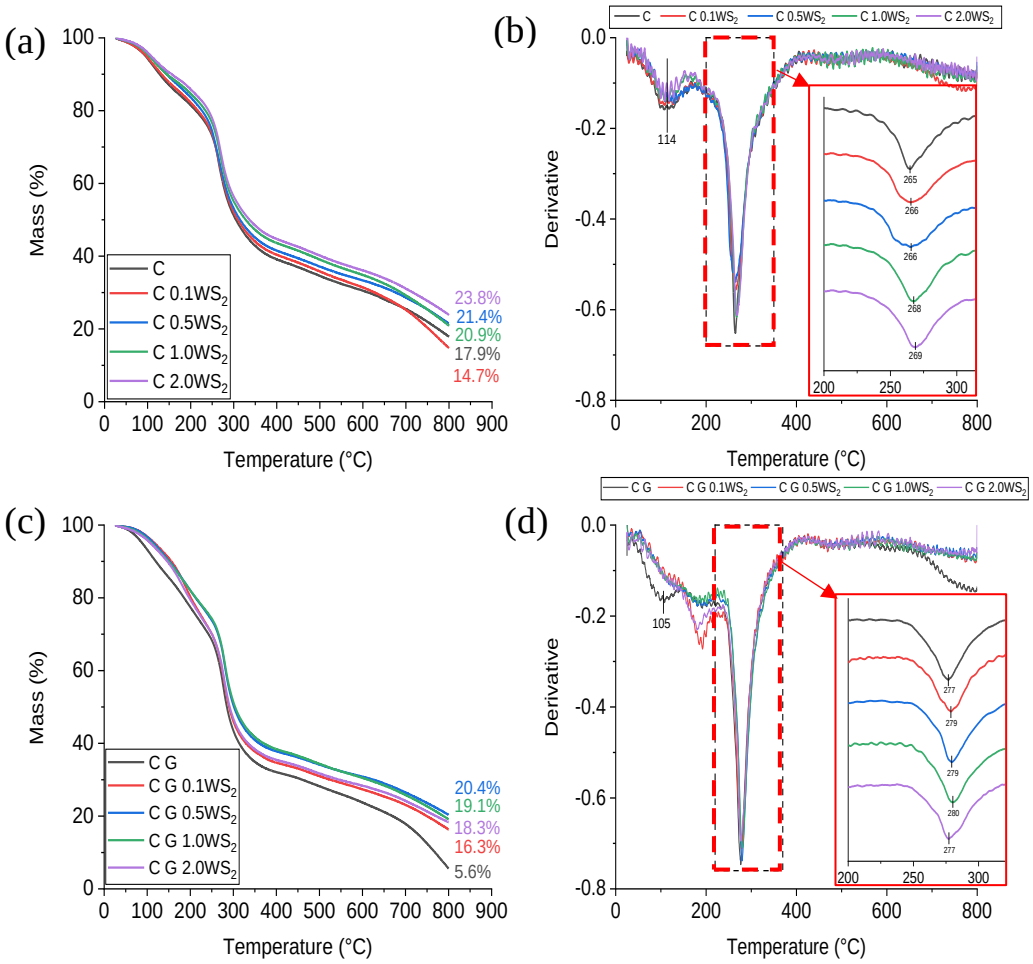

Figure 6.6 a) TGA and b) DTGA curves for chitosan and composites of chitosan and WS_2 NTs and, c) TGA and d) DTGA curves for CG (80:20) blend and composites of CG and WS_2 NTs in an N_2 atmosphere.

the chitosan as well as strong interaction with chitosan's protonated amines [354, 355], and represents 15.2% mass loss. Most significant weight loss occurring from 200°C - 350°C (T_d =265°C), corresponding to a further 43.7% weight loss due to the degradation of organic material loss of chitosan molecules, and further degradation up to 800°C caused by decomposition of residual organic group of chitosan [356]. WS_2 NTs have shown to be stable in an inert atmosphere at over 1000°C as discussed in Chapter 4, and the incorporation of NTs to chitosan matrix at all wt% have shown to not significantly alter the thermal properties of composite films.

The addition of glycerol to chitosan and chitosan WS_2 composites films identify an additional degradation step at T ≅ 182 °C as shown in Figure 6.6d which has been deemed related to the loss of unbound glycerol. Furthermore, it can also be observed that the presence of glycerol increases the main degradation peak from 265°C to 279°C, irrespective of the presence of WS_2 NTs. This can be attributed to the formation of a complex network induced through hydrogen bonding between the glycerol and chitosan and NTs and improved interfacial interactions.

It is also critical to extrapolate if changes in the properties of chitosan are due to the inclusion of the WS_2 NTs alone or from the effect the NTs have on the crystallinity of chitosan. XRD analysis of chitosan and corresponding composites films are identifed in Figure 6.7. The XRD curve of unprocessed chitosan powder (Figure 6.7a) show peaks at 2θ =11.6° (d-spacing=0.76nm) and 20.2° (d-spacing=0.43nm) corresponding to (020) and (110) crystallographic planes, respectively. This correlates with previous reports and confirms the highly amorphous nature of this polysaccharide [357].

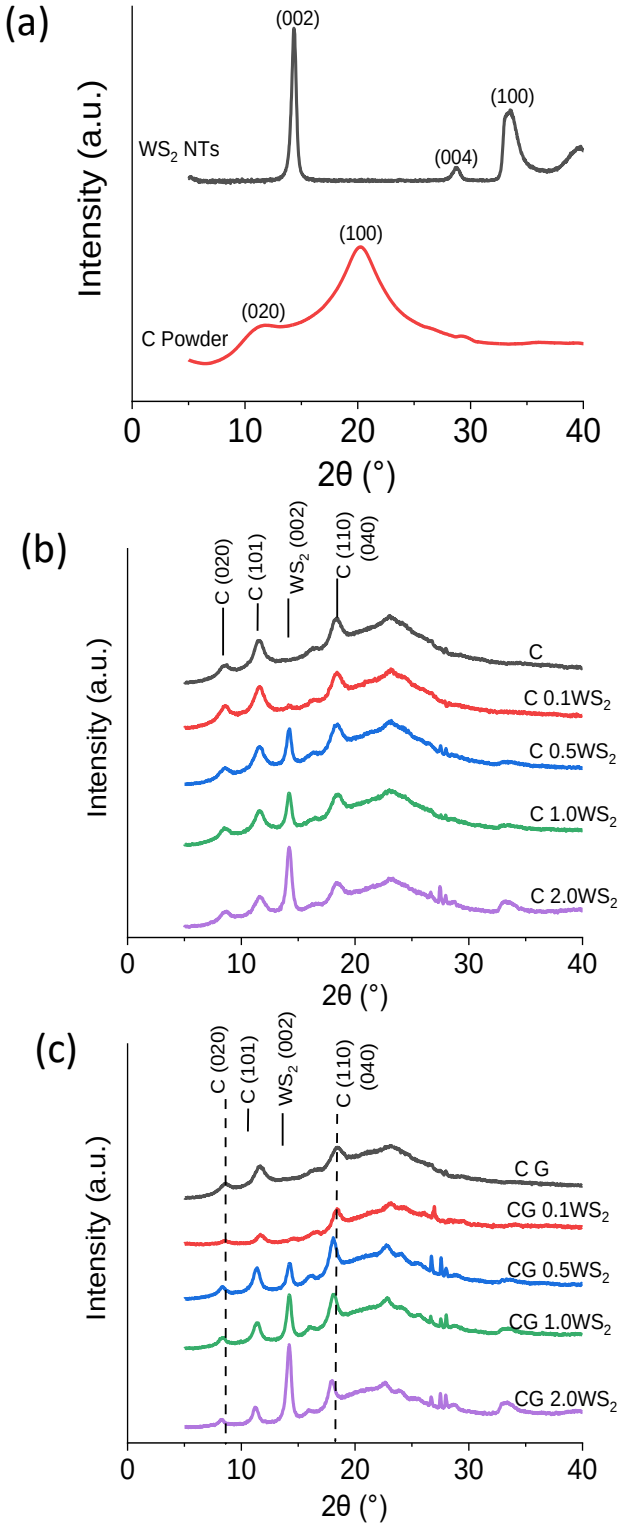

Figure 6.7 XRD patterns of a) WS_2 NTs and unprocessed chitosan powder b) composites of chitosan and WS_2 NTs and c) CG blend and WS_2 NTs.

XRD curves of chitosan (i.e. processed) and composites of chitosan and WS_2 NTs with and without glycerol are shown in Figure 6.7 b-c). All these curves display similar features however, they do differ to that of unprocessed chitosan. The curve for processed chitosan (Figure 6.6a) shows additional peaks at 2θ=8.5° and 18.3° in comparison to chitosan powder. Additionally, a shift of the (110) peak from 2θ=20.2° to 23.1° is observed, indicating a reduction in d-spacing of the chitosan crystal lattice to 0.37nm. The change in XRD pattern of processed chitosan in comparison to that of the unprocessed chitosan powder is from the processing with acetic acid almost fully destroying the original chitosan crystalline structure and, subsequently, new biopolymer crystals were formed [345, 358].

The impact of inclusion of the WS_2 NTs on the crystalline behaviour of chitosan can be seen in Figure 6.7 b). Characteristic peaks of WS_2 NTs can be observed at 14.2° (002), 28.7° (104) and 33.4° (100), and the intensity of these peaks increases with increasing WS_2 NT content, as expected. The addition of WS_2 NTs to chitosan also realises the appearance of small peaks at 26.5° (101) and 27.5° (130), consistent with the α-crystalline structures of chitosan, the NTs can act as nucleating agent and induce a small amount of crystallisation of chitosan polysaccharide [359, 360]. Figure 6.6 b) shows the XRD curves for CG and composites of chitosan and WS_2 NTs with and without glycerol. All peaks associated with the crystalline structure of chitosan are shifted to lower 2θ values when both glycerol and WS_2 NTs are added to chitosan increasing the d-spacing with increasing NT loading. Additionally, the peaks associated with chitosan become narrower and more intense, indicating a more perfect crystalline chitosan on addition of glycerol, perhaps not expected as this indicates that glycerol plays a role in inducing, although low in content, the crystalline structure of chitosan [361].

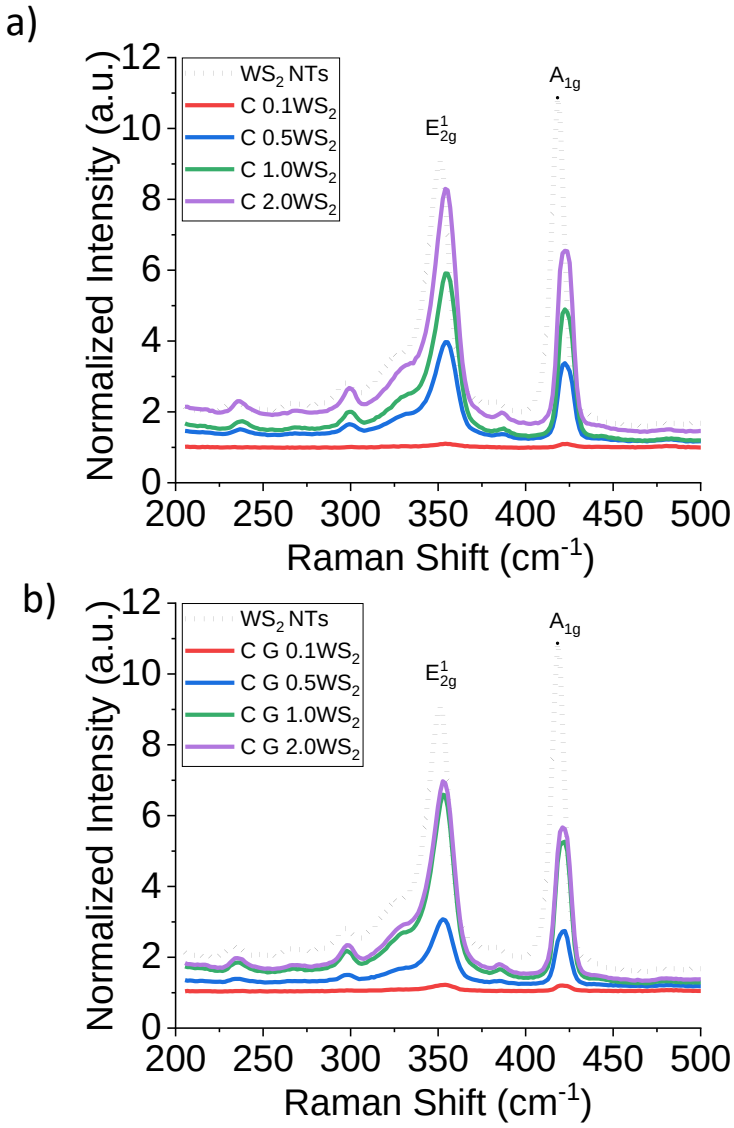

Figure 6.8 Raman spectra of WS_2 NTs and composites of a) chitosan and WS_2 NTs and b) CG and WS_2 NTs showing the E^1_{2g} and A_{1g} modes.

Raman spectroscopy was also used to try and identify changes in chemical structure of the composites through detection of the vibrational frequencies of the WS_2 NTs. Figure 6.8 shows the characteristic modes for WS_2 NTs, E^1_{2g} and A_{1g} at 351.1cm^{-1} and 419.0cm^{-1}. These are the most prominent Raman modes found in the spectra associated with the in-plane vibrations of chalcogen atoms and out-of-plane vibrations of chalcogen and transition metal atoms, respectively, as discussed in previous chapters [300].

The full Raman spectra (200cm^{-1} to 3000cm^{-1}) of chitosan, glycerol and composites of chitosan and WS_2 NTs with and without glycerol are shown in Appendix Figure A6, however due to the significant Raman active modes in WS_2 NTs, chitosan and glycerol peaks could not be determined due to signal to noise ratio. The prominent peak positions for the WS_2 NTs listed in Table 6.5. The E^1_{2g} and A_{1g} modes are indistinguishable for lower WS_2 NTs (0.1wt%) loadings, in comparison to higher loadings in Figure 6.8. However, the ratio of the intensity of the $E^1_{2g}$to A_{1g} modes (IE^1_{2g}/ A_{1g}) (Table 6.5) identifies increases when the NTs are added to chitosan and the CG matrix, along with a blueshift of both peak positions.

Table 6.5 Peak positions for the E^1_{2g} and A_{1g} modes and the ratio of E^1_{2g} to A_{1g} peak intensities for WS_2 NTs and composites of WS_2 NTs with chitosan and with CG.

Sample	Wavenumber (cm^{-1})		$I E^1_{2g}/I A_{1g}$
	E^1_{2g}	A_{1g}	
WS_2 NTs	350	419	0.83
C 0.1WS_2	354	423	1.00
C 0.5WS_2	355	423	1.18
C 1.0WS_2	355	423	1.20
C 2.0WS_2	355	423	1.27
C G 0.1WS_2	354	421	1.02
C G 0.5WS_2	353	422	1.11
C G 1.0WS_2	353	422	1.25
C G 2.0WS_2	353	422	1.23

Typically, the main Raman modes E_{2g} and A_{1g} are used to distinguish WS_2 structures as a function of the number of layers, it is known that the peak positions are affected by several factors. The E^1_{2g} mode is very sensitive to uniaxial strain while doping can change the A_{1g} mode of vibration [362, 363]. In this instance, it is likely

the significant changes in intensity and A_{1g} peak position is due to the surface modification of the WS_2 NTs and interaction with chitosan and glycerol. Additionally, Deka et al. [364] suggested the E^1_{2g} vibration is suppressed due to dispersion of NTs in confined chitosan and glycerol matrices. $IE^1_{2g}/\ A_{1g}$ (Table 6.6) decreases for CG with 2wt% WS_2 NTs, evidence the WS_2 NTs are less well dispersed and interacted poorly with chitosan and glycerol, in agreement with our previous data.

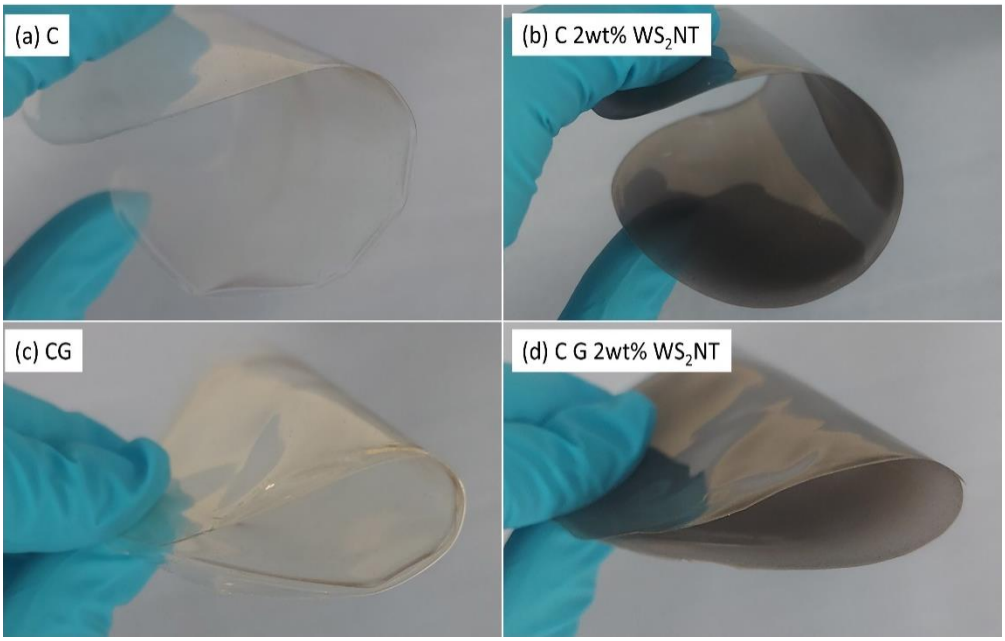

Figure 6.9 a) photographs showing the increased flexibility of chitosan films containing glycerol and WS_2 NTs a) chitosan, b) composites of chitosan and WS_2 NTs, c) CG and d) composite of CG and 2wt% WS_2 NTs.

The application of chitosan-based films in food packaging requires a strong, flexible and relatively tough film, all these properties can be achieved by the inclusion of WS_2 NTs to a CG matrix. The photographs in Figure 6.9 a) show how brittle chitosan Additionally, it is highly desirable that such films are also good barriers to different gases and have some degree of antibacterial efficacy.

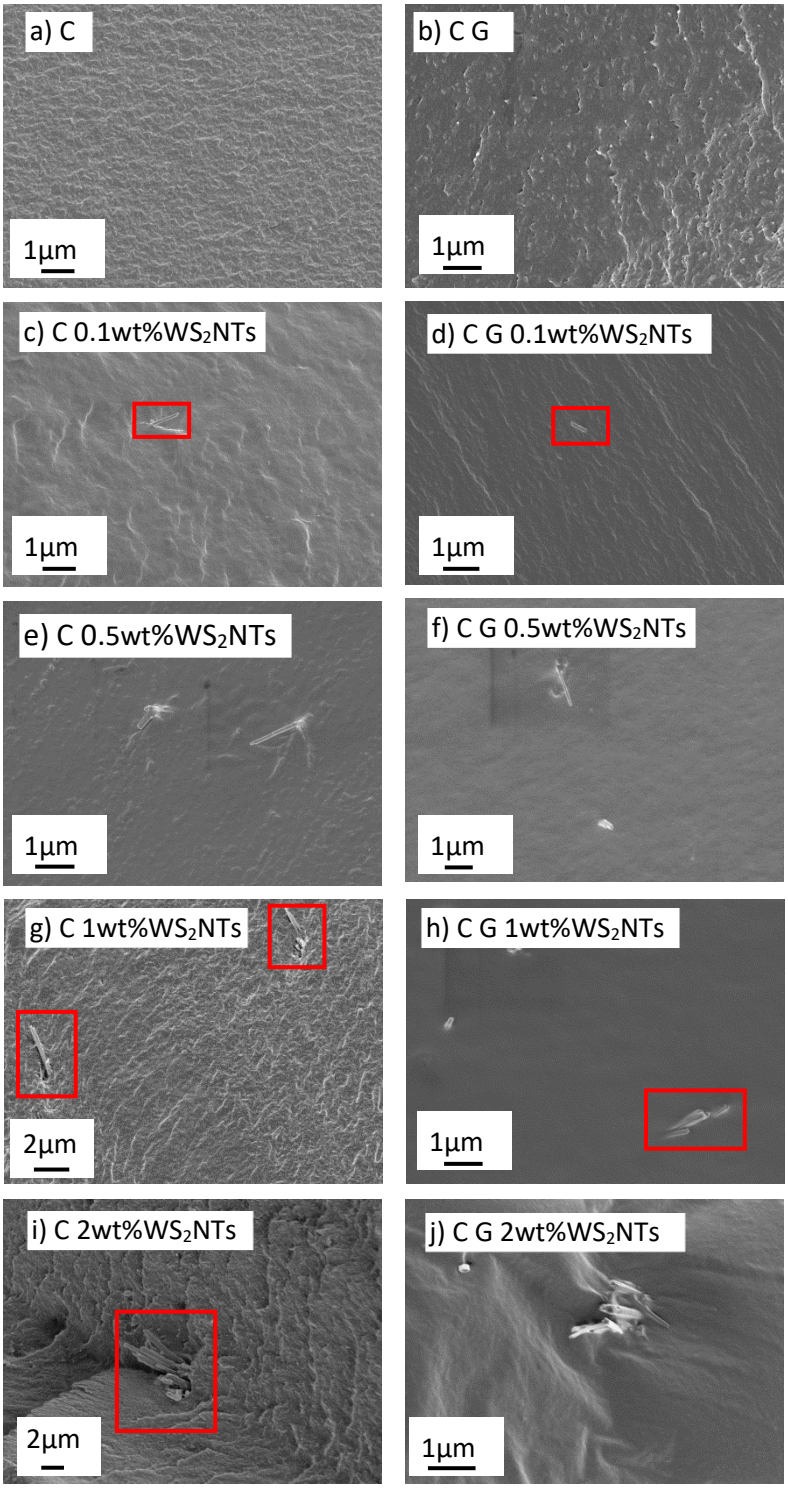

Figure 6.10 SEM micrographs of Chitosan WS_2 composites in comparison to Chitosan WS_2 Glycerol composites of corresponding wt% WS_2 NTs.

The microstructure determines the mechanical, physical and barrier properties of the film. Figure 6.8c-d) show the influence of addition of glycerol and WS_2 NTs on the flexibility of the chitosan film. The impact of the plasticising effect of glycerol on chitosan is clear as the brittle chitosan can be flexed without breaking or causing permanent damage to the film's structure.

SEM was used to examine cryo-fractured cross-sections through the film thickness for all chitosan composite films shown in Figure 6.10 WS_2 NTs were widely shown to disperse effectively in chitosan and chitosan glycerol composites at wt% <1wt% WS_2 NTs. However, the interfacial interaction between NTs surface and chitosan matrix can clearly identify limited interaction with gaps surround NTs surface (Figure 6.10g,i) in the cryo-fractured film. While in comparison, corresponding composites containing glycerol (Figure 6.9 h,j) identify a significant increase interaction with NTs surface. For the 2.0wt% WS_2 NT loading agglomerations of NTs can be seen, Figure 6.9i). The addition of glycerol to chitosan (Figure 6.9 j) reveals a change in surface to a more cohesive texture possibly due to the distribution of glycerol in the chitosan matrix. It may be that at 20% glycerol phase separates in chitosan to some extent [365].

The Zeta potential was used to assess the surface charge of the composites as this property is known to have an impact on the antimicrobial activity of polymer films. Neat chitosan films, Figure 6.11, had a neutral charge which correlated with the pH value of the samples at approximately 6 [366, 367]. The neutral charge is a consequence of the protonation of the amine functionalities. The WS_2 NTs had a significant negative charge, a value of -26.79±0.4mV, as previously discussed in

Chapter 5 [328]. The composites of chitosan and WS_2 NTs were positively charged due to presence of the protonated amino group ($–NH^{3+}$) of chitosan induced by the incorporation of the NTs. The zeta potential decreased with increasing WS_2 NTs loading up to 2wt%, behaviour attributed to less well dispersed NTs in the chitosan matrix.

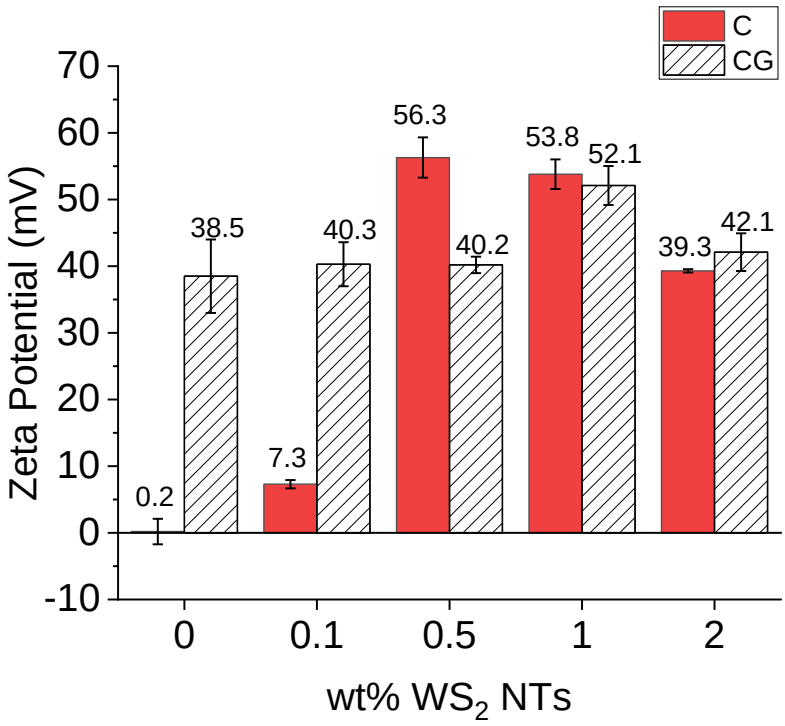

Figure 6.11 ζ potenial values for chitosan alone in comparison to composites of chitosan and WS2 NTs with (CG) and without glycerol.

The addition of glycerol, which has a positive charge of 5.26±0.8mV and when added to the chitosan matrix results in a significantly higher positive surface charge as the functional groups of chitosan interact with the hydroxyl group of glycerol, as reported in the FTIR data presented earlier. The change of surface charge of the chitosan film on inclusion of WS_2 NTs up to 1.0wt% combined with the addition of glycerol results in a reduction in the zeta potential. This is a consequence of the

insertion of glycerol (plasticizer) molecules in between the chitosan chains, resulting in partial neutralisation and net zeta potential [342]. However, at higher WS_2 NTs loading, the added ions help counterbalance the effect of glycerol in reducing the zeta potential of the solution, leading eventually to an increase in the zeta potential of the solution.

A measure of the barrier properties of these films to various gases is crucial so as to evaluate the preservation effects of products and their intended use, such as in food packaging or a material to promote wound healing [368]. Lower oxygen and carbon dioxide permeability is beneficial for food packaging, while a moist environment gas exchange is desired. Oxygen, carbon dioxide and water vapour permeability ($P'O_2$, $P'CO_2$, and P'WV, respectively) values for chitosan and composites of chitosan and WS_2 NTs with and without glycerol were measured and the values obtained listed in Table 6.6. The inclusion of WS_2 NTs results in a decrease in oxygen permeability by approximately 50% for all composites, an outcome also related to the excellent dispersion of the NTs in the chitosan matrix.

Table 6.6 Permebility coefficient for oxygen (P'O2), carbon dioxide (P'CO2) and water vapour (P'WV) for chitosan, CG and composites of chitosan and WS_2 NTs with and without glycerol.

Sample	Permeability Coefficients @ 23 °C, 65% R.H.		
	P'O_2 [$cm^3/(m^2 \cdot 24h) \cdot \mu m$]	**P'CO_2 [$cm^3/(m^2 \cdot 24h) \cdot \mu m$]**	**P'WV [$g/(m^2 \cdot 24h) \cdot \mu m$]**
C	1,196	1,044	14,291
C 0.1 wt% WS_2	481	128,384	18,237
C 0.5 wt% WS_2	405	126,082	17,405
C 1.0 wt% WS_2	573	124,072	15,311
C 2.0 wt% WS_2	587	160,069	19,593
CG	4,764	2,269	N.D.*
CG 0.1 wt% WS_2	N.D.*	223,946	16,210
CG 0.5 wt% WS_2	3,007	254	N.D.*
CG 1.0 wt% WS_2	5,617	921	N.D.*
CG 2.0 wt% WS_2	7,266	1,044	1,417

N.D* ppm of water vapour too high in measurement

However, P'O_2 increases with the addition of glycerol as it is a liquid and fills small voids in composite matrix, resulting in an increase of P'O_2 [369, 370]. Conversely, P'CO_2 increases significantly on addition of WS_2 NTs to chitosan, while the further addition of glycerol reverses this trend and better barrier properties against CO_2 are obtained. For CG with the lowest WS_2 NT loading (0.5wt%) the lowest P'CO_2 value of 253.8 $cm^3/(m^2 \cdot 24h) \cdot \mu m$ is achieved, a direct outcome of the network formed due to polyelectrolyte complex formation. These results agree with previous reports where it was shown that WS_2 TMDs can contribute to highly enhanced gas adsorption

properties [371-373]. The limitations of chitosan as a barrier to moisture are well documented and the P'WV values obtained are typical, behaviour due to the hydrophilic nature of this polysaccharide. The addition of WS_2 NTs to chitosan did not yield any significant change in P'WV. Moreover, the addition of glycerol to chitosan resulted in a significantly high reading, to ppm level of water vapor and too high to be measured with the instrument available. However, for the composites of CG and 2.0wt% WS_2 NTs, P'WV decreased by about 90% to a value of 10% of that measured for the chitosan film alone. This excellent enhancement in water barrier properties is due to the interaction of the NTs with the hydrophilic –OH and –NH groups of chitosan and glycerol matrix [374], therefore lowering the available hydrophilic groups for sorption of water vapor on the film surface.

Furthermore, the antibacterial activity of chitosan, WS_2 and corresponding films with glycerol was examined for application in medical and possibly food packaging films. Resazurin assay was used to determine the viability of bacterial cells exposed to chitosan WS_2 NTs composites with and without glycerol. Viable bacteria that are metabolically active reduce resazurin, a blue-purple weak fluorescent compound (excitation: 530-570nm) to resorufin, a pink highly fluorescent compound (emission: 580-590nm). Unviable bacteria lack the ability to reduce resazurin which is characterized by the absence of a colour change and unaltered fluorescence intensity. Composites of chitosan and WS_2 NTs exhibited antibacterial activity against both Gram-positive and Gram-negative bacteria. In *S. aureus*, a significant reduction in bacterial viability was observed over a period of 8 hours (Figure 6.12 a) i) and Table 6.7). However, the introduction of WS_2 NTs has an impartial impact on the antibacterial activity of chitosan, with 85±2% decrease in cell viability with the

exception of 0.1wt% WS_2 loading the antibacterial performance varied as indicated by the large error bar. In uropathogenic *E. coli*, antibacterial activity increased with increasing concentrations of WS_2 in chitosan composites was observed (Figure 6.12 a ii), Table 6.7). Observed survival rates, suggest that chitosan WS_2 composites strong antibacterial agents against *P. fluorescens* as seen by the sharp decline in bacterial viability with increased concentration NTs (Figure 6.12a iii). Therefore, as indicated by % decrease in bacterial viability (Table 6.7), the NTs display varying degrees of antibacterial activity against both Gram-positive and Gram-negative bacteria. Chitosan is known to be antibacterial in nature due to the interaction of its cationic amino group with the anionic bacterial cell wall [375]. Recent studies report the antibacterial potential of WS_2 nanoparticles due to its ability to adhere to bacterial cell wall and compromise the organisation of this cell structure [376] Therefore, this study indicates that a combination of chitosan and WS_2 NTs into a stable nanotube could potentially enhance antibacterial activity.

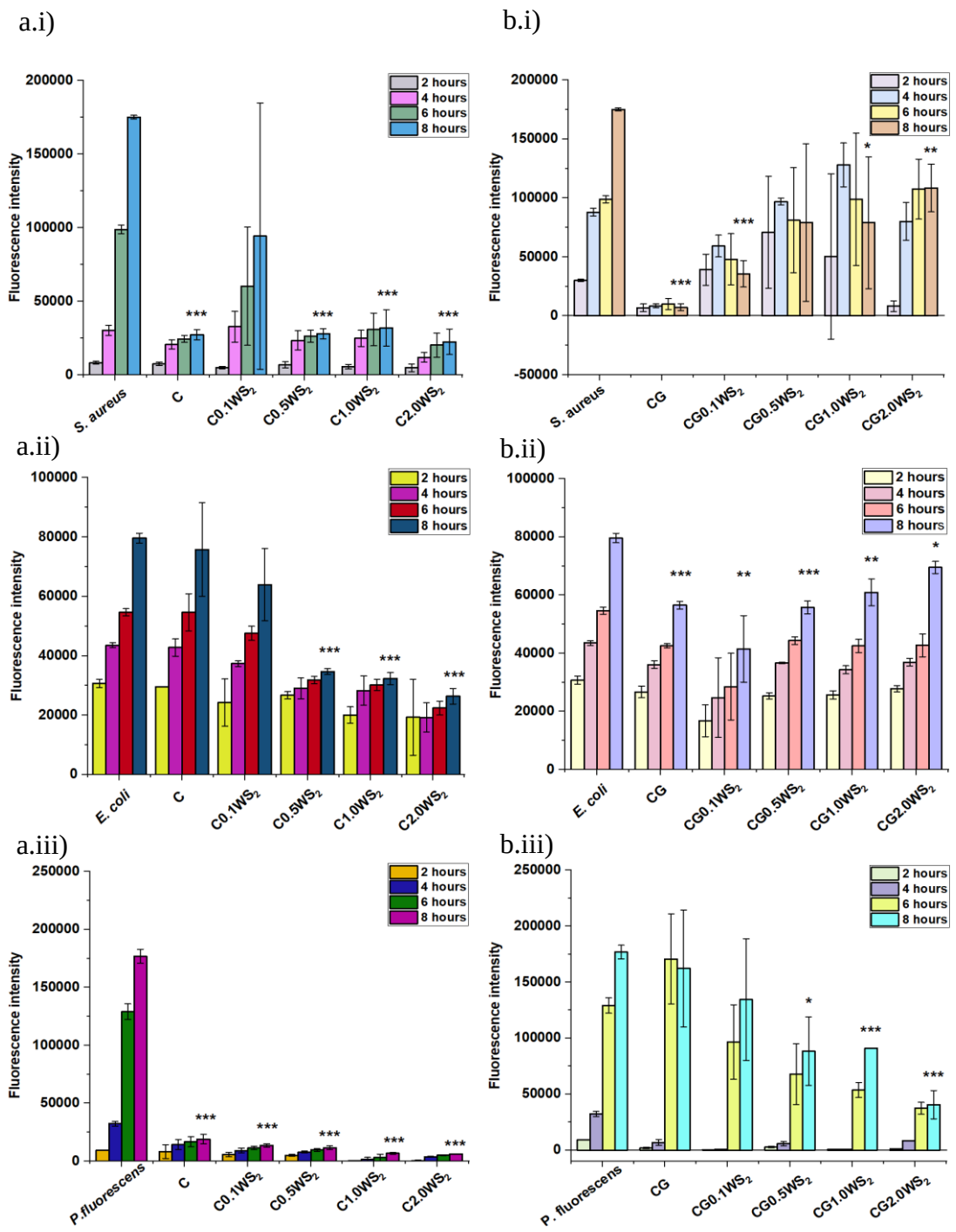

Figure 6.12 Antibacterial effect of bacterial a) Chitosan and WS_2 NTs composites and b) Chitosan Glycerol WS_2 composites viability against **i))** *S. aureus* (, **(i))** *E. coli*, **iii))** *P. fluorescens* viability over a period of 8 hours. Decrease in fluorescence intensity indicating unviable bacteria for each NTs were calculated every 2 hours in comparison with positive control – (*=p<0.05, **=p<0.01, ***=p<0.001).

Table 6.7 Percentage decrease in bacterial viability from relative fluorescence intensity measured after 8 hours for Chitosan and Chitosan WS_2 NTs films.

Sample	% Decrease in viability		
	S. aureus	***E.coli***	***P.fluorescens***
Chitosan	84	15	89
Chitosan 0.1wt% WS_2 NTs	55	26	92
Chitosan 0.5wt% WS_2 NTs	84	29	93
Chitosan 1.0wt% WS_2 NTs	82	38	96
Chitosan 2.0wt% WS_2 NTs	87	51	97

Table 6.8 Percentage decrease in bacteria viability from relative fluorescence intensity measured after 8 hours for Chitosan Glycerol and Chitosan Glycerol WS_2 NTs films.

Sample	% Decrease in viability		
	S. aureus	***E. coli***	***P.fluorescens***
Chitosan Glycerol	96	29	17
Chitosan Glycerol 0.1wt% WS_2 NTs	80	64	28
Chitosan Glycerol 0.5wt% WS_2 NTs	55	30	31
Chitosan Glycerol 1.0wt% WS_2 NTs	55	23	49
Chitosan Glycerol 2.0wt% WS_2 NTs	38	13	57

Furthermore, the antibacterial effect of chitosan WS_2 NTs containing glycerol plasticizer was evaluated. In the presence of glycerol in chitosan films with lower concentrations of WS_2 showed antibacterial activity against *E. coli* and *S. aureus*, however, with increasing concentrations of WS_2, NTs an increase of in bacterial viability was observed (Figure 6.12b i), ii), Table 6.8). In comparison to the NTs

without glycerol, addition of glycerol could potentially alter the structure and active sites of the NTs by filling the space between hydrogen bond thereby weakening chitosan strength and reducing the antibacterial activity of WS_2 [377]. The bacterial-growth-favouring properties of chitosan glycerol films with increasing concentrations of WS_2 NTs may also be due to the ability of *E. coli* and *S. aureus* to utilize glycerol as carbon source via the dehydrogenation and/or phosphorylation pathways [378].

Since the antibacterial assay is performed in a multi-well plate, bacteria can grow both in planktonic state and by producing biofilms. As biofilms typically form a surface barrier, bacteria may not be in direct contact with the active sites of NTs, thereby protecting bacteria from the antibacterial activity of chitosan and/or chitosan WS_2. However, in the absence of WS_2, chitosan glycerol exhibited a notable decrease in *E. coli* and *S. aureus* viability (Figure 6.12 b i), ii), Table 6.8). In contrast, chitosan glycerol with increasing WS_2 decreased the viability of *P. fluorescens* (Figure 6.12 b iii), Table 6.8). As *P. fluorescens* is a non-lactose/lactic-acid fermenter, it is unable to use glycerol as a carbon source for survival, and therefore is sensitive to the antibacterial action of chitosan and/or chitosan-WS_2 composite.

6.3 Conclusion

In this work Chitosan based nanocomposite films with loadings of 0.1-2.0wt% loadings of WS_2 NTs, with and without glycerol as plasticiser were produced by solvent casting technique and were studied for understanding of intermolecular bonding as well as structural, thermal and mechanical properties as well as gas barrier and antimicrobial efficiency for application in areas such as packaging or medical devices.

WS_2 NTs were found to effectively disperse within the chitosan matrix, while glycerol enhanced this dispersion up to 1.0wt% WS_2 while enhancing the interfacial interaction forming a strong intermolecular hydrogen bonding as well as involving the amide groups to form a polyelectrolyte complex with NTs interaction with chitosan and glycerol.

The impact of WS_2 NTs in chitosan (without glycerol) identify minimal impact on the mechanical properties of chitosan films. It was found that the addition of 1.0wt% WS_2 NTs to the chitosan glycerol matrix producing a significantly stronger and tougher material. This is deemed due to the combined effect of NTs and plasticiser, though hydrogen and amine bonding network within he composites, allowing for effective stress-transfer in the reinforcement phase and improving the mechanical properties.

The addition of WS_2 NTs to chitosan matrix identifies significant impact on the gas barrier properties, with a 50% reduction of oxygen permeability, while the addition of glycerol and WS_2 to chitosan effectively reduces the carbon dioxide permeability by 80% in comparison to chitosan only. Additionally, all composite films showed antimicrobial properties, where WS_2 NTs identified, at times, an enhancement of antimicrobial efficacy against both Gram-positive and Gram-negative bacteria. Therefore, the developed composite films can undergo further application in food packaging or possibilities for medical applications such as wound dressings.

Chapter 7: Conclusions and Recommendations for Future Work

7.1 Conclusions

There continues to be intense research interest in the fundamental study of the properties and applications of tungsten disulphide nanotubes (WS_2 NTs) across a range of scientific and engineering fields, including for the enhancement of biopolymer properties, specifically for the food packaging and medical device sectors.

This aim of this PhD project was to investigate the fundamental properties of WS_2 NTs and examine the dispersion and distribution of these NTs in two model biopolymers, one synthetic - poly(lactic acid) (PLA) and the other derived from the naturally occurring polymer chitin - chitosan. A particular focus of the work was on the optimisation of interfacial interactions between the WS_2 NTs and the PLA matrix. To promote interfacial interactions with PLA silane functionalisation of the WS_2 NTs was developed. In a further aspect, the effect of the shear forces applied during melt mixing PLA and WS_2 NTs on the aspect ratio of the nanotubes was studied. The effect of polyelectrolyte complexation on the properties of composites of chitosan and WS_2 NTs with and without glycerol was also explored.

Critical understanding of the interactions possible between both biopolymers and WS_2 NTs was achieved from extensive characterisation of WS_2 using a range of techniques. The structural composition and crystallinity of the NTs was studied using a combination of SEM/TEM, as well as XRD and Raman. The NTs were shown to be highly crystalline and multiwalled (8-28 walls with a consistent wall spacing of 0.65 nm) nanostructures having widths in the range 52−110 nm and lengths in the range 2.45−65.6 μm. The thermal stability of WS_2 NTs was extensively studied using TGA-

MS and it was discovered that the WS_2 NTs were thermally stable in an inert atmosphere and in air atmosphere up to 400°C. Further heating in the region between 400 and 550 °C induced oxidation of tungsten via the formation of SO_2/SO gas, ultimately producing yellow micron sized WO_3 particles. This confirmed that WS_2 NTs can be used as a functional nanofiller for mixing with polymer melts up to 400°C without thermally inducing damage to the NTs. Additionally, analysis of the surface chemistry of the NTs by XPS and STEM-EDS detected oxygen and carbon, determined to be physiosorbed on the surface of NTs from atmospheric contamination as well as from inside the layers of the tubular nanostructure. Critically, this gives the NTs a hydrophilic (negatively charged) surface.

To date, there have been limited studies where composites of PLA and WS_2 NTs have been prepared using melt mixing methods, such as extrusion, a sustainable continuous process that does not require the use of organic solvents. For the composites of PLA and WS_2 NTs prepared by melt mixing in a twin-screw extruder, it was found the WS_2 NTs are readily dispersed and distributed into PLA matrix, however, the shear stresses applied during extrusion processing resulted in significant damage to NTs and a reduction of the aspect ratio (AR) of the NTs of >95%. The lengths of NTs were reduced to between 200 and 800 nm. Consequently, the ability for NTs to reinforce PLA was significantly limited and no change in mechanical properties of PLA were obtained. WAXS/SAXS analysis confirmed a homogeneous distribution of the WS_2 NTs in the PLA post-extrusion. Furthermore, the interaction between the NTs and polymer was determined to be minimal. Although, the WS_2 NTs were are an effective nucleating agent, even in a highly amorphous PLA, a significant increase in the T_c of PLA with increasing WS_2 NT loading was recorded as was a slightly higher degree of crystalline content. POM further established the dramatic

increase in the rate of crystallisation at 145°C from 9 min for extruded PLA to approximately 45s for WS_2 NT filled PLA.

Although, the WS_2 NTs were shown to be effectively dispersed in the PLA matrix and act as nucleating agents for this polymer, the shear forces exerted on the NTs during compounding were too severe such that mechanical reinforcement of the polymer may not be possible if the composites were prepared by this route. Furthermore, it is clear that strong interfacial interactions between the NTs and PLA are required if effective stress transfer at the interface is allowed.

To enhance the interfacial interaction between the WS_2 NTs and PLA, the possibility for exploitation of oxygen and carbon functionalities on the surface of NTs was further examined, and solvent casting was adopted as the composite preparation method to preserve the AR of the NTs. (3-aminopropyl)triethoxysilane (APTES) was successfully grafted to the surface of the WS_2 NTs in ratios of 1:1, 1:2 and 1:4 WS_2 NTs: APTES. Extensive characterisation of the APTES functionalised NTs showed there was a greater concentration of APTES bound to the surface of the WS_2 NTs with increasing APTES concentration. XPS studies found that the APTES formed siloxane networks bound to the surface of the NTs via surface oxygen and carbon moieties on the WS_2 NTs. This was further confirmed from FTIR analysis which revealed shifting of Si-O-Si vibrations, as well as the evolution of new bands associated with Si-CH_2-CH_2, symmetric and asymmetric and NH^{3+} deformation modes. Further evidence from a combination of Raman spectroscopy, TGA, as well as Zeta potential measurements confirmed a high level of APTES grafting on the NT surface.

APTES functionalised WS_2 NTs were found to be most effectively dispersed while still in solution and produce a homogeneous composite film. STEM-EDS

analysis showed that APTES modification of the WS_2 NT surface significantly improved the extent of WS_2 NT dispersion in the PLA matrix and promoted strong interfacial interactions between the NTs and the polymer. Most interestingly, the tensile mechanical properties of the composites of functionalised NTs and PLA composites increased significantly relative to the unfilled polymer, including the elongation at break, by 600%, and the tensile toughness of PLA from 1.0kJm^{-3} to 6.8kJm^{-3} (600%) on inclusion of WS_2 NTs: APTES (1:4), while maintaining the stiffness and strength of PLA. This behaviour is due to presence of the pendant amine and hydroxyl groups of APTES promoting strong interfacial interactions with the polymer matrix. This work highlighted the effective interaction of WS_2 NTs and polymer though the promotion of surface functionalities using hydroxyl and amine functionality.

Unfunctionalized WS_2 NTs were shown to be easily dispersed another biopolymer, therefore WS_2 NTs were studied as a functional filler in chitosan both with and without 20wt% glycerol added as a plasticiser. Extensive ATR-FTIR mapping combined with examination of SEM images found the WS_2 NTs effectively disperse and distribute within the chitosan matrix, while glycerol enhanced the dispersion even further for up to 1.0wt% WS_2 NTs Additionally, the glycerol plays a major role in the interfacial interactions between the NTs and chitosan, forming both strong intermolecular hydrogen bonds as well as interacting with the amide groups of chitosan to form a polyelectrolyte complex where the NTs interact with the chitosan and glycerol. The strong interfacial interactions generated were translated into the improved mechanical properties including an increase of 74% in film toughness, 40% increase in maximum tensile stress as well as a 46% increase in elongation at break in comparison to neat chitosan.

The addition of WS_2 NTs to chitosan matrix also had a significant impact on the gas barrier properties, with a 50% reduction in oxygen permeability for all composites, while the inclusion of glycerol and WS_2 NTs to chitosan effectively reduces the carbon dioxide permeability by 90% in comparison to chitosan only. Additionally, all composite films showed some degree of antimicrobial efficacy against both Gram-positive and Gram-negative bacteria.

That the inclusion of WS_2 NTs in chitosan resulted in improvements in tensile mechanical properties, particularly ductility and toughness and, reduced permeability to oxygen and moisture combined with antimicrobial efficacy against Gram positive and Gram-negative bacteria. This provides strong evidence that WS_2 NTs filled chitosan may have application as a sustainable source of food packaging.

7.2 Recommendations for Future Work

This work described the outputs from a fundamental study of the structure and properties of WS_2 NTs and yielded significant knowledge and understanding around the requirements for effective dispersion and enhanced interfacial interactions with two model biopolymers, PLA and chitosan biopolymers. This study was the first to report the effective silane functionalisation of WS_2 NTs as a route to promoting interfacial interactions with PLA. It was also the first time that the polyelectrolyte complexation of negatively charged WS_2 NTs and positively charged chitosan was reported. However, the following are studies are recommended for further research and interest.

The melt mixing of composites of PLA and WS_2 NTs highlighted significant limitations in that the shear forces applied during compounding significantly degraded the aspect ratio of the NTs, by > 90%. Therefore, significantly more research is required to optimize the extrusion process such that effective dispersion and distribution of the NTs is achieved in the PLA matrix without the NT aspect ratio being reduced. Further experiments where modification of the screw profile, screw speed as well as the temperature profile along the extruder are required. It may be that the extensional forces applied during single screw extrusion could be more effective at dispersing and distributing the NTs in the PLA matrix.

Concerning the silane functionalisation of WS_2 NTs, further examination of the ratio of WS_2 NTs to silane agent should be explored. While improvements in certain properties were achieved at low NT loading, it cannot be assumed that the system was optimised. Additionally, the functionalisation of WS_2 NTs should be attempted using other silane, including vinyltrimethoxysilane (VTMS) or (3 mercaptopropyl)trimethoxysilane (MPTS). There is a whole catalogue of cheap

silanes, already used as sizing agents for glass fibres which could also react with the surface of the NTs via the siloxane and leave a free pendant group (e.g. vinyl, thiol or amine) free to react with the polymer of interest.

With regards polyelectrolyte complexation of chitosan and WS_2 NTs, different plasticizer types and concentration should be explored to find the optimum formulation where complex formation is the strongest. The antibacterial study of composites of CG and WS_2 NTs should be extended to include a broader range of Gram positive and Gram-negative bacteria. It would also be interest to investigate if the same composites displayed any antifungal or antiviral efficacy. Furthermore, as composites of PLA and WS_2 NTs composites have potential for use in a range of biomedical applications, such as bioresorbable polymeric scaffolds, further in-vitro toxicity and antimicrobial/antiviral studies must be completed

PLA and chitosan are well known for their biocompatibility and biodegradable properties. Therefore, it would be beneficial to perform biodegradation studies in order to examine the impact that inclusion ofWS_2 NTs in the PLA and chitosan matrix has on biodegradability, as well as identifying the impact of APTES surface modification and the potential impact of glycerol on the biodegradation mechanism of chitosan. This would develop the understanding and any environmental impact these novel composites may have if retained in the environment

Journal Publications and Conference Presentations

- Magee, E., et al., *WS_2 Nanotubes as a 1D Functional Filler for Melt Mixing with Poly(lactic acid):Implications for Composites Manufacture.* ACS Applied Nano Materials, 2022. **5**(5): p. 6385-6397.

- Magee, E., et al., *Silane functionalization of WS_2 nanotubes for interaction with poly (lactic acid). Nanoscale. 2023;15(16):7577-90.*

- Magee, E., et al., *Polyelectrolyte Complexation of Chitosan and WS_2 Nanotubes.* Submission to Advanced Materials Interfaces 2023

Conference Presentation

- *WS_2 Nanotubes as a Functional Filler for Biopolymers,* The 17th Pacific Polymer Conference (PPC17), 11-14th Dec 2022.-Presented by Prof. T.McNally

Appendix

Results and Discussion I: WS_2 NTs and Composites of PLA

XPS Deconvoluted graphs and corresponding atomic percentages

Table A.1 WS_2 NTs XPS deconvoluted data

O 1s region		
Binding energy (eV)	% of region	Bonding environment
530.94	6.6	WO_3
532.28	71.8	O-C
533.61	21.6	O*-(C=O)
C 1s region		
Binding energy (eV)	% of region	Bonding environment
284.09	48.6	C-C/C-H
285.45	41.8	C-O
286.98	4.1	C=O
289.23	5.5	O=C-O
S 2p region		
Binding energy (eV)	% of region	Bonding environment
162.38	50.0	S $2p_{3/2}$ - WS_2
163.56	50.0	S $2p_{1/2}$ - WS_2
W 4f & W 5p3/2 region		
Binding energy (eV)	% of region	Bonding environment
32.75	35.6	W $4f_{7/2}$ - WS_2
34.89	34.0	W $4f_{5/2}$ - WS_2
36.05	3.0	W $4f_{7/2}$ - WO_3
38.19	2.9	W $4f_{5/2}$ - WO_3
38.56	24.5	W $5p_{3/2}$

Table A.2 WS_2 NTs XPS deconvoluted data

O 1s region		
Binding energy (eV)	% of region	Bonding environment
530.59	77.6	O=C/ WO_3
532.88	21.4	O-C
533.21	1.0	O*-(C=O)
C 1s region		
Binding energy (eV)	% of region	Bonding environment
285.00	77.8	C-C/C-H
286.69	11.1	C-O
289.08	11.1	O=C-O
W 4f & W 5p3/2 region		
Binding energy (eV)	% of region	Bonding environment
35.79	51.2	W $4f_{7/2}$ - WO_3
37.93	48.8	W $4f_{5/2}$ - WO_3
Na 1s region		
Binding energy (eV)	% of region	Bonding environment
1071.78	100.0	Na_2O/NaOH/Na

Results and Discussion II: APTES Functionalised WS_2 NTs and Composites of PLA

Table A.3. FTIR tabulated Peak wavenumber assignment of APTES in comparison to WS_2-APTES samples

Peak Wavenumber cm^{-1}	**Neat APTES**	**Peak Wavenumber cm^{-1}**	**WS_2 APTES**
3383 2974	NH_2 stretching	3348 3270	N-H vibrations
2927 2883	Asymmetric CH Symmetric CH	2925 2860	Asymmetric CH Symmetric CH
1604 1483	NH_2 deformation bending	1628 1570 1470	scissor modes of -NH_2 (shoulder) asymmetric -NH_3^+ symmetric -NH_3^+
1442 1390	O-H bending	1383	O-H bending
1294 1165	C-O stretching	1232 1191	Si-CH_2-CH_2 C-O stretching
1073 765	Asymmetric Si-O-Si Symmetric Si-O-Si	1108 (WS_2: APTES1:1) 1100 (WS_2: APTES1:2) 1092 (WS_2:APTES1:4) 745	Asymmetric Si-O-Si Symmetric Si-O-Si
1100	Si-O-C asymmetric	1012 (WS_2: APTES1:1) 1005 (WS_2: APTES1:2) 999 (WS_2: APTES 1:4)	Si-O-C asymmetric
954 853	Si-OH stretching Si-OH bending	933 (WS_2: APTES 1:1) 929 (WS_2: APTES 1:2) 925 (WS_2: APTES 1:4) 858	Si-OH stretching Si-OH bending
677	N-H bending	690	N-H bending

Table A.4 WS_2 NTs- APTES 1:1 XPS deconvoluted data

C 1s region		
Binding energy (eV)	**% of region**	**Bonding environment**
285	59.2	C-C/C-H
286.19	16.3	C-O
287.74	2.3	C=O
288.8	2.7	O=C-O
285.72	19.5	C-N
O 1s region		
Binding energy (eV)	**% of region**	**Bonding environment**
531.17	8.5	O=C / WO_3
532.51	87.3	O-C / O-Si
534.11	4.2	O*-(C=O)
N 1s region		
Binding energy (eV)	**% of region**	**Bonding environment**
399.54	90.8	N-C (APTES)
401.14	9.2	NR4+
Si 2p region		
Binding energy (eV)	**% of region**	**Bonding environment**
102.6	50.5	Si $2p_{3/2}$
103.21	49.5	Si $2p_{1/2}$
S 2s region		
Binding energy (eV)	**% of region**	**Bonding environment**
226.29	100	WS_2
W 4f region		
Binding energy (eV)	**% of region**	**Bonding environment**
32.43	29.6	W $4f_{7/2}$ - WS_2
34.59	28.3	W $4f_{5/2}$ - WS_2
38.28	29.0	W $5p_{3/2}$
35.2	6.7	W $4f_{7/2}$ - WO_3
37.36	6.4	W $4f_{5/2}$ - WO_3

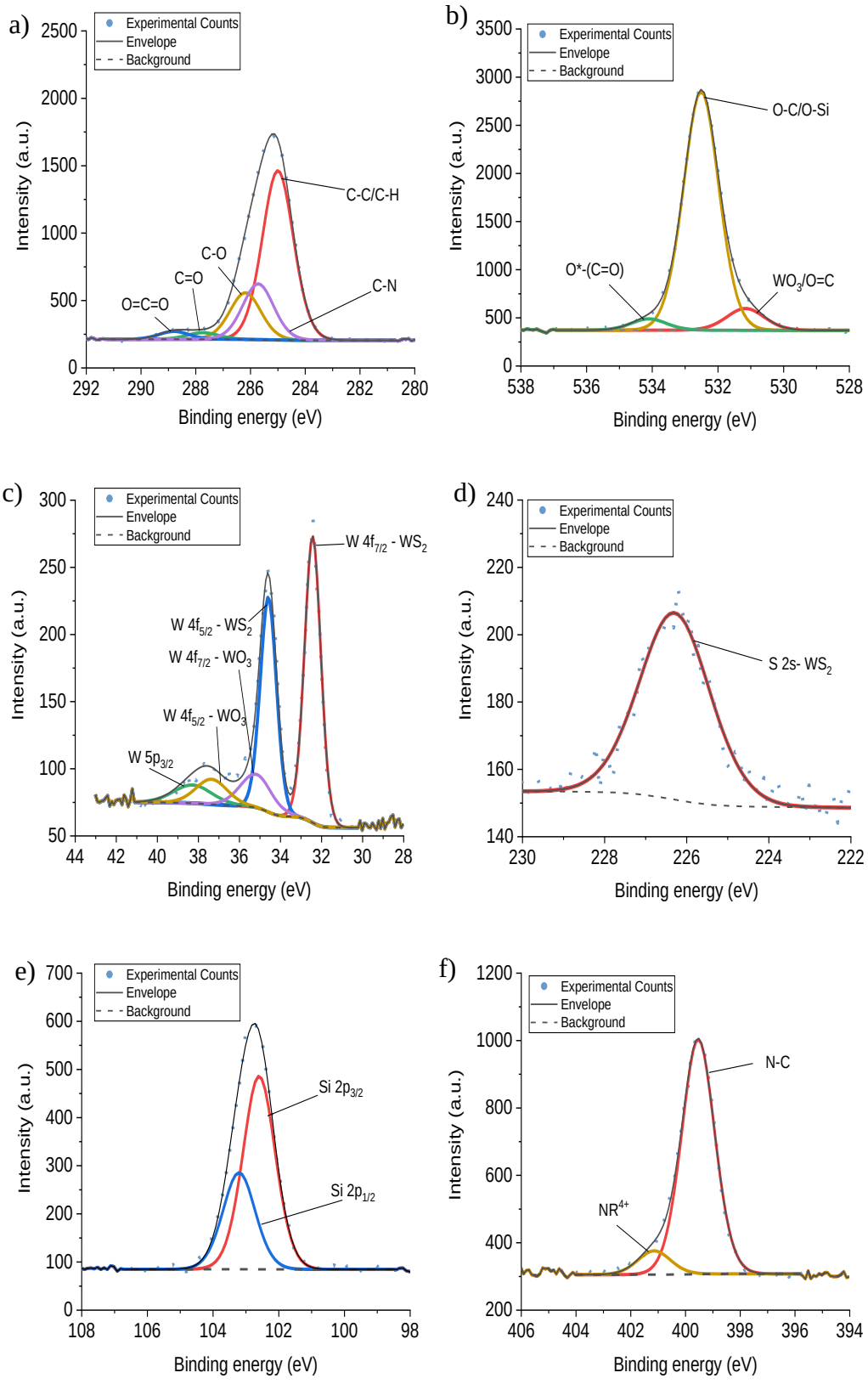

Figure A.1 Deconvoluted XPS spectra a) C1s b) O 1s c) W 4f 1:2, d)Si 2p, e)N 1s f)S 2s regions of XPS spectra for WS_2-APTES 1:1 sample

Table A.5 WS_2 NTs- APTES 1:2 XPS deconvoluted data

C 1s region		
Binding energy (eV)	**% of region**	**Bonding environment**
285	68.3	C-C/C-H
286.44	14.0	C-O
287.74	0.4	C=O
288.8	8.9	O=C-O
285.7	8.4	C-N
O 1s region		
Binding energy (eV)	**% of region**	**Bonding environment**
530.54	2.3	O=C / WO_3
532.34	79.4	O-C / O-Si
533.55	18.3	O*-(C=O)
N 1s region		
Binding energy (eV)	**% of region**	**Bonding environment**
399.51	90.8	N-C (APTES)
401.12	9.2	NR4+
Si 2p region		
Binding energy (eV)	**% of region**	**Bonding environment**
102.48	50.5	Si $2p_{3/2}$
103.09	49.5	Si $2p_{1/2}$
S 2s region		
Binding energy (eV)	**% of region**	**Bonding environment**
226.24	100	WS_2
W 4f region		
Binding energy (eV)	**% of region**	**Bonding environment**
32.28	31.8	W $4f_{7/2}$ - WS_2
34.44	30.3	W $4f_{5/2}$ - WS_2
38.13	31.2	W $5p_{3/2}$
35.05	3.4	W $4f_{7/2}$ - WO_3
37.21	3.3	W $4f_{5/2}$ - WO_3

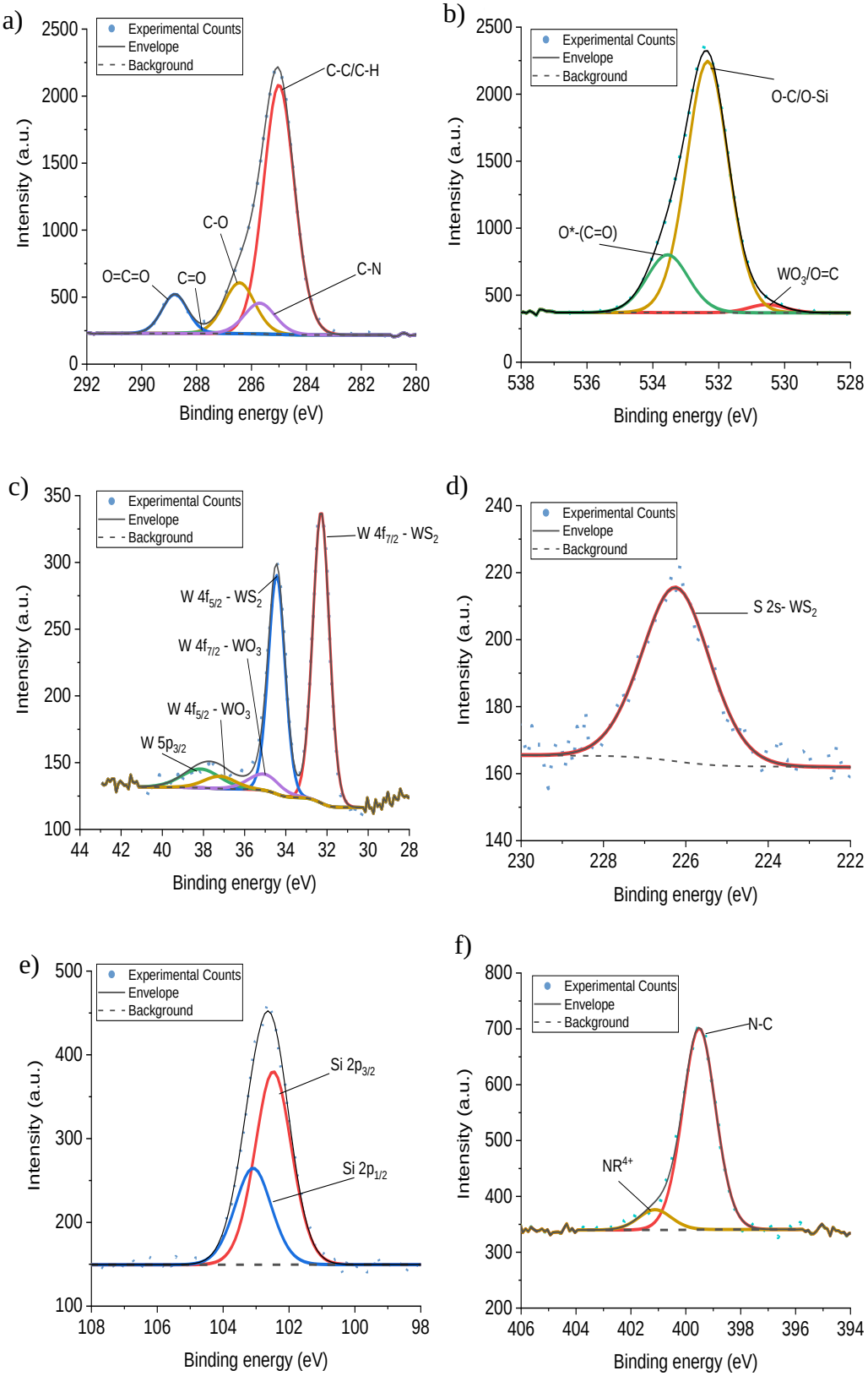

Figure A.2 Deconvoluted XPS spectra a) C1s b) O 1s c) W 4f 1:2, d)Si 2p, e)N 1s f)S 2s regions of XPS spectra for WS_2-APTES 1:2 sample

Table A.6 WS_2 NTs- APTES 1:4 XPS deconvoluted data

C 1s region		
Binding energy (eV)	**% of region**	**Bonding environment**
285	69.0	C-C/C-H
286.44	10.8	C-O
287.74	1.2	C=O
288.8	6.7	O=C-O
285.7	12.3	C-N
O 1s region		
Binding energy (eV)	**% of region**	**Bonding environment**
530.82	3.8	O=C / WO_3
532.35	83.8	O-C / O-Si
533.56	12.4	O*-(C=O)
N 1s region		
Binding energy (eV)	**% of region**	**Bonding environment**
399.42	81.3	N-C (APTES)
401.03	8.3	NR4+
396.66	10.4	W-N
Si 2p region		
Binding energy (eV)	**% of region**	**Bonding environment**
102.44	50.5	Si $2p_{3/2}$
103.05	49.5	Si $2p_{1/2}$
S 2s region		
Binding energy (eV)	**% of region**	**Bonding environment**
226.2	100	WS_2
W 4f region		
Binding energy (eV)	**% of region**	**Bonding environment**
32.3	31.9	W $4f_{7/2}$ - WS_2
34.46	30.4	W $4f_{5/2}$ - WS_2
38.15	31.3	W $5p_{3/2}$
35.07	3.3	W $4f_{7/2}$ - WO_3
37.23	3.1	W $4f_{5/2}$ - WO_3

Results and Discussion III: Composites of Chitosan WS_2 NTs and Glycerol

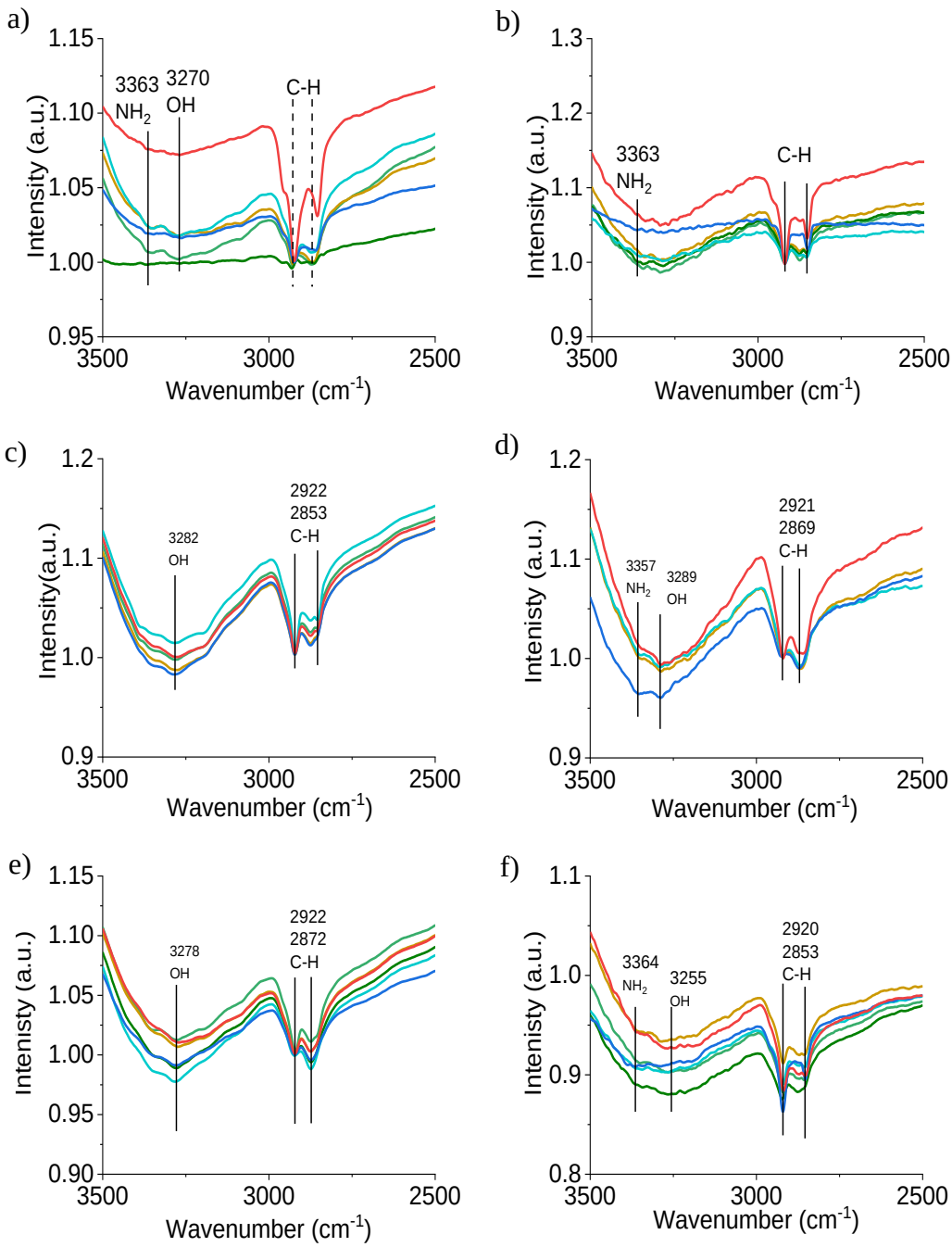

Figure A.3 ATR FTIR region 3500-2500cm^{-1} a) Chitosan, b) Chitosan Glycerol, c) Chitosan Glycerol 0.1wt%WS_2, d) Chitosan Glycerol 0.5wt%WS_2, e) Chitosan Glycerol 1.0wt%WS_2, f) Chitosan Glycerol

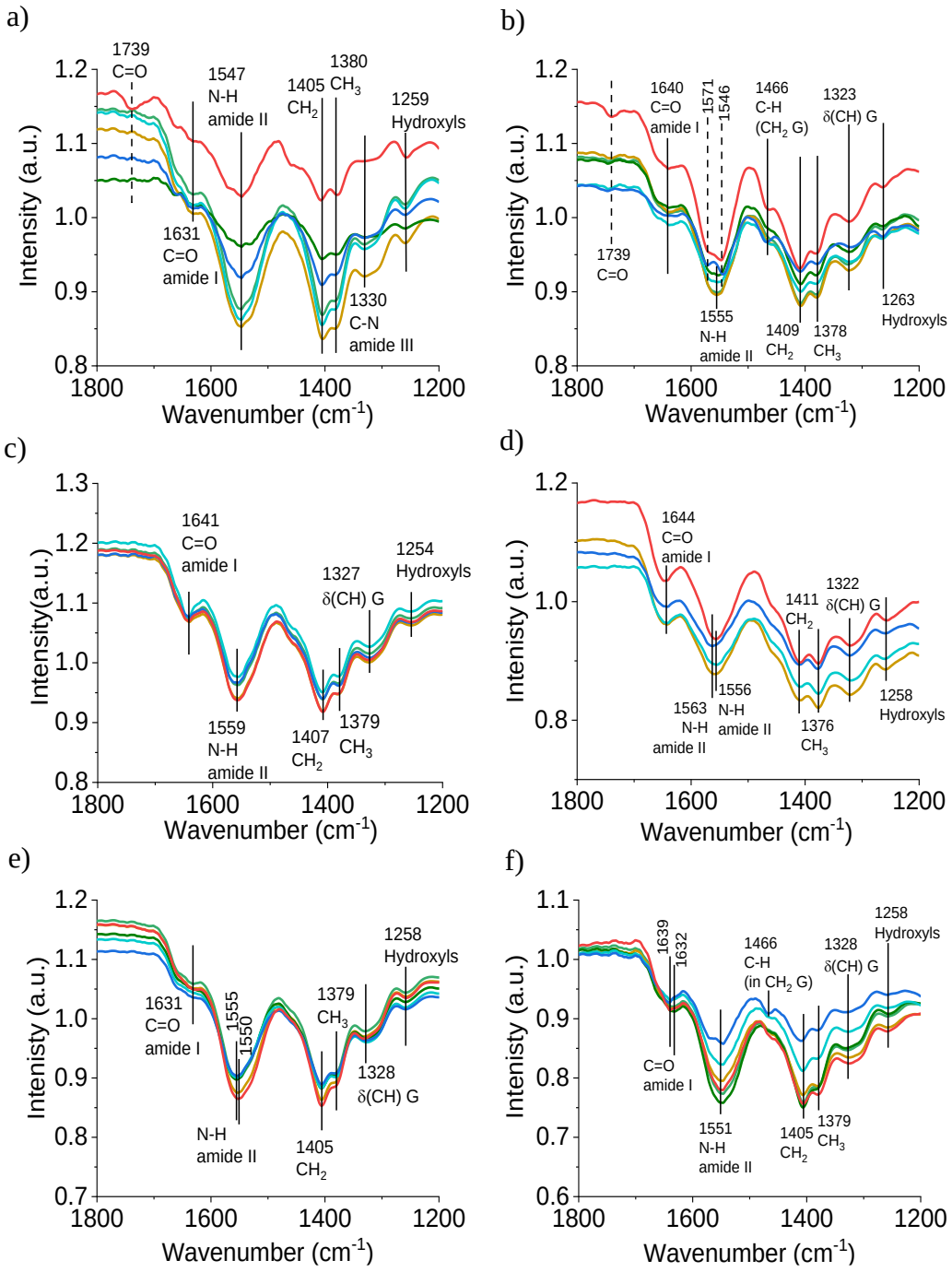

Figure A.4 ATR FTIR region 1800-1200cm^{-1} a) Chitosan, b) Chitosan Glycerol, c) Chitosan Glycerol 0.1wt%WS_2, d) Chitosan Glycerol 0.5wt%WS_2, e) Chitosan Glycerol 1.0wt%WS_2, f) Chitosan Glycerol 2.0wt%WS_2

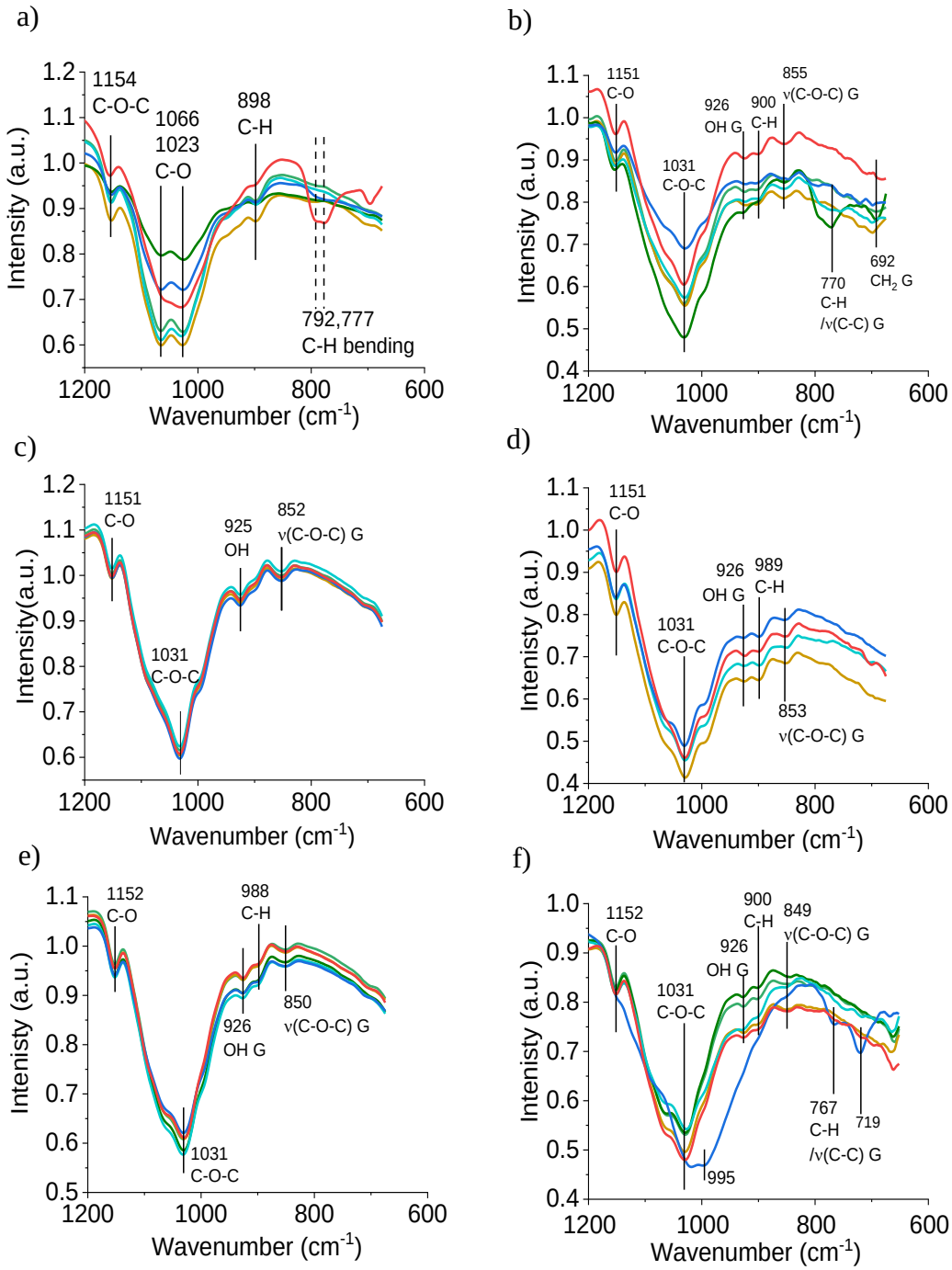

Figure A.5 ATR FTIR region 1200-600cm^{-1} a) Chitosan, b) Chitosan Glycerol, c) Chitosan Glycerol 0.1wt%WS_2, d) Chitosan Glycerol 0.5wt%WS_2, e) Chitosan Glycerol 1.0wt%WS_2, f) Chitosan Glycerol 2.0wt%WS_2

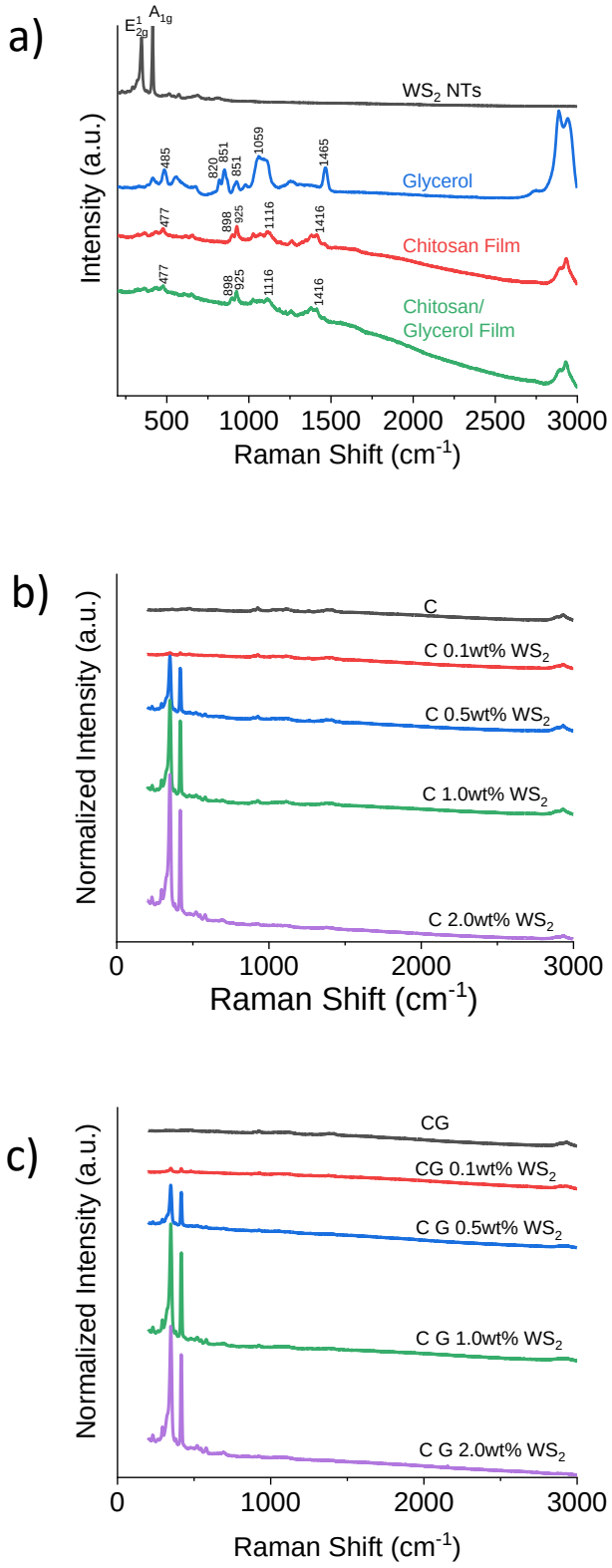

Figure A.6 Raman Spectra a) WS_2 NTs, glycerol. Chitosan film and Chitosan glycerol film. b) chitosan and WS_2 composite films c) Chitosan glycerol and WS_2 films

References

1. Byakodi, M., et al., *Emerging 0D, 1D, 2D, and 3D nanostructures for efficient point-of-care biosensing.* Biosensors and Bioelectronics: X, 2022. **12**: p. 100284.
2. Ealia, S.A.M. and M. Saravanakumar. *A review on the classification, characterisation, synthesis of nanoparticles and their application*. in *IOP conference series: materials science and engineering*. 2017. IOP conference series: materials science and engineering IOP Publishing.
3. Gao, Y. and Z.Y. Tang, *Design and Application of Inorganic Nanoparticle Superstructures: Current Status and Future challenges.* Small, 2011. **7**(15): p. 2133-2146.
4. Hasan, S., *A review on nanoparticles: their synthesis and types.* Res. J. Recent Sci, 2015. **2277**: p. 2502.
5. Tenne, R. and L. Margulis, *Polyhedral and cylindrical structures of tungsten disulphide.* Nature, 1992. **360**(6403): p. 444.
6. Margulis, L., et al., *Nested fullerene-like structures.* Nature, 1993. **365**(6442): p. 113-114.
7. Tenne, R. and C. Rao, *Inorganic nanotubes.* Philosophical Transactions of the Royal Society of London. Series A: Mathematical, Physical and Engineering Sciences, 2004. **362**(1823): p. 2099-2125.
8. Kaplan-Ashiri, I., et al., *On the mechanical behavior of WS2 nanotubes under axial tension and compression.* Proceedings of the National Academy of Sciences, 2006. **103**(3): p. 523-528.
9. Garel, J., et al., *Ultrahigh torsional stiffness and strength of boron nitride nanotubes.* Nano Letters, 2012. **12**(12): p. 6347-6352.
10. Deng, S., A.V. Sumant, and V. Berry, *Strain engineering in two-dimensional nanomaterials beyond graphene.* Nano Today, 2018. **22**: p. 14-35.
11. Gong, F., H.M. Duong, and D.V. Papavassiliou, *Review of recent developments on using an off-lattice monte carlo approach to predict the effective thermal conductivity of composite systems with complex structures.* Nanomaterials, 2016. **6**(8): p. 142.
12. Maharaj, D. and B. Bhushan, *Characterization of nanofriction of MoS2 and WS2 nanotubes.* Materials Letters, 2015. **142**: p. 207-210.
13. Frey, G.L., et al., *Optical Properties of MS2 (M = Mo, W) Inorganic Fullerenelike and Nanotube Material Optical*

Absorption and Resonance Raman Measurements. Journal of Materials Research, 1998. **13**(9): p. 2412-2417.
14. Wilson, J.A. and A.D. Yoffe, *The transition metal dichalcogenides discussion and interpretation of the observed optical, electrical and structural properties.* Advances in Physics, 1969. **18**(73): p. 193-335.
15. Sedova, A., et al., *Dielectric and electrical properties of WS2 nanotubes/epoxy composites and their use for stress monitoring of structures.* Journal of Nanomaterials, 2017. **2017**.
16. Cheng, F. and J. Chen, *Storage of hydrogen and lithium in inorganic nanotubes and nanowires.* Journal of Materials Research, 2006. **21**(11): p. 2744-2757.
17. Darr, J.A., et al., *Continuous Hydrothermal Synthesis of Inorganic Nanoparticles: Applications and Future Directions.* Chemical Reviews, 2017. **117**(17): p. 11125-11238.
18. Epelle, E.I., et al., *Advances in the Applications of Nanomaterials for Wastewater Treatment.* Environments, 2022. **9**(11): p. 141.
19. Singh, R. and H.S. Nalwa, *Medical applications of nanoparticles in biological imaging, cell labeling, antimicrobial agents, and anticancer nanodrugs.* Journal of biomedical nanotechnology, 2011. **7**(4): p. 489-503.
20. Zhao, M.X., E.Z. Zeng, and B.J. Zhu, *The Biological Applications of Inorganic Nanoparticle Drug Carriers.* Chemnanomat, 2015. **1**(2): p. 82-91.
21. Wang, W.J., et al., *Recent Advances in Microbial Biosynthesis of Inorganic Nanomaterials.* Chinese Journal Of Inorganic Chemistry, 2020. **36**(5): p. 777-794.
22. Wang, H.L., et al., *Update on Nanoparticle-Based Drug Delivery System for Anti-inflammatory Treatment.* Frontiers In Bioengineering And Biotechnology, 2021. **9**: p. 630352.
23. Bhattacharyya, S., et al., *Inorganic Nanoparticles in Cancer Therapy.* Pharmaceutical Research, 2011. **28**(2): p. 237-259.
24. Hofmann-Amtenbrink, M., D.W. Grainger, and H. Hofmann, *Nanoparticles in medicine: Current challenges facing inorganic nanoparticle toxicity assessments and standardizations.* Nanomedicine: Nanotechnology, Biology and Medicine, 2015. **11**(7): p. 1689-1694.
25. Shen, W.-Z., S. Cetinel, and C. Montemagno, *Application of biomolecular recognition via magnetic nanoparticle in nanobiotechnology.* Journal of Nanoparticle Research, 2018. **20**(5): p. 130.

26. Yoo, S.C., et al., *Recent progress in low-dimensional nanomaterials filled multifunctional metal matrix nanocomposites.* Progress in Materials Science, 2023. **132**.
27. Paul, D.R. and L.M. Robeson, *Polymer nanotechnology: Nanocomposites.* Polymer, 2008. **49**(15): p. 3187-3204.
28. Papageorgiou, D.G., I.A. Kinloch, and R.J. Young, *Mechanical properties of graphene and graphene-based nanocomposites.* Progress in Materials Science, 2017. **90**: p. 75-127.
29. Kuilla, T., et al., *Recent advances in graphene based polymer composites.* Progress in Materials Science, 2010. **35**(11): p. 1350-1375.
30. Hussain, F., et al., *Review article: Polymer-matrix nanocomposites, processing, manufacturing, and application: An overview.* Journal of Composite Materials 2006. **40**(17): p. 1511-1575.
31. Huang, Z.M., et al., *A review on polymer nanofibers by electrospinning and their applications in nanocomposites.* Composites Science And Technology, 2003. **63**(15): p. 2223-2253.
32. Bhattacharya, M., *Polymer Nanocomposites-A Comparison between Carbon Nanotubes, Graphene, and Clay as Nanofillers.* Materials, 2016. **9**(4).
33. Kausar, A., *Current state-of-the-art of carbonaceous nanofiller coated carbon fiber in polymeric nanocomposites.* Journal of Thermoplastic Composite Materials, 2022: p. 08927057221139590.
34. Rai, M., et al., *An introduction to biopolymer-based nanofilms, their applications, and limitations*, in *Biopolymer-Based Nano Films*. 2021, Elsevier. p. 3-17.
35. Jain, R., S. Shetty, and K.S. Yadav, *Unfolding the electrospinning potential of biopolymers for preparation of nanofibers.* Journal of Drug Delivery Science and Technology, 2020. **57**: p. 101604.
36. Mtibe, A., et al., *Synthetic biopolymers and their composites: Advantages and limitations—an overview.* Macromolecular Rapid Communications, 2021. **42**(15): p. 2100130.
37. Nagarajan, V., A.K. Mohanty, and M. Misra, *Perspective on Polylactic Acid (PLA) based Sustainable Materials for Durable Applications: Focus on Toughness and Heat Resistance.* ACS Sustainable Chemistry & Engineering, 2016. **4**(6): p. 2899-2916.
38. Baranwal, J., et al., *Biopolymer: A sustainable material for food and medical applications.* Polymers, 2022. **14**(5): p. 983.

39. Xiong, R., et al., *Naturally-derived biopolymer nanocomposites: Interfacial design, properties and emerging applications.* Materials Science & Engineering R-Reports, 2018. **125**: p. 1-41.
40. Rhim, J.W., H.M. Park, and C.S. Ha, *Bio-nanocomposites for food packaging applications.* Progress in Polymer Science, 2013. **38**(10-11): p. 1629-1652.
41. Rhim, J.W. and P.K.W. Ng, *Natural biopolymer-based nanocomposite films for packaging applications.* Critical Reviews In Food Science and Nutrition 2007. **47**(4): p. 411-433.
42. Rezaei, F.S., et al., *Chitosan films and scaffolds for regenerative medicine applications: A review.* Carbohydrate Polymers, 2021. **273**: p. 118631.
43. Okamoto, M. and B. John, *Synthetic biopolymer nanocomposites for tissue engineering scaffolds.* Progress in Polymer Science, 2013. **38**(10-11): p. 1487-1503.
44. Sohn, Y.J., et al., *Recent advances in sustainable plastic upcycling and biopolymers.* Biotechnology Journal, 2020. **15**(6): p. 1900489.
45. Jaiswal, L., S. Shankar, and J.-W. Rhim, *Chapter 3 - Applications of nanotechnology in food microbiology*, in *Methods in Microbiology*, V. Gurtler, A.S. Ball, and S. Soni, Editors. 2019, Academic Press. p. 43-60.
46. Basavegowda, N. and K.-H. Baek, *Advances in functional biopolymer-based nanocomposites for active food packaging applications.* Polymers, 2021. **13**(23): p. 4198.
47. Ganguly, P., A. Breen, and S.C. Pillai, *Toxicity of Nanomaterials: Exposure, Pathways, Assessment, and Recent Advances.* ACS Biomaterials Science & Engineering, 2018. **4**(7): p. 2237-2275.
48. Višic, B., L.S. Panchakarla, and R. Tenne, *Inorganic Nanotubes and Fullerene-like Nanoparticles at the Crossroads between Solid-State Chemistry and Nanotechnology.* Journal of the American Chemical Society, 2017. **139**(37): p. 12865-12878.
49. Díez-Pascual, A.M., *Nanoparticle Reinforced Polymers.* Polymers, 2019. **11**(4): p. 625.
50. Idumah, C.I. and C.M. Obele, *Understanding interfacial influence on properties of polymer nanocomposites.* Surfaces and Interfaces, 2021. **22**: p. 100879.
51. Díez-Pascual, A.M., *Inorganic-nanoparticle modified polymers*. 2022, MDPI. p. 1979.
52. Sanes, J., et al., *Extrusion of polymer nanocomposites with graphene and graphene derivative nanofillers: An overview of recent developments.* Materials, 2020. **13**(3): p. 549.

53. Sypabekova, M., et al., *3-Aminopropyltriethoxysilane (APTES) Deposition Methods on Oxide Surfaces in Solution and Vapor Phases for Biosensing Applications.* Biosensors, 2022. **13**(1): p. 36.
54. Mujtaba, M., et al., *Current advancements in chitosan-based film production for food technology; A review.* International journal of biological macromolecules, 2019. **121**: p. 889-904.
55. Kumar, S., A. Mukherjee, and J. Dutta, *Chitosan based nanocomposite films and coatings: Emerging antimicrobial food packaging alternatives.* Trends in Food Science & Technology, 2020. **97**: p. 196-209.
56. Sethulekshmi, A.S., et al., *Insights into the reinforcibility and multifarious role of WS2 in polymer matrix.* Journal of Alloys and Compounds, 2021. **876**: p. 160107.
57. Serra, M., R. Arenal, and R. Tenne, *An overview of the recent advances in inorganic nanotubes.* Nanoscale, 2019. **11**(17): p. 8073-8090.
58. Trabelsi, K., et al., *Enhancing the photoelectrochemical response of TiO2 nanotubes through their nanodecoration by pulsed-laser-deposited Ag nanoparticles.* Journal of Applied Physics, 2017. **122**(6): p. 64503.
59. Brüser, V., et al., *Single- to Triple-Wall WS2 Nanotubes Obtained by High-Power Plasma Ablation of WS2 Multiwall Nanotubes.* Inorganics, 2014. **2**(2): p. 177-190.
60. Balati, A., et al., *Simultaneous formation of ultra-thin MoSe2 nanosheets, Inorganic Fullerene-Like MoSe2 and MoO3 quantum dots using fast and ecofriendly Pulsed Laser Ablation in Liquid followed by microwave treatment.* Materials Science in Semiconductor Processing, 2019. **99**: p. 68-77.
61. Li, X.H., W.M. Liu, and H.L. Li, *Template synthesis of well-aligned titanium dioxide nanotubes.* Applied Physics A: Materials Science & Processing, 2005. **80**(2): p. 317.
62. Levi, R., et al., *Field-effect transistors based on WS2 nanotubes with high current-carrying capacity.* Nano Letters, 2013. **13**(8): p. 3736-3741.
63. Tehrani, M., et al., *Synthesis of WS2 nanostructures from the reaction of WO3 with CS2 and mechanical characterization of WS2 nanotube composites.* Nanotechnology, 2011. **22**(28): p. 285714.
64. Chen, Y., et al., *Thin WS2 nanotubes from W18O49 nanowires.* Materials Research Letters, 2017. **5**(7): p. 508-515.
65. Dominko, R., et al., *Dichalcogenide Nanotube Electrodes for Li-Ion Batteries.* Advanced Materials, 2002. **14**(21): p. 1531.

66. Feldman, Y., et al., *Bulk Synthesis of Inorganic Fullerene-like MS2 (M = Mo, W) from the Respective Trioxides and the Reaction Mechanism.* Journal of the American Chemical Society, 1996. **118**(23): p. 5362-5367.
67. Krasnikov, D.V., et al., *Side reaction in catalytic CVD growth of carbon nanotubes: Surface pyrolysis of a hydrocarbon precursor with the formation of lateral carbon deposits.* Carbon, 2018. **139**: p. 105-117.
68. Baig, N., I. Kammakakam, and W. Falath, *Nanomaterials: A review of synthesis methods, properties, recent progress, and challenges.* Materials Advances, 2021. **2**(6): p. 1821-1871.
69. Chen, J., et al., *Synthesis and characterization of WS2 nanotubes.* Chemistry of materials, 2003. **15**(4): p. 1012-1019.
70. Rothschild, A., J. Sloan, and R. Tenne, *Growth of WS2 nanotubes phases.* Journal of the American chemical Society, 2000. **122**(21): p. 5169-5179.
71. Therese, H.A., et al., *Facile large scale synthesis of WS2 nanotubes from WO3 nanorods prepared by a hydrothermal route.* Solid State Sciences, 2005. **7**(1): p. 67-72.
72. Zhu, Y.Q., et al., *Production of WS2 nanotubes.* Chemistry of materials, 2000. **12**(5): p. 1190-1194.
73. Rahman, M.A., et al., *Improved synthesis of WS2 nanotubes with relatively small diameters by tuning sulfurization timing and reaction temperature.* Japanese Journal of Applied Physics, 2021. **60**(10): p. 100902.
74. Feldman, Y., et al., *New reactor for production of tungsten disulfide hollow onion-like (inorganic fullerene-like) nanoparticles.* Solid State Sciences, 2000. **2**(6): p. 663-672.
75. Margolin, A., et al., *Study of the growth mechanism of WS2 nanotubes produced by a fluidized bed reactor.* Journal of Materials Chemistry, 2004. **14**(4): p. 617-624.
76. Rosentsveig, R., et al., *WS2 Nanotube Bundles and Foils.* Chemistry of Materials, 2002. **14**(2): p. 471-473.
77. Zak A, S.-E.L.M.A.G.M.T.R., *Insight into the growth mechanism of WS2 nanotubes in the scaled-up fluidized-bed reactor.* Nano, 2009. **4**(2): p. 91-98.
78. Zak, A., et al., *Scaling Up of the WS2 Nanotubes Synthesis.* Fullerenes, Nanotubes & Carbon Nanostructures, 2010. **19**(1): p. 18-26.
79. Sinha, S.S., et al., *MoS2 and WS2 Nanotubes: Synthesis, Structural Elucidation, and Optical Characterization.* The Journal of Physical Chemistry C, 2021. **125**(11): p. 6324-6340.

80. Zak, A., et al., *Large-scale Synthesis of WS2 Multiwall Nanotubes and their Dispersion, an Update.* Sensors & Transducers, 2011. **12**(Special Issue): p. 1-9.
81. Zak, A., et al., *Scaling Up of the WS2 Nanotubes Synthesis.* Fullerenes, Nanotubes and Carbon Nanostructures, 2010. **19**(1-2): p. 18-26.
82. Chithaiah, P., et al., *Solving the "MoS2 Nanotubes" Synthetic Enigma and Elucidating the Route for Their Catalyst-Free and Scalable Production.* ACS Nano, 2020. **14**(3): p. 3004-3016.
83. Zhang, Y.J., et al., *Enhanced intrinsic photovoltaic effect in tungsten disulfide nanotubes.* Nature, 2019. **570**(7761): p. 349.
84. Tenne, R. and M. Redlich, *Recent progress in the research of inorganic fullerene-like nanoparticles and inorganic nanotubes* Chemical Society Reviews, 2010. **39**(5): p. 1423-1434.
85. Rothschild, A., et al., *Morphology of Multiwall WS2 Nanotubes.* The Journal of Physical Chemistry B, 2000. **104**(38): p. 8976-8981.
86. Sugahara, M., et al., *Ambipolar transistors based on random networks of WS2 nanotubes.* Applied physics express, 2016. **9**(7): p. 075001.
87. Seifert, G., et al., *Structure and electronic properties of MoS 2 nanotubes.* Physical Review Letters, 2000. **85**(1): p. 146.
88. Maya, B.S., et al., *Atom by Atom: HRTEM Insights into Inorganic Nanotubes and Fullerene-Like Structures.* Proceedings of the National Academy of Sciences of the United States of America, 2008. **105**(41): p. 15643.
89. Golub, A.S., et al., *Single-layer dispersions of transition metal dichalcogenides in the synthesis of intercalation compounds.* Russian Chemical Reviews, 2003. **72**(2): p. 123.
90. Damnjanovic, M., T. Vukovic, and I. Miloševic, *Symmetry-based Study of MoS2 and WS2 Nanotubes.* Israel Journal of Chemistry, 2017. **57**(6): p. 450.
91. Polyakov, A.Y., et al., *Nanocomposites based on tubular and onion nanostructures of molybdenum and tungsten disulfides: inorganic design, functional properties and applications.* Russian Chemical Reviews, 2018. **87**(3): p. 251-271.
92. Rao, C.N.R. and A. Nag, *Inorganic Analogues of Graphene.* European Journal of Inorganic Chemistry, 2010. **2010**(27): p. 4244-4250.
93. Višic, B., et al., *Direct Synthesis of Palladium Catalyst on Supporting WS2 Nanotubes and its Reactivity in Cross-Coupling Reactions.* Chemistry, An Asian Journal, 2015. **10**(10): p. 2234-2239.

94. Kopnov, F., et al., *X-Ray Photoelectron Spectroscopy and Tribology Studies of Annealed Fullerene-like WS2 Nanoparticles*, in *Functionalized Nanoscale Materials, Devices and Systems*. 2008, Springer Netherlands: Dordrecht. p. 51-59.
95. Spetter, D., et al., *Surface Defects as a Tool to Solubilize and Functionalize WS2 Nanotubes.* European Journal of Inorganic Chemistry, 2017. **2017**(15): p. 2190.
96. Houben, L., et al., *Diffraction from Disordered Stacking Sequences in MoS2 and WS2 Fullerenes and Nanotubes.* The Journal of Physical Chemistry C, 2015. **116**(45): p. 24350-24357.
97. Khan, I., K. Saeed, and I. Khan, *Nanoparticles: Properties, applications and toxicities.* Arabian journal of chemistry, 2019. **12**(7): p. 908-931.
98. Weber, J., et al., *One-dimensional nanostructures: fabrication, characterisation and applications.* International Materials Reviews, 2008. **53**(4): p. 235-255.
99. Harish, V., et al., *Review on nanoparticles and nanostructured materials: Bioimaging, biosensing, drug delivery, tissue engineering, antimicrobial, and agro-food applications.* Nanomaterials, 2022. **12**(3): p. 457.
100. Paszkiewicz, S., et al., *Comparative study on the properties of poly(trimethylene terephthalate) -based nanocomposites containing multi-walled carbon (MWCNT) and tungsten disulfide (INT-WS2) nanotubes.* Polymers for Advanced Technologies, 2017. **28**(6): p. 645.
101. Otorgust, G., et al., *Important insights into polyurethane nanocomposite-adhesives; a comparative study between INT-WS2 and CNT.* European Polymer Journal, 2017. **89**: p. 281-300.
102. Kaplan-Ashiri, I. and R. Tenne, *Mechanical properties of WS2 nanotubes.* Journal of Cluster Science, 2007. **18**(3): p. 549-563.
103. Rapoport, L., et al., *Hollow nanoparticles of WS2 as potential solid-state lubricants.* Nature, 1997. **387**(6635): p. 791-793.
104. Zheng, N., X. Bu, and P. Feng, *Synthetic design of crystalline inorganic chalcogenides exhibiting fast-ion conductivity.* Nature, 2003. **426**(6965): p. 428-432.
105. Wang, G., et al., *Tungsten disulfide nanotubes for lithium storage.* Electrochemical and solid-state letters, 2004. **7**(10): p. A321.
106. Liu, H., et al., *An ordered mesoporous WS 2 anode material with superior electrochemical performance for lithium ion batteries.* Journal of Materials Chemistry, 2012. **22**(34): p. 17437-17440.
107. Qin, F., et al., *Superconductivity in a chiral nanotube.* Nature communications, 2017. **8**(1): p. 14465.

108. Zhang, Y., et al., *Enhanced intrinsic photovoltaic effect in tungsten disulfide nanotubes.* Nature, 2019. **570**(7761): p. 349-353.
109. Wang, F., et al., *Strain-induced phonon shifts in tungsten disulfide nanoplatelets and nanotubes.* 2D Materials, 2016. **4**(1): p. 015007.
110. Appel, J.H., et al., *Low cytotoxicity and genotoxicity of two-dimensional MoS2 and WS2.* ACS Biomaterials Science & Engineering, 2016. **2**(3): p. 361-367.
111. Goldman, E.B., et al., *Biocompatibility of tungsten disulfide inorganic nanotubes and fullerene-like nanoparticles with salivary gland cells.* Tissue engineering. Part A, 2015. **21**(5-6): p. 1013-1023.
112. Pardo, M., et al., *Low Cytotoxicity of Inorganic Nanotubes and Fullerene-Like Nanostructures in Human Bronchial Epithelial Cells: Relation to Inflammatory Gene Induction and Antioxidant Response.* Environmental Science & Technology, 2014. **48**(6): p. 3457-3466.
113. Teo, W.Z., et al., *Cytotoxicity of exfoliated transition-metal dichalcogenides (MoS2, WS2, and WSe2) is lower than that of graphene and its analogues.* Chemistry–A European Journal, 2014. **20**(31): p. 9627-9632.
114. Adini, A.R., M. Redlich, and R. Tenne, *Medical applications of inorganic fullerene-like nanoparticles.* Journal of Materials Chemistry, 2011. **21**(39): p. 15121.
115. Lalwani, G., et al., *Tungsten disulfide nanotubes reinforced biodegradable polymers for bone tissue engineering*. 2013. p. 8365-8373.
116. Katz, A., et al., *Self-lubricating coatings containing fullerene-like WS2 nanoparticles for orthodontic wires and other possible medical applications.* Tribology Letters, 2006. **21**(2): p. 135-139.
117. Lin, H. and R.H. Datar, *Medical applications of nanotechnology.* The National Medical Journal of India, 2006. **19**(1): p. 27-32.
118. Jordan, J., et al., *Experimental trends in polymer nanocomposites—a review.* Materials science and engineering: A, 2005. **393**(1-2): p. 1-11.
119. Fu, S., et al., *Some basic aspects of polymer nanocomposites: A critical review.* Nano Materials Science, 2019. **1**(1): p. 2-30.
120. Niaounakis, M., *Biopolymers: applications and trends*. 2015: William Andrew.
121. Kumar, S., et al., *An Overview of Natural Biopolymers in Food Packaging.* Biopolymer-Based Food Packaging; John Wiley & Sons, Ltd.: Hoboken, NJ, USA, 2022: p. 1-28.

122. Mallakpour, S., F. Sirous, and C.M. Hussain, *A journey to the world of fascinating ZnO nanocomposites made of chitosan, starch, cellulose, and other biopolymers: Progress in recent achievements in eco-friendly food packaging, biomedical, and water remediation technologies.* International Journal of Biological Macromolecules, 2021. **170**: p. 701-716.
123. Torres-Giner, S., et al., *Emerging trends in biopolymers for food packaging.* Sustainable Food Packaging Technology, 2021: p. 1-33.
124. Varma, K. and S. Gopi, *Chapter 7 - Biopolymers and their role in medicinal and pharmaceutical applications*, in *Biopolymers and their Industrial Applications*, S. Thomas, S. Gopi, and A. Amalraj, Editors. 2021, Elsevier. p. 175-191.
125. Wróblewska-Krepsztul, J., et al., *Biopolymers for Biomedical and Pharmaceutical Applications: Recent Advances and Overview of Alginate Electrospinning.* Nanomaterials, 2019. **9**(3): p. 404.
126. Biswas, M.C., et al., *Recent Advancement of Biopolymers and Their Potential Biomedical Applications.* Journal of Polymers and the Environment, 2022. **30**(1): p. 51-74.
127. Gheorghita, R., et al., *Applications of Biopolymers for Drugs and Probiotics Delivery.* Polymers, 2021. **13**(16): p. 2729.
128. Bibire, T., et al., *Biopolymers for surgical applications.* Coatings, 2022. **12**(2): p. 211.
129. Kabir, E., et al., *Prospects of biopolymer technology as an alternative option for non-degradable plastics and sustainable management of plastic wastes.* Journal of Cleaner Production, 2020. **258**: p. 120536.
130. Yaashikaa, P.R., P. Senthil Kumar, and S. Karishma, *Review on biopolymers and composites – Evolving material as adsorbents in removal of environmental pollutants.* Environmental Research, 2022. **212**: p. 113114.
131. Samir, A., et al., *Recent advances in biodegradable polymers for sustainable applications.* npj Materials Degradation, 2022. **6**(1): p. 68.
132. Biswal, T., *Biopolymers for tissue engineering applications: A review.* Materials Today: Proceedings, 2021. **41**: p. 397-402.
133. Udayakumar, G.P., et al., *Biopolymers and composites: Properties, characterization and their applications in food, medical and pharmaceutical industries.* Journal of Environmental Chemical Engineering, 2021. **9**(4): p. 105322.
134. Moohan, J., et al., *Cellulose Nanofibers and Other Biopolymers for Biomedical Applications. A Review.* Applied Sciences, 2020. **10**(1): p. 65.

135. Wróblewska-Krepsztul, J., et al., *Biopolymers for biomedical and pharmaceutical applications: Recent advances and overview of alginate electrospinning.* Nanomaterials, 2019. **9**(3).
136. Al-Ghraibah, A.M., M. Al-Qudah, and F.M. AL-Oqla, *Medical implementations of biopolymers*, in *Advanced processing, properties, and applications of starch and other bio-based polymers*. 2020, Elsevier. p. 157-171.
137. Rebelo, R., M. Fernandes, and R. Fangueiro, *Biopolymers in Medical Implants: A Brief Review.* Procedia Engineering, 2017. **200**: p. 236-243.
138. Sivakanthan, S., et al., *Antioxidant and antimicrobial applications of biopolymers: A review.* Food Research International, 2020. **136**: p. 109327.
139. Yadav, P., et al., *Biomedical biopolymers, their origin and evolution in biomedical sciences: A systematic review.* Journal of clinical and diagnostic research: JCDR, 2015. **9**(9): p. ZE21.
140. Nakajima, H., P. Dijkstra, and K. Loos, *The Recent Developments in Biobased Polymers toward General and Engineering Applications: Polymers that are Upgraded from Biodegradable Polymers, Analogous to Petroleum-Derived Polymers, and Newly Developed.* Polymers, 2017. **9**(10): p. 523.
141. Rao, M.G., P. Bharathi, and R. Akila, *A comprehensive review on biopolymers.* Sci. Revs. Chem. Commun, 2014. **4**(2): p. 61-68.
142. Singh, T.V. and L.S. Shagolsem, *Biopolymer based nano-structured materials and their applications.* Nanostructured materials and their applications, 2021: p. 337-366.
143. Reddy, M.S.B., et al., *A comparative review of natural and synthetic biopolymer composite scaffolds.* Polymers, 2021. **13**(7): p. 1105.
144. Oniszczuk, T., et al., *Effect of Processing Conditions on Selected Properties of Starch-based Biopolymers.* Agriculture and Agricultural Science Procedia, 2015. **7**: p. 192-197.
145. Sarder, R., et al., *Copolymers of starch, a sustainable template for biomedical applications: A review.* Carbohydrate Polymers, 2022. **278**: p. 118973.
146. Zakaria, N., N. Muhammad, and M. Abdullah. *Potential of starch nanocomposites for biomedical applications*. in *IOP Conference Series: Materials Science and Engineering*. 2017. IOP Publishing.
147. Zafar, R., et al., *Polysaccharide based bionanocomposites, properties and applications: A review.* International journal of biological macromolecules, 2016. **92**: p. 1012-1024.

148. Ferreira, A.R., V.D. Alves, and I.M. Coelhoso, *Polysaccharide-based membranes in food packaging applications.* Membranes, 2016. **6**(2): p. 22.
149. Jones, O.G. and D.J. McClements, *Functional biopolymer particles: design, fabrication, and applications.* Comprehensive Reviews in Food Science and Food Safety, 2010. **9**(4): p. 374-397.
150. Luo, Y., Q. Wang, and Y. Zhang, *Biopolymer-based nanotechnology approaches to deliver bioactive compounds for food applications: a perspective on the past, present, and future.* Journal of Agricultural and Food Chemistry, 2020. **68**(46): p. 12993-13000.
151. Rhim, J.-W. and P.K. Ng, *Natural biopolymer-based nanocomposite films for packaging applications.* Critical reviews in food science and nutrition, 2007. **47**(4): p. 411-433.
152. Gupta, P. and K.K. Nayak, *Characteristics of protein-based biopolymer and its application.* Polymer Engineering & Science, 2015. **55**(3): p. 485-498.
153. Pakornpadungsit, P., W. Smitthipong, and A. Chworos, *Self-assembly nucleic acid-based biopolymers: learn from the nature.* Journal of Polymer Research, 2018. **25**: p. 1-9.
154. Kubicek, C.P., *Synthetic biopolymers.* Synthetic Biology, 2016: p. 307-335.
155. Ilyas, R.A., et al., *Polylactic Acid (PLA) Biocomposite: Processing, Additive Manufacturing and Advanced Applications.* Polymers, 2021. **13**(8): p. 1326.
156. Carothers, W.H., G.L. Dorough, and F.J.v. Natta, *Studies Of Polymerization And Ring Formation. X. The Reversible Polymerization Of Six-Membered Cyclic Esters.* Journal of the American Chemical Society, 1932. **54**(2): p. 761-772.
157. Davachi, S.M. and B. Kaffashi, *Polylactic Acid in Medicine.* Polymer-Plastics Technology and Engineering, 2015. **54**(9): p. 944-967.
158. Balla, E., et al., *Poly(lactic Acid): A Versatile Biobased Polymer for the Future with Multifunctional Properties—From Monomer Synthesis, Polymerization Techniques and Molecular Weight Increase to PLA Applications.* Polymers, 2021. **13**(11).
159. Ioannidou, S.M., et al., *Techno-economic risk assessment, life cycle analysis and life cycle costing for poly(butylene succinate) and poly(lactic acid) production using renewable resources.* Science of The Total Environment, 2022. **806**: p. 150594.
160. McKeen, L., *12 - Renewable Resource and Biodegradable Polymers*, in *The Effect of Sterilization on Plastics and*

Elastomers (Third Edition), L. McKeen, Editor. 2012, William Andrew Publishing: Boston. p. 305-317.
161. Sreekumar, K., B. Bindhu, and K. Veluraja, *Perspectives of polylactic acid from structure to applications.* Polymers from Renewable Resources, 2021. **12**(1-2): p. 60-74.
162. Avinc, O. and A. Khoddami, *Overview of Poly (lactic acid)(PLA) Fibre.* Fibre Chemistry, 2009. **41**(6): p. 391-401.
163. Avérous, L., *Chapter 21 - Polylactic Acid: Synthesis, Properties and Applications*, in *Monomers, Polymers and Composites from Renewable Resources*, M.N. Belgacem and A. Gandini, Editors. 2008, Elsevier: Amsterdam. p. 433-450.
164. Jem, K.J. and B. Tan, *The development and challenges of poly (lactic acid) and poly (glycolic acid).* Advanced Industrial and Engineering Polymer Research, 2020. **3**(2): p. 60-70.
165. Lunt, J., *Large-scale production, properties and commercial applications of polylactic acid polymers.* Polymer Degradation and Stability, 1998. **59**(1): p. 145-152.
166. Balla, E., et al., *Poly(lactic Acid): A Versatile Biobased Polymer for the Future with Multifunctional Properties—From Monomer Synthesis, Polymerization Techniques and Molecular Weight Increase to PLA Applications.* Polymers, 2021. **13**(11): p. 1822.
167. Masutani, K. and Y. Kimura, *PLA synthesis. From the monomer to the polymer*. 2014.
168. Masutani, K., Y. Kimura, and R.S.o. Chemistry, *PLA Synthesis. From the Monomer to the Polymer*, in *Poly(lactic acid) Science and Technology: Processing, Properties, Additives and Applications*, A. Jiménez, M. Peltzer, and R. Ruseckaite, Editors. 2014, The Royal Society of Chemistry.
169. Cheng, Y., et al., *Polylactic acid (PLA) synthesis and modifications: a review.* Frontiers of chemistry in China, 2009. **4**(3): p. 259-264.
170. Drumright, R.E., P.R. Gruber, and D.E. Henton, *Polylactic acid technology.* Advanced materials, 2000. **12**(23): p. 1841-1846.
171. Farah, S., D.G. Anderson, and R. Langer, *Physical and mechanical properties of PLA, and their functions in widespread applications — A comprehensive review.* Advanced Drug Delivery Reviews, 2016. **107**: p. 367-392.
172. Tan, B.H., et al., *Recent Progress in Using Stereocomplexation for Enhancement of Thermal and Mechanical Property of Polylactide.* ACS Sustainable Chemistry & Engineering, 2016. **4**(10): p. 5370-5391.
173. Park, H.-S. and C.-K. Hong, *Relationship between the Stereocomplex Crystallization Behavior and Mechanical*

Properties of PLLA/PDLA Blends. Polymers, 2021. **13**(11): p. 1851.
174. Auras, R., B. Harte, and S. Selke, *An Overview of Polylactides as Packaging Materials.* Macromolecular Bioscience, 2004. **4**(9): p. 835-864.
175. Carrasco, F., et al., *Processing of poly(lactic acid): Characterization of chemical structure, thermal stability and mechanical properties.* Polymer Degradation and Stability, 2010. **95**(2): p. 116-125.
176. Casalini, T., et al., *A perspective on polylactic acid-based polymers use for nanoparticles synthesis and applications.* Frontiers in bioengineering and biotechnology, 2019: p. 259.
177. Rasal, R.M., A.V. Janorkar, and D.E. Hirt, *Poly(lactic acid) modifications.* Progress in Polymer Science, 2010. **35**(3): p. 338-356.
178. Vink, E.T.H., et al., *Applications of life cycle assessment to NatureWorks™ polylactide (PLA) production.* Polymer Degradation and Stability, 2003. **80**(3): p. 403-419.
179. Raquez, J.-M., et al., *Polylactide (PLA)-based nanocomposites.* Progress in Polymer Science, 2013. **38**(10-11): p. 1504-1542.
180. Yu, J., et al., *Current trends and challenges in the synthesis and applications of chitosan-based nanocomposites for plants: A review.* Carbohydrate Polymers, 2021. **261**: p. 117904.
181. Wang, J. and S. Zhuang, *Chitosan-based materials: Preparation, modification and application.* Journal of Cleaner Production, 2022. **355**: p. 131825.
182. Prudden, J.F., et al., *The discovery of a potent pure chemical wound-healing accelerator.* The American Journal of Surgery, 1970. **119**(5): p. 560-564.
183. Crini, G., *Historical review on chitin and chitosan biopolymers.* Environmental Chemistry Letters, 2019. **17**(4): p. 1623-1643.
184. Pal, J., et al., *Biological method of chitin extraction from shrimp waste an eco-friendly low cost technology and its advanced application.* International Journal of Fisheries and Aquatic Studies, 2014. **1**(6): p. 104-107.
185. Giri, T.K., et al., *Modified chitosan hydrogels as drug delivery and tissue engineering systems: present status and applications.* Acta Pharmaceutica Sinica B, 2012. **2**(5): p. 439-449.
186. Jiang, Z., et al., *Construction of chitosan scaffolds with controllable microchannel for tissue engineering and regenerative medicine.* Materials Science and Engineering: C, 2021. **126**: p. 112178.

187. Jin, T., et al., *Chitin and chitosan on the nanoscale.* Nanoscale Horizons, 2021. **6**(7): p. 505-542.
188. Sahariah, P. and M. Másson, *Antimicrobial chitosan and chitosan derivatives: a review of the structure–activity relationship.* Biomacromolecules, 2017. **18**(11): p. 3846-3868.
189. Kou, S.G., L.M. Peters, and M.R. Mucalo, *Chitosan: A review of sources and preparation methods.* International Journal of Biological Macromolecules, 2021. **169**: p. 85-94.
190. He, X., et al., *The production of fully deacetylated chitosan by compression method.* The Egyptian Journal of Aquatic Research, 2016. **42**(1): p. 75-81.
191. Pillai, C.K.S., W. Paul, and C.P. Sharma, *Chitin and chitosan polymers: Chemistry, solubility and fiber formation.* Progress in Polymer Science, 2009. **34**(7): p. 641-678.
192. Zargar, V., M. Asghari, and A. Dashti, *A review on chitin and chitosan polymers: structure, chemistry, solubility, derivatives, and applications.* ChemBioEng reviews, 2015. **2**(3): p. 204-226.
193. Balau, L., et al., *Physico-chemical properties of chitosan films.* Central European Journal of Chemistry, 2004. **2**(4): p. 638-647.
194. AlMohammed, H.I., et al., *Chitosan-Based Nanomaterials as Valuable Sources of Anti-Leishmanial Agents: A Systematic Review.* Nanomaterials, 2021. **11**(3): p. 689.
195. Kassem, A., G.M. Ayoub, and L. Malaeb, *Antibacterial activity of chitosan nano-composites and carbon nanotubes: A review.* Science of The Total Environment, 2019. **668**: p. 566-576.
196. Rodríguez-Vázquez, M., et al., *Chitosan and its potential use as a scaffold for tissue engineering in regenerative medicine.* BioMed research international, 2015. **2015**.
197. Sandoval-Sánchez, J.H., et al., *A new bilayer chitosan scaffolding as a dural substitute: experimental evaluation.* World neurosurgery, 2012. **77**(3-4): p. 577-582.
198. Qu, B. and Y. Luo, *Chitosan-based hydrogel beads: Preparations, modifications and applications in food and agriculture sectors–A review.* International journal of biological macromolecules, 2020. **152**: p. 437-448.
199. Pakdel, P.M. and S.J. Peighambardoust, *Review on recent progress in chitosan-based hydrogels for wastewater treatment application.* Carbohydrate polymers, 2018. **201**: p. 264-279.
200. Chadha, U., et al., *Retracted: Advances in chitosan biopolymer composite materials: from bioengineering, wastewater treatment to agricultural applications.* Materials Research Express, 2022. **9**(5): p. 052002.

201. Michalik, R. and I. Wandzik, *A mini-review on chitosan-based hydrogels with potential for sustainable agricultural applications.* Polymers, 2020. **12**(10): p. 2425.
202. Kashyap, P.L., X. Xiang, and P. Heiden, *Chitosan nanoparticle based delivery systems for sustainable agriculture.* International journal of biological macromolecules, 2015. **77**: p. 36-51.
203. Choudhary, R.C., et al., *Chitosan nanomaterials for smart delivery of bioactive compounds in agriculture*, in *Nanoscale engineering in agricultural management*. 2019, CRC Press. p. 124-139.
204. Leceta, I., P. Guerrero, and K. de la Caba, *Functional properties of chitosan-based films.* Carbohydrate Polymers, 2013. **93**(1): p. 339-346.
205. Shrivastava, N.K., et al., *Nanotube/Biopolymer Nanocomposites.* Bio-based Polymers and Nanocomposites: Preparation, Processing, Properties & Performance, 2019: p. 129-156.
206. Leudjo Taka, A., et al., *Recent development in antimicrobial activity of biopolymer-inorganic nanoparticle composites with water disinfection potential: a comprehensive review.* Environmental Science and Pollution Research, 2021. **28**: p. 26252-26268.
207. Morimune-Moriya, S., *Polymer/nanocarbon nanocomposites with enhanced properties.* Polymer Journal, 2022. **54**(8): p. 977-984.
208. Jiang, J., G. Oberdörster, and P. Biswas, *Characterization of size, surface charge, and agglomeration state of nanoparticle dispersions for toxicological studies.* Journal of Nanoparticle Research, 2009. **11**(1): p. 77-89.
209. Tofighy, M.A. and T. Mohammadi, *5 - Carbon nanotubes-polymer nanocomposite membranes for pervaporation*, in *Polymer Nanocomposite Membranes for Pervaporation*, S. Thomas, S.C. George, and T. Jose, Editors. 2020, Elsevier. p. 105-133.
210. Tevet, O., et al., *Friction mechanism of individual multilayered nanoparticles.* Proceedings of the National Academy of Sciences, 2011. **108**(50): p. 19901-19906.
211. Jordan, J., et al., *Experimental trends in polymer nanocomposites—a review.* Materials Science and Engineering: A, 2005. **393**(1): p. 1-11.
212. Naffakh, M., et al., *Opportunities and challenges in the use of inorganic fullerene-like nanoparticles to produce advanced polymer nanocomposites.* Progress in Polymer Science, 2013. **38**(8): p. 1163-1231.

213. Naskar, A.K., J.K. Keum, and R.G. Boeman, *Polymer matrix nanocomposites for automotive structural components.* Nature nanotechnology, 2016. **11**(12): p. 1026-1030.
214. Kamal, A., et al., *Fabrication techniques of polymeric nanocomposites: A comprehensive review.* Proceedings of the Institution of Mechanical Engineers, Part C: Journal of Mechanical Engineering Science, 2021. **236**(9): p. 4843-4861.
215. Rhim, J.-W., *Potential use of biopolymer-based nanocomposite films in food packaging applications.* Food science and Biotechnology, 2007. **16**(5): p. 691-709.
216. He, S., et al., *Nanotube/Biopolymer Nanocomposites in Bio-based polymers and nanocomposites : preparation, processing, properties and performance.* Composites Science and Technology, 2017. **153**(1): p. 209-221.
217. Mu, M., et al., *Correlation between MWCNT aspect ratio and the mechanical properties of composites of PMMA and MWCNTs.* Materials Research Express, 2018. **5**(4): p. 045305.
218. Pan, P., et al., *Crystallization behavior and mechanical properties of bio-based green composites based on poly (L-lactide) and kenaf fiber.* Journal of Applied Polymer Science, 2007. **105**(3): p. 1511-1520.
219. Shameem, M.M., et al., *A brief review on polymer nanocomposites and its applications.* Materials Today: Proceedings, 2021. **45**: p. 2536-2539.
220. Moniruzzaman, M. and K.I. Winey, *Polymer Nanocomposites Containing Carbon Nanotubes.* Macromolecules, 2006. **39**(16): p. 5194-5205.
221. Khan, W., R. Sharma, and P. Saini, *Carbon nanotube-based polymer composites: synthesis, properties and applications*, in *Carbon Nanotubes-Current Progress of their Polymer Composites*. 2016, InTech: Croatia.
222. Gojny, F.H. and K. Schulte, *Functionalisation effect on the thermo-mechanical behaviour of multi-wall carbon nanotube/epoxy-composites.* Composites Science and Technology, 2004. **64**(15): p. 2303-2308.
223. Sperling, R.A. and W.J. Parak, *Surface modification, functionalization and bioconjugation of colloidal inorganic nanoparticles.* Philosophical Transactions of the Royal Society A: Mathematical, Physical and Engineering Sciences, 2010. **368**(1915): p. 1333-1383.
224. Neouze, M.-A. and U. Schubert, *Surface modification and functionalization of metal and metal oxide nanoparticles by*

organic ligands. Monatshefte für Chemie-Chemical Monthly, 2008. **139**: p. 183-195.
225. Takami, S., *Surface modification of inorganic nanoparticles by organic functional groups*, in *Nanoparticle technology handbook*. 2018, Elsevier. p. 809-812.
226. Rong, M., M. Zhang, and W. Ruan, *Surface modification of nanoscale fillers for improving properties of polymer nanocomposites: a review.* Materials science and technology, 2006. **22**(7): p. 787-796.
227. Erathodiyil, N. and J.Y. Ying, *Functionalization of inorganic nanoparticles for bioimaging applications.* Accounts of chemical research, 2011. **44**(10): p. 925-935.
228. Kango, S., et al., *Surface modification of inorganic nanoparticles for development of organic–inorganic nanocomposites—A review.* Progress in Polymer Science, 2013. **38**(8): p. 1232-1261.
229. Naffakh, M., C. Marco, and G. Ellis, *Development of novel melt-processable biopolymer nanocomposites based on poly(l-lactic acid) and WS2 inorganic nanotubes.* CrystEngComm, 2014. **16**(23): p. 5062-5072.
230. Naffakh, M., C. Marco, and G. Ellis, *Non-Isothermal Cold-Crystallization Behavior and Kinetics of Poly(l-Lactic Acid)/WS2 Inorganic Nanotube Nanocomposites.* Polymers, 2015. **7**: p. 2175-2189.
231. Naffakh, M. and C. Marco, *Isothermal crystallization kinetics and melting behavior of poly(l-lactic acid)/WS2 inorganic nanotube nanocomposites.* Journal of Materials Science, 2015. **50**(18): p. 6066-6074.
232. Shalom, H., et al., *Strong, tough and bio-degradable polymer-based 3D-ink for fused filament fabrication (FFF) using WS2 nanotubes.* Scientific Reports, 2020. **10**(1): p. 1-8.
233. Loffredo, F., et al., *Effect of tungsten disulfide nanotubes on crystallization of polylactide under uniaxial deformation and annealing.* Functional Composite Materials, 2021. **2**(1): p. 3.
234. Tammaro, L., et al. *Effect of tungsten disulfide (WS2) nanotubes on structural, morphological and mechanical properties of poly (L-lactide)(PLLA) films*. in *AIP Conference Proceedings*. 2018. AIP Publishing LLC.
235. Rocher, L., et al., *Interaction of Poly L-Lactide and Tungsten Disulfide Nanotubes Studied by In Situ X-ray Scattering during Expansion of PLLA/WS2NT Nanocomposite Tubes.* Polymers, 2021. **13**(11): p. 1764-1783.
236. Shalom, H., et al., *Nanocomposite of Poly(l-Lactic Acid) with Inorganic Nanotubes of WS2.* Lubricants, 2019. **7**(3): p. 28.

237. Naffakh, M. and A.M. Díez-Pascual, *WS2 inorganic nanotubes reinforced poly(l-lactic acid)/hydroxyapatite hybrid composite biomaterials.* RSC advances, 2015. **5**(80): p. 65514-65525.
238. Golan, O., et al., *Poly(L-lactic acid) Reinforced with Hydroxyapatite and Tungsten Disulfide Nanotubes.* Polymers, 2021. **13**(21).
239. Naffakh, M., A.M. Díez-Pascual, and C. Marco, *Polymer blend nanocomposites based on poly(l-lactic acid), polypropylene and WS2 inorganic nanotubes.* RSC Advances, 2016. **6**(46): p. 40033-40044.
240. Naffakh, M., *Nanocomposite Materials Based on TMDCs WS2 Modified Poly(l-Lactic Acid)/Poly(Vinylidene Fluoride) Polymer Blends.* Polymers, 2021. **13**(13).
241. Naffakh, M. and P.S. Shuttleworth, *Investigation of the Crystallization Kinetics and Melting Behaviour of Polymer Blend Nanocomposites Based on Poly(L-Lactic Acid), Nylon 11 and TMDCs WS2.* Polymers, 2022. **14**(13).
242. Samui, A.B. and T. Kanai, *Polyhydroxyalkanoates based copolymers.* International Journal of Biological Macromolecules, 2019. **140**: p. 522-537.
243. Naffakh, M., C. Marco, and G. Ellis, *Inorganic WS2 nanotubes that improve the crystallization behavior of poly(3-hydroxybutyrate).* CrystEngComm, 2014. **16**(6): p. 1126-1135.
244. Silverman, T., et al., *Morphology and thermal properties of biodegradable poly(hydroxybutyrate-co-hydroxyvalerate)/tungsten disulphide inorganic nanotube nanocomposites.* Materials Chemistry and Physics, 2016. **170**: p. 145-153.
245. Silverman, T., et al., *Effect of WS2 Inorganic Nanotubes on Isothermal Crystallization Behavior and Kinetics of Poly(3-Hydroxybutyrate-co-3-hydroxyvalerate).* Polymers, 2018. **10**(2): p. 166.
246. Chen, Z.Y., et al. *Crystallization behavior of poly (3-hydroxybutyrate-co-3-hydroxyvalerate) with WS2 as nucleating agent*. in *Materials Science Forum*. 2017. Trans Tech Publ.
247. Xiang, H., et al., *Melt-spun microbial poly(3-hydroxybutyrate-co-3-hydroxyvalerate) fibers with enhanced toughness: Synergistic effect of heterogeneous nucleation, long-chain branching and drawing process.* International Journal of Biological Macromolecules, 2019. **122**: p. 1136-1143.
248. Asadi, V., et al., *Poly (ethylene succinate) nanocomposites containing inorganic WS2 nanotubes with improved thermal*

properties: a kinetic study. Composites Part B: Engineering, 2016. **98**: p. 496-507.
249. Asadi, V., et al., *Incorporation of inorganic fullerene-like WS 2 into poly (ethylene succinate) to prepare novel biodegradable nanocomposites: A study on isothermal and dynamic crystallization.* RSC advances, 2016. **6**(6): p. 4925-4935.
250. Lalwani, G., et al., *Tungsten disulfide nanotubes reinforced biodegradable polymers for bone tissue engineering.* Acta biomaterialia, 2013. **9**(9): p. 8365-8373.
251. Lalwani, G., et al. *Carbon and Inorganic Nanostructure Reinforced Polymeric Nanocomposites for Bone Tissue Engineering*. in *Electrochemical Society Meeting Abstracts 225*. 2014. The Electrochemical Society, Inc.
252. Balguri, P.K., D.H. Samuel, and U. Thumu, *A review on mechanical properties of epoxy nanocomposites.* Materials Today: Proceedings, 2021. **44**: p. 346-355.
253. Shneider, M., et al., *Nanoinduced morphology and enhanced properties of epoxy containing tungsten disulfide nanoparticles.* Polymer Engineering & Science, 2013. **53**(12): p. 2624-2632.
254. Gu, H., et al., *An overview of multifunctional epoxy nanocomposites.* Journal of Materials Chemistry C, 2016. **4**(25): p. 5890-5906.
255. Shneider, M., et al., *Tribological performance of the epoxy-based composite reinforced by WS2 fullerene-like nanoparticles and nanotubes.* Physica Status Solidi.A: Applications & Materials Science, 2013. **210**(11): p. 2298.
256. Zohar, E., et al., *The Effect of WS2 Nanotubes on the Properties of Epoxy-Based Nanocomposites.* Journal of Adhesion Science & Technology, 2011. **25**(13): p. 1603.
257. Marjanović, M., et al., *Inorganic fullerene-like nanoparticles and nanotubes of tungsten disulfide as reinforcement of carbon-epoxy composites.* Fullerenes, Nanotubes and Carbon Nanostructures, 2021. **29**(12): p. 1034-1044.
258. Kenig, S., et al., *The mechanical and tribological properties of epoxy nanocomposites with WS2 nanotubes.* Sens. Transducers, 2011. **12**: p. 53-65.
259. Bertasius, P., et al., *Dielectric Properties of Epoxy-Matrix Composites with Tungsten Disulfide Nanotubes.* Journal of Nanomaterials, 2019. **2019**.
260. Zheng, J., R. Ozisik, and R.W. Siegel, *Phase separation and mechanical responses of polyurethane nanocomposites.* Polymer, 2006. **47**(22): p. 7786-7794.

261. Dodiuk, H., et al., *The effect of tungsten disulphide nanoparticles on the properties of polyurethane adhesives.* Journal of Adhesion Science and Technology, 2014. **28**(1): p. 38-52.
262. Zhang, J., *Study of poly (trimethylene terephthalate) as an engineering thermoplastics material.* Journal of applied polymer science, 2004. **91**(3): p. 1657-1666.
263. Ghosh, S., et al., *Reinforcement of poly (methyl methacrylate) by WS2 nanotubes towards antiballistic applications.* Composites Science and Technology, 2021. **207**: p. 108736.
264. Reddy, C.S., A. Zak, and E. Zussman, *WS2 nanotubes embedded in PMMA nanofibers as energy absorptive material.* journal of materials chemistry, 2011. **21**: p. 16086-16093.
265. Naffakh, M. and A.M. Díez-Pascual, *Nanocomposite biomaterials based on poly(ether-ether-ketone) (PEEK) and WS2 inorganic nanotubes.* Journal of Materials Chemistry B, 2014. **2**(28): p. 4509-4520.
266. Levin, T., et al., *Innovative functional polymerization of pyrrole-N-propionic acid onto WS2 nanotubes using cerium-doped maghemite nanoparticles for photothermal therapy.* Scientific Reports, 2021. **11**(1): p. 18883.
267. Raichman, D., D.A. Strawser, and J.-P. Lellouche, *Covalent functionalization/polycarboxylation of tungsten disulfide inorganic nanotubes (INTs-WS 2).* Nano Research, 2015. **8**: p. 1454-1463.
268. Raichman, D., R.B.-S. Binyamini, and J.-P. Lellouche, *A new polythiophene-driven coating method on an inorganic INT/IF-WS 2 nanomaterial surface.* RSC advances, 2016. **6**(6): p. 4490-4504.
269. Tahir, M.N., et al., *Enzyme-mediated deposition of a TiO2 coating onto biofunctionalized WS2 chalcogenide nanotubes.* Advanced Functional Materials, 2009. **19**(2): p. 285-291.
270. Shahar, C., et al., *Surface functionalization of WS2 fullerene-like nanoparticles.* Langmuir, 2010. **26**(6): p. 4409-4414.
271. Sade, H., et al., *Testing of WS2 Nanoparticles Functionalized by a Humin-Like Shell as Lubricant Additives.* Lubricants, 2018. **6**(1): p. 3.
272. Fakhri, A., et al., *Preparation and characterization of WS2 decorated and immobilized on chitosan and polycaprolactone as biodegradable polymers nanofibers: Photocatalysis study and antibiotic-conjugated for antibacterial evaluation.* International Journal of Biological Macromolecules, 2018. **120**: p. 1789-1793.
273. Liu, B.H., et al., *Morphology-modeled chitosan nanoparticles/WS2 nanosheets for advancing the sensing properties of triboelectric acetone sensor*, in *International*

Conference On Optoelectronic And Microelectronic Technology And Application. 2020.
274. Tang, C., et al., *Preparation and properties of chitosan nanocomposites with nanofillers of different dimensions.* Polymer Degradation and Stability, 2009. **94**(1): p. 124-131.
275. Zhang, Y.Z., et al., *Electrospun biomimetic nanocomposite nanofibers of hydroxyapatite/chitosan for bone tissue engineering.* Biomaterials, 2008. **29**(32): p. 4314-4322.
276. Cao, W., L. Yue, and Z. Wang, *High antibacterial activity of chitosan – molybdenum disulfide nanocomposite.* Carbohydrate Polymers, 2019. **215**: p. 226-234.
277. Sethulekshmi, A.S., et al., *MoS2 based nanomaterials: Advanced antibacterial agents for future.* Journal of Controlled Release, 2022. **348**: p. 158-185.
278. Abdeen, Z.I., A.F. El Farargy, and N.A. Negm, *Nanocomposite framework of chitosan/polyvinyl alcohol/ZnO: Preparation, characterization, swelling and antimicrobial evaluation.* Journal of Molecular Liquids, 2018. **250**: p. 335-343.
279. Kumar, S., et al., *Bio-based (chitosan/PVA/ZnO) nanocomposites film: Thermally stable and photoluminescence material for removal of organic dye.* Carbohydrate Polymers, 2019. **205**: p. 559-564.
280. Murali, S., et al., *Bio-based chitosan/gelatin/Ag@ ZnO bionanocomposites: synthesis and mechanical and antibacterial properties.* Cellulose, 2019. **26**: p. 5347-5361.
281. Sirelkhatim, A., et al., *Review on zinc oxide nanoparticles: antibacterial activity and toxicity mechanism.* Nano-micro letters, 2015. **7**: p. 219-242.
282. Vicentini, D.S., A. Smania, and M.C.M. Laranjeira, *Chitosan/poly (vinyl alcohol) films containing ZnO nanoparticles and plasticizers.* Materials Science and Engineering: C, 2010. **30**(4): p. 503-508.
283. Boura-Theodoridou, O., et al., *Performance of ZnO/chitosan nanocomposite films for antimicrobial packaging applications as a function of NaOH treatment and glycerol/PVOH blending.* Food Packaging and Shelf Life, 2020. **23**: p. 100456.
284. Chang, X., et al., *Physicochemical and antimicrobial properties of chitosan composite films incorporated with glycerol monolaurate and nano-TiO2.* Food Hydrocolloids, 2021. **119**: p. 106846.
285. Cano, L., et al., *Effect of TiO2 nanoparticles on the properties of thermoplastic chitosan-based nano-biocomposites obtained by mechanical kneading.* Composites Part A: Applied Science and Manufacturing, 2017. **93**: p. 33-40.

286. Susilowati, E., et al., *Effect of glycerol on mechanical and physical properties of silver-chitosan nanocomposite films.* IOP Conference Series: Materials Science and Engineering, 2016. **107**(1): p. 012041.
287. Chen, Z., et al., *A rapid hemostatic sponge based on large, mesoporous silica nanoparticles and N-alkylated chitosan.* Nanoscale, 2018. **10**(43): p. 20234-20245.
288. Cobos, M., et al., *Chitosan–graphene oxide nanocomposites: Effect of graphene oxide nanosheets and glycerol plasticizer on thermal and mechanical properties.* Journal of Applied Polymer Science, 2017. **134**(30): p. 45092.
289. Cobos, M., et al., *Study on the effect of graphene and glycerol plasticizer on the properties of chitosan-graphene nanocomposites via in situ green chemical reduction of graphene oxide.* International journal of biological macromolecules, 2018. **114**: p. 599-613.
290. Lunkov, A., A. Ilyina, and V. Varlamov, *Antioxidant, antimicrobial, and fungicidal properties of chitosan based films.* Applied Biochemistry and Microbiology, 2018. **54**: p. 449-458.
291. Jia, S., et al., *Morphology, crystallization and thermal behaviors of PLA-based composites: Wonderful effects of hybrid GO/PEG via dynamic impregnating.* Polymers, 2017. **9**(10): p. 528.
292. Haba, D., et al., *Comparative investigation of different silane surface functionalizations of fullerene-like WS2.* Journal of Materials Science, 2015. **50**: p. 5125-5135.
293. Chen, Y., H. Deniz, and L.-C. Qin, *Accurate measurement of the chirality of WS2 nanotubes.* Nanoscale, 2017. **9**(21): p. 7124-7134.
294. Remškar, M. and A. Mrzel, *High-temperature fibres composed of transition metal inorganic nanotubes.* Current Opinion in Solid State and Materials Science, 2004. **8**(2): p. 121-125.
295. Martínez, J.I., et al., *Modelling of adsorption and intercalation of hydrogen on/into tungsten disulphide multilayers and multiwall nanotubes.* Physical Chemistry Chemical Physics, 2018. **20**(17): p. 12061-12074.
296. Schuffenhauer, C., et al., *How stable are inorganic fullerene-like particles? Thermal analysis (STA) of inorganic fullerene-like NbS2, MoS2, and WS2 in oxidizing and inert atmospheres in comparison with the bulk material.* Physical Chemistry Chemical Physics, 2004. **6**(15): p. 3991-4002.
297. Sekine, T., et al., *Raman scattering in layered compound 2H-WS2.* Solid State Communications, 1980. **35**(4): p. 371-373.

298. Staiger, M., et al., *Excitonic resonances in WS 2 nanotubes.* Physical Review B, 2012. **86**(16): p. 165423.
299. Grinberg, O., et al., *Raman scattering from single WS2 nanotubes in stretched PVDF electrospun fibers.* Physical Chemistry Chemical Physics: PCCP, 2017. **19**(28): p. 18443-18451.
300. Berkdemir, A., et al., *Identification of individual and few layers of WS2 using Raman Spectroscopy.* Scientific Reports, 2013. **3**(1755).
301. Daniel, M.F., et al., *Infrared and Raman study of WO3 tungsten trioxides and WO3, xH2O tungsten trioxide tydrates.* Journal of Solid State Chemistry, 1987. **67**(2): p. 235-247.
302. Anukul, K.T., et al., *Controlled synthesis of WO3 nanostructures: optical, structural and electrochemical properties.* Materials Research Express 2019. **6**(2): p. 025006.
303. Liang, F., et al., *Carbon nanotubes decorated with gold nanoparticles.* Nanomedicine: Nanotechnology, Biology, and Medicine, 2018. **14**(5): p. 1788.
304. Sedova, A., et al., *Synthesis of magnetic FeWO4 nanoparticles and their decoration of WS2 nanotubes surface.* Journal of Materials Science, 2017. **52**(11): p. 6376–6387.
305. Piskunov, S., et al., *First-Principles Evaluation of the Morphology of WS2 Nanotubes for Application as Visible-Light-Driven Water-Splitting Photocatalysts.* ACS Omega, 2019(1): p. 1434.
306. Morgan, D.J., *Core-level spectra of powdered tungsten disulfide, WS2.* Surface Science Spectra, 2018. **25**(1): p. 014002.
307. Tsverin, Y., et al., *Synthesis and characterization of WS2 nanotube supported cobalt catalyst for hydrodesulfurization.* Materials Research Bulletin, 2012. **47**(7): p. 1653-1660.
308. lu, Z., S. M. Kanan, and C.P. Tripp, *Synthesis of high surface area monoclinic WO3 particles using organic ligands and emulsion based methods.* The Royal Society of Chemistry, 2002. **12**: p. 983-989.
309. Kavoori, N., et al., *Torsional Stick-Slip Behavior in WS(2) Nanotubes.* Physical review letters, 2008. **101**: p. 195501.
310. Eriksson, M., J.G.P. Goossens, and T. Peijs, *Influence of the Solidification Process on the Mechanical Properties of Solid-State Drawn PCL/Sepiolite Nanocomposite Tapes.* Fibers, 2020. **8**: p. 70.
311. Zarinwall, A., et al., *Comprehensive Characterization of APTES Surface Modifications of Hydrous Boehmite Nanoparticles.* Langmuir, 2021. **37**(1): p. 171-179.
312. Meroni, D., et al., *A Close Look at the Structure of the TiO2-APTES Interface in Hybrid Nanomaterials and Its Degradation*

Pathway: An Experimental and Theoretical Study. The Journal of Physical Chemistry C, 2017. **121**(1): p. 430-440.
313. Liu, Y., et al., *APTES Modification of Molybdenum Disulfide to Improve the Corrosion Resistance of Waterborne Epoxy Coating.* Coatings, 2021. **11**: p. 178.
314. Wang, Y., et al., *Enhanced quantum efficiency from a mosaic of two dimensional MoS2 formed onto aminosilane functionalised substrates.* Nanoscale, 2016. **8**(24): p. 12258-12266.
315. Ryu, S., K. Kim, and J. Kim, *Silane surface treatment of boron nitride to improve the thermal conductivity of polyethylene naphthalate requiring high temperature molding.* Polymer Composites, 2018. **39**: p. E1692-E1700.
316. Miranda, A., L. Martínez, and P.A.A. De Beule, *Facile synthesis of an aminopropylsilane layer on Si/SiO2 substrates using ethanol as APTES solvent.* MethodsX, 2020. **7**: p. 100931.
317. Leung, Y.S.S., *Novel biopolymer constructs: physical properties and antimicrobial efficacy*, in *Warwick Manufacturing Group*. 2018, University of Warwick

318. Majoul, N., S. Aouida, and B. Bessaïs, *Progress of porous silicon APTES-functionalization by FTIR investigations.* Applied Surface Science, 2015. **331**: p. 388-391.
319. Jiang, T., et al., *Enhanced mechanical properties of silanized silica nanoparticle attached graphene oxide/epoxy composites.* Composites Science and Technology, 2013. **79**: p. 115-125.
320. Haeri, S.Z., M. Asghari, and B. Ramezanzadeh, *Enhancement of the mechanical properties of an epoxy composite through inclusion of graphene oxide nanosheets functionalized with silica nanoparticles through one and two steps sol-gel routes.* Progress in Organic Coatings, 2017. **111**: p. 1-12.
321. Maria Chong, A.S. and X.S. Zhao, *Functionalization of SBA-15 with APTES and Characterization of Functionalized Materials.* The Journal of Physical Chemistry B, 2003. **107**(46): p. 12650-12657.
322. Selli, D., et al., *Optimizing pegylation of TiO2 nanocrystals through a combined experimental and computational study.* Chemistry of Materials, 2019. **31**(18): p. 7531-7546.
323. Wei, S., et al., *Improved Electrochemical Performance of NTs-WS2@ C Nanocomposites for Lithium-Ion and Sodium-Ion Batteries.* ACS Applied Materials & Interfaces, 2022. **14**(41): p. 46386-46400.

324. Bertolazzi, S., et al., *Molecular chemistry approaches for tuning the properties of two-dimensional transition metal dichalcogenides.* Chemical Society Reviews, 2018. **47**(17): p. 6845-6888.
325. Voiry, D., et al., *Covalent functionalization of monolayered transition metal dichalcogenides by phase engineering.* Nature chemistry, 2015. **7**(1): p. 45-49.
326. Sade, H. and J.P. Lellouche, *Functionalization of Tungsten Disulfide Nanotubes with a Conformal Humin-Like Shell.* Advanced Materials Interfaces, 2016. **3**(20): p. 1600307.
327. Rennhofer, H. and B. Zanghellini, *Dispersion State and Damage of Carbon Nanotubes and Carbon Nanofibers by Ultrasonic Dispersion: A Review.* Nanomaterials, 2021. **11**(6): p. 1469.
328. Chibowski, E. and A. Waksmundzki, *A relationship between the zeta potential and surface free energy changes of the sulfur/n-heptane—water system.* Journal of Colloid and Interface Science, 1978. **66**(2): p. 213-219.
329. Talavera-Pech, W., et al., *Effects of different amounts of APTES on physicochemical and structural properties of amino-functionalized MCM-41-MSNs.* Journal of Sol-Gel Science & Technology, 2016. **80**(3): p. 697-708.
330. Meng, X., et al., *Supertough PLA-Silane Nanohybrids by in Situ Condensation and Grafting.* ACS Sustainable Chemistry & Engineering, 2018. **6**(1): p. 1289-1298.
331. Naffakh, M., C. Marco, and G. Ellis, *Development of novel melt-processable biopolymer nanocomposites based on poly(L-lactic acid) and WS2 inorganic nanotubes*. 2014. p. 5062.
332. Tammaro, L., et al. *Effect of tungsten disulfide (WS2) nanotubes on structural, morphological and mechanical properties of poly(L-lactide) (PLLA) films*. in *9TH International Conference on "Times of Polymers and Composites"*. American Institute of Physics.
333. Wan, C., et al., *Stress-oscillation behaviour of semi-crystalline polymers: the case of poly(butylene succinate).* Soft Matter, 2018. **14**(45): p. 9175-9184.
334. Lu, Y., et al., *Improved mechanical properties of polylactide nanocomposites-reinforced with cellulose nanofibrils through interfacial engineering via amine-functionalization.* Carbohydrate Polymers, 2015. **131**: p. 208-217.
335. Metın, D., et al., *The effect of interfacial interactions on the mechanical properties of polypropylene/natural zeolite composites.* Composites Part A: Applied Science and Manufacturing, 2004. **35**(1): p. 23-32.

336. Lim, H. and S.W. Hoag, *Plasticizer effects on physical-mechanical properties of solvent cast Soluplus® films.* AAPS PharmSciTech, 2013. **14**(3): p. 903-910.
337. Naffakh, M., et al., *The Effect of WS2 Nanosheets on the Non-Isothermal Cold- and Melt-Crystallization Kinetics of Poly(l-lactic acid) Nanocomposites.* Polymers, 2021. **13**(13): p. 2214.
338. Pawlak, A. and M. Mucha, *Thermogravimetric and FTIR studies of chitosan blends.* Thermochimica Acta, 2003. **396**(1): p. 153-166.
339. Brugnerotto, J., et al., *An infrared investigation in relation with chitin and chitosan characterization.* Polymer, 2001. **42**(8): p. 3569-3580.
340. Kumari, S., et al., *Extraction and characterization of chitin and chitosan from fishery waste by chemical method.* Environmental Technology & Innovation, 2015. **3**: p. 77-85.
341. Mauricio-Sánchez, R.A., et al., *FTIR spectroscopy studies on the spontaneous neutralization of chitosan acetate films by moisture conditioning.* Vibrational Spectroscopy, 2018. **94**: p. 1-6.
342. Prateepchanachai, S., et al., *Mechanical properties improvement of chitosan films via the use of plasticizer, charge modifying agent and film solution homogenization.* Carbohydrate Polymers, 2017. **174**: p. 253-261.
343. Kongjao, S., S. Damronglerd, and M. Hunsom, *Purification of crude glycerol derived from waste used-oil methyl ester plant.* Korean Journal of Chemical Engineering, 2010. **27**(3): p. 944-949.
344. Nanda, M., et al., *Purification of crude glycerol using acidification: effects of acid types and product characterization.* Austin J. Chem. Eng, 2014. **1**(1): p. 1-7.
345. Chen, P., et al., *Unexpected Plasticization Effects on the Structure and Properties of Polyelectrolyte Complexed Chitosan/Alginate Materials.* ACS Applied Polymer Materials, 2020. **2**(7): p. 2957-2966.
346. Lawrie, G., et al., *Interactions between Alginate and Chitosan Biopolymers Characterized Using FTIR and XPS.* Biomacromolecules, 2007. **8**(8): p. 2533-2541.
347. Chen, Z., et al., *Intermolecular interactions in electrospun collagen–chitosan complex nanofibers.* Carbohydrate Polymers, 2008. **72**(3): p. 410-418.
348. Rivero, S., et al., *An Insight into the Role of Glycerol in Chitosan Films.* Food Biophysics, 2016. **11**(2): p. 117-127.
349. Kachel-Jakubowska, M., A. Matwijczuk, and M. Gagoś, *Analysis of the physicochemical properties of post-manufacturing waste*

derived from production of methyl esters from rapeseed oil. International Agrophysics, 2017. **31**(2): p. 175.
350. Wahba, M.I., *Enhancement of the mechanical properties of chitosan.* Journal of Biomaterials Science, Polymer Edition, 2020. **31**(3): p. 350-375.
351. Nunthanid, J., et al., *Physical Properties and Molecular Behavior of Chitosan Films.* Drug Development and Industrial Pharmacy, 2001. **27**(2): p. 143-157.
352. Lavorgna, M., et al., *Study of the combined effect of both clay and glycerol plasticizer on the properties of chitosan films.* Carbohydrate Polymers, 2010. **82**(2): p. 291-298.
353. Zawadzki, J. and H. Kaczmarek, *Thermal treatment of chitosan in various conditions.* Carbohydrate Polymers, 2010. **80**(2): p. 394-400.
354. Rodrigues, C., et al., *Mechanical, Thermal and Antimicrobial Properties of Chitosan-Based-Nanocomposite with Potential Applications for Food Packaging.* Journal of Polymers and the Environment, 2020. **28**(4): p. 1216-1236.
355. Khouri, J., A. Penlidis, and C. Moresoli, *Heterogeneous method of chitosan film preparation: Effect of multifunctional acid on film properties.* Journal of Applied Polymer Science, 2020. **137**(18): p. 48648.
356. Tao, Y., et al., *Tensile strength optimization and characterization of chitosan/TiO2 hybrid film.* Materials Science and Engineering: B, 2007. **138**(1): p. 84-89.
357. Jampafuang, Y., A. Tongta, and Y. Waiprib, *Impact of Crystalline Structural Differences Between α- and β-Chitosan on Their Nanoparticle Formation Via Ionic Gelation and Superoxide Radical Scavenging Activities.* Polymers, 2019. **11**(12): p. 2010.
358. Hajji, S., et al., *Structural differences between chitin and chitosan extracted from three different marine sources.* International Journal of Biological Macromolecules, 2014. **65**: p. 298-306.
359. Gbenebor, O.P., et al., *Acetylation, crystalline and morphological properties of structural polysaccharide from shrimp exoskeleton.* Engineering Science and Technology, an International Journal, 2017. **20**(3): p. 1155-1165.
360. Hao, G., et al., *Physicochemical characteristics of chitosan from swimming crab (Portunus trituberculatus) shells prepared by subcritical water pretreatment.* Scientific Reports, 2021. **11**(1): p. 1-9.
361. Susilowati, E., et al., *Effect of glycerol on mechanical and physical properties of silver-chitosan nanocomposite films.* IOP

Conference Series: Materials Science and Engineering, 2016. **107**: p. 012041.
362. Barbosa, A.N., et al., *Straightforward identification of monolayer WS2 structures by Raman spectroscopy.* Materials Chemistry and Physics, 2020. **243**: p. 122599.
363. Wang, F., et al., *Strain-induced phonon shifts in tungsten disulfide nanoplatelets and nanotubes.* 2D Materials, 2016. **4**(1): p. 015007.
364. Deka, B., D. Mohanta, and A. Saha, *Featuring exfoliated 2D stacks into fractal-like patterns in WS2/carboxy methyl cellulose nanocomposites.* Surfaces and Interfaces, 2022. **29**: p. 101727.
365. Castelló, M.E., et al., *Production and characterization of chitosan and glycerol-chitosan films.* MRS Advances, 2018. **3**(61): p. 3601-3610.
366. Theerakarunwong, C. and D. Boontong, *Removal and recyclable chitosan nanowires: Application to water soluble dyes*. Results in Chemistry, 2020. **2**: p. 100024.
367. Chang, S.-H., et al., *pH Effects on solubility, zeta potential, and correlation between antibacterial activity and molecular weight of chitosan.* Carbohydrate Polymers, 2015. **134**: p. 74-81.
368. Yilmaz Atay, H., *Antibacterial activity of chitosan-based systems*, in *Functional chitosan*. 2019, Springer. p. 457-489.
369. Srinivasa, P.C., M.N. Ramesh, and R.N. Tharanathan, *Effect of plasticizers and fatty acids on mechanical and permeability characteristics of chitosan films.* Food Hydrocolloids, 2007. **21**(7): p. 1113-1122.
370. Akter, N., et al., *Thermomechanical, barrier, and morphological properties of Chitosan-reinforced starch-based biodegradable composite films.* Journal of Thermoplastic Composite Materials, 2012. **27**: p. 933-948.
371. Geng, Z., et al., *Mixed matrix membranes composed of WS2 nanosheets and fluorinated poly(2,6-dimethyl-1,4-phenylene oxide) via Suzuki reaction for improved CO2 separation.* Journal of Membrane Science, 2018. **565**: p. 226-232.
372. Cha, J.-H., et al., *2D WS2-edge functionalized multi-channel carbon nanofibers: effect of WS2 edge-abundant structure on room temperature NO2 sensing.* Journal of Materials Chemistry A, 2017. **5**(18): p. 8725-8732.
373. Hassani, N., et al., *Gas Permeability and Selectivity of a Porous WS2 Monolayer.* JOURNAL OF PHYSICAL CHEMISTRY C, 2021. **125**(45): p. 25055-25066.
374. Siripatrawan, U. and P. Kaewklin, *Fabrication and characterization of chitosan-titanium dioxide nanocomposite film*

as ethylene scavenging and antimicrobial active food packaging. Food Hydrocolloids, 2018. **84**: p. 125-134.
375. Escárcega-Galaz, A.A., et al., *Mechanical, structural and physical aspects of chitosan-based films as antimicrobial dressings.* International journal of biological macromolecules, 2018. **116**: p. 472-481.
376. Liu, X., et al., *Membrane destruction-mediated antibacterial activity of tungsten disulfide (WS 2).* RSC advances, 2017. **7**(60): p. 37873-37880.
377. Agustin, Y.E. and K.S. Padmawijaya, *Effect of glycerol and zinc oxide addition on antibacterial activity of biodegradable bioplastics from chitosan-kepok banana peel starch.* IOP Conference Series: Materials Science and Engineering, 2017. **223**(1): p. 012046.
378. Doi, Y., *Glycerol metabolism and its regulation in lactic acid bacteria.* Applied Microbiology and Biotechnology, 2019. **103**(13): p. 5079-5093.